Enhancing Retention Properties of Sulphide Scale Inhibitor for High Pressure and Temperature Environments with High Salinity

Yasmin Hayatgheib
School of Mechanical Engineering
University of Leeds

Submitted in accordance with the requirements for the degree of
Doctor of Philosophy

8th of June 2022

Intellectual Properties

The candidate confirms that the work submitted is her own and that appropriate credit has been given where reference has been made to the work of others.

Dedication

I am dedicating this thesis to my grandparents whom I lost during this PhD degree.
Mamani, Babaei I love you both dearly. You will forever remain alive in my heart and memories.
I wished I spent more time with you guys when I had the chance.

Acknowledgements

In the accomplishment of my PhD research project, I had the help and guidance of phenomenal people, who deserve my deepest gratitude. Firstly, I am indebted to Prof.Anne Neville that gave me the unique and life-changing opportunity of working in her research group, iFs (Institute of Functional Surfaces) at the University of Leeds. Deepest gratitude to her, Dr Richard Barker and Dr Wassim Taleb for their supervision, encouragement, support, interest and invaluable comments throughout this project. Many thanks to Dr Thibaut Charpentier, Dr Gregory de Boer, Dr Frederick Pessu, Dr Paul Thornton for their endless support, ideas, and guidance.

I would like to expand my gratitude to Dr Salima Baraka-Lokmane for her endless support, directly and indirectly. Her invaluable advice during difficult times of the pandemic and the twisted journey of this PhD, helped me to keep my hopes strong and make the impossible possible, thanks Salima! Without you, this would have not come true! Very special gratitude goes to all in the TotalEnergies research team for giving me the chance to research by sponsoring this interesting and novel project and providing me with the scholarship. A unique project that not only added an immeasurable amount of knowledge, skills, and experience to me but also helped me to build up my networks, character and enriched my personality.

Many thanks to the technician team Jordan Thomas, Ryan Smith, Michael Huggan for their tireless help in the maintenance of the labs and testing equipment and as well as the administrative team at the University of Leeds and iFS group, Vicky Masters, Tom Lynch and Fiona Slade.

I would like to deeply appreciate my dear sister, Dr Niki Dourver Hayatgheib who has backed me through tremendous moral and emotional support in my whole life, without that I would have not been able to achieve any of this. Thank you, Greg, Alexandre, Edona, Eli, Eni, Ryan and Pedro for being such great companions and friends. For supporting and encouraging me to move forward, to aim high, strive for my goals and never to give up. A big thank you to my parents, Roya Ghadessi and Dr Hamid Hayatgheib. I know there will be nothing compared to what they have dedicated to my education and self-growth, thanks mum, thanks dad!

Abstract

With raising potential for nearly all producing oil wells to sour over time, prevention of sulphide scale is a developing area of focus, specifically in relation to sandstone reservoirs. Market demand has pushed the industry to extract oil and gas from wells with harsher reservoir conditions i.e. high temperatures and pressures (HTHP) containing high saline formation water that are accompanied by a range of scaling issues such as barium sulphate, calcium carbonate ($BaSO_4$ and $CaCO_3$), mixed zinc, lead and iron sulphide (ZnS/PbS/FeS).

Based on laboratory test results, sulphonic-*co*-maleic acid-based scale inhibitor (SI), FL1-DETA successfully disperses freshly formed ZnS scales at threshold concentration. However, Elgin field trial at HTHPHS (i.e. 196 °C, 15000 psi, 292.3 g/L) conditions has shown that the inhibitor suffers from poor retention properties on sandstone reservoirs when applied as a squeeze treatment and has no effect on PbS scale.

By characterising FL1-DETA, the source of its poor retention on sandstone particles was identified and a modified version based on soluble polyaniline structure was synthesised. PSS-*co*-MA—PANI, showed enhanced adsorption on sandstone with thermal stability up to 385°C. The SI was fully compatible with Elgin production water composition, i.e. [calcium] > 20 g/L, [barium] > (3 g/L, [zinc] > 100 g/L and [Pb] > 10 g/L.

Static test results indicate disrupted sulphide scale crystal growth caused by PSS-*co*-MA—PANI wrapping around ZnS crystals and successful inhibition of $BaSO_4$ and $CaCO_3$ crystals. The minimum effective dose at 125 °C and 635 psi were identified as < 5 mg/L against ZnS and <100 mg/L against PbS, using dynamic tube blocking tests. Sandpack profiles show pure adsorption and gradual release of the inhibitor at room temperature over more than 200 pore volumes. Therefore, it is anticipated that PSS-*co*-MA—PANI can perform as a successful squeeze treatment candidate against ZnS with performance against PbS.

Abbreviations

Γ_{app}	Apparent Adsorption
AA	Acrylate acid
AAS	Atomic adsorption spectroscopy
AMPS	2-Acrylamido-2-methylpropane sulfonic acid
[**Ca^{2+}**]	Calcium Concentration
[**FL1-DETA**]	FL1-DETA Concentration
AFM	Atomic Force Microscopy
ATMP	Amino Trimethylene Phosphonic Acid (Scale Inhibitor)
ATR-FTIR	Attenuated Total Reflectance Fourier Transform Infrared
amu	Atomic mass unit
AW	Anionic water i.e. Brine Consist of Anions of the Production Water composition
AW*	Anionic water i.e. Brine Consist of Anions of the Simple Brine Composition
Ba^{2+}—SI	Barium Scale Inhibitor Complex
BET	Brunauer-Emmett-Teller (BET) Surface Area Analysis
BHPMP	Bis-hexamethylenetriamine penta phosphonate acid
CW	Cationic Water i.e. Brine Consist of Cations of the Production Water Composition
CW*	Cationic water i.e. Brine Consist of Cations of the Simple Brine Composition
D—R Model	Dubinin-Kaganer-Radushkevich Model
Da	Dalton (Unit)
DETPMP	Diethylene Triamine Penta (Methylene Phosphonic Acid) (Scale Inhibitor)
DI	Dionized Water
dP	Differential pressure
DV	Dead Volume

EDS/EDX	Energy-Dispersive Xray Spectroscopy
EOR	Enhanced Oil Recovery
FAU	Formazine attenuation unit-turbidity measurement unit
FW	Formation Water
HDTMP	Hexamethylene Diamine-N,N,N',N'-Tetra Kis (Scale Inhibitor)
HEDP	Hydroxy,1-Hydroxyethylidene-1,1-Diphosphonic Acid (Scale Inhibitor)
HP	High Pressure
HS	High Salinity
H_2S	Hydrogen Sulphide
HT	High Temperature
I	Ionic Strength
ICP	Inductive Coupled Plasma Spectroscopy
IE	Inhibitor Efficiency
LDH	Layered Double Hydroxide
LSSW	Low-Sulphate Seawater
M^{2+}—SI	Complex of Metallic Cation Divalent With Scale Inhibitor
MIC	Minimum Inhibitor Concentration
MED	Minimum Effective Dose
MT	Main treatment
PF	Post flush
pH	Potential hydrogen activity i.e. $-\text{Log}_{10}$ $[H^+]$ ($[H^+]$ in mol/L)
pKa	$-\text{Log}_{10}$ Ka
PMA	Poly(methyl acrylate)
PPCA	Polyphosphono Carboxylic Acid (Scale Inhibitor)
ppm	Parts Per Million (Unit)
PV	Pore Volume
S_{BET}	Surface Area Calculated by BET Method
S_{BJH}	Surface Area Calculated by BJH Method
SEM	Scanning Electron Microscopy
SI/FW	Scale Inhibitor Blended in Formation Water

SI/FW—Sand	Static Jar Test System for Coupled Adsorption/Precipitation
SI/NaCl 3.5 %	SI blended in NaCl 3.5% Brine
SI	Scale Inhibitor
SR	Saturation Ratio
SRP	Sulphate Reduction Plant
SW	Seawater
TDS	Total Dissolved Salt
TGA	Thermogravimetric Analysis
UV-Vis	UV-Visible Spectroscopy
$\mathbf{V}_{BET}$	Volume Calculated by BET Method

Contents

List of Figures

List of Tables

LIST OF TABLES

List of Equations

CHAPTER 1

Introduction

1.1 Background

Oilfield scale deposition is one of the most important flow assurance challenges facing the industry, particularly in mature water-flooded basins. High salinity reservoir water carries various elements of the contacting rock into the production water and causes scale deposits inside the installation pipes or blockage of the reservoir pores [2]. There are various methods to mitigate oilfield scale, amongst which chemical inhibition is particularly recommended. The scaling process is inhibited by either stopping the nucleation or decelerating crystal growth. The inhibiting chemicals can generally be injected in a dedicated continuous injection line, or bull-headed as a batch treatment into the formation, commonly known as squeeze treatment. A squeeze treatment is carried out by injecting a large amount of polymeric SI into the reservoir with the expectation of gradual release above the minimum effective dose (MED) over a period of time [3]. As shown in Figure 1.1, despite shutdown periods being required for squeeze treatment, the approach is preferable as the treatment protects from the wellbore area to the top side.

Successful squeeze treatment has long lifetime of SI gradual release and its beneficial

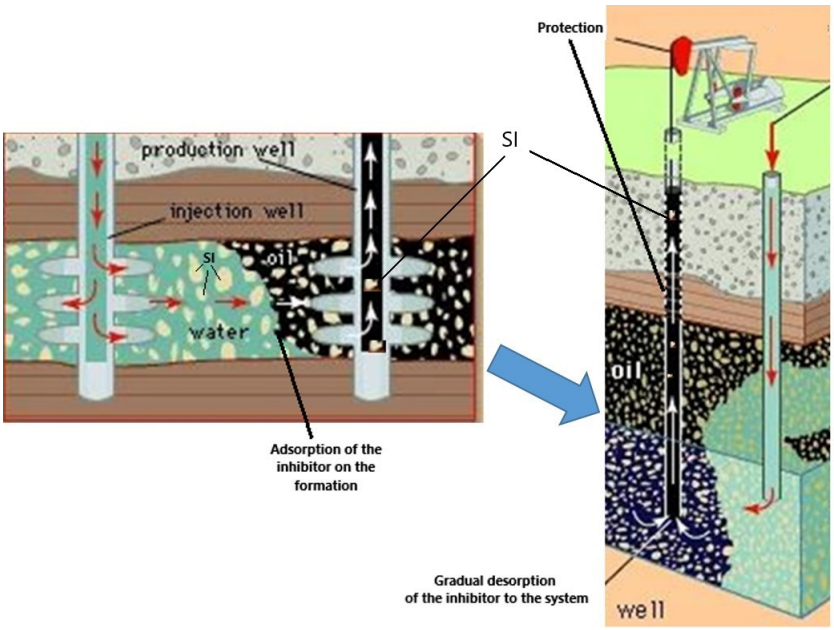

Figure 1.1: Schematic of squeezed inhibitor. Injection the SI to the formation, adsorption of it and the gradual release of it upon production return, giving protection to the tubing and top refinery equipment, such as pumps, hydrocyclones and separators.

effect can be sustained for more than 6 months [4]. Nevertheless, in practice, the total amount of the injected SI will not adsorb effectively on the rock formation. Thus, it desorbs at a higher rate from the reservoir rock and drops the inhibitor concentration

below MED [1]. This forces another squeeze treatment on the well whereby considering the demanded shutdown periods and the followed production loss during the procedure, it is economically preferable to prolong the squeeze lifetime and its effect [4].

Due to the increasing market value and demand for oil and gas, matured reservoirs are exploited over time. This means that extraction needs to be from the reservoir with harsher conditions [5]. The development of high pressure/ high temperature/ high salinity (HTHPHS) fields means the thermal and retention stability of the SI will be of paramount importance, mainly because the inhibitors' functional groups are expected to survive in the formation for an extended period of time (squeeze lifetime). However, designing suitable chemistry that can be deployed during a squeeze treatment at HTHPHS conditions has further challenges. Field results analysis have proven that scale inhibitors, in general, are less effective in HT fields. This is attributable to the fact that at these conditions, crystal growth inhibition becomes more difficult due to the thermal degradation of the deployed SI diminishing the SI adsorption on to the reservoir rock [6]. Furthermore, most HTHP reservoirs contain hydrogen sulphide (H_2S) gas produced by biotic and abiotic reactions [7]. Due to the chemical decomposition of already deployed chemicals over many years of production, as well as drilling products, there is a high potential that nearly all reservoirs sour over time including the ones currently producing only routine scales such as barite [8]. This means along with routine scales, the formation of exotic scales i.e. sulphide scales, are a raising concern for the oil and gas industry. Hence, a successful SI candidate should ideally suppress the formation of both scale types.

For many years, phosphonate-based chemicals showed promising inhibition efficacy during squeeze treatment by mitigating scale deposition of routine scales such as $CaCO_3$, $BaSO_4$ and $CaSO_4$. However, these chemistries have low thermal stability for HTHP squeeze treatments [6] purposes and show poor or temporary performance toward exotic scales i.e. sulphide scales [5]. With the implementation of environmental legislation in the North Sea entailing phase substitution of phosphonate-based inhibitors, polymeric based SI [9] are the next candidate to this end. However, polymeric SIs inherently suffer from poor retention properties in squeeze treatment procedure as compared to their old rivals, phosphonates [6, 9]. Similar to phosphonates, polymeric SIs are more or less effective for routine scales and they offer little or no performance for sulphide scales [9, 10]. Unfortunately most candidates of this group of SIs, have shown to be sensitive to the salinity levels of the brine and are not suitable for high salinity fields [11] such as Elgin. Elgin fields, Figure 1.2, are deep HPHT (1100 bars (15954 psi) and 196°C (385°F)) gas condensate reservoirs situated in the Central Graben of the UKCs $\sim$ 240 km East of Aberdeen. The field's reservoir lithology is mainly sandstone and the water composition salinity has identified as one of the highest with 292030 mg/L total dissolved salt and 35 ppm of H_2S [6].

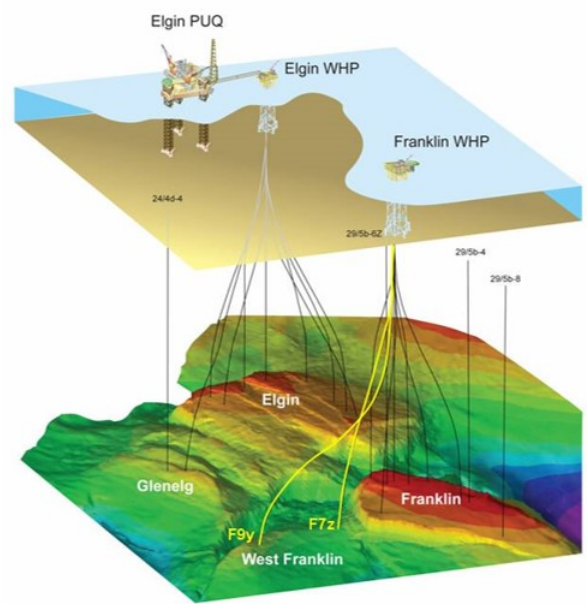

Figure 1.2: Elgin field and its location

FL1-DETA is a polystyrene sulfonic acid polymer that is co-polymerised with maleic acid and doped with diethylene tri-amine (DETA). Figure 1.3, schematically depicts this doping reaction and each compounds' structure. It is anticipated that every two DETA molecules are able to bridge up to five FL1 compounds at the same time.

Theoretically, the polystyrene sulfonic acid *co*-maleic acid copolymer named as FL1, should be able to inhibit the formation of $CaCO_3$ and $BaSO_4$ by its (-COOH) functional groups and the sulfonic acid group through steric repulsion effect [12]. By doping FL1 with DETA, thermal stability of FL1 improves up to 250 °C. This addition has shown to help with the inhibition of ZnS, through the existence of non-paired active electrons that are located on the DETA (nitrogen) structure [12]. The non paired electrons bond with Zn^{2+}, Fe^{2+} thus it is anticipated to delay the ZnS formation. It is worth noting, that the addition of DETA to FL1 structure reduces the number of carboxylic acid groups as an active site on the main compound, thus the decrease in inhibiting efficiency for routine scales such as $CaCO_3$. FL1 on its own also, shows inhibition performance toward ZnS by dispersing the scale through its negative charges. Therefore, it is believed that the presence of non paired electrons on DETA structure will improve FL1 performance on dispersing the formed ZnS [12]. Similar to FL1-DETA, FL1 has no performance toward PbS inhibition. According to previous research [12], polymeric scale inhibitor FL1-DETA, has shown positive performance in ageing and tube blocking tests toward zinc sulphide scale at high temperatures for low to medium salinity brine (maximum of 90 g/L TDS[1]) compositions with no barium cation included. This means that when applied as a continuous injection, FL1-DETA can disperse ZnS at very small doses (i.e.

[1]Total dissolved salt

7 mg/L). Unfortunately, FL1-DETA has shown no performance against PbS as well as limited to no retention properties in Elgin field trials on sandstone reservoirs during squeeze treatment application.

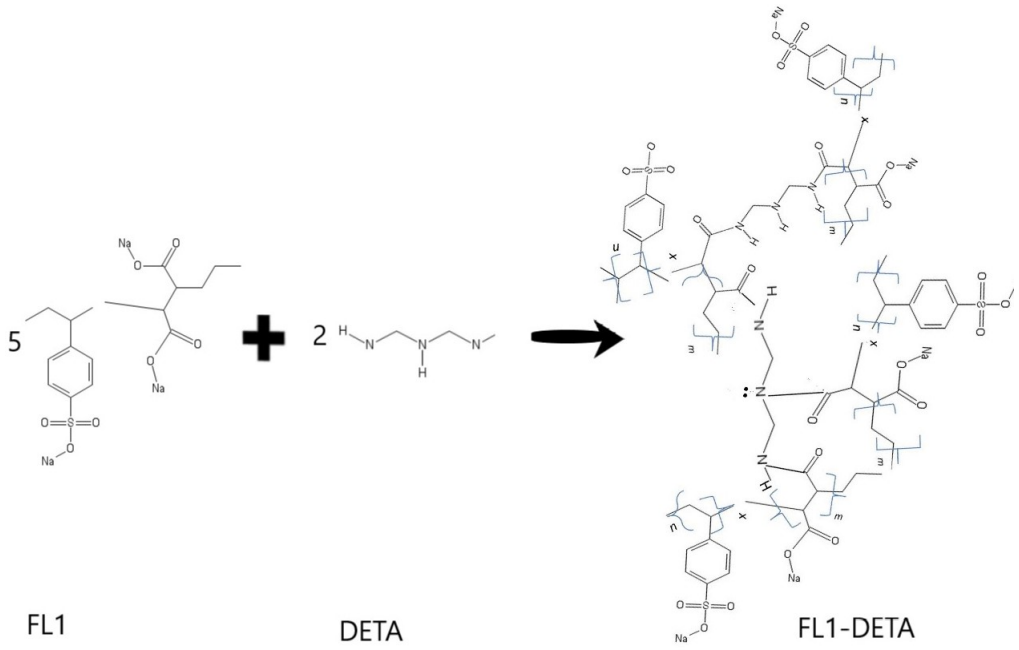

Figure 1.3: Schematic of DETA, FL1 and FL1-DETA structure with their stoichiometric reaction

1.2 Motivation

As the mechanism of sulphide scales (i.e. formation and inhibition, for HTHPHS and gas condensate field) is not fully clear, finding a suitable squeeze inhibitor for these types of scales is even more perplexing [6]. However, it is known that $CaCO_3$, ZnS, PbS and FeS solubility increases as fluid acidity increases [13, 14], whilst $BaSO_4$ solubility remains intact, with pH only affecting its morphology [15]. Therefore, acid wash treatment can be a good remedy for most scale build up. However, such treatment is accompanied by major drawbacks since it creates an additional risk to construction material such as corrosion and on-site employees especially considering the high temperature and pressure conditions such as producing/releasing H_2S gas [16, 17]. To this end, the development of squeezable SI that specifically withstands the severe conditions of HTHPHS fields that could not only suppress the formation of routine scales but sulphide scales is a crucial ongoing demand for the relevant industries. Many researchers have attempted to develop a sulphide scale inhibitor for HTHPHS squeeze treatment purposes with chemistry that will be compliant with the new environmental legislation [8]. Nevertheless, the majority of the deployed chemistries were mostly acting as dis-

persants with a naturally poor squeeze and retention abilities and more suitable for continuous injection [18, 19, 20, 21].

1.3 Aims and objectives

This project aims to enhance the retention properties of a specific sulfonic-*co*-maleic acid based SI (FL1-DETA) onto the sandstone rock formation while maintaining its thermal stability. The overall objective of this work is to modify FL1-DETA to be applied as a squeeze treatment chemical in Elgin field. The newly developed / modified inhibitor with improved retention properties, should be suitable for HTHPHS field and present long squeeze lifetime through controlled desorption kinetics. It is expected that the final product shows successful inhibition performance toward routine as well as exotic scale with low minimum inhibition concentration value (MIC). This means that the scale inhibitor should be effective at sub-stoichiometric concentrations. To this end, the first step of the project is to identify the main reason for the FL1-DETA poor affinity to sandstone particles through determining its method of interaction with the reservoir and brine chemistry followed by the research question of how to improve it in accordance with industrial applications and environmental regulations. As a result, modification methods are reviewed, and the method of choice is assessed. The modified SI is then tested under various oilfield scenarios, including different scaling environments and flow regimes changes. This is summarised in the flow chart presented in Figure 1.4.

Overall, the project starts with a focused literature review to explore the state of the art in chemical retention stability enhancement and attempts to:

1. ***Fill the gaps of available information on FL1 and FL1-DETA*:**

   This includes characterisation of both active moieties of the SI which are FL1 and DETA, separately and together such as:

   - Thermal stability
   - Zeta potential
   - Identification of available functional groups
   - Compatibility with production water and injection water

   As the project is mainly focusing on the retention and thermal stability of the SI on the sandstone reservoir rock, the characterisation of sandstone particles is also required, like as:

   - Morphology identification
   - Porosity characterisation
   - Composition and structural nature

Furthermore, the interaction of FL1-DETA and the rock should be considered by:

- Identifying the current mechanism of action
- Characterising of the adsorption isotherm of the current mechanism
- Measuring and quantification of the desorption rate in both static and dynamic conditions

2. ***Attempts to identify and implement the proper method of modification*:**

Weak electrostatic interactions between the reservoir and polyelectrolyte based inhibitors can be responsible for poor adsorption of the polymers to the rock leading to its quick release in the produced water rather than remaining near the well bore vicinity. The desired modification approach should lead to:

- An ideal candidate that shows stability in the adverse environment such as heat, temperature fluctuations and contact with undesired species i.e. H_2S, oil, corrosion products, other chemicals such as inhibitors, surfactants in the system.
- Improve the retention of the scale inhibitor
- Control the desorption/dissolution rate of the scale inhibitor

3. ***Optimisation of SI and the dopant ratio for maximum retention properties*:**

The ratio optimisation of the dopant and the SI is paramount as enough amount of —COOH groups should be left available on FL1 structure to inhibit the formation of $CaCO_3$ and $BaSO_4$. Moreover, if the dopant is also a polymer, the size increase of the structure should be controlled in order not to block the pores of the reservoir rock.

4. ***Implementing the method/approach of modification*:**

The modification method of choice should be analysed and investigated. The amount of retention and thermal stability enhancement should be reported through the:

- Characterisation of the adsorption isotherm of the modified mechanism
- Measurement and quantification of the desorption rate in both static and dynamic conditions based on the new implemented approach
- Optimisation of rock/inhibitor interface to give an adsorption/desorption profile that would maintain above the MIC.

1.4 Outline of the thesis

This thesis will consist of nine chapters in the following structure :

Chapter 2: Literature review
A review on different scale formation scenarios, types, and control techniques. The chapter will then focus on scale inhibitors, their classification and method of administration by considering their pros, cons and challenges.
this chapter also, presents the two main constraints of the project for HTHP fields: thermal and retention stability and reviews suitable methods of modification based on these constraints. In the end, a method of modification is suggested, and the idea is backed up with extensive Literature support from previous research works.

Chapter 3: Materials and experimental methodology
Defines materials specifications and instruments course of action. Then it elaborates experimental methods and setups which was designed or modified based on the aim and objectives of this project. It also defines a method for concentration measurement of the scale inhibitor in the brine.

Chapter 4: Basic characterisations This Chapter presents basic individual characterisation on the main components of this project: sandstone, scale inhibitor and brine.

Chapter 5: FL1-DETA Behaviour in Full Brine Without H_2S
Presents experimental results and discussion on scale inhibitor, FL1-DETA interaction with the full brine and sandstone particles in the absence of H_2S gas. Illustrates adsorption/ desorption isotherms of FL1-DETA and discuss them based on fitted adsorption models available in the literature. In the end, it highlights the shortcomings of FL1-DETA and clarifies how the current structure would be unsuitable for squeeze treatment purposes and high salinity wells.

Chapter 6: Overcoming the Incompatibility
Explains the method of polymerisation and development of PSS-*co*-MA-PANI composites. It also includes primary characterisation of these composites individually and in the interaction with the brine composition and sand particles.

Chapter 7: Comparison of FL1-DETA and PSS-*co*-MA—PANI
Compares the original scale inhibitor FL1-DETA performance with newly developed PSS-*co*-MA-PANI composites in ambient as well as H_2S environment through a series of static and dynamic tests in the presence and absence of sand particles.

Chapter 8: Conclusion and Future Works

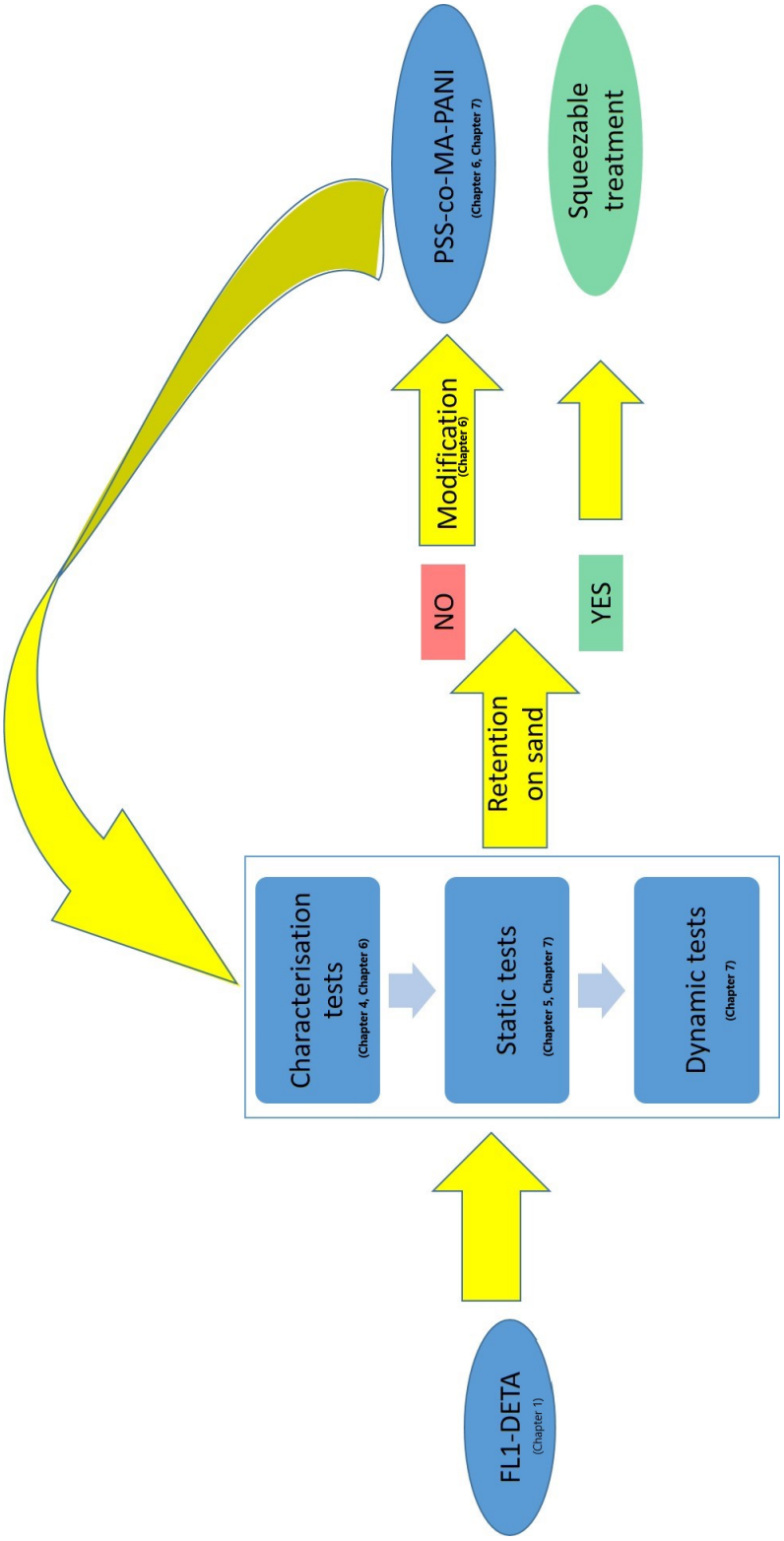

Figure 1.4: Work flow of this PhD project

CHAPTER 2

Literature review

Introduction

Most reservoir rocks are established in water by deposition of rock grains or biological detritus. Sediments compact and bind and during this procedure, water becomes trapped in the pores. This water is called connate or fossil water where its composition depends on the environmental deposition. i.e. freshwater for lakes and river deposits and sea water for marine sediments, Figure 2.1 [22]. On the other hand, formation water properties varies from one reservoir to another and depends mostly on the mineralogy of the formation as well as influx and migration of fluids. Figure 2.2 shows the water movement and the evolution of formation water [22].

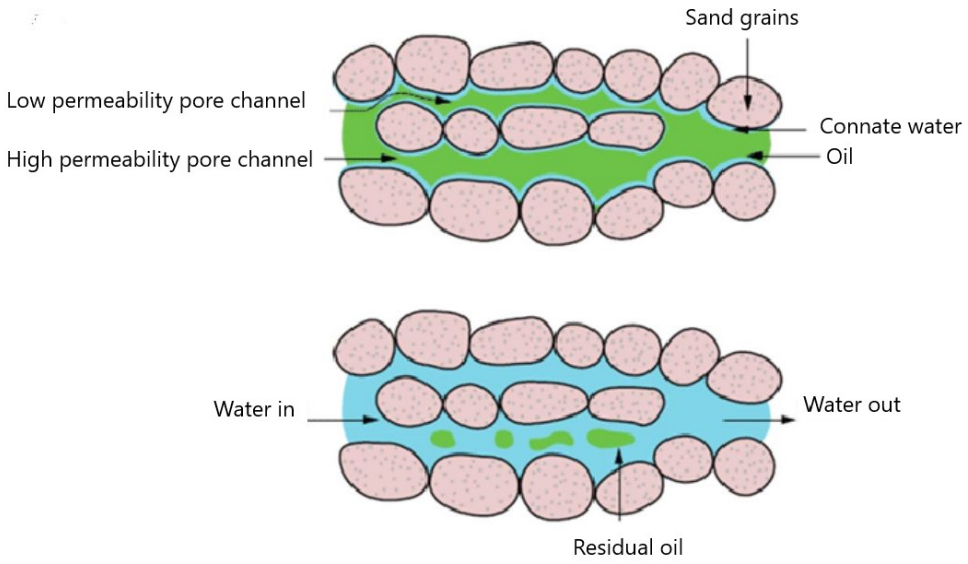

Figure 2.1: Schematic of connate water [23]

Produced water contains soluble and non-soluble oil/organics, suspended solids, dissolved solids, and various chemicals used in the production process and is naturally occurring water that comes out of the ground along with oil and gas. Hence, production water is a mixture of formation and injected water, production chemicals, connate and even drilling water as shown in Figure 2.3.

The thermodynamic instability and incompatibility of different types of waters often cause a series of technical problems in oil and gas extraction, such as scale formation, that fully or partially obstructs equipment, reservoir pores and pipes, leading to serious damage and economic losses such as loss of production rate, treatment costs and shutdown periods[24, 25]. Severe scaling can also cause a serious failure of safety or production equipment as well as formation damage by having a dramatic impact on reservoir characteristics through pore blockage or reduction of the pore size [26]. Thus scaling problems count as one of the major topics facing the petroleum industry [27]. Its

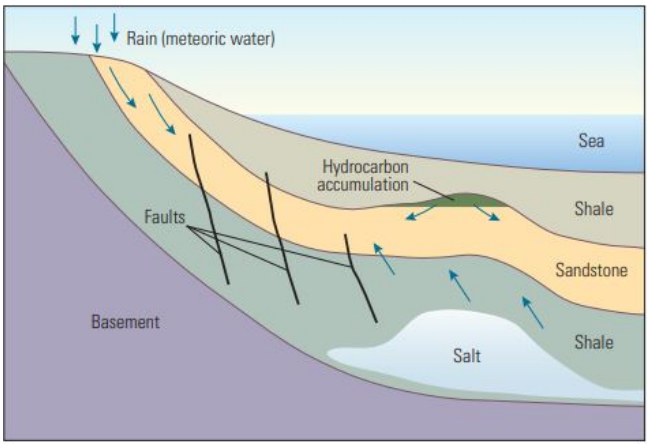

Figure 2.2: Formation water evolution. Composition of original formation water filling the sandstone reservoir can be changed by the influx and migration of other sources of water [22]

management is a key production and flow assurance issue which is one of the most difficult to resolve and especially critical in certain fields (i.e. the North Sea and Canada) [12, 2].

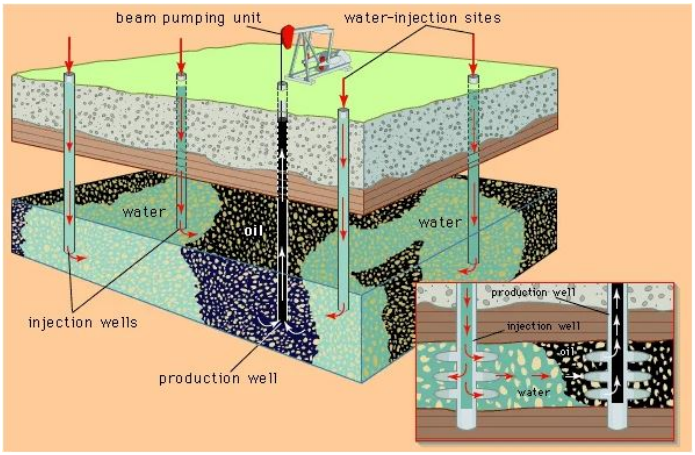

Figure 2.3: Water flooding system, Production water i.e. injection water and formation water[28]

There are various scale types based on oilfield complex water composition at different geographical locations. The most routine scales are barium, calcium and strontium sulphate ($BaSO_4$, $CaSO_4$, $SrSO_4$) and calcium and iron carbonates ($CaCO_3$, $FeCO_3$). Exotic scales i.e. zinc and lead sulphide (ZnS, PbS) are less common but they have recently raised great concern due to their low solubility and fast kinetic same as iron Sulphide (FeS) which is the by-product of iron corrosion in the presence of dissolved H_2S gas [16].

2.1 Theory of scale formation

Deposition can be found in reservoirs and upstream production tubing, sub-surface safety valves, water injection lines to top side refining equipment such as heat exchangers and transport lines. Basically, any surfaces in contact with a salty Aqueous phase is highly affected by environmental conditions such as pressure, temperature, salt content or pH and prone to scale [26, 29]. The alteration in environmental conditions can cause the liquid to over saturate causing complexes of contained ions to precipitate out of the solution where they then deposit and grow on surfaces [27]. Categorising by groups, scaling can occur due to one or several of the following general scenarios:

1. Incompatibility mixing :
   Two fluids are called incompatible if they interact chemically and precipitate minerals as a result of their mixture, Figure 2.4. As an example, typical sea water contains concentration of SO_4^{2-} whilst formation water usually carries high concentrations of cations divalent such as Ca^{2+}, Ba^{2+}. Therefore, mixing of these two waters could form precipitates of $CaSO_4/BaSO_4$ [26]. Other type of scales that are formed by fluid incompatibility are sulphide scale, where H_2S gas dissolves in formation water enriched with Fe, Zn or Pb causing the formation of various sulphide species, ZnS, PbS and FeS [7].

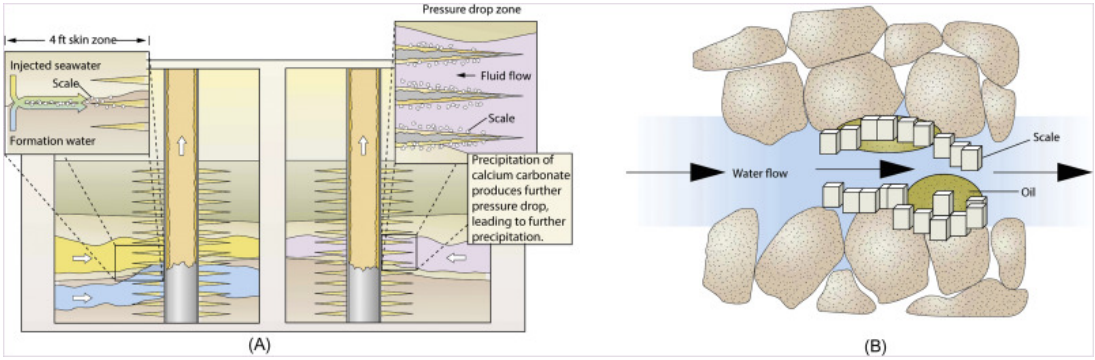

Figure 2.4: Schematic of scaling caused by incompatible mixing [30].

2. Auto scaling:
   Any condition alteration such as temperature or pressure while producing reservoir fluid can cause auto scaling. These variations, can push the fluid composition beyond the solubility limits for a mineral, thereby leading to scale precipitation [3].

3. Evaporation-induced scale:
   This occurs as a result of simultaneous production of hydrocarbon gas and formation brine. A pressure drop caused by reduced hydro-static pressure leads to an

expansion of the hydrocarbon gas and evaporation of the hot brine phase. Thus, the salt concentration increases above the solubility limit and precipitates. Halite scale (NaCl) can be named as an example that is one of the most common scale type of HP/HT wells. [3].

4. Fluid flood:
   For a secondary recovery [1]the formation is flooded with CO_2 gas. Hence, water containing CO_2 becomes acidic and dissolves calcite in the formation. As a result, pressure drops in the formation surrounding the producing well and thus causing the CO_2 to break out of solution. CO_2 reacts with divalent ions available in the FW and form precipitation of carbonate scale in the perforations and in the formation pores near the wellbore [3]. Another way of maintaining the pressure in the oil reservoir, is by injecting seawater. However, sulphate-containing sea water can encourage sulphate reducing bacteria (SRB) to grow near the injection wells, leading to the chemical reduction of sulphate to sulphide and producing H_2S. Which this could later promote the formation of sulphide scales in the system.

5. Thermodynamic instability:
   Thermodynamically, precipitation or crystallisation becomes likely when the solution is supersaturated and the activity of ions in solution is above their saturation limit [31]. When supersaturation exceeds a critical value, nucleation of scale formation on particle surfaces induces growth of crystals. In addition to supersaturation conditions, kinetics of precipitation should be also considered as it is a key factor in the severity of scaling [31]. As an example, low concentration of nucleation sites slows down the crystallisation kinetics [32] while increasing ionic strength of the solution decreases the kink spacing by reducing the interfacial energy and enhancing the step velocities during growth and dissolution [33].

In order for a mineral salt to form a hard, consolidated scale deposit it is generally accepted that three conditions should be satisfied:

- Brine to be supersaturated with respect to the scaling minerals
- Adequate nucleation sites be available for crystal growth
- There should be sufficient contact time to enable the growth of a consolidated deposit

[1]Secondary recovery includes methods of petroleum production that are based on the use of man-made energy to produce oil. This means injecting fluids to increase the pressure of the reservoir and creating an artificial drive. This includes water injection and natural gas injection

2.1.1 Supersaturation

Supersaturation is one of the primary causes of scale formation in a solution. Saturation extent can be expressed by saturation index or saturation ratio. Basically, saturation index is the logarithmic form of the saturation ratio. Saturation ratio is calculated as follow:

$$SR = \frac{IAP}{K_{SPX}} \tag{2.1}$$

Where IAP and K_{spx} are the ion activity product and the solubility product constant for mineral salt, respectively [34]. Although scaling tendency can be estimated by saturation index yet, it does not give information about the interaction of ionic species and the precipitation kinetics [35]. The saturation of a solution is a key factor for crystallisation in the bulk solution and seeded crystals. From a thermodynamic point of view if:

$SR < 1$: The solution is under-saturated which means the solution conditions are undersaturated with respect to the macromolecule formation. Hence, spontaneous homogeneous nucleation would be unable to occur, and crystals placed in the solution will dissolve. In other words, there is no tendency of scaling and/or previously formed scales are likely to dissolve [36].

$SR = 1$: The solution is saturated and at equilibrium which means that the rate of scale formation is equal to the rate of dissolution. Thus, no visual scale is expected to form i.e. spontaneous and homogeneous nucleation will not take place and any crystals added to the solution will not dissolve or increase in size [36].

$SR > 1$: The solution is supersaturated and thermodynamically there is a tendency for the scaling to occur. Supersaturation is subdivided into three separate conditions, metastable saturation, liable supersaturation and precipitation zone. In the metastable supersaturation condition, there are low chances for new crystals to form as the spontaneous homogeneous nucleation does not take place in a reasonable length of time. However, the introduced crystals can continue to grow in this solution. The liable supersaturation represents the region where both spontaneous homogeneous nucleation and crystal growth could occur. Further this region, amorphous precipitation would happen and deposition will form as a result of aggregation [36].

2.1.2 Crystal nucleation

Crystal nucleation occurs at high supersaturated solutions in which stable nuclei forms after allotted induction time[1]. Nucleation can either be primary type or secondary. Pri-

[1]Duration of time initiating at the creation of supersaturated system until the first appearance of a secondary solid phase (critical nuclei). Induction time is a function of saturation extent and temperature of the solution [37]

mary nucleation itself is subdivided into homogeneous and heterogeneous nucleation.

Primary nucleation occurs in the absence of a crystalline surface. In homogeneous nucleation, crystallisation is not induced by the presence of foreign particles and nucleation only occurs at highly supersaturated levels in which the ions pair by electrostatic interaction and reach a critical size. However, in heterogeneous nucleation, the presence of a foreign particle and surface induces the nucleation even at very low levels of supersaturation.

As homogeneous nucleation occurs in the absence of a foreign substance, it would be unlikely for any natural environment to be free from foreign substances. Thus, homogeneously formed scale particles do not necessarily deposit or grow onto a surface and could flow through the system without causing too many issues[3]. Whereas in heterogeneous nucleation the foreign substance can be scale nuclei or corrosion products, welds/stress points, corrosion sites, scratches on metal surfaces, or small particles of suspended solids. Therefore, heterogeneously formed scale is more probable and scale particles can build up on solid surfaces[3]. Unlike primary nucleation (homogeneous and heterogeneous), secondary nucleation results from the presence of a crystalline surface, the parent crystal which presents in the supersaturated solution. The parent crystal has a catalytic effect on the nucleation process, thus compared to both homogeneous and heterogeneous nucleation (primary nucleation), lower supersaturation levels would be sufficient for the nucleation process to occur [38]. FeS can be named as an example of heterogeneous scaling [7]

2.1.3 Crystal growth

After the formation of stable nuclei, a single crystal enlarges by the addition of the molecule from the supersaturated solution. Both the supersaturation ratio and temperature play important roles in this process [39]. Although the ionic strength of brine can affect the growth direction of a crystal by lowering its interfacial energy caused by the decrease in the kink space[1], it will not affect the overall growth rate and amount [33]. The mechanisms of crystal growth are affected by the smoothness or roughness of the crystal surface and thus the surface area and the surface energy. Surface irregularities result in higher surface energy sites and favour crystal growth, whereas low surface energy and surface area have been shown to promote stability [39]. In an ideal scenario, growth is centred around imperfections, predominantly kinks on the crystal surface in 2D, 3D or a combination of a 2D followed by a 3D growth [40]. Whilst in low supersaturation, crystallisation growth follows screw dislocation theory in which the crystal face is constantly rotating around the dislocation point and a continuous growth occurs resembling the thread of a screw [41].

[1] Kink is dislocation defects on crystal along its glide plane

2.2 Routine scale formation: influencing factors

Salty reservoirs water contain a range of elements coming from the contacting rock. Moreover, seawater is injected into oilfield reservoirs as a well-established mature operation that helps with maintaining the pressure and improving the secondary recovery [26]. Whether it is formation water returning or injected seawater into the reservoir, all dissolved elements contained can be carried into the production water, causing deposits inside the installation pipes or blocking the reservoir pores. Scale deposition results from the diverse range of elements and ionic components present in these fluids caused by water incompatibility or supersaturation.

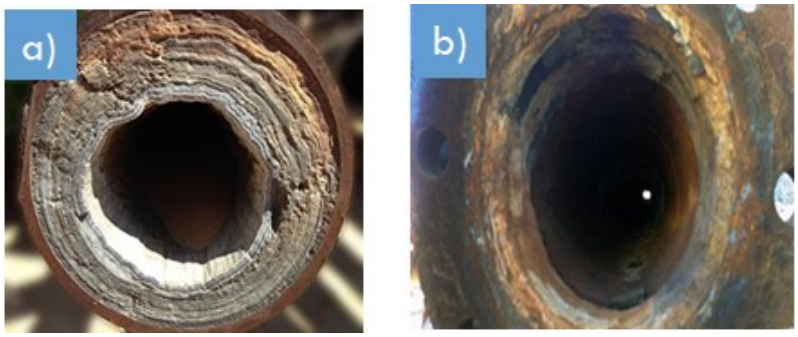

Figure 2.5: Barium sulphate scale in a pipe, a) Scaled pipe, b) Treated pipe[42]

2.2.1 Divalent cations

Divalent cations Ca^{2+}, Sr^{2+}, Ba^{2+} and Mg^{2+} that are present in the formation water and other divalent cations available in seawater affect the nucleation and growth process of different types of scales; although their concentration differs depending on the origin source. Divalent cations can compete with each other or embed in one an others scale crystal structure. For example, the presence of calcium ions during the formation of barium sulphate results in co-crystallisation of calcium in the barium sulphate lattice [43, 44, 45]. Also, it has been reported that about 6% of Ba^{2+} is substituted by calcium [43]. These substitutions can increase or decrease the solubility of the result product. As an example calcium ion inclusion in $BaSO_4$ structure tends to decrease the barium lattice parameter, which retards the lattice growth (i.e. increasing the solubility of barium sulphate in the solution) or makes the lattice growth easy for inhibition [43, 44, 45, 46]. Similarly, the Sr^{2+} may also have the same effect as described for Ca^{2+} [43], but the concentration of strontium ions in the formation water is very low; making the effect less important than that of Ca^{2+}. Another example can be the rivalry of two cations while forming a complex with an inhibitor. Tantayakom *et al.* [47] showed in their research that the presence of Mg ions has a significant effect on the equilibrium concentration of the Ca-phosphonate inhibitor precipitate which is necessary for the inhibition mechanism. The addition of impurity especially Mg ions

inhibits the nucleation of Ca-ATMP [1] precipitation. Furthermore, Valiakhmetova *et al.* [48] research on efficiency of phosphonate SI shows that any change of Mg/Ca molar ratio in a brine during SI re-dissolution causes a redistribution of Ca, Mg, and [SI] between a precipitate and bulk solution, leading to the solubility variation .

2.2.2 Saturation ratio

As discussed in section 2.1.1, saturation ratio is the thermodynamic driving force of scale formation and is based on solubility constant of each mineral, showing how far they have been pushed off their limit from being soluble to forming a precipitate. Many studies show saturation ratio has an effect on crystal size and morphology of the formed scale. As an example, Todd *et al.* [49] showed that in brines containing both Ba^{2+} and Sr^{2+} cations, the morphology and size of formed of $BaSO_4$ and $SrSO_4$ crystals highly depends on the saturation ratio od each cation. Whereas, Kitamura *et al.* [50], observed that the reactant concentration inversely affects the crystallisation of $CaCO_3$. There are reports showing that certain forms of scale are more susceptible to build-up at high supersaturation ratio (SR=12) such as aragonite, whilst calcite forms at lower supersaturation ratios (SR=9.8) [51]. Ben Amor *et al.* [52], reported that type of nucleation predominance depends on the supersaturation ratio. At low degrees of SR, heterogeneous nucleation prevails as compare to homogeneous type. Moreover, the degree of saturation ratio is inversely proportional to the induction period [53]. Todd *et al.* [49] showed that at higher supersaturation ratio, 67% of initial permeability was lost in a shorter time from injection of the brine compare to lower saturation ratio which only 15% of the initial permeability was lost. This shows that the saturation ratio influences the scaling tendency, morphology and size of crystals formed.

2.2.3 Temperature/pressure

Scale can form when the solubility limit for one or more components in a solution is exceeded. Mineral solubility has a complicated dependence on temperature and pressure knowing that both temperature and pressure are related with the supersaturation ratio of a system. Generally, an increase in temperature increases the water solubility of most minerals. Similarly, decreasing pressure tends to decrease solubility and, as a rule-of-thumb, for every 7000-psi (48-MPa) decrease in pressure, the solubility of most minerals decreases by a factor of two [2].

However, not all minerals conform to the typical temperature/pressure trend. For example as shown in Figure 2.6, the solubility of carbonate ($CaCO_3$) increases as temperature is reduced yet decreases as the pressure is reduced. The effect of pressure, however, is negligible compare to the effect of temperature [2, 6] that means in carbonate scale deposits, temperature effect often dominates pressure effect. As an example, as the flow progresses up the tubing to surface temperature and well head pressure,

[1] composite of calcium with amino trimethylene phosphonic acid scale inhibitor

temperature plummets and it overrides the pressure effect. As a result, the scale formation reduces in the tubing. On the other hand, moving from the well head to the surface these subsequent release of pressure lead to massive deposits of scale in surface equipment and tubing [3].

The same theory is applicable for $BaSO_4$ where the effect of pressure on scaling tendency is less compared to that of temperature i.e the influence of pressure variation on scaling tendency of $BaSO_4$, must occur with a synergistic effect of increase in temperature. The temperature alteration controls the scaling trend of $BaSO_4$. The solubility of $BaSO_4$ increases with respect to temperature increase as the dissociation of $BaSO_4$ is an endothermic reaction [30, 54], however the general effect on solubility is minimal as compared to other scales due to small solubility constant of $BaSO_4$. In fact, the solubility of $BaSO_4$ increases by a factor of two in the temperature range 25°C to 100°C (77°to 212°F) and then decreases by the same magnitude as temperatures approach 200°C (392 °F). This trend is itself influenced by the background brine salinity [2].

In general, increase in pressure reduces the scaling tendency of sulphate scales [55] like that the sulphate of barium, calcium and strontium are more soluble at high pressure. Consequently, $BaSO_4$ will be precipitated when there is a reduction in pressure [54].

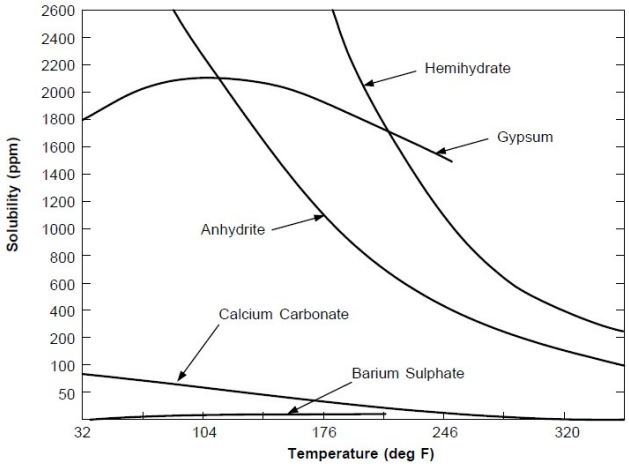

Figure 2.6: Effect of temperature on solubility of different scales [56].

2.2.4 Ionic strength, salinity

The salt content of the brine plays a vital role in the scaling tendency of various scales. The ionic strength is a function of the concentration of ion present in the solution. Ionic strength of any solution can be calculated by equation 2.2.4 where C_i is the ion

concentration in mol/L and Z it the charge of each ion:

$$I = \frac{1}{2}\sum_{i=1}^{n} c_i Z_i^2 \tag{2.2}$$

As an example of this factor, Figure 2.7 (a) shows strontium sulphate scaling tendency that depends on the degree of salinity and temperature. Regarding $BaSO_4$, solubility is strongly affected by the ionic strength of the solution i.e increase in sodium and chloride ion concentration will increase the solubility of $BaSO_4$ and vice versa, Figure 2.7 (b) [2, 57]. This explains why $BaSO_4$ occurs in hot wells that produces high salinity brine [57].

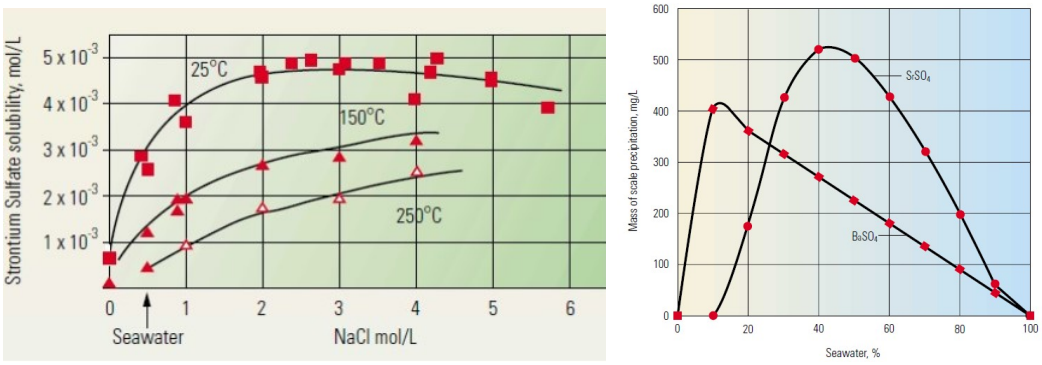

(a) $SrSO_4$ at different temperature

(b) $SrSO_4$ in comparison with $BaSO_4$ at specific temperature and pressure.

Figure 2.7: Effect of salinity on solubility of sulphate scales [2]

2.2.5 pH

pH as a measure of $[H^+]$ activity, is one of the other main factors affecting scaling and mineral-inhibitor complex formation. Even though the pH at different locations in the oil plant is generally in the range of 4 - 7 [47], CO_2 or H_2S at high pressure supply significant acidity. Carbonate minerals' solubility increases in the presence of acid gases such as carbon dioxide (CO_2) and hydrogen sulphide(H_2S) [58, 14]. Consequently, formation waters, in contact with both carbonate rock and acid gases, can be rich in dissolved carbonate [2]. This trend has a complex nonlinear dependence on brine composition, temperature and the pressure of the gas above the liquid phase. Generally, as pressure falls, CO_2 leaves the water phase causing the pH to rise—leading to calcite scale formation [2]. The solubility of barium compounds increase when the pH decreases including any complexes formed [54]. However, as fluid acidity increases $BaSO_4$ solubility remain intact and the pH can only affect its morphology [15].

2.3 Exotic scale formation: influencing factors

Zinc and lead ions available in the formation water are due to dissolution of formation minerals like sphalerite and galena caused by connate and aquifer water contact or injected fresh/sea water for pressure supporting purposes. Approximately, 10-15ppm [Zn] and [Pb] can also be sourced from heavy brine completion fluid (zinc bromide) into formation during drilling or well operations [59]. Iron can be produced from the formation, especially sandstone reservoirs and is also present downhole as a result of various corrosion processes. With mature reservoirs being exploited and natural gas market value increasing, lead and zinc sulphide scale have raised a growing concern especially for HT/HP/HS oil and gas fields in North Sea and Gulf of Mexico (GOM) [5]. There is high potential for nearly all producing oil wells to sour over time, including those already experiencing the formation of the routine mineral scales i.e. barite and calcite [16]. Biotic and abiotic reactions produce H_2S in downhole environment [7], likewise, decomposition of drilling compounds and corrosion inhibitors over many years of production is the other source of sulphide ions [8]. As an example of the biotic mechanism, H_2S is produced because of the sulphate-reducing bacteria (SRB) in injection wells that utilise water with high sulphate content such as seawater and produced water. The abiotic mechanism involves releasing H_2S from acid treatments, thermal hydrolysis of the organic sulphur compounds, thermodynamic sulphur reduction, or hydrolysis of metal sulphides. Insufficient acid in the chemical removal process can form elemental sulphur that is associated with the pH rises within the spent acid solution [60].

Figure 2.8: Metal sulphide scaling in 14" pipes close to wellhead. The metal sulphides form a tough scale on the downstream pipe surfaces [61].

Sulphide scales have low solubility and mostly observed in deep wells with elevated temperature (>250°C) and pressure (>15,000psi). Table 2.1 shows the solubility constant of some sulphide scales at ambient condition and pH 7, whereby, FeS has the highest solubility and PbS the lowest amongst all.

Table 2.1: Solubility constant of exotic mineral scales at room temperature [58].

Scale type	Solubility constant (K_s)
FeS	1.29 x 10^{-19}
PbS	3.80 x 10^{-28}
ZnS	2.03 x 10^{-25}

Sulphide scale formation has high kinetic and can cause a remarkable reduction in pressure and production rate. In fact, the most noticeable performance reduction in topside process equipment low-pressure separators and hydrocyclone were known to be caused by zinc sulphide scale deposition [62]. Moreover, crevice corrosion and under deposit corrosion are dominantly caused by sulphide scale deposition [62]. Even though, acid wash removes most forms of sulphide scales, but there are significant risk associated with it and the recurrence of the scale deposition is definite [60].

ZnS structure is formed by the penetration of two FCC lattices of Zn^{2+} atoms and S^{2-} atoms and the atoms of two kinds are connected tetrahedrally [63]. PbS is Halite, Rock Salt structured and crystallises in the cubic $Fm^{-3}m$ space group. The structure is three-dimensional. Pb^{2+} is bonded to six equivalent S^{2-} atoms to form a mixture of corner and edge-sharing PbS6 octahedra [64]. Both structures are shown in Figure 2.9.

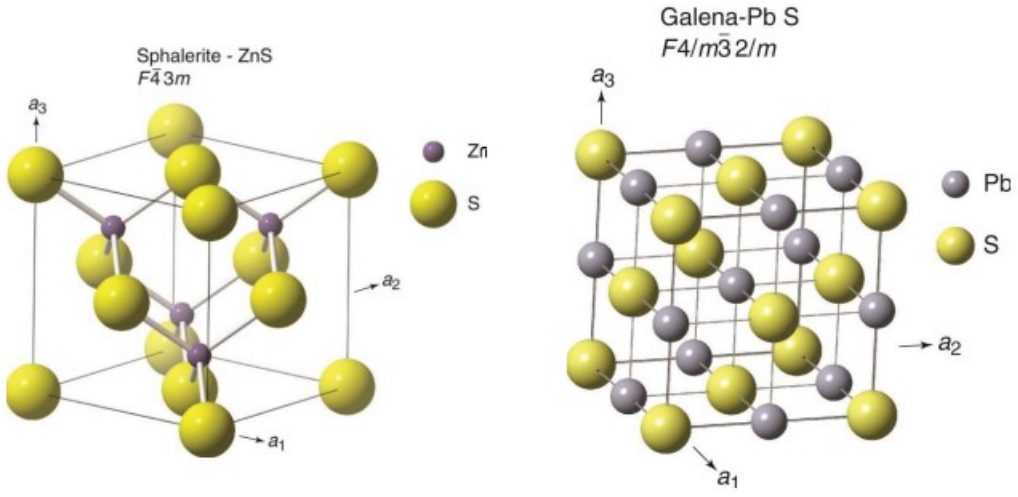

Figure 2.9: Zinc sulphide and lead sulphide crystal structures [64]

2.3.1 Co-existence of other scales

Sulphide scales are formed by two mechanisms; auto scaling and cation displacement. Reactions listed at 2.3 and 2.4 show possible mechanism for auto scaling. In both

reactions, sulphide scales are formed, while releasing protons into solution, and, subsequently, lowering the pH.

$$\begin{aligned} HS^- + Fe^{2+} &\rightarrow FeS + H^+ \\ HS^- + Zn^{2+} &\rightarrow ZnS + H^+ \\ HS^- + Pb^{2+} &\rightarrow PbS + H^+ \end{aligned} \tag{2.3}$$

$$\begin{aligned} H_2S_{(aq)} + Fe^{2+} &\rightarrow FeS + H^+ \\ H_2S_{(aq)} + Zn^{2+} &\rightarrow ZnS + H^+ \\ H_2S_{(aq)} + Pb^{2+} &\rightarrow PbS + H^+ \end{aligned} \tag{2.4}$$

Depending on the conditions such as alkalinity, temperature and mechanical disturbance, PbS and ZnS can also be formed through cation displacement where Pb and Zn compound react with the more soluble scale [65, 66]. Reaction 2.5 illustrates this displacement [67].

$$\begin{aligned} ZnS + Pb^{2+} &\rightarrow PbS + Zn^{2+} \\ FeS + Pb^{2+} &\rightarrow PbS + Fe^{2+} \\ FeS + Zn^{2+} &\rightarrow ZnS + Fe^{2+} \end{aligned} \tag{2.5}$$

It has been shown that zinc sulphide and lead sulphide precipitation impact the precipitation of carbonates and its deposition on stainless steel surface [68, 69]. Regarding co-precipitation with $BaSO_4$, Kan *et. al* [70] have shown that the presence of zinc sulphide can significantly improve inhibition efficacy of DTPMP and BHPMP, whilst FeS does the opposite.

2.3.2 pH

Figure 2.10 shows the dependence of sulphide scales based on pH. As a result of injection water mixing with production water, pH will increase, leading to sulphide scale formation [8]. However, ZnS, PbS and FeS solubility increases as fluid acidity increases upon pH decrease [58, 14]. Therefore, acid wash treatment can be a good remedy for most scale build up especially at low temperature where acid washing with hydrogen chloride is the most effective method of chemical removal [60].

Due to the greater solubility of iron sulphide, it will be preferentially dissolved as compared to zinc sulphide and lead sulphide upon decrease of the pH in the system. It is worth noting that acid washing does not deal with the source of scale formation itself, thus dissolved sulphide scales will very likely solidify with slight increase in pH and cause blockage further down the production line. Furthermore, Przybylinski [62] study on iron (ferrous) sulphide and its removal by acid dissolution, shows as with zinc

sulphide and lead sulphide scale, iron sulphide will evolve hydrogen sulphide gas with acid washing.

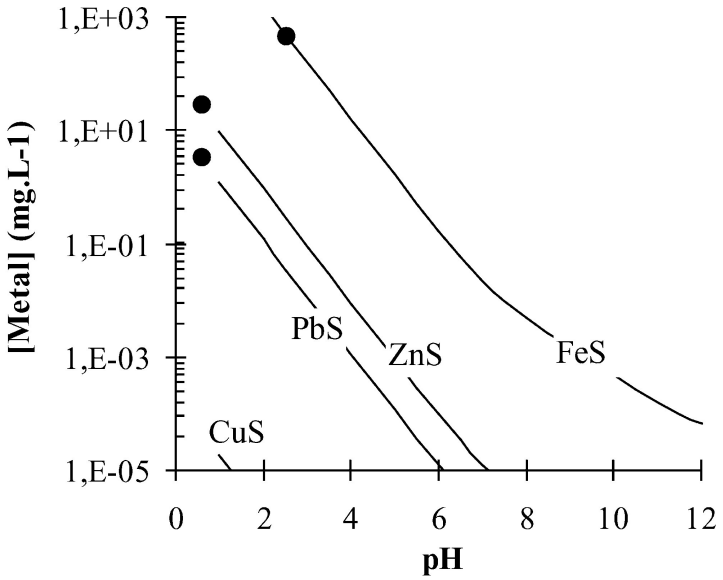

Figure 2.10: Effect of pH on solubility of some common scale. The initial metal concentration in the solution is indicated in the curve of the correspondent metal precipitate, as a thick black dot [14]

2.3.3 Concentration

ZnS and PbS have been observed to form in wells containing very low concentration of Zn and Pb and sulphide. For example, only 2ppm of H_2S can form a significant amount of ZnS deposit while mixing with completion fluid containing zinc bromide in UK sectors or that 20-25ppm of H_2S and 40-70ppm of Zn deposited as ZnS, on a crude oil cooler and high pressure hydrocylones in the Norwegian sector. In Gulf of Mexico (GOM) PbS and ZnS deposited in the presence of 5ppm Pb, 50ppm Zn and 25ppm of H_2S [58]. Laboratory results have also proved that dissolved levels of H_2S can transform sulphide scales structures such as FeS from sulphur-deficient to sulphur-rich iron sulphide especially at high pressures [71].

2.3.4 Temperature and salinity

Regarding sulphide scale such as FeS, ZnS and PbS, the mechanism of scale formation for HTHP and gas condensate field is not fully clear [6]. However, it has been shown that zinc sulphide and lead sulphide precipitation is considerably affected by temperature and salinity. The reduction of temperature reduces the solubility of these scales whereas it increases the solubility of FeS [58]. Hence, high temperature brines cooling

withing the production system will cause sulphide scale formation [8]. On the other hand the dilution of high saline brine will lead to pH increase and therefore scaling of sulphides. Figure 2.11 depicts the solubility of ZnS and PbS at different temperature and salinity levels.

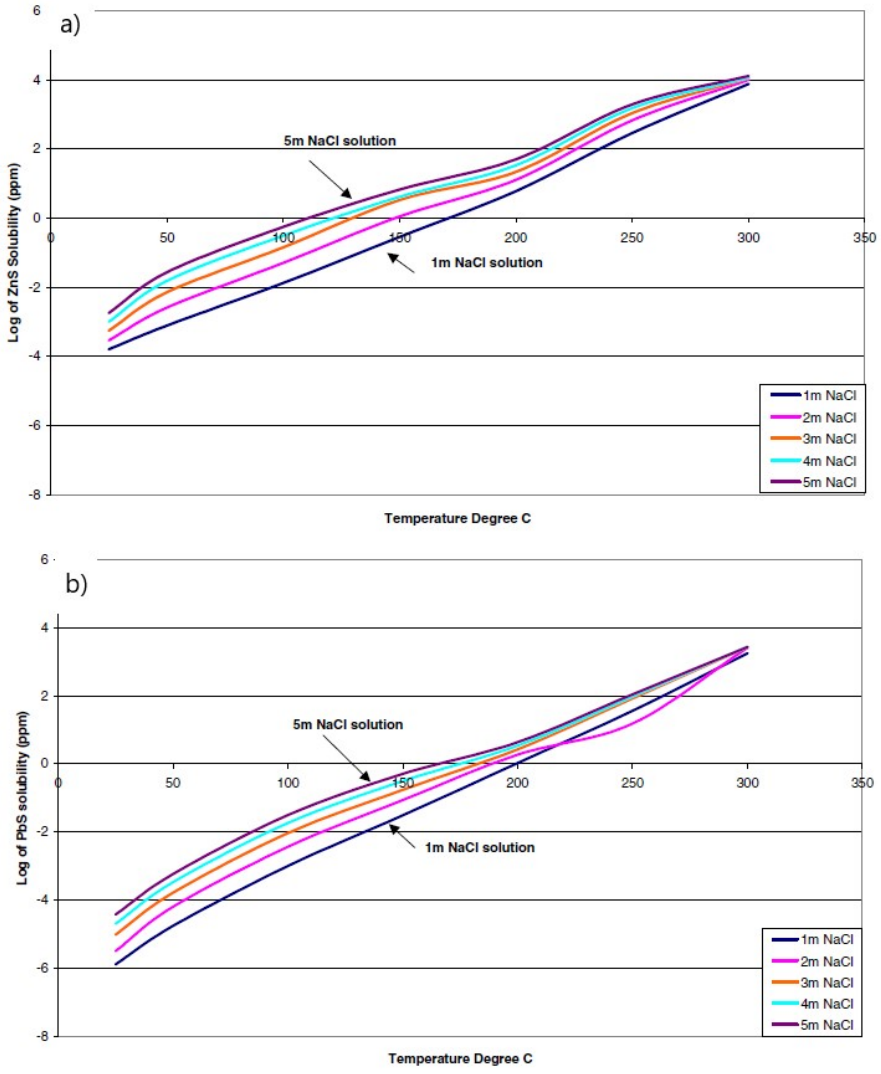

Figure 2.11: Exotic scale solubility based on temperature and salinity [72]. a) ZnS, b) PbS

To summarise what was discussed in this section, Table 2.2 represents the dominant factors affecting scaling tendencies [26]:

Table 2.2: Common scales and affecting factors [26]

Name	Chemical formula	Primary variable
Calcium carbonate	$CaCO_3$	Partial pressure of CO_2, temperature, total dissolved salt ,pH
Calcium sulphate(all types)	$CaSO_4$	Temperature, total dissolved salts, pressure
Barium sulphate	$BaSO_4$	Temperature, pressure
Strontium sulphate	$SrSO_4$	Temperature, pressure
Iron compounds (Ferrous carbonate, Ferrous sulphide, Ferrous Hydroxide)	$FeCO_3$, FeS, $Fe(OH)_2$, $Fe(OH)_3$	Corrosion , dissolved gas , pH
Zinc sulphide	ZnS	Corrosion, dissolved gas, pH
Lead sulphide	PbS	Corrosion, dissolved gas, pH

2.4 Scale control and mitigation

Scale formation is reported to occur by two crystallisation pathways, namely surface crystallisation and bulk crystallisation which both depend on available contact site and time [73, 74, 75, 76]. The surface of the pipes, valves and heat exchanger, become rough due to the production flow, finishing an other parameters. The same will be with the rough porous natural structure of a reservoir. Hence, there will be enough nucleation sites available for a scale crystal to grow on the substrate. Regarding the contact time, it will be proportional to the production rate. This means that based on individual company policies there will be a fixed range of production rate, hence, the contact time is usually constant and nonadjustable. Therefore, controlling the salinity of oilfield waters as well as presence of other salts or metal ions [57]; prior to water injection plays a key role in inhibiting scale and the exploration and production of petroleum since the incompatibility of cation and anion in water is the main cause of scale formation [3, 26]. Various operating conditions such as pH [58], temperature [30, 2], operating pressure [2, 3], permeation rate [77], flow velocity can all influence the scale formation in oil and gas fields [78]. Thus, scale management and mitigation methods ranges from pre-emptive to reactive means and these can be applied individually or combined [3]:

- Mechanical Removal (Pigging/jetting/reaming): If access is available, useful techniques for removing thick, hard, old formed scales [2, 59]. However depending on the severity of the exotic or routine scaling involved, it is likely that removal will need to be repeated regularly unless chemical treatments to inhibit or prevent its recurrence are successfully employed. The deferred oil costs and equipment rental costs can be high if removal is needed within the production string. Milling may

be required if the restriction is severe [60].

- Chemical removal (Acidizing/chelating): Generally, sulphuric acid or hydrochloric acid is used for pH adjustment of the feed water to 5–7 in order to increase the solubility of alkaline scale [35]. However, there are risks associated with chemical treatments, especially in high temperature and high pressure wells. At high temperatures acid general corrosion and hydrogen and chloride stress cracking are more probable [17, 59]. As it was explained earlier, chemical removal of sulphide scale is possible with acid washes due to their pH sensitivity but it should be bared in mind that FeS, ZnS and PbS could produce H_2S gas when dissolved with acid. For exotic scale, Usually 15% to 30% v/v hydrochloric is used [59]. Use of other acids, such as mixed organic acids resulted in less corrosion and hydrogen cracking effects, but due to the reduced reaction rate, longer contact times were needed [60]. Same as mechanical removal, acid washing will recover production, but will not resolve the main source of the scale formation thus, new scale will form over a similar time period and another treatment would be required. Furthermore, acid washing will result in safety issues by generating hydrogen sulphide gas resulting in safety issues, which this will be exacerbated at conditions with high pressure and temperature [17, 59]. A further problem linked to acid washing may be the re-depositing of iron sulphide further down the system. This may also be true for zinc sulphide and lead sulphide scales.
- Reduction of scale potential by coagulation techniques or ion exchange softeners[35] (Injection of LSSW[1] with SRP[2])
- Scale prevention inhibitors (Inorganic phosphates, organic polymers): will be discussed in details in section 2.4.1.
- Surface engineering (Coatings/SLIPS[3]): Changing the wettability of pipes and reservoir surface in order to repulse scale settlements [79].
- Other (Smart completions with ICD[4], rotation filtration, feed flow reversal, intermediate chemical demineralisation [35])

2.4.1 Scale inhibitor

Scale inhibitors (SI) as a primary control technique are chemicals which have been applied in oilfields and other industrial systems such as water purification and water treatment industries, and are used to prevent and hinder the formation of mineral scales. However, failure of predicting scale buildup in advance and inadequate placement of the chemical solutions, because of the heterogeneity of the reservoir, reduce the efficiency of the scale inhibitors [80]. SIs can have an organic or inorganic structure and contain one or some of the mentioned functional groups listed in Table 2.3.

[1] Low-Sulphate Seawater
[2] Sulphate Reduction Plant
[3] Slippery Liquid Infused Porous Surfaces
[4] Inflow control devices

Table 2.3: Common coordination groups and properties [27]

Group	Property
-COOH	Hydrophilic group, Good water solubility. Oxygen atom contains solitary electrons, Capable of forming the five- and six-membered ring chelates with metal ions to improve its solubility in water hence enhancing the effect of antiscaling and scale removal.
-SO_3H	Strong polar groups, water soluble, easy to dissolve in polar solvents. Sulfonic group containing two π bonds and three negatively charged oxygen atoms that are resistant to cation, this plays an important role in temperature and salt tolerance
-COOR	Resistance of polymers in the condensed action groups, ester of high electron density, good adsorption effect, changes the scale removal effect.
-CHO	The carbonyl group could participate the Mannich reaction due to its active chemical property, and the carbonyl group containing the lone pair of electrons can be chelated with metal ions .
-OH	Containing a lone pair of electrons, hydrophilic, can enhance the solubility of molecules in water.
-NH_2	Containing a lone pair of electrons, hydrophilic, can enhance the solubility of molecules in water, can chelate with transition metals.

Conventional scale inhibitors are hydrophilic, i.e., they dissolve in water. In the case of downhole squeezing, it is desirable that the scale inhibitor is adsorbed on the rock to avoid washing out the chemical before it can act as aimed. However, adsorption on the rock may change the surface tension and the wettability of the system. To overcome these disadvantages, oil-soluble scale inhibitors have been developed. Coated inhibitors are also available [81]. The ideal scale inhibitor should have the following properties [77, 82, 83]:

- Effective scale control at low inhibitor concentration (threshold inhibition): The chemical should be capable of inhibiting scale formation at very low concentrations, typically of the order of 1–50 ppm.
- Compatibility with sea and formation water and other chemical additives for enhanced oil recovery (EOR).
- Balanced adsorption-desorption properties allowing the chemicals to be slowly and homogeneously released into the production water and providing a long squeeze lifetime.
- High thermal stability. The SI should not undergo thermal degradation under downhole conditions.

- Low toxicity and high biodegradability.
- Low cost.

Scale inhibitor performance can be affected by pH and temperature conditions as well as divalent presence. Graham *et. al* [84], have shown that polymeric scale inhibitors which contain sulphonate functional groups have pKa <<2.5 and are strongly acidic and those which contain carboxylic functional group have pKa ∼4.5 value and are weakly acidic. In order for an SI to function effectively, it should be dissociated which means that available functional groups on its structure become ionised. Hence, a minimum amount of pH would be required based on the defined pKa of each inhibitor while considering the effect of temperature. Yuan *et. al* [85], studied the effect of pH on adsorption of DETPMP [1] scale inhibitor and revealed that by changing the pH from 2 to 6 at a constant temperature, the adsorption isotherm would firstly move to higher amounts at pH=2, decrease at pH=4 and increase to lower amount of that in pH=2 for pH=6. Furthermore, Farooqi [86] showed that by increasing temperature form 50°to 95°C, the apparent adsorption of PPCA would increase at pH 5.

Another affecting factor is the presence of divalent ions which could form a complex of M^{2+}−SI. Farooqi *et. al* [86], showed that PPCA[2] can from a complex with available Ca^{2+} cations in the FW, if the concentration of Ca^{2+} is above 2000ppm. Therefore, for a particular scale inhibitor with defined concentration under mildly acidic conditions, a subsequent increases in pH, temperature and $[M^{2+}]$, especially $[Ca^{2+}]$ may lead to a phase change occurring or changes in its IE[3] values.

2.4.1.1 Mechanisms of scale inhibitors

A scale inhibitor functions depending on its chemical nature and it can function by one or more mechanisms at a same time. The two main inhibition mechanisms of an SI are acting as a chelating (or sequestering) agent or threshold inhibition [87]. Atom-containing compounds with a lone pair of electrons, in principle, have better chelation properties. Therefore, scale inhibitor molecules with many lone pairs of electrons can chelate better and disrupt the balance of sediments, so that the scales disperse. Whereas, an organic chemical compound that can slow and act on nucleation, growth steps and crystallisation of a scale, has a threshold effect that disturbs the thermodynamics of the nuclei growth at sub-stoichiometric concentrations between 2-20ppm, that is the threshold concentration [2]. In order to disrupt nucleation and prevent growth of crystals, scale inhibitors must attach to the surface of nuclei and growing crystals [88].

Inhibitors can also have adherence effect thereby adsorb on surfaces to inhibit formation or growth of scale. The interaction of the SI with the formation should result

[1] diethylenetriaminepenta(me- thylenephosphonicacid)
[2] Polyphosphono carboxylic acid
[3] inhibitor efficiency

in low concentration return to provide longer squeeze lifetime around 3-12 months independent of its mechanism of action [47, 84]. As it was mentioned earlier, there are four main mechanisms of action for scale inhibition; thermodynamic inhibition, adherence inhibition and kinetic inhibition, which includes "nucleation inhibition", "crystals growth retardation".

1. Nucleation inhibition:
   Nucleation inhibition could occur through two different schemes:
   Dispersion: This process allows the inhibitors to prevent and reduce agglomeration of scale deposits through electrostatic repulsion scheme. During adsorption of the SI on the surface of the scale, the chemicals will get electrically charged and repulse. These inhibitors are able to react with certain ions (ex. Calcium) and therefore ceasing/retarding the scale formation [89].

   Adsorption effect: Due to adsorption effects, the inhibitor molecules occupy the nucleation sites which are preferred by the scale-forming molecules. Thus, crystals cannot find active places to adhere to the surface and, therefore, crystal nucleation is not promoted [81].

2. Crystal growth retardation:
   Inhibition mechanism via crystals' distortion is based on acting and modifying the morphology of grown crystal. Adhesion of scale is lowered because scale inhibitors adsorb on the surface. Depending on the inhibitor characteristics and the nature of the substrate, it is possible that the inhibitor will be adsorbed over the crystalline net, forming complex surfaces or nets which have difficulty remaining and growing in active places [81].

   All scale inhibitors show the ability to work through both nucleation and crystal growth mechanisms. However, in most SI species one of these mechanisms is more dominant to attain scale inhibition.

3. Adherence inhibition:
   Another mechanism of scale inhibition is based on adherence inhibitors. Some chemicals simply suppress the adherence of crystals to the metal surfaces. These are surface active agents [81].

4. Thermodynamic inhibition:
   Thermodynamic inhibitors are complexing and chelating agents, suitable for specific scales. For example, for scale inhibition of barium sulphate, common chemicals are ethylenediamine tetraacetic acid (EDTA) and nitrilotriacetic acid. Chelating and complex formation will disrupt the balance of sediments and disperse scale [27], however, they are able to prevent the scaling process only for a certain

limited level of oversaturation and the precipitation reoccurs, if the equilibrium system is disturbed [87].

2.4.2 Types of scale inhibitors

The most common inhibitor chemicals are inorganic phosphates, organo phosphorous compounds, and organic polymers. Polymers are good nucleation inhibitors and dispersants, whereas, phosphonates tend to be better crystal growth retarders. However, both types of SI act through both of these mechanisms to some extent [84, 43]. Based on the reported literature, effective inhibitors towards exotic scales mostly belong to one of the four following groups [80]:

- Low molecular weight **organic** inhibitors such as sodium triphosphate and pyrophosphates.

- Low molecular weight **inorganic** inhibitors such as citric acid, succinic acid, tartaric acid, and ethylenediaminetetraacetic acid (EDTA).

- **Synthetic polymers** with:

  1. Acid group such as poly(acrylic acid) and poly(maleic acid);
  2. Sulfonate group
  3. Phosphate groups such as polyphosphates and polyphosphates esters.

2.4.2.1 Phosphonate scale inhibitor

For many years, phosphonate-based chemicals showed promising inhibition efficacy during squeeze treatment by mitigating scale deposition of $CaCO_3$, $BaSO_4$ and $CaSO_4$. However, they exhibit low thermal stability for HT/HP squeeze treatments [6]. Scale inhibitors containing phosphine are mainly classified as non-polymeric phosphate (inorganic phosphates) and polymeric phosphate, and they are able to control the growth of crystals and cause lattice distortion [27]. It is known that phosphonates tend to have a lower "cut off" temperature. That means phosphonate are sensitive to temperature and perform poorly at low and very high temperatures [86]. However, it has been recently shown that phosphonate inhibitors are somehow effective at 200°C under strictly anoxic conditions and in NaCl brines [90]. Nonetheless, these chemistries show poor or temporary performance toward sulphide scales [5]

Phosphonate SI group have:

- Good chemical stability

- Can be applied to a wide range of pH values,

- Are not easily hydrolysed

- Can chelate with metal ions and form a stereo ring complex [91].

The primary bonding mechanism for the phosphonate group appears to be ionic interaction between the PO_3^{2-} group and the M^{2+} ions [86]. It is mostly observed that the non-polymeric class of phosphate oilfield scale inhibitors, perform better than polymeric phosphonates, especially for the inhibition of $CaCO_3$, $Mg(OH)_2$, and $BaSO_4$ scales [27]. The two commercially well known phosphate scale inhibitors are sodium triphosphate and sodium hexametaphosphat which their chemical structure is showing in Figure 2.12.

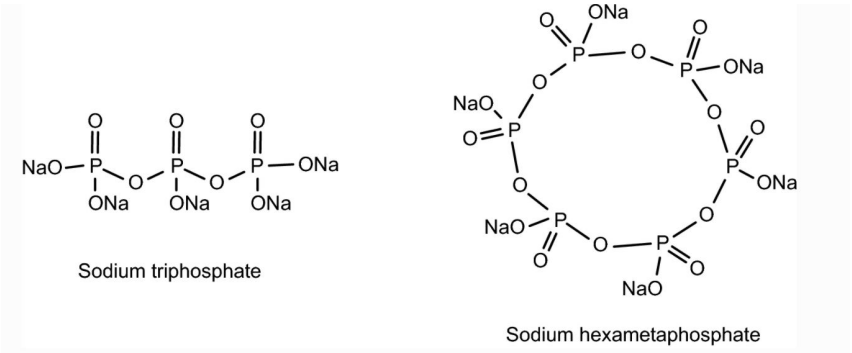

Figure 2.12: Chemical structure of inorganic phosphates inhibitors [87].

Polymeric scale inhibitor containing phosphine is synthesised by inorganic monomer phosphate and other organic monomers. Phosphonate polymeric scale inhibitors or Organophosphorus are less sensitive to temperature and the performance of the SI could be increased at lower pH, by incorporating the groups like –OH, $-CO_2H$ and $–NH_3^+$ [86]. Examples of organophosphorus SI are: ATMP[1], HEDP[2], DETPMP[3], HDTMP[4]. The chemical structure of these inhibitors are showed in Figure 2.13.

Several authors have noted that polymeric SIs are favoured in terms of environmental friendliness of the products, but in terms of IE, phosphonates SIs are often comparatively better inhibitors. Davis *et. al* [92], improved the inhibitor efficiency of the polymeric SIs containing phosphonates by end-capping the functional groups, but this decreased the biodegradability of the polymer.

[1]amino trimethylene phosphonic acid
[2]hydroxy,1-hydroxyethylidene-1,1-diphosphonic acid
[3]diethylene triamine penta (methylene phosphonic acid)
[4]hexamethylene diamine-N,N,N',N'-tetra kis

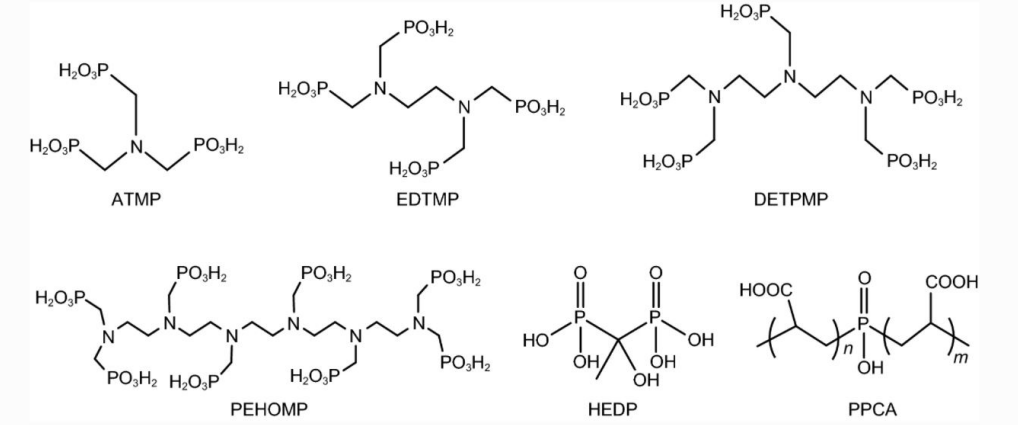

Figure 2.13: Chemical structure of organophosphorus inhibitors [87].

2.4.2.2 Polymeric scale inhibitors

The implementation of environmental legislation in the North Sea entails phase substitution of phosphonate-based inhibitors with polymeric based SI [9]. Despite polymeric SI being more or less effective for routine scales, they offer little or no performance for sulphide scales [9, 10]. This group of chemicals are very sensitive to the salinity levels of the brine and are not suitable for HS fields. They inherently suffer from poor retention properties in squeeze treatment procedure as compared to their old rivals, phosphonates [6, 9]. Polymeric SIs mainly operate through nucleation inhibition [86]. SIs belonging to this group include polycarboxylic acids and their derivatives such as salts or esters with low alcohols, usually methanol or ethanol [87]. It has been found that copolymers are more effective in scale inhibition than homopolymers, thus, in most cases, they are co-polymerised or tre-polymerised with other monomers such as acrylamide, vinyl sulfonic acid, sulfonated styrene, and itaconic acid, Figure 2.14.

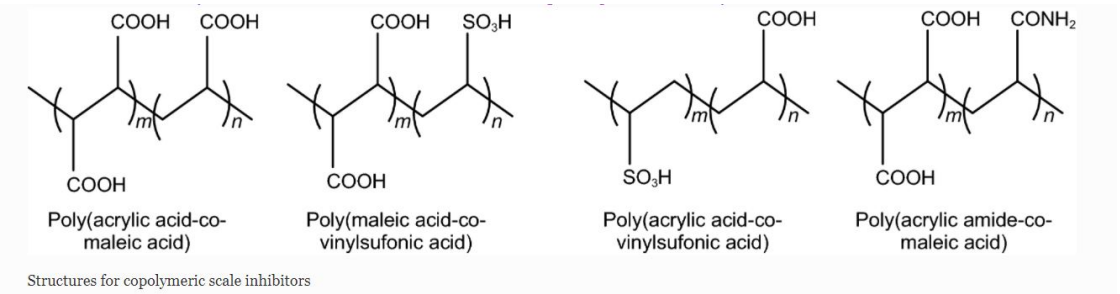

Figure 2.14: Chemical structure of polymeric scale inhibitor [87].

It is worth noting that sulphonate groups do not have an affinity to bind to Ca^{2+} or Mg^{2+} cations. One theory can be that sulphonate functional groups are highly dissociative, and the hydrolyse radius of Ca^{2+} and Mg^{2+} is bigger compared to other available cations in the brine like as Ba^{2+}, hence they are less mobile and quick [93]. The

polymeric SIs (MW[1] $< 10^4$) with a polycarboxylate base exhibit good performance over a range of pH and temperature conditions. However, their effectiveness degrades quite significantly as the pH decreases. The polycarboxylate inhibitors are expected to have good performance and IE due to the numerous option of functional groups bonding between the inhibitor and the surface in the polymeric species. A polymeric scale inhibitor can have both dissociated and un-dissociated acid groups that co-ordinate to the surface [86].

2.4.2.3 Green inhibitors

The oil industry is facing severe restrictions on disposal of oilfield chemicals into the environment [87]. More and more severe environmental constraints have prompted users to rationally manage industrial waters and brines and its disposal. Many of the organic phosphates and phosphonates that are widely used as scale inhibitors are quite toxic to the environment. Thus, the use of phosphonates due to their poor ecotoxicity and many polymers, due to their failure to meet minimum biodegradation requirements have been hindered [94]. Nevertheless, to overcome the need of industry, many P-tagged polymers are still needed to be produced, such as PPCA. However, these products typically contain $< 5\%$ phosphorus, and rather than fully green, they are considered as yellow products, [86]. The main problem associated with green polymers, containing no phosphorus and no sulphur, is that they do not show high IE performance, particularly over longer periods of time [86]. An ideal green inhibitor should be non-toxic, readily biodegradable and shows no bio accumulation [95].

2.4.2.4 High reservoir temperature scale inhibitors

In general increasing Mw, extending branches and adding aromatic groups to a polymeric structure as well as co-polymerisation can increase SI thermal stability. However, all above mentioned techniques can adversely affect other aspects of the SI such as IE. Bulky hydrphobic groups can hinder the SI sterically in order to approach scale surface or adsorb on water-wet reservoir. SI belonging to this group, are homopolymers of vinylsulfonate and copolymers of acrylic acid (AA) and vinylsulfonate. Other polymers, such as poly(maleic acid), poly(itaconic acid), and maleic acid/AA copolymers, may offer similar thermal stability. Typically, common thermal stability tests, influence on pH, ionic strength, and oxygen can help to identify the thermal stability of conventional polymer and phosphonate scale inhibitors [81].

In this chapter, possible effective methods of SI modification that withstand HTHPHS conditions and enhance its retention on sandstone rock are described. Based on the chemical specifications, FL1 is a co-polymer with a size in range of 20 kDa to 100kDa. This means that the expected dimension of FL1-DETA should be bigger than 20 nm. Table 2.4, provides the reservoir rock information. Although the pore size is

[1] molecular weight

not available, it is believed that a chemical compound with a minimum 20 nm diameter is a big structure to fit easily into the typical reservoir pores or a nano container. Hence, in this chapter, the only modification methods will be reviewed which considers SI retention enhancement as well as its thermal stability and dimension with respect to the reservoir pore size.

Table 2.4: Reservoir information

Property	Value
Lithology	sandstone (centre containing clay and carbonates)
Porosity	18%
Permeability	22mD [1]
Grain size	no info
Pore size	no info

2.5 Thermal stability enhancement

Figure 2.15 defines the condition on HTHP wells and their classification and highlights Elgin field conditions at 350 °F and 15000 psi. HTHP fields are spread around the world and some of the well known locations are shown in Figure 2.16 [96]. When applied in geothermal installations, the efficacy of commonly used inhibitors can decrease considerably due to the existing conditions such as high pressure, high temperature, high salinity or content of corrosive or scale-forming chemicals [97].

Field results analysis have proven that scale inhibitors, in general, are less effective in HT fields. This is attributable to the fact that in this condition, crystal growth inhibition becomes more difficult due to the thermal degradation of the deployed SI and the thermal agitation, diminishing the adsorption of SI to the reservoir rock [6]. For many years, phosphonate-based chemicals showed promising inhibition efficacy during squeeze treatment by mitigating routine scale deposition of $CaCO_3$, $BaSO_4$ and $CaSO_4$. Nonetheless, these chemistries exhibit low thermal stability for HTHP squeeze treatments [6]. Likewise, despite polymeric SI being more or less effective for routine scales and resisting HTHP conditions, they are very sensitive to the salinity levels of the brine and are not suitable for HS fields. In addition, they inherently suffer from poor retention properties in squeeze treatment procedure as compared to their old rivals, phosphonates [6, 9].

In order to improve the thermal properties of a chemical compound without altering their structure, a shell or a carrier can be used. Based on the reservoir information given in Table 2.4, Table 2.5, outlines the possible carrier candidates to increase the thermal stability of a scale inhibitor which they will each be discussed separately in

[1] mD is milli Darcy. A medium with permeability of 1 darcy permits a flow of 1 cm^2/s of a fluid with viscosity of 1 cp ($1mPa^-1$)under a pressure gradient of 1 atm/cm acting across an area of 1 cm^2

up-coming sections. It should be bared in mind that the suitable carrier should also have a great affinity to the sandstone rock, to help with the retention of the SI.

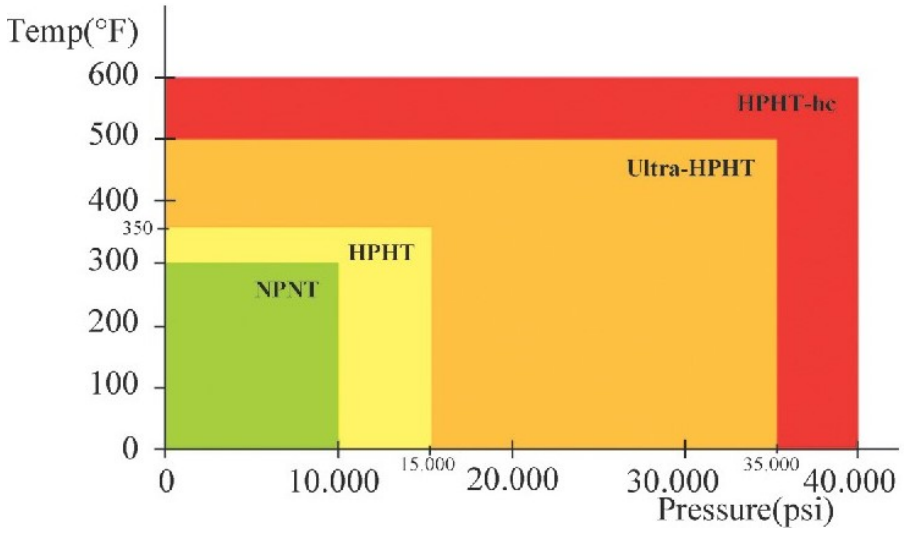

Figure 2.15: HPHT classification system: Normal pressure-Normal temperature (NPNT), High pressure-High temperature (HPHT), Ultra High pressure-High temperature (Ultra-HPHT), High pressure-High temperature hors category (HPHT-hc) [98].

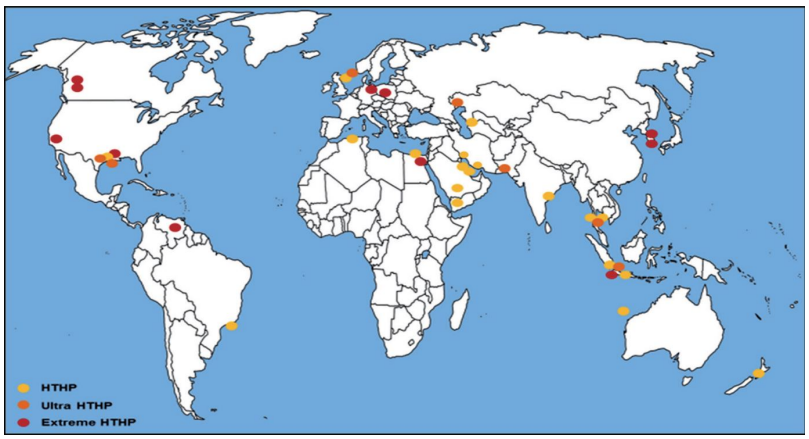

Figure 2.16: Locations of High temperature/ High pressure oil fields around the the globe [96].

[1]Layered double hydroxide

Table 2.5: List of possible carriers for thermal stability purpose

Carrier	Size	Facing Challenge
Ceramics	structure:$> 0.5\mu m$, pore size: $< 4 - 5$nm	small pores, uncontrolled desorption,big size
Polymers	100-500nm	Core-shell structure: appropriate shell thickness, thermally stability of the shell, Web structure: corsslinking density and thermal stability
LDH[1]	Ion exchange clay nano particles with size 200-400nm	Lateral size that is in mm or microns scale
Halloysite	inner diameter : 15-100nm	Structure size: 500-1000nm

2.5.1 Mineral carriers

2.5.1.1 Ceramics

To be used as a carrier, these mesoporous particles should be small enough to penetrate through the pores of the reservoir without blocking them. However, in reality this could be challenging as particles can aggregate and number of particles could approach one reservoir pore ending up in plugging it. Furthermore, the pores on these ceramic particles should be wide enough for carrying the inhibitor. Nevertheless, these small particles generally have small pores that FL1-DETA with dimensions more than 20nm cannot fit inside. Table 2.6, briefly describes the candidate of this group.

Table 2.6: Examples of mesoporous nano ceramic containers and their properties [99]

Type	Particle Size	Pore size
Propylcarboxylic acid functionalized silica mesoporous, TCP- prophine labeled	200nm (nanoparticles)	4nm
Propylamine functionalized silica mesoporous	200nm (nanoparticles)	4nm
Silica mesoporous	$0.5\mu m$	2nm
Silica mesoporous	$1\mu m$	2nm
Silica MCM-41	pellet	diameter x thickness 2mm x 5mm
Silica mesoporous SBA-15 (thiol functionalized)	$< 150\mu m$	6nm

2.5.1.2 Halloysite

This group of materials are interesting candidates to encapsulate big size scale inhibitors in their structure, owing to their wide inner diameter (Table 2.5 shown in Figure 2.17). Moreover, they are in tubular shape that will help them to float rather than blocking the pores of the reservoir. They have high thermal stability as they are mainly made of clays and they can help with the retention of the SI as their tubular structure allows them to release the content gradually through the inlets/outlets. The shortcoming of this method is the material itself that is made of clays. Figure 2.18 shows the Zeta potential of clays and the quartz, which shows that halloysite structure will be negatively charged regardless of the pH value. As a result, the mentioned structure will have no affinity to the sandstone reservoir as is mainly consisting of quartz.

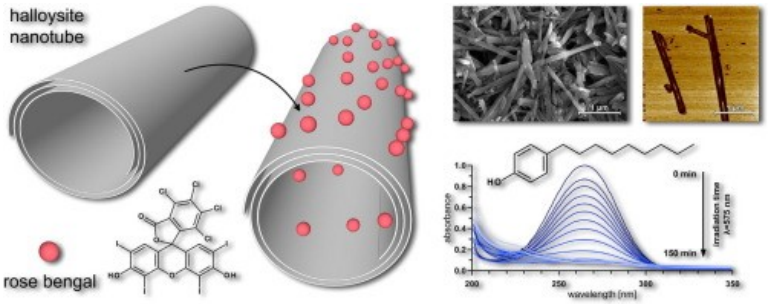

Figure 2.17: Halloysite schematic and SEM. The Rose Bengal can be replaced with SI co-polymer in our case [100]

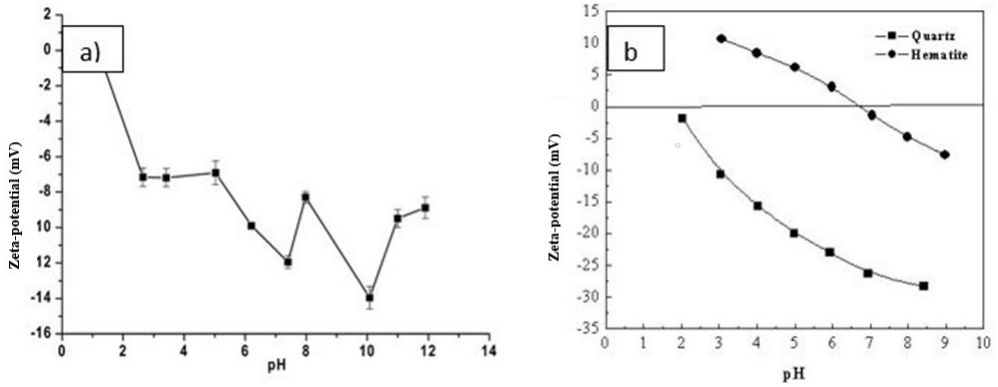

Figure 2.18: Zeta potential over pH range. a) Zeta potential of a sample Halloysite [101], b) Zeta potential of sandstone [102]

2.5.1.3 LDH

These layered clay based materials, can trap the inhibitor between their layers and protect them from the thermal fluctuations, high temperature and pressures. The mechanism of action is as illustrated schematically in Figure 2.19. The structure will be exfoliated gradually due to the high pressure. The aim is that the exfoliation would happen layer by layer, however this can be challenging in practice [103].

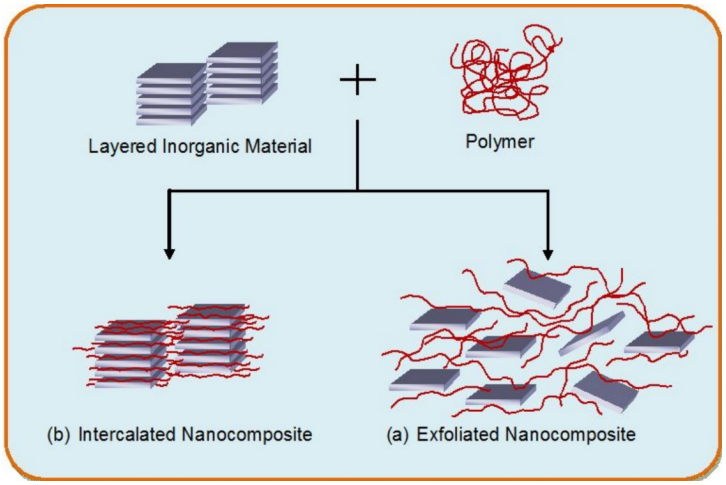

Figure 2.19: The LDH mechanism of action [103]

The polymer can be the FL1-DETA scale inhibitor in this schematic. Ion exchange is the routine method for filling these layered structures whilst the gap between the layers can be designed big enough to locate the inhibitors in between. However, the whole structure is in millimetres scale with no functional groups on its surface area. Therefore, stating a proper affinity between these carriers and the reservoir is challenging. Figure 2.20 [104] shows the SEM micrograph of this material and its layered structure.

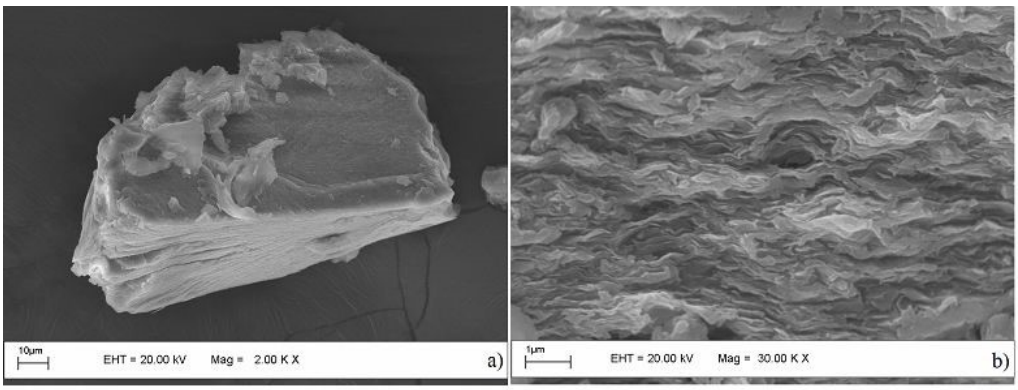

Figure 2.20: SEM micrograph of a sample LDH and its layered structure [104]

2.5.2 Polymeric carriers

With the purpose of being a carrier, polymers can be sub-categorised into three major groups:

2.5.2.1 Hydrogel

Hydrogels, are materials consisting of a permanent, three-dimensional network of hydrophilic polymers that water fills the space between the polymer chains. Hydrogels have number of applications, from biomedical to sensors and agriculture [105]. Due to their morphology and ability to be swollen in electrolytes, they can either trap the inhibitor in the interface of their own structure and the reservoir or embed it, Figure 2.21 [106].

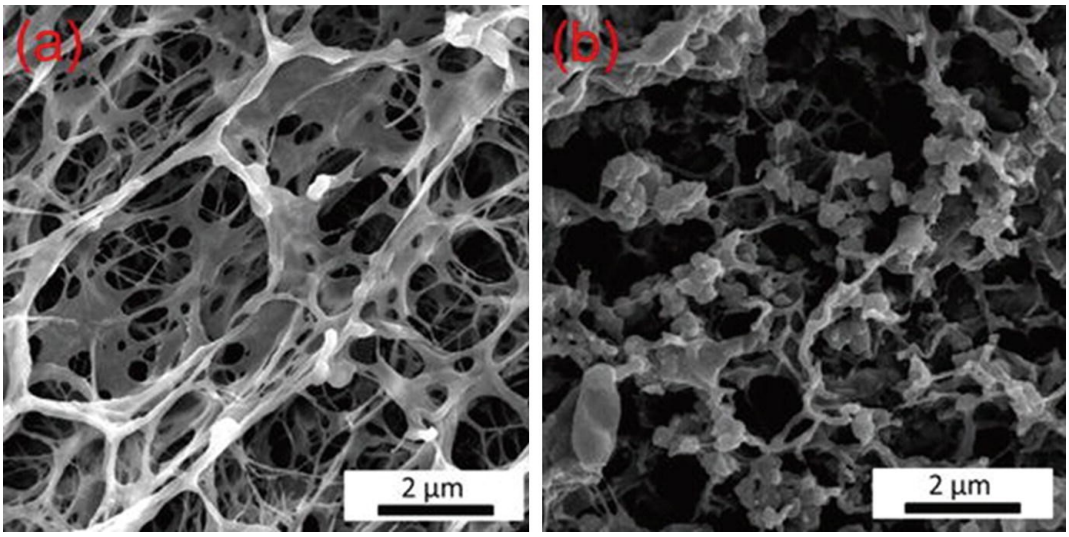

Figure 2.21: Hydrogels, a) Plane hydrogel structure, b)Nanosilica embedded in hydrogel structure [106]

This can slightly improve the retention of the SI in the system while avoiding blocking the pores by taking advantage of their web shape morphology. Yet, hydrogels usually have lower thermal stability than the prerequisite, 180 °C unless they would be modified. Moreover, they are polymers and copolymers with abundant hydrophilic groups which make them reluctant to bind with solid surfaces such as the reservoir. Hence, they would be a challenging candidate as a carrier.

2.5.2.2 Core/Shell structures

Due to their ability for gradual and smart release of the core material as well as high amount of loading up to 60%, this group of carriers were firstly used in the drug in-

dustry [107] and were spread through the smart coating industry [108] and later on to characteristics [109]. Based on the polymeric material used for the shell, they can have different thermal stability and withstand temperature fluctuations. However, in this method it is challenging to both reduce the carrier size and retain the shell thickness that can overcome high pressures. In terms of retention, these particles should be able to float inside the reservoir pores or adsrob on the reservoir rock and release the core gradually. Hence, plausible challenges of this category will be the ideal polymer candidate and releasing method, size distribution and stabilisation, Figure 2.22 [107].

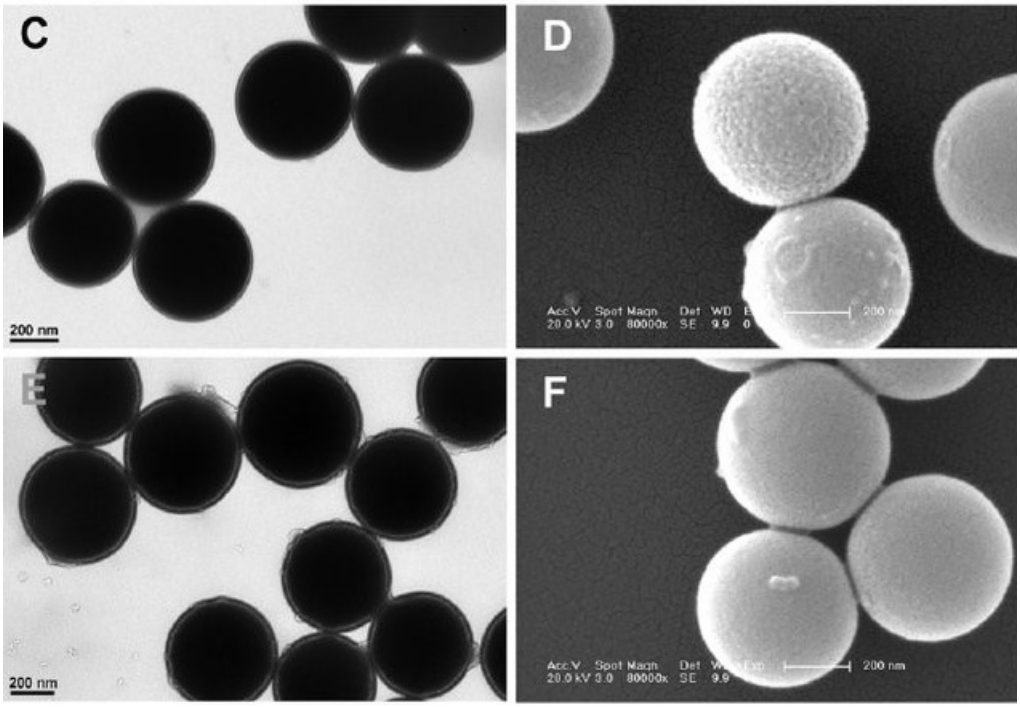

Figure 2.22: SEM images (left) and TEM (right) of a core shell structure. The size can be reduced with sonication or increasing the stirrer speed. The shell can become rough or smooth depending on the core material and the chosen polymer [107]

2.5.2.3 Nano-fibre polymers

By forming a membrane structure, fibre shape polymers can act like a claw i.e while not blocking the pores, twist around the inhibitor and attach it to the reservoir. As most of these polymers have long structure, they usually tangle and have the ability to trap the SI, enhancing its thermal stability and retention. Conductive polymers such as Polyaniline (PANI) are from this group that will be discussed in Section 2.8.1 of this chapter, Figure 2.23 [110]. Details on conductive polymers are presented in Appendix A.

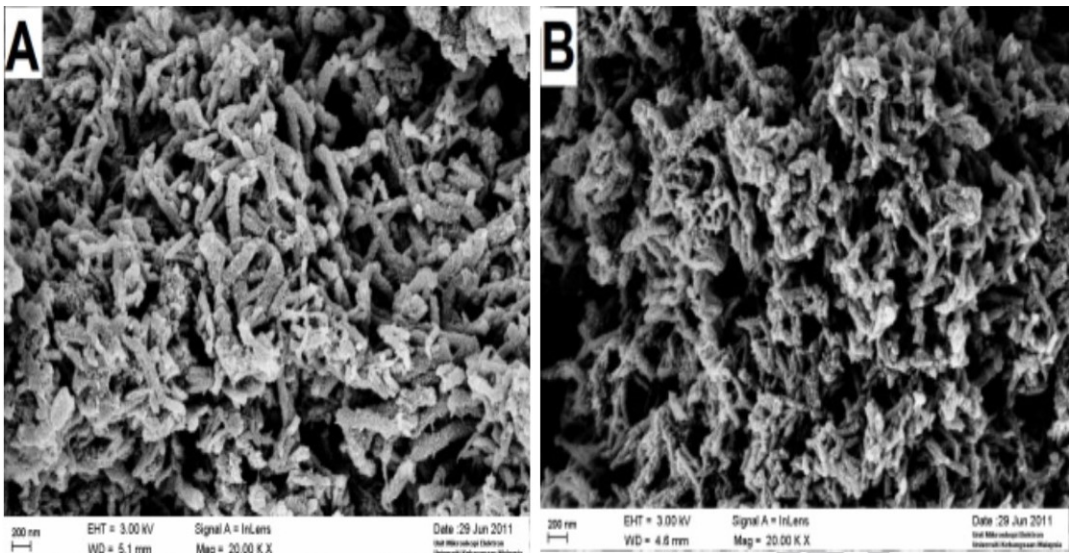

Figure 2.23: PANI SEM micrograph. The polymer morphology is dependent on the method of polymerisation and speed of stirring, (A) interfacial (B) rapid mixing [110]

.

2.6 Scale inhibitor administration methods

Common SI methods of administration are listed in Table 2.7 and the pros and cons [87] are named. In this PhD project the interest is in relation to scale prevention through inhibiting method i.e the use of scale inhibitor and squeeze treatment as a method of administration.

To suppress aforementioned depositions, the inhibiting chemicals can generally be injected in a dedicated continuous injection line, or bull-headed as a batch treatment into the formation, commonly known as squeeze treatment. Continuous injection is more expensive and is mainly effective when inter-well distances are relatively short [87]. Squeeze treatment is carried out by injecting a large amount of scale inhibitor (SI) into the reservoir with the expectation of gradual release above the minimum effective dose (MED) over a period of time [3]. Despite the requirements for shutdown periods, the squeeze treatment approach is desirable for being more effective as the applied treatment protects from the wellbore area to topside, especially when SI lifetime and its effect prolongs for more than 6 months [4].

[1]such as mixture of scale and corrosion inhibitors, foaming agents, cleaning agents, etc.

Table 2.7: Common scale inhibitor treatment methods [87]

Method	Pros	Cons
Squeeze treatment	• More effective in carbonate reservoirs. • Cost-effective for slowly leaching inhibitors (phosphonates) • Ensures a long lifetime, (up to 24 months.)	• Ineffective for non-carbonate reservoirs. • Not the best option for strongly leaching inhibitors. • Production stops during treatments. • May cause formation damage. • Time-consuming. • Several steps are involved
Continuous injection	• Less periodical treatments. • Chemical costs and labour requirements are reduced. • More effective for non-carbonate reservoirs. • More effective for strongly leaching inhibitors, (polyester based). • Less production shutdown time. • Less time-consuming • Can be done in combination with other treatments[1]	• Relatively more expensive. • Ineffective where there is a considerable inhibitor retention on the rock matrix. • Sensitive to inter-well distances, i.e., considered to be effective only where inter-well distances are relatively short.
Batch treatment	Relatively effective	• Production stops during treatments • Short lifetimes

2.6.1 Squeeze treatment

Squeeze treatment usually means any treatment of an unfractured producing well performed by injecting a chemical inhibitor (i.e., corrosion or scale inhibitor) into the

wellbore of the producing well to place the inhibitor into the formation. Squeeze treatment is one of the most common and efficient methods of inhibitor administration to prevent scale formation in oil reservoirs [111]. It is widely used in order to prevent scale formation in oil reservoirs, near oil well bores, production tubing, and to protect safety valves from scaling [112].

The steps of squeeze procedures are [86]:

1. Pre-flush: Consists of cleaning and conditioning near well bore for the scale inhibitor. To this end, a volume of brine (usually a very dilute solution of scale inhibitor in seawater – 10s – 100s ppm SI) is firstly injected into the formation. This overrides the tubing volume and production fluids back into the formation and it also has additional advantages including:

   (a) Decreasing the temperature near wellbore as injection brine has a lower temperature. Elevated wellbore temperature reduces SI adsorption on the sand reservoir. Decreasing the temperature with a pre-flush will prepare the well for treatment and efficient adsorption.

   (b) Acting as an intermediate, providing space between the in situ reservoir fluids and the injected main (high concentration) scale inhibitor slug

   (c) Changing the near well wetting state to more water wet conditions if mutual solvent (or possible some surfactant) is applied. This leads to higher SI adsorption in the warmer region away from the wellbore.

2. Main treatment: The main scale inhibitor slug is pumped into the water producing zone, Figure 2.3, normally in the concentration range of 2.5% to 20% wt/wt [102]. The function of this SI is to propagate into the formation where it is retained by either chemical adsorption or by temperature/chemical activated precipitation. For some specific treatments, this inhibitor solution may contain other additives.

3. Over flush: Consists of flushing/pushing the chemicals deeper in the formation. An over-flush of fluid is usually brine, seawater or sometimes diesel or even gas and is injected into the well to push the main treatment further into the formation. The aim of over flush is to pipe the SI further into the formation and away from the wellbore. Due to this action the SI may absorb and/or precipitate further away from the well bore giving it a longer treatment life.

4. Shutdown: Shutting down the production for a short period (usually 62-4 hours) to allow adsorption or temperature/chemically induced precipitation to occur and reach close to equilibrium.

5. Post flush: Resuming the production (production water should consist inhibitors). Oil production can then resume, while the scale inhibitors desorb slowly into the produced water in order to prevent scale formation. The success of the treatment is defined by the squeeze lifetime which is specified in terms of how long the SI is back produced at a concentration level greater than the 'MIC', more specifically 1–50 ppm.

6. Re-treatment: Treatment lifetimes can be from 3 to 6 months [87]. When the inhibitor concentration falls below the MIC, a new treatment must be initiated.

The two major retention release mechanisms that have been found to occur in a formation are adsorption/desorption and precipitation/dissolution. Vazquez believed that adsorption squeeze process is the most effective method for inhibitors to retain and adsorb on sandstone formations whilst precipitation squeeze treatment is the most suitable method for carbonate formations [113].

2.6.1.1 Adsorption squeeze treatment

In the case of adsorption squeeze, the chemical inhibitor adsorbs onto the rock by a physicochemical process. Adsorption of inhibitors is thought to occur through electrostatic and van der Waals interactions between the inhibitor and formation minerals. The surfaces of sand particles carry net negative charges [102], as a result, they attract cations and repel anions, both of which originate from the aqueous medium. The zeta potential measurement of sandstone is discussed in section 2.8.1.1, Figure 2.30.

The interaction between an SI and reservoir could be described by adsorption isotherms, which are associated with the interaction between the scale inhibitor and reservoir rock matrices. The adsorption isotherms $\Gamma(C)$ with the unit of $\frac{mg}{g}$, determines an existing equilibrium between the amount of scale inhibitor adsorbed onto the rock substrate and the scale inhibitor concentration in the bulk aqueous phase. Appendix B represents some of the frequently used adsorption isotherm theories. However, commonly used adsorption isotherms for squeeze treatment are Langmuir and Freundlich isotherms [87]. The adsorption isotherms are a function of several factors such as the pH, temperature, rock substrate, brine salinity, the inhibitor type, its composition and molecular weight. A schematic of an apparent adsorption isotherm is depicted at Figure 2.24. The term apparent is used as scale inhibitor can function through a pure adsorption, precipitation or coupled adsorption/precipitation behaviour [114]. Typically a good adsorption level in a static inhibitor adsorption test, would be in the range Γ = 0.5- 4 mg/g (mg of SI per g of core) at a moderate inhibitor concentration ($\sim$ 2500ppm) [86].

High salinity of a brine can also be a crucial factor affecting the amount of SI adsorption on the reservoir. Graham *et.al* [115], concluded that the bonding possibilities are greatly increased as the diffuse layer thickness reduces to zero (or a very low value) in

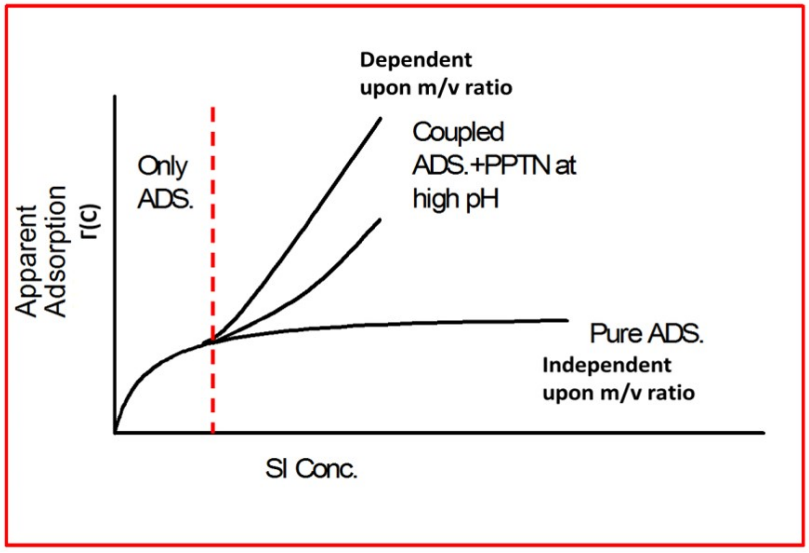

Figure 2.24: Schematic diagram of pure adsorption and Coupled adsorption/ precipitation behavior [114]. Acronyms used on the figure, ADS: adsorption, PPTN: precipitation

which case, the counter charge resides entirely within the Stern layer. The reduction in diffusion layer thickness allows polymeric species to approach closer to the surface that is free from electrostatic counterion repulsion mainly because the counterions present at the surface are drawn closer to surface charge sites leaving a larger area for hydrogen bonded polymers to adsorb onto [86].

2.6.1.2 Precipitation squeeze treatment

Precipitated squeeze treatment extends the squeeze lifetime by precipitation or phase separation. This technique is commonly carried out by adjusting the solution chemistry ($[Ca^{2+}]$, pH, temperature) of polymeric and phosphonate inhibitor solutions that reacts to form an insoluble salt complex. As a result, the chemical inhibitor precipitates or phase separates in a gel-like semi-solid structure within the pores in the formation onto the rock surfaces for a precipitation squeeze [113, 116]. For instance, phosphonate scale inhibitors can be precipitated as calcium salts, however, inhibitors such as phosphate esters are not suitable because they encourage the formation of soluble calcium salts or salt complexes. During squeezing on a carbonate formation, an acidic solution of a phosphonate is squeezed down a wellbore into a limestone or dolomite-containing reservoir. Thus, the calcium ions are released into the solution as the acid reacts with the carbonate from the limestone or dolomite. Thereby, released Ca^{2+} reacts with the inhibitor and form an insoluble salt. To achieve such a squeeze in non-carbonate (or sandstone) reservoirs, both metal ions, $[Ca^{2+}]$, and scale inhibitor must be included in the solution placed in the reservoirs. Precipitation of scale inhibitor takes place within the pore spaces of the rock, on adjusting the pH and increasing a calcium ion

concentration [3, 87]. Following precipitation, the well is returned to production and the level of inhibitor in the return curve is governed by the solubility (C_s) of the inhibitor / calcium complex and the release rate (r_2) of inhibitor into the produced water. The precipitation inhibitor is intended to place more inhibitor per squeeze, and to extend the treatment lifetime; treatment lifetimes generally exceed 1 year. Thus, precipitation squeezes are generally superior to adsorption squeezes [116].

2.6.1.3 Challenges for squeeze treatments

When the applied pressure down the well is reversed, one of the major challenges for downhole squeezing widely encountered is the desorption of the chemical inhibitor due to weak retention properties. In fact, about 30% of the chemical inhibitor is often immediately flushed from the rock due to the weak retention properties at early stages [116]. Hence, the scale inhibition is carried out by the remaining adsorbed SI onto the rock surface, until it gradually washes away from the rock surface during oil production and that another descaling treatment is required [116]. Changes in wettability and permeability of the rock formation are another challenge facing downhole squeeze treatment. Any adsorption on the rock surface can change its surface properties and wettability similarly to the the aqueous solutions of applied scale inhibitors.

This could change the water permeability of the rock and lead to a so-called water coning effect, wherein a water channel could over time open up into a water pocket. The well may then be damaged irreversibly and not to reach its optimal productivity again [117]. Furthermore, the precipitated inhibitors can cause clogging of pores or formation damage [118], thus, reducing the permeability of the rock formation which can cause reduced fluid flow. In horizontal hydrocarbon well formations and some regions where hydrocarbon formations have low permeability, scale inhibitors as a Newtonian fluids have difficulties reaching into the formations, thus, the squeeze treatment will not be efficient enough. Therefore, these will be the regions were scaling block and decrease the production rates [119]. Non-carbonate reservoirs are challenging and practical results shows that precipitation squeeze treatments are less effective as compared to the carbonate reservoirs, as non-carbonate reservoirs do not offer sufficient amounts of calcium ions to cause precipitation and complex formation of scale inhibitors.

2.6.1.4 Squeeze treatment life time

The squeeze treatment best result is gained when when during the production a gradual release of a scale inhibitor is achieved whilst the production resumes. One of the main qualities of a successful scale inhibitors is that they reduce costs and prolongs squeeze lifetime. Hence, oil and gas industries' biggest challenge, is to maximise squeeze lifetime through development and deployment of new technology to increase the retention of the inhibitor in the system.

Ideally, in a squeeze treatment, the scale inhibitor concentration return curve would

have a high adsorption rate and a slow desorption rate [111, 120] as shown in Figure 2.25(a), however, in practice as shown in Figure 2.25(b), the SI concentration drops dramatically after the production resumes to levels below the MIC in a short period. One method to increase the lifetime of a squeeze treatment is by increasing the retention or thermal stability of the scale inhibitor. As a result, desorption of the SI will be less rapid and gradual. Using different types of carriers for similar purposes has been discussed repeatedly by many researchers in different field of science, including medication and drug delivery [121, 122, 123, 124]. A proper carrier helps the core (i.e. SI) to be protected from temperature and pressure fluctuations and a smart carrier can help with the gradual release of the core.

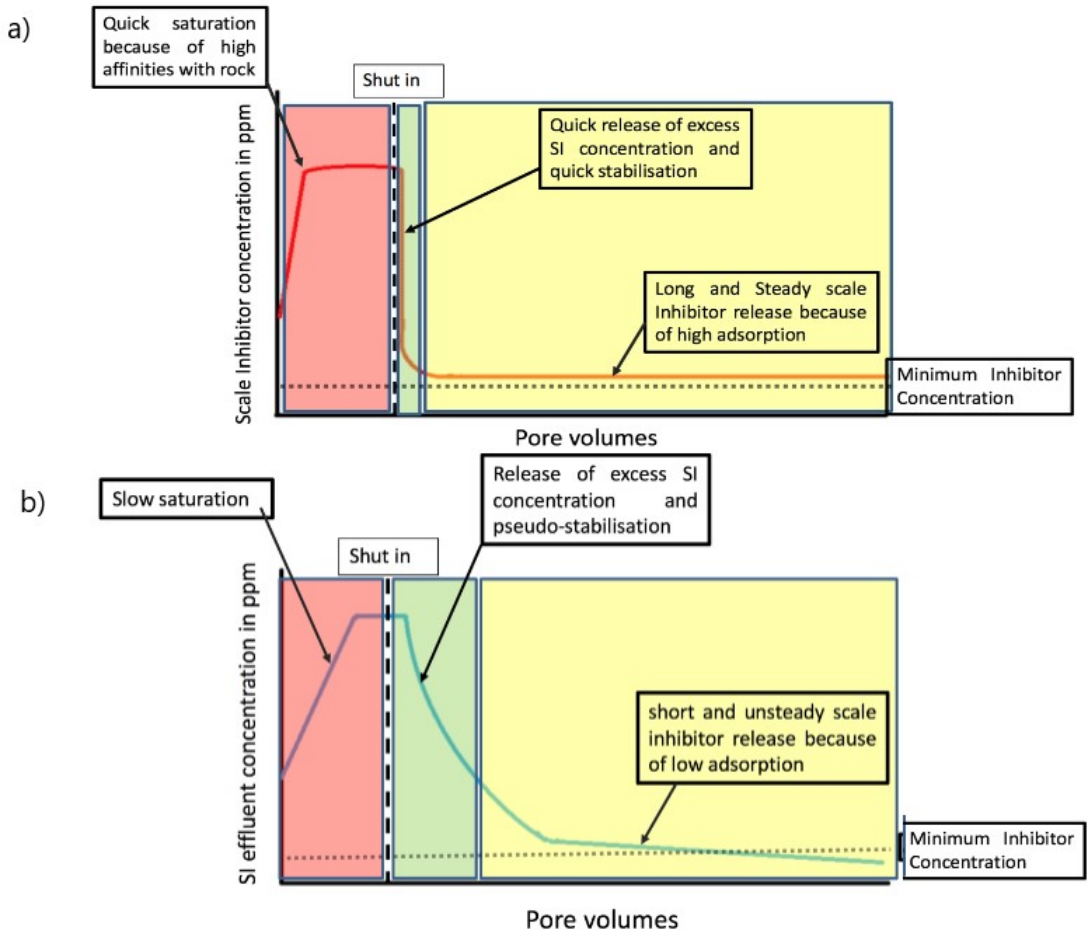

Figure 2.25: Squeeze treatment curve, a) Ideal curve, it is expected that the SI concentration remains above the MIC at a constant level for a long period. b) Reality curve, the SI concentration falls dramatically as the production is resume and drop below the MIC threshold in a short period [120].

2.6.1.5 Retention stability enhancement for squeeze treatment

The process of colloidal attachment onto surfaces of a large material is called retention. As schematic in Figure 2.26 illustrates, there are three main types of retention mechanism on porous media [1]:

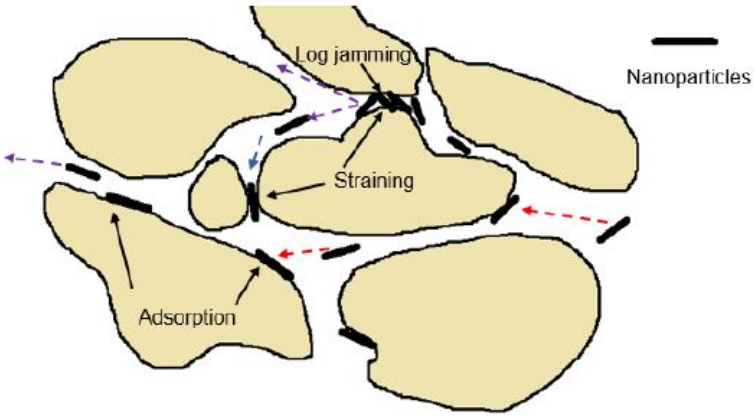

Figure 2.26: Different types of retention: adsorption, straining and log jamming [1]

1. *Adsorption*: Mechanism of adsorption is defined as adsorption of particles onto rock surface as a result of Brownian motion, through which electrostatic interaction between the migration particles and the solid surface of the pores is formed [125].

2. *Straining*: Another element of retention is straining that is also known as mechanical entrapment or deep-bed filtration in small pores. On the downside, straining, could lead to blocking of narrow pore throats by larger particles [125]. As a result of the created mechanical entrapment, the particle concentration in the production water will not reach the initial injected amount unless a larger volume would be injected [125].

3. *Log-jamming*: Log-jamming is an advanced form of straining in which particles can block pores larger than their own size [125]. The main factors governing the log–jamming effect are particle concentration, effective hydrodynamic size, pore size distribution, and flow rate [125]. In general, density difference between moving particles and carrying fluid causes sedimentation and/or gravity settling due to the mobility of the water molecules compared to heavy particles agglomeration will occur. Gravity settling or adsorption, will gradually reduce pores' throat and eventually block them [125].

In the past various techniques have been practised to increase scale inhibitor retention and enhance its squeeze lifetime [126], Some of which are listed as below :

- Precipitation squeeze treatment
- Raising the pH in the reservoir
- Changing reservoir wettability
- Use of kaolinite or clay to enhance inhibitor adsorption
- Use of cross-linked inhibitors
- Use of micro particles
- Use of surfactants

As an example techniques such as NAST[1] propose surface modification on the formation rock in advance to inhibitor injection. The surface modification of the sandstone [1] facilitates the establishment of a strong bond between the available functional groups on SI and the sandstone. Another approach could be fitting the SI inside a carrier that would have the affinity to bind to the reservoir formation through its functional groups [127]. Carriers will protect the SI in the core from severe environment conditions (HTHP and high salinity) and based on the type, a smart carrier can release the core on demand. The carrier can bond to the reservoir chemically or physically. For both chemisorption and physiosorption methods, doping, bridging with a third material or functionalisation of the carrier might be needed to improve the bonding strength. In the case of physisorption as a method of modification, the carrier could be trapped inside the pores of the reservoir rock or be attached through weak electrostatic dipole attractions. In the case of chemisorption, the SI (/carrier) will form an irreversible bonding to the reservoir rock. Reservoir damage and pore blockage are main factors to be considered while choosing a method. Hence, it is crucial to consider design factors that could be straining such as the size of the carrier structure its pore size for locating the SI inside and reservoir pore size.

In order to achieve an effective scale inhibitor treatment for a rock formation with low permeability, the use of fully viscosified scale squeeze fluids has been suggested in

[1] Nanotechnology Assisted Squeeze Treatment

order to optimise the squeeze treatment by allowing the fluid to reach the low permeability region and the horizontal zones [119]. Moreover, for the use of precipitation squeezes in non-carbonate reservoirs it is suggested to include both metal ions and scale inhibitor in the solution placed in the reservoir. The added metal ions are expected to undergo precipitation reactions with the scale inhibitor such as phosphonates, thus the scale inhibitor life time is increased [87].

Even though all of above stated techniques will more or less improve the retention ability of most of the SI available in the market, however, they may not be as effective or even ineffective for newly designed eco-friendly SI that have remarkable inhibiting effects. Solution to better retention can be laid down in the chemical compound structure which might need to be modified. Plausible modification methods that can help with the retention enhancement of the SI/carrier on the reservoir are listed in Table 2.8.

Table 2.8: Retention methods and their means of action

Retention method	Means of action
Chemisorption /physiosorption on the reservoir	Doping,bridging, functionalisation, polymerisation on the surface
Floating in the reservoir pores	Stabilisation with organic/inorganic tails

2.7 Inhibition/ dispersion of sulphide scales

With the decrease in temperature, brine is diluted and pH increases during production and so the tendency for zinc sulphide and lead sulphide scaling will increase [128]. Therefore, zinc sulphide and lead sulphide form promptly due to their low solubility. Both sulphide scales are significantly less soluble than other common mineral scales such as calcium sulphate, calcium carbonate and barium sulphate, hence, more difficult to control using threshold inhibitors. Along with the fast kinetics, constrains on forming hydrogen sulphide gas and using anaerobic conditions in laboratory environment, has caused further challenge to find the suitable chemistry to inhibit the formation of such scales. As a result most test has been conducted as field trials.

In a research work done by Przybylinski [62], laboratory tests on number of common commercial SIs, defined an MED of 400-600 ppm against sulphide scales. However, Emmons and Chesnut[129] showed that with 4-10 ppm active concentration of a polymeric based inhibitor (hydroxyethylacrylate/acrylate co-polymer), the pump life will be increased from ∼21 days to over 4-6 months against zinc sulphide. Lopez *et. al* [130] confirmed the performance of different potential polymeric sulphide scale inhibitors with the concentration ranging form 25 ppm to 50 ppm in the presence of saline

formation water consisting 50 ppm of Zn^{2+} and 5 ppm of Pb^{2+}, using an anaerobic tube-blocking apparatus at 166 °C. Savin *et. al* [10] reported that sulphonated/ carboxlic acid co-polymer and phosphorus functionalised polymer at high concentrations could provide partial ZnS inhibition at 20 °C and at pH 7. However, the sulphonated SI failed to prevent PbS formation when it was co-exist with ZnS. In this work they also reported that the inhibition performance of sulphonated SI against ZnS dramatically decreased by the increase of the brine salinity and temperature to 95°C, at pH 4.5 where zinc sulphide completely precipitate. Collin and Jordan [60] work in a low salinity 5% NaCl brine, studied the performance of conventional sulphate and carbonate scale inhibitors as well as chelating agents against zinc sulphide were studied. At a medium to low concentration of zinc ∼ 75 ppm, AMPS/AA, PHOS/MA, PMA/AMPS and PAA_2 and DTPMP were effective against zinc sulphide scale by threshold scale concentration. HEDP and ATMP, Na_4EDTA, and Na_5EDTA provided the chelating performance with 60 - 70% chelation of Zn^{2+} at a molar ratio of 1:1. However, all these inhibitors were less effective with an increase in zinc concentration and/or brine salinity. They also showed that TEAPE failed to inhibit zinc sulphide.

Field trials by Kaplan [131] increased well operation time consisting 2 ppm zinc, up to 9 months using combined scale inhibitor (for calcium carbonate) and alkyldiphenyl ether sulphonate dispersant (for zinc sulphide). In another work by Jordan *et. al* [8], field trials in the Gulf of Mexico and both the UK and Norwegian sectors of the North Sea, showed successful inhibition of zinc sulphide and lead sulphide using low molecular weight acid polymer which did not show any adverse effect against the performance of sulphate and carbonate SIs. This chemical with an MIC of 25-30 ppm, avoids further build up layers of zinc sulphide and removed the zinc sulphide scale from the crude oil cooler.

From all above trials, it is shown that to this date no inhibitors were found with the threshold concentration to show retention and be applied as squeeze treatment with the purpose of sulphide scale inhibition on sandstone reservoirs; as at least 30-50 ppm of any polymeric scale inhibitor is needed for an acceptable performance to be observed against sulphide scales. Furthermore, none of the above suggested chemicals fully suppress the formation of ZnS, FeS or PbS, and the seen performance was solely based on the dispersion of formed scales. It has also been proven that conventional SI for carbonate and sulphate scales are ineffective against sulphide scales or show very poor performance. In the next section, SI administration methods will be discussed and the advantage of squeeze treatment over continues injection will be explained.

2.8 Suggested strategy for FL1-DETA enhancement

Based on the aforementioned literature, in order to achieve HTHPHS resistance and better retention properties of FL1-DETA on the sandstone, application of physisorp-

tion method is suggested. Based on the negative charge of sandstone rock, positively charged carriers can have an advantage of more powerful physorption through electrostatic interactions. Furthermore, the carrier needs to have high thermal stability and has the ability to release the inhibitor whilst needed. The web shape morphology is also preferential, as it will avoid the blockage of the pores.

The proposed polymer candidate is PANI (polyaniline) which is a conductive fibre shape polymer and can form a web shape morphology. This polymer can be synthesised through many techniques depending on the application. However, rapid oxidation polymerisation as a cost effective and eco-friendly method leading to high yield is proposed. PANI as a positively charged polymer could increase the affinity between the SI and the sandstone through opposite charge interaction and has an increased number of non paired electrons compared to DETA. The advantages of using this polymer will be discussed in more details in the following section.

2.8.1 Polyaninline (PANI)

Polyaniline is one of the members of the conductive polymer family. This eco-friendly polymer has been used in biosensors [132, 133, 134] smart coatings[135, 136] and other applications such as water treatment[137, 138] and corrosion inhibitors [139]. Due to its especial structure and non paired electrons that are located on the nitrogen atom, PANI molecules are highly reactive and positively charged. While PANI reduces with hydroxide, it can not only act as a buffer and control the pH in the media which is used, but also operates as a scale inhibitor by scavenging HS^- ions. Another advantage of these positively charged nitrogen atoms can be the affinity that they might show toward sulphide scales with their inherent opposite charge and affect their crystal growth. Polyaniline is proposed as a candidate as it is one of the conjugated polymers with following properties:

- easy synthesis,
- low production cost,
- eco-friendliness,
- good environmental and thermal stability,
- simple doping/undoping chemistry,
- nontoxic nature.

Polyaniline can be synthesised through different methods such as in-situ polymerisation, electropolymerisation and radical polymerisation whereas each gives different morphology for different applications. However, synthesis of PANI nanostructure, particularly nanotube without using any external template is a really challenging task.

Polyaniline nanotubes (PNTs) have many advantages over carbon nanotubes (CNTs). PNT is economically cheap and easy to synthesise; apart from this, it has large specific surface areas, a hollow tube and porous structure that makes excellent adsorbent material. Literature review has shown that PNTs have high specific surface area (SSA) and are hollow tubular in nature with enough adsorption sites available for wastewater treatment. Owing to the presence of the large number of amine and imine groups, PNTs have already shown to act as successful candidates for water purifiers [140]. As a result, it is expected that PANI will have a double action by not only assisting the scale inhibition process, but also increasing the thermal stability of the FL1-DETA. Tangled PANI fibres are adhesive to rough surfaces and due to their positive charge, have high affinity to the negatively charged sandstone reservoir. Hence, it is anticipated that PANI fibres attach to the reservoir through physisorption followed by strong electrostatic absorption.

Polyaniline can be found in one of three idealised oxidation states:

- $(C_6H_4NH)_n$ leucoemeraldine – white / clear & colourless
- $((C_6H_4NH)_2(C_6H_4N)_2)_n$ emeraldine – green for the emeraldine salt, blue for the emeraldine base
- $(C_6H_4N)_n$(per)nigraniline – blue/violet

Emeraldine base is regarded as the most useful form of polyaniline due to its high stability at room temperature and the fact that, upon doping with acid, the resulting emeraldine salt (ES) form of polyaniline is highly electrically conductive (Figure 2.27); moreover, ES is water-soluble.

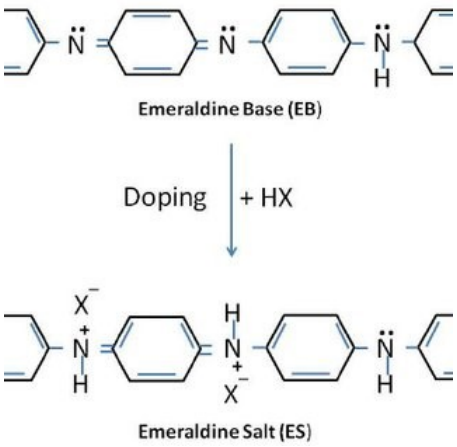

Figure 2.27: EB to ES transformation. HX represents a weak acid like —COOH

2.8.1.1 PANI mechanism of action

PANI can be doped by the FL1 through the -COOH groups located on the structure. The schematic is provided in Figure 2.28.

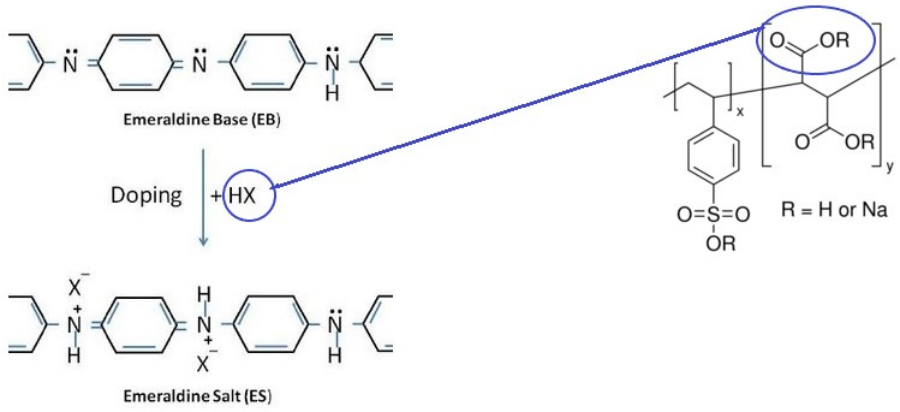

Figure 2.28: Schematic of doping FL1 to PANI

As the study on investigating corrosion properties of PANI/GO[1] composite [136] suggests, the thermal stability of FL1-DETA should remarkably improve by doping with PANI. Figure 2.29, shows the TGA results of plane GO, plane PANI and the composite of GO/PANI. It can be clearly seen from the trend that the thermal stability of the GO has increased through this doping action [136].

Moreover, PANI will not fully wrap the SI structure due to their membrane shape morphology; this will allow the SI to be exposed enough to the scaling environment and perform its action otherwise the gradual release of the SI would be possible through undoping mechanism that is sensitive to pH increase caused by losing the positive charge [141]. This can be vital, as increased pH is one of the main factors contributing to scaling. By undoping any reacted SI, non paired electrons would be available once again and this time they can scavenge the HS^- ion in the system and retard the scaling action while acting as a buffer [142]. In each undoping followed by HS^- reduction, the ES will gradually transform to EB and become more prone to release the left doped SIs. Ultimately, the full structure will become an EB with no charge and less solubility, which will help to be flushed away by the production water and avoiding to block the pores on the reservoir.

There is not much information on toxicity/ bio-accumulation / or biodegradability of PANI or its derivatives based on oil and gas industry reports, however, many researches on tissue engineering have reported PANI and PANI composites, to be biodegradable and bio compatible with rats tissues [143]. Another advantage of PANI

[1] Graphene oxide

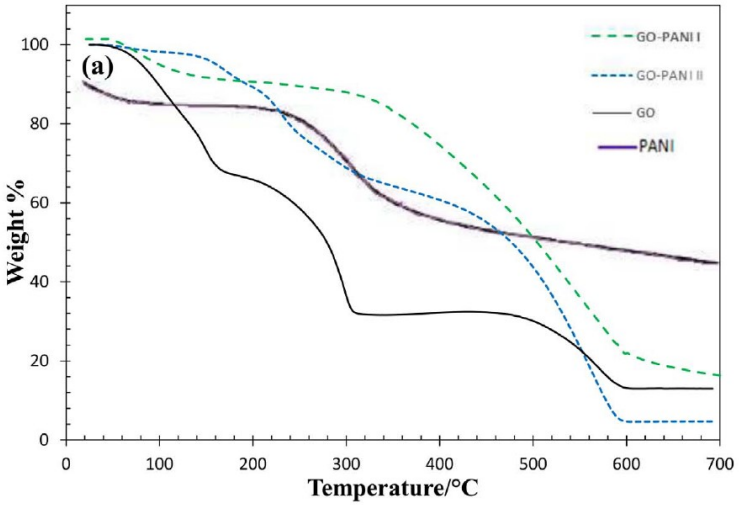

Figure 2.29: TGA results for PANI, GO and PANI /GO composite. Thermal stability of GO has significantly improved by doping with PANI [136].

can be the existence of the unpaired electrons on its structure. If the ratio between the scale inhibitor and the PANI is properly managed, the left non-paired electrons in PANI structure can act as DETA through same scheme and inhibit the formation of ZnS and PbS on top of the buffer behaviour that was discussed earlier.

It is expected that PANI has enough affinity to the sandstone according to its zeta potential data. Sandstone is negatively charged through most of the pH range while PANI is positively charged, Figure 2.30. Since PANI is a polymer that has long chain and higher amount of chargeable sites than a single surfactant or a nano or micro particle, effective electrostatic adhesion to the sandstone is anticipated.

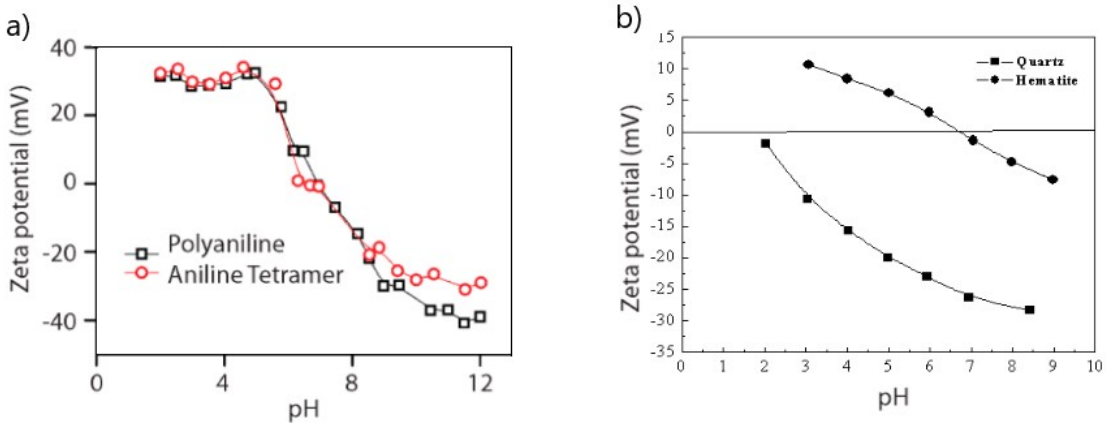

Figure 2.30: Zeta potential of a) PANI[144] and b) Quartz [102]. Sandstone is mainly consists of Quartz

2.8.1.2 Challenges while using PANI

Although other groups of polymers have been used widely as scale inhibitors in the oil and gas industry, the use of conductive polymers have not been reported. This is mainly due to the fact that most conductive polymers are insoluble in water without modification or should be electrodeposited to be conductive. Hence, using a conductive polymer as an SI carrier is a new topic and there are no publications suggesting their role in scale inhibition application to the best of author knowledge. On the other hand, PANI is another member of this family with easier polymerisation pathways, which is available in salt form, helping with its method of application. However, considering PANI properties and the information available on the literature regarding this polymer, possible facing challenges are as listed below:

- PANI solubility needs to be improved. Hence, plausible use of GO as a bridge to improve the water solubility or affinity to sand stone.
- The novelty of this project is that PANI has widely been used as an anti-corrosion inhibitor; however, it has never been used as a scale inhibitor.
- Another challenge of this project can be the optimisation of the ratio between the SI and PANI since enough amount of -COOH groups should be left available on FL1 structure to inhibit the formation of $CaCO_3$ and $BaSO_4$. Moreover, the unpaired electrons of nitrogen should not be all used in PANI structure as it was explained thoroughly, earlier.
- Since, the SI can be trapped by the PANI growth and physically being attached to the reservoir, the morphology design is crucial and is highly dependent on the method of polymerisation.

2.9 Summary

In this chapter, scaling as a flow assurance issue was introduced and general scaling scenarios were explained. Scaling is themormodynamically possible if the saturation ratio>1. Alterations in conditions such as temperature, pressure and pH can induce scaling through affecting the SR value. Furthermore, homogeneous and heterogeneous crystal formation and growth theories were discussed in detail. Mineral scales can be divided into two min families of routine ($CaCO_3$ and $BaSO_4$) and exotic scales (ZnS, PbS). Both routine and exotic scale natures were explained and the effect of influencing factors on each scale type formation such as temperature, pressure, pH and pressure were reviewed based on literature. In general, sulphide scales have shown to have low solubility, fast kinetics and they are more likely to form deposits in upstream facilities, caused by temperature drop and pH increase. However, due to their fast kinetics it is believed that this scale nucleate and form before reaching the upstream facilities and close to the well bore.

Different methods of scale control, fighting/prevention and removal were explained. In general whilst mechanical removal can be useful solution, the adverse effect of it such as facility damage, and shutdown period should be considered. This method would only be effective, if the scaling occurrence would not be frequent. Acid washing as another common method of scale fighting, is associated with high risk to the employees as well as the facilities based on HTHP conditions and the release of H_2S gas in gas condensates fields such as Elgin. As a result, squeeze treatment as a prevention method of choice in scale inhibitor administration shows the most promising and economical solution to mineral scale mitigation. However, a scale inhibitor to be squeezed in HTHPHS fields would require high thermal stability and retention properties. To justify the choice of SI in this project, different types of scale inhibitor were compared through their application and limitations. Based on the inhibitor classifications, FL1-DETA is a polymeric scale inhibitor. Polymeric scale inhibitor have better thermal stability however, weaker performance against routine scales and poor to no performance against exotic scales.

HTHPHS fields properties were also explained and possible methods of modification options based on the constraining conditions for both retention and thermal stability enhancement of FL1-DETA is discussed separately. The aim of modification is mainly to improve the retention of FL1-DETA on sandstone reservoir whilst improving/ maintaining its thermal stability without alteration of the SI chemical structure. To this end, pros and cons of mineral and various types of polymeric carriers were discussed and the constraints on retention improvement based on each type were reviewed. Nominated candidate was narrowed down by considering both objectives of thermal stability and retention on sandstone reservoir simultaneously as well as reservoir lithology and porosity properties.

Due to the reservoir condition in this project the final designed/modified inhibitor should be an eco-friendly, polymer-base inhibitor which:

1. Withstand HT
2. Withstand HP
3. Withstand HS
4. Be used as an Squeeze treatment:
    - Retention on sandstone
    - Quick adsorption slow desorption
    - Long life time
    - Small MIC

As the suitable candidate must survive the harsh conditions of high temperature, high pressure and high salinity levels (HTHPHS) in the reservoir, Polyaniline as a member of conductive polymer family, was suggested. Based on literature review provided PANI can be a suitable candidate to for FL1-DETA to be modified with, due to its promising properties such as:

1. Thermal stability
2. Web shape morphology
3. Ease and low cost of production
4. Simple doping/undoping chemistry
5. Eco-Friendly

Based on the reviewed literature, the anticipated challenges for modifying FL1-DETA with PANI are:

1. The ratio optimisation of SI and PANI mainly to avoid blockage of both parties functional groups, (Evaluated in the results, Chapter 6).
2. The solubility of final product in water, (Evaluated in the results, Chapter 6).
3. Thermal stability of final product, (Evaluated in the results, Chapter 6).
4. The compatibility of final product with the brine, (Evaluated in the results, Chapter 7).

CHAPTER 3

Materials and Experimental Methodology

Introduction

In this Chapter, the materials used for this research project are introduced. Characterisation techniques and the method of measurements are explained and the experimental set up and test methods are defined. the experimental setups are divided to two section of with and without H_2S gas.

3.1 Materials

3.1.1 FL1-DETA preparation

FL1 and FL1-DETA SI was prepared through the exact scheme which was stated in Patent US 2016033325 A1 [12]. To prepare FL1, 4-styrenesulfonic acid-co-maleic acid (PSSMA), purchased from Sigma Aldrich (CAS: 68037-40-1: $CH_2CH(C_6H4SO_3R)$-$CH(CO_2R)$ $CH(CO_2R)$, R=H or Na), has a molar mass of about 20 kDa. The polymer has a ratio of three styrene sulphonic acid functions for one maleic acid function. Ten grams of PSSMA weighed in a 100 mL bottle. The mass is then adjusted to 100 grams by adding ultra-pure water. The pH of about 7.5, is adjusted to 4.5 by successive adding of 6M hydrochloric acid.The obtained product is labelled as FL1.

In order to prepare an inhibiting solution of FL1-DETA, in a 100mL bottle, 10 g of obtained FL1, is reacted with 2 g of diethylenetriamine with a molar mass of 103.17 g/mole purchased from Sigma Aldrich (CAS: 111-40-0; (NHCHCH-) 2NH). The pH of about 11 is adjusted to 4.5 by adding 6M hydrochloric acid.

3.1.2 Polymerisation methodology

To find the appropriate PSS-*co*-MA—PANI composite with the highest thermal and dispersion stability that will be compatible with CW, different mass ratios of aniline/oxidiser and aniline/FL1b were tested whilst the effect of added HCl (1M) volume and mixing sequence of FL1b was also considered in the experiments. The list of produced composite samples are summarised in Table 3.1.

FL1b i.e. PSS-*co*-MA, with a CAS number of 68037-40-1 and Aniline monomer were purchased from Sigma Aldrich. The oxidiser APS (ammonium persulfate), and HCl (1M) were purchased from Honeywell. PSS-*co*-MA preparation was exactly as it was described in Section 3.1.1, however, on the last step i.e. after setting the pH, 10.96 g of NaCl was added to the polymer mixture to increase the solution conductivity to 82258.0 μS/cm. Increasing the conductivity, helps with the stability and shelf life of PSS-*co*-MA as well as its doping ability with PANI at later stages. As Figure 3.1 shows, without increasing the conductivity, both FL1 and FL1b forms deposit in their own solution and suffer from short shelf life.

Table 3.1: List of PSS-*co*-MA—PANI samples and their composition

Name of the sample	Aniline/APS (wt/wt)	Aniline/FL1 (wt/wt)	Aniline/ HCl(1M) (wt/ml)
AA-1	5.96	0.2	0.03
AA-2	3.61	0.2	0.03
AA-3	2.24	0.2	0.03
AA-4	3.61	0.19	0.03
AA-5	2.24	0.2	0.12
X5-25	1.63	0.2	0.024
X5-20	1.63	0.2	0.03
X5-6.6	1.63	0.2	0.090
X5-5	1.63	0.2	0.12
X5+-25	1.63	0.19	0.024
X5+-20	1.63	0.19	0.03
X5+-5	1.63	0.19	0.12
X/5-20	1.63	5	0.03
X/5-5	1.63	5	0.12
X10-5	1.63	0.1	0.12
X10-6	1.63	0.1	0.099
X10-6.4	1.63	0.1	0.093
X10-6.6	1.63	0.1	0.090
X10-7	1.63	0.1	0.085
X10-8	1.63	0.1	0.074
X10-10	1.63	0.1	0.06
X10-20	1.63	0.1	0.03
X10-25	1.63	0.1	0.024
X20-5	1.63	0.1	0.12
X25-5	1.63	0.1	0.12
X50-5	1.63	0.02	0.12
X100-5	1.63	0.01	0.12
Pure PANI-5	1.63	0	0.12
Pure-PANI-20	1.63	0	0.03
Pure-PANI-25	1.63	0	0.024
PANI→FL1b	1.63	0.2	0.03
P(Aniline+FL1b)	1.63	0.2	0.03

PSS-*co*-MA-PANI composites preparation follows polyaniline oxidation polymerisation with layer by layer assembly of PSS-*co*-MA [136] by which in a 100 mL bottle, 6.4 mmol of aniline was dissolved in a mixture of HCl and DI water and APS. Later, APS was gradually added over 5 minutes to the stirring solution. In the next step, certain mass of PSS-*co*-MA was weighed and added to the blend followed by the addition of 20 mL of DI water. In all syntheses the total volume of HCl+ H_2O was set to 40-45

ml. The mixture was stirred overnight at room temperature and moderate speed. The final product was centrifuged and rinsed with DI water 6 times and the non-reacted materials were removed. The pH of the final product was adjusted with extra HCl (1M) to 4.5-4.6. To identify the appropriate PSS-*co*-MA—PANI composite with the highest thermal and dispersion stability, different mass ratios of Aniline/ PSS-*co*-MA and Aniline/ HCl were tested.

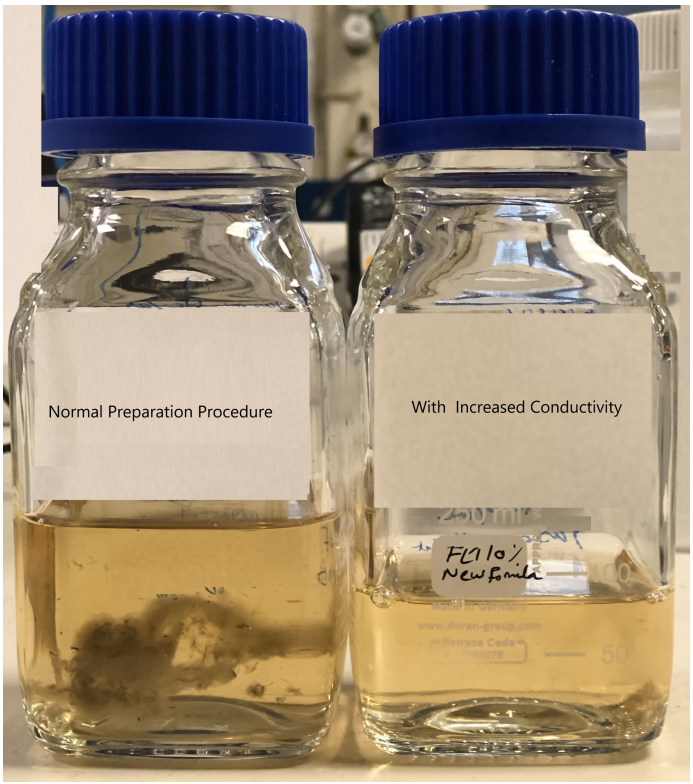

Figure 3.1: Normal preparation procedure Vs. increased conductivity. The increased conductivity helps with the shelf life of PSS-*co*-MA

3.1.3 Sandstone sample preparation

Silica sand is considered a moderately adsorbent rock type for inhibitor adsorption [1]. Thus, silica sand as representative of sandstone rock composed of quartz (SiO_2) was chosen as an adsorbent for static jar experiments and sand pack dynamic test. However, in this PhD project silica and kaolinite particles were mixed in the laboratory to mimic a more realistic representation of sandstone rock. Kaolinite used for this purpose is a clay mineral of hydrous aluminium silicates that has an average diameter of 10 to 30 μm. Both silica and Kaolinite were purchased from Sigma Aldrich.

3.1.4 Full brine compositions

The full brine composition of the Elgin field is listed in Table 3.2. As it can be seen, the TDS is above (> 250g/L) which is in the range of high salinity brine, furthermore high levels of [Ca^{2+}]∼ 20g/L and high [Fe^{2+}] (450 mg/L) is reported in the water composition. From details provided of the field the temperature of reservoir is high above 190°C up to 215 °C. Reservoir information was listed earlier in Table 2.4 as it was mentioned the formation rock lithology is sandstone.

Table 3.2: Production water composition

Ion	Concentration (mg/L, ppm)
Na^+	83,691
K^+	9,986
Mg^{2+}	981
Ca^{2+}	17,691
Ba^{2+}	2,454
Sr^{2+}	2,128
Fe^{2+}	421
Cl^-	174,647
SO_4^{2-}	24
HCO_3^-	222
Zn^{2+}	≈100-200
Pb^{2+}	≈1-10
TDS[1]	292,345
$mNaCl_{eq}$	5.00222
H_2S [2]	≈ 34

As the production brine composition (Table 3.2), has a high tendency to scale, especially at room temperature, the brine is divided into two separate streams of AW[3] and CW[4]. The scaling tendency of the brine will be investigated and explained in Chapter 4, Section 4.2.1.

Table 3.3 shows these two streams and the amount of salt that is needed to prepare them. Separating the two streams will help with scaling control and storage of the brine, furthermore, it will provide grounds for precise investigations on the impact and behaviour of SI in brine for later experiments. It should be noted that although FeS would be one of the forming scales based on the prediction of Multiscale software calculations, however, for the sets of experiments in this thesis, $FeCl_2$ was eliminated from the CW composition due to facilities limitation in the laboratory. Mainly as

[1] Total dissolved solve
[2] it was measured at separator
[3] Anion water
[4] Cation water

$FeCl_2$, alters the brine colour in the presence of H_2S as well as atmospheric condition due to the presence of O_2 and that special glovebox is required to this purpose.

Table 3.3: AW and CW composition

Salts	Amount of salt g/L	Type of stream
KCl	19.04	CW
$MgCl_2.6H_2O$	8.203	CW
$CaCl_2.2H_2O$	8.2032	CW
$SrCl_2.6H_2O$	64.88	CW
$BaCl_2.2H_2O$	6.476	CW
$FeCl_2$	4.365	CW
Na_2SO_4	0.0355	AW
$NaHCO_3$	0.3056	AW
$PbCl_2$	0.00134	CW
$ZnCl_2$	0.2084	CW
NaCl	212.50	AW

3.1.5 Simplified brine

To evaluate the SI effectiveness in the presence of dissolved H_2S gas and sulphide scale particularly, the simplified brine composition listed in Table 3.4 was used. The simplified brine is designed to only have S^{2-} as scaling anion and avoid other scaling interference.

Table 3.4: Simplified brine composition

Ion	Brine 1 (mg/L)	Brine 2 (mg/L)	Stream
Na^+	29,505	29,505	AW*
Mg^{2+}	255	255	CW*
Ca^{2+}	3,611	3,611	CW*
Zn^{2+}	100	0	CW*
Pb^{2+}	0	25	CW*
Cl^-	100	100	AW*
H_2S_{eq}	5	5	AW*
TDS	90,587	90,512	AW*, CW*

3.1.6 Seawater brine composition (SW)

Seawater brine composition is listed in Table 3.5 was used in the Post flush stage of sand pack tests. The sand pack test will be explained in Section 3.3.2 of this Chapter.

Table 3.5: North seawater composition (SW)

Ion	Concentration (mg/L, ppm)
Na^+	10,890
K^+	460
Mg^{2+}	1368
Ca^{2+}	428
Ba^{2+}	0
Sr^{2+}	0
SO_4^{2-}	2960
Cl^-	19,773

3.2 Analytical techniques

3.2.1 X-ray diffraction (XRD)

X-ray diffraction (XRD) identifies a crystalline nature structures. To this end, oven dried powder samples were analysed by XRD instrument model D8, manufactured by Bruker with an incident beam parabolic mirror (CoKα), a 25mm sample diameter, and a VANTEC-1TM linear detector.

In XRD analysis, the X-rays which as generated by the cathode tube, filters through a monochromator. After collimating, incident rays interacts with the surface of a crystalline sample and produces constructive interference (and a diffracted ray) by satisfying Bragg's Law (Eq.3.1) [145].

$$\lambda = 2dsin\theta \tag{3.1}$$

The law relates the wavelength of electromagnetic radiation to the diffraction angle and the lattice spacing in a crystalline sample with "d" as the distance between atomic layers in a crystal, and λ as the wavelength of the incident X-ray beam, 1.504 Å [146].

XRD helps us to measure the average spacing between layers or rows of atoms. It also determines the orientation of a single crystal or grain and identifies the crystal structure of an unknown material by measuring the size, shape and internal stress of small crystalline regions. In general, the characteristic X-ray diffraction pattern generated in a typical XRD analysis provides a unique "fingerprint" of the crystals present in the sample. When properly interpreted, by comparison with standard reference patterns and measurements, this fingerprint allows identification of the crystalline form [147].

3.2.2 Scanning electron microscopy (SEM/EDX)

Scanning electron microscopy (SEM) is useful for detailed study of a specimen's surface. SEM (Scanning electron microscopy) micrographs and EDX (Energy-dispersive X-ray spectroscopy) elemental mapping in chapter 5 were conveyed by Carl Zeiss EVO MA15. The machine has variable pressure W SEM with Oxford Instruments, AZtecEnergy EDX software and system with 80 mm X-Max SDD detector. This machine has the ability of both secondary and back scattered imaging and line scanning. However, the same analysis in Chapter 4 ,basic characterisation, were conducted with Hitachi TM3030Plus SEM device that own an auto stage.

In this technique a high-energy electron beam scans across the surface of a specimen. As the beam scans across the sample's surface, interactions between the sample and the electron beam result in different types of electron signals emitted at or near the specimen surface. These electronic signals are collected, processed, and eventually translated as pixels on a monitor to form an image of the specimen's surface topography that appears three dimensional [148]. Low-energy secondary electrons (SE) excited on the sample's surface are the most common signal detected that builds the topography image of the surface. High-energy back-scattered electrons and X-rays are emitted from below of the specimen surface and provides information on specimen composition. Since back-scattering increases with the atomic number increase, there will be more back-scattering for heavier atoms. The dependence of the number of BSE on the atomic number helps to distinguish between different phases, providing imaging that conveys information on the sample's composition [149].

Sample preparation, includes an early stage of sputtering a thin layer of carbon coating. This improves the image quality and eliminates the charging effect on non conductive samples. Other methods can be sputtering the sample surface with gold/silver or using back-scattering filter in a low voltage, depending on the nature and sensitivity of the sample itself. Imaging was done with SE beam of 15 and 20 kV and BSE of 5 kV with the working distance (WD) of 9 mm and different magnification as labelled on the images convened.

3.2.3 Zeta potential

Zeta potential measurements were carried by Malvern Zetasizer ZS instrument. Zeta potential of FL1 and FL1-DETA is measured at 25°C and pH 4.5 with 2 ml of the sample. For Zeta potential measurement of the sand particles ZetProbe device using 30 g of sand was utilised. The measurement was carried at room temperature and pH 5.5.

Electrokinetic phenomena and electroacoustic phenomena are the usual sources of data for calculation of zeta potential.

Electrokinetic phenomena: Subdivides into two separate methods of measurement relative to sample nature that are electrophoresis and streaming potential/current. In both methods, the zeta potential of dispersion is measured by applying an electric field across the dispersion. As particles within the dispersion will migrate toward the electrode of opposite charge, the migration velocity can be measured by observing the Laser Doppler shift in the scattered light that is proportional to the magnitude of the zeta potential at the shear plane [150].

Electroacoustic phenomena: Subdivides into colloid vibration current and electric sonic amplitude method. The former arises when ultrasound propagates through a fluid that contains ions, solid particles or emulsion droplets. The pressure gradient in an ultrasonic wave moves particles relative to the fluid, disturbing the double layer that exists at the particle-fluid interface. As every particle in the fluid carries a surface charge, the drag caused by the fluid motion will generate dipole moments leading to an electric field that can be measurable as an electric current. However, the latter operates exactly in reverse to the mentioned method occurring under the influence of an oscillating electric field, moving particles relative to the liquid that generates ultrasound [151].

3.2.4 Brunauer-Emmett-Teller (BET) surface area analysis

BET technique is used to measure the average volume of the pores and active surface area of porous particles by using nitrogen absorption [152]. Results gathered by using Micromeritics Tristar 3000 instrument. For the sample preparation, 6.13 g of sand sample was dried and degassed under nitrogen at 170°C overnight to make sure that no water molecules or moist is adsorbed or attached on to the sample surface as it can interfere the results. The test was repeated for 4 times.

In BET surface area analysis, nitrogen is usually used because of its availability in high purity and its strong interaction with most solids. Because the interaction between gaseous and solid phases is usually weak, the surface is cooled using liquid N_2 to obtain detectable amounts of adsorption. Known amounts of nitrogen gas are then released step wised into the sample cell [152]. Relative pressures less than atmospheric pressure are achieved by creating conditions of partial vacuum. After the saturation pressure, no more adsorption occurs regardless of any further increase in pressure, Figure 3.2. Highly precise and accurate pressure transducers monitor the pressure changes due to the adsorption process. After the adsorption layers are formed, the sample is removed from the nitrogen atmosphere and heated to cause the adsorbed nitrogen to be released from the material and quantified. The data collected is displayed in the form of a BET isotherm, which plots the amount of gas adsorbed as a function of the relative pressure. More detailed explanation on BET isotherms is presented in the Appendix B.

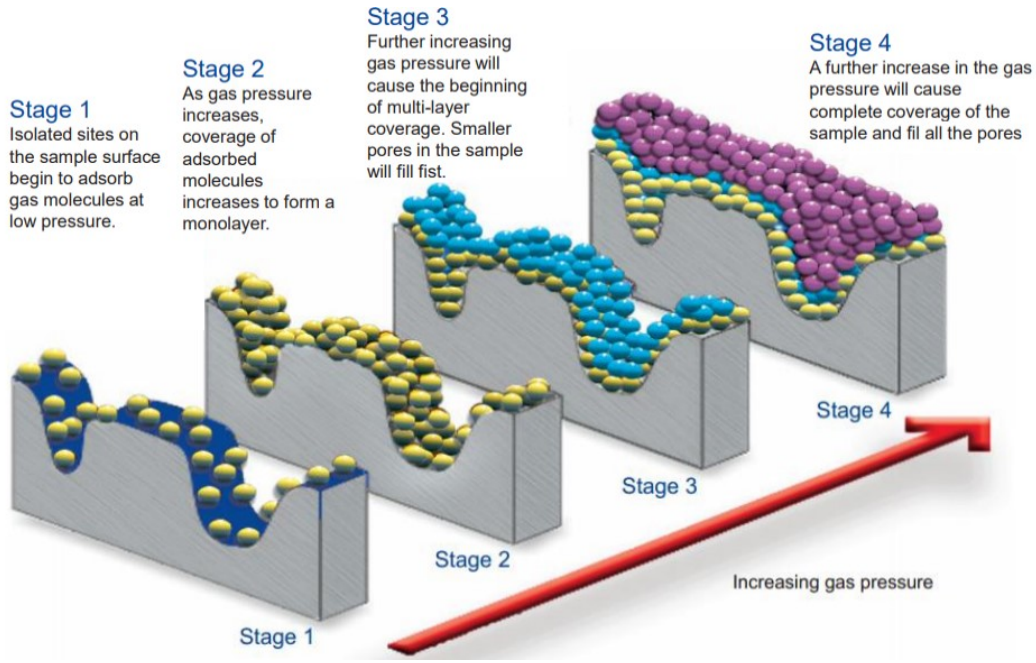

Figure 3.2: Schematic of BET technique [127]

3.2.5 Attenuated total reflectance Fourier Transform Infrared (ATR-FTIR)

Available functional groups of a chemical compound structure can be identified, using Fourier Transform Infrared (FTIR) spectra. The spectra forms from detected reflection of resonated bonds under IR radiation [153]. In the sample preparation stage, pallet was formed by pressing the 0.2 g of dried powder under 3 Tones weight for 3 minutes. However, as the out come pallet was too adsorbent and the Mid-IR range was sufficient, ATR accessory was used to continue with the analysis.

Attenuated total reflectance (ATR) is special accessory units which can be used with FTIR spectrometers. This is a sampling technique used in conjunction with infrared spectroscopy which enables samples to be examined directly in the solid or liquid state without further preparation [153]. The ATR-FTIR spectrometer used in this project is manufactured by Thermofisher with Model of Nicolet iS10.

3.2.6 Thermogravimetric analysis (TGA)

Thermogravimetric analysis or thermal gravimetric analysis (TGA) is a method of thermal analysis in which the mass loss of a sample is measured over time as the temperature increases. The analysis were run with Toledo TGA/DSC 3 manufactured

by Mettler. To this end 10 g of each sample was weighed and heated with the ramp of 10°/minute in a temperature range of 25°-700°C.

3.2.7 UV-Vis spectrophotometry

Ultraviolet–visible spectroscopy or spectrophotometry (UV–Vis), refers to absorption spectroscopy or reflectance spectroscopy in part of the ultraviolet and the full, adjacent visible spectral regions. This means it uses light in the visible and adjacent ranges. Light absorption is the responsible element of producing colour in different materials and can be used as a method of material identification [154]. Experiments were run in the range of 150 nm-700 nm by Perkin Elmer UV-Vis spectrophotometer model lambda 950 and the data was collected with Perkin Elmer uvwinlab software. Samples were poured in 10 mm width clear quartz cell manufactured by Perkin with a slit width of 2 nm.

3.2.8 Sand particle size measurement

Sand particles size were measured by Malvern Panalytical Mastersizer 3000 with Aero S air dispersion unit fitted with a standard Venturi dispenser and general purpose tray, as well as attached PC running Mastersizer software v3.81 for instrument control and data analysis. The dispersion unit was run using compressed air at 1 bar and a feed rate of 50 %, with a 1 mm hopper gap. A background measurement was made for 10 s, followed by sample measurement for up to 60 s to ensure all sample had passed though the measurement cell. The data was analysed using the general purpose model, with a refractive index of 1.457 and absorption coefficient of 0.1.

3.2.9 Turbidity test

Turbidity is used as a water quality indicator. A turbidity meter measures the loss in light beam intensity as it passes through of a fluid with suspending particles [155]. Ideally, for a water sample, the suspending particles allows the incident light to scatter at an angle of 90 degrees with respect to the light source, however, according to the particle size, the angle of light differs [155]. A smaller angle of scatter indicates larger particles and hence a highly turbid water sample. In this study,calorimeter model HACH/DR 890 is used to measure the turbidity of the mixture of the two streams [1]of the brine.

[1] AW and CW will be explained in the next chapter.

3.3 Experimental setups and test methodologies without H_2S

3.3.1 Static jar test

For an effective scale inhibitor, the chemical needs to be stable to thermal degradation under the wells downhole condition and also be compatible in the particular brine system. Brine compatibility is a major issue of concern since premature precipitation of inhibitor complexes during injection may lead to the formation of pseudo-scale with associated fines plugging. The scale inhibitor should be fully compatible with both brines i.e without any precipitate formation. In case of formation water containing high concentrations of Ca^{2+}, the scale inhibitor is considered compatible with the formation water if turbidity is not observed within 24 hours which in this case concentration of Ca^{2+}in the formation water is the main factor on the inhibitor efficiency [156].

3.3.1.1 Coupled adsorption/precipitation (Sand static test)

In static inhibitor adsorption tests, under a known set of test conditions, the equilibrium is established between the scale inhibitor solution and crushed reservoir core from the formation into which the chemical is to be squeezed. Solutions of FL1-DETA and modified scale inhibitor X10-6 were prepared by diluting down the pure SI with the brine into six different concentrations of 1000 ppm, 500 ppm, 200 ppm, 100 ppm, 30 ppm and 5 ppm. Solutions were poured in separate beakers and the initial pH was measured for each sample. The beakers were covered and left still overnight at room temperature, 23°C. After 24 hours, samples were filtered with 0.4 micron syringe filters and analysed with UV-vis technique or compared with a fresh sample after the pH was recorded [86]. For the static adsorption tests, the experiments were performed using different masses of sand (m = 10 g, 20 g and 30 g) at a fixed volume (V= 0.08 L) of SI solution to evaluate the apparent adsorption or coupled adsorption/precipitation behaviour. Sampling was done with a syringe and after 24 hours from top 10 ml of each beaker without disturbing the solution.

For the static desorption tests, the top solution (supernatant) of each beaker was emptied and replaced with a fresh 80 ml of CW brine. In this way the formed precipitation in each beaker should stay intact and remained in the container. As the added fresh CW is free of inhibitor, the SI will be under-saturated in the system and the desorption from the adsorbate should take place. The aim of this experiment is to evaluate the amount of desorption from the already adsorbed/precipitated scale inhibitor of the previous experiments i.e. adsorption/precipitation.

3.3.1.2 Compatibility test (Bulk static test)

In the corresponding static compatibility tests, the experiments were performed under the same setup, yet with no minerals present. Compatibility test, evaluates the

pure precipitation behaviour, since no mineral is used. The combination of static compatibility tests and static coupled adsorption/precipitation test results, specially using different masses of sand helps to differentiate between pure adsorption (Γ) and coupled adsorption/precipitation and identify the behaviour of the scale inhibitor [86].

3.3.2 Dynamic Sandpack test

The sand pack is designed to carry low pressure flooding experiments. The main components are a sand column, a pump to flush the brine through the porous media and a sample collector. Figure 3.3 shows the schematic of this experimental setup [1]. The sand column is made of polycarbonate that enables a clear view of the packing and has an inner diameter of 20 mm, outer diameter of 24 mm and a packing length of 10 cm. An unconsolidated packing method is selected because it allows a straight forward way to squeeze the sand uniformly across the sand pack. The fluids injected are flushed through the porous pack using a peristaltic pump (Ismatec ISM596), and the fluids that exit are collected in a fraction collector that rotates by regular time intervals. To create a return curve, the concentration of the SI at the outlet is analysed by UV-vis spectrophotometer[157].

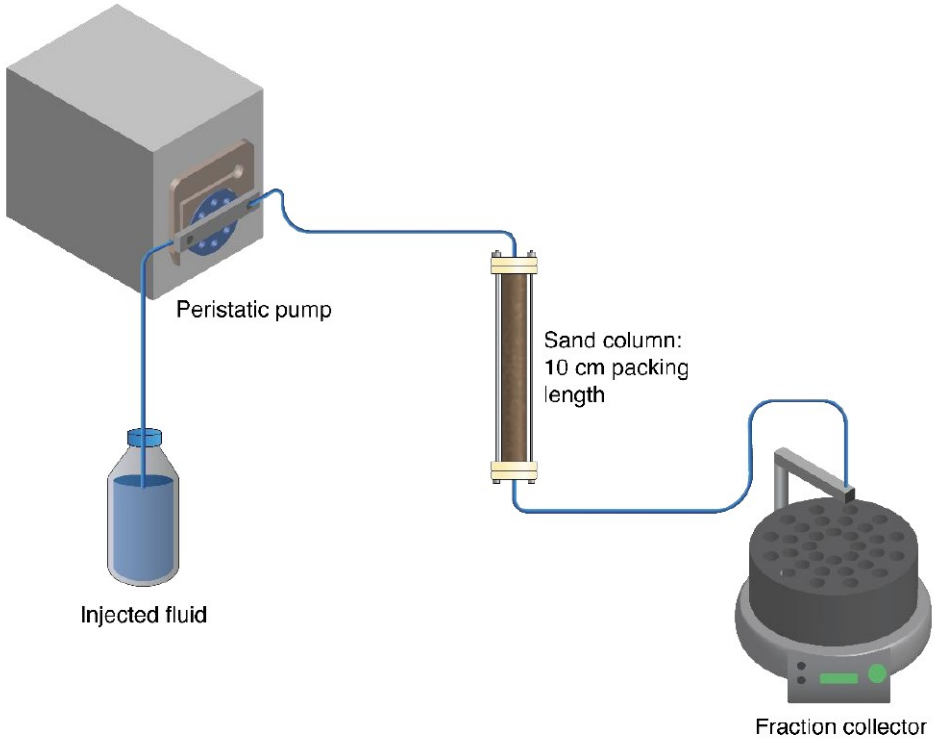

Figure 3.3: Schematic of sandpack setup [1].

3.3.2.1 Column packing

Columns were packed and prepared using dry pack method introduced by Bahun-Wilson [1]. Compared to wet packing defined by FAST group [86], dry packing is easier, quicker and repeatable, resulting in same properties such as porosity and permeability.

To this end, a qualitative filter paper with pore size of ≈8-15 μm is placed on top and the bottom end cap, so that the sand only remains in the sand pack. The certain grams of sand is poured in the sand pack column through a funnel and the top cap is then screwed in. The packing settles using the vibration technique with an electric engraver (Burgess model 74) as shown in Figure 3.4. The vibration helps the sand pack to to be tightened and the small grains fit in the gaps of the bigger ones. The top cap will be tightened on each round of vibration until no sand particle movements can be visually observed. Figure 3.5 shows the actual sandpack used in this research.

Figure 3.4: Modified engraver to tight pack the sand column

Figure 3.5: A packed column

3.3.2.2 Experimental procedure

Pore volume and porosity measurement [86]

1. The sandpack will be weighed when is dry.
2. DI water should be pumped for 3-5 hours with 20 ml/hour flow rate until the pack is completely wet.
3. The wetted sandpack will be weighed
4. The Pore volume (PV) can be calulated through equation Eq.3.2

$$Pore\ volume = \frac{mass\ _{wet\ sand} - mass\ _{dry\ sand}}{\rho\ of\ the\ liquid} \tag{3.2}$$

5. The porosity can be calculated through equation Eq.3.3

$$\begin{aligned} Porosity &= \frac{Pore\ volume}{Bulk\ volume} \\ Bulk\ volume &= \frac{\pi D^2}{4} \times L \end{aligned} \tag{3.3}$$

Main treatment (MT) and post flush (PF)[157]

1. Preconditioning: The preconditioning is done at room temperature with 1 % NaCl solution. Flush with brine (no tracer / pH= experimental pH) at 150 ml/hr for an hour and continue at 20 ml/hr for 5 hours to precondition the sand pack column. The sand pack column is now ready for main treatment.
2. Main treatment (MT): The main treatment consist of two main stages :
   (a) Lithium tracer that is 20-50 ppm of standard lithium solution for AAS and ICP application which is blended with SW[1]
   (b) The treatment which is usually 3000-5000 ppm active inhibitor diluted in SW .

   Both stages are run at room temperature with 20 ml/hr flow rate for up to 20 PV. Samples are analysed with AAS for the lithium and UV-vis for the inhibitor concentration.
3. For the Shut-in stage of the sand pack column, the flow will be stopped after ≈20 pore volumes (20 PV) by closing valves. Shut in times may vary between 8-24 hours.

[1] seawater

4. Post-flush treatment (PF): The post-flush treatment is performed at the same flow rate as the main treatment, i.e. 20 ml/hour with SW until the effluent concentration drops below the minimum inhibitor concentration (MIC).

5. Sample Collection:

   (a) A fine sampling regime is recommended in the early stages of both MT and PF (approximately $\frac{1}{10}$ to $\frac{1}{5}$ of a pore volume per sample). This may be increased to $\frac{1}{2}$ to 1 pore volume after the first 5 pore volumes of flow. Samples should be collected as for both stages of the main treatment

   (b) Samples are then analysed for concentration of the major ions of interest (in this case Lithium) and the inhibitor. Different dilutions may be required for different stages. Analysis and monitoring of samples, especially from the post flush, in small batches covering 5-10 pore volumes each time is recommended to keep track of changes and update analysis regimes.

A sandpack test, is a simplified coreflood with no confinement pressure. This test helps to evaluate inhibitor's retention on sand particles. The test was run at room temperature and procedure is defined explicitly in Chapter 4. Using dry packing method in a polycarbonate based column the setup shown in Figure 3.6 was put together. The idea behind sandpack is to feed the column with a tracer as a none reacting chemical and the reacting inhibitor, separately and compare the difference in their return profile. This will evaluate the gradual release of the inhibitor overtime after period of shutdown until it reaches the MIC or MED value. Table 3.6 shows the experimental detail of the sandpack test carried out for both X10-5 and FL1-DETA. Column IDs of 4 repeats are also listed in Table 3.7 showing repeatable packing properties with mean PV= 5.3 ml and porosity of 34.30%.

Table 3.6: Non-Equilibrium sandPack experiments on X10-5 and FL1-DETA Scale Inhibitor applied in both adsorption and precipitation treatments

Number	Description	Flow rate (ml/hour)	PV (ml)
0	1% NaCl (preconditioning)	150	10
1	Lithium tracer 50 ppm (MT_1)	20	20
2	Inhibitor 3000 ppm (MT_2)	20	20
3	Shutdown 18 hours	0	0
4	SW (PF_1)	20	30
5	1% NaCl (PF_2)	20	10
6	Shutdown 8 hours	0	0
7	CW (PF_3)	20	105

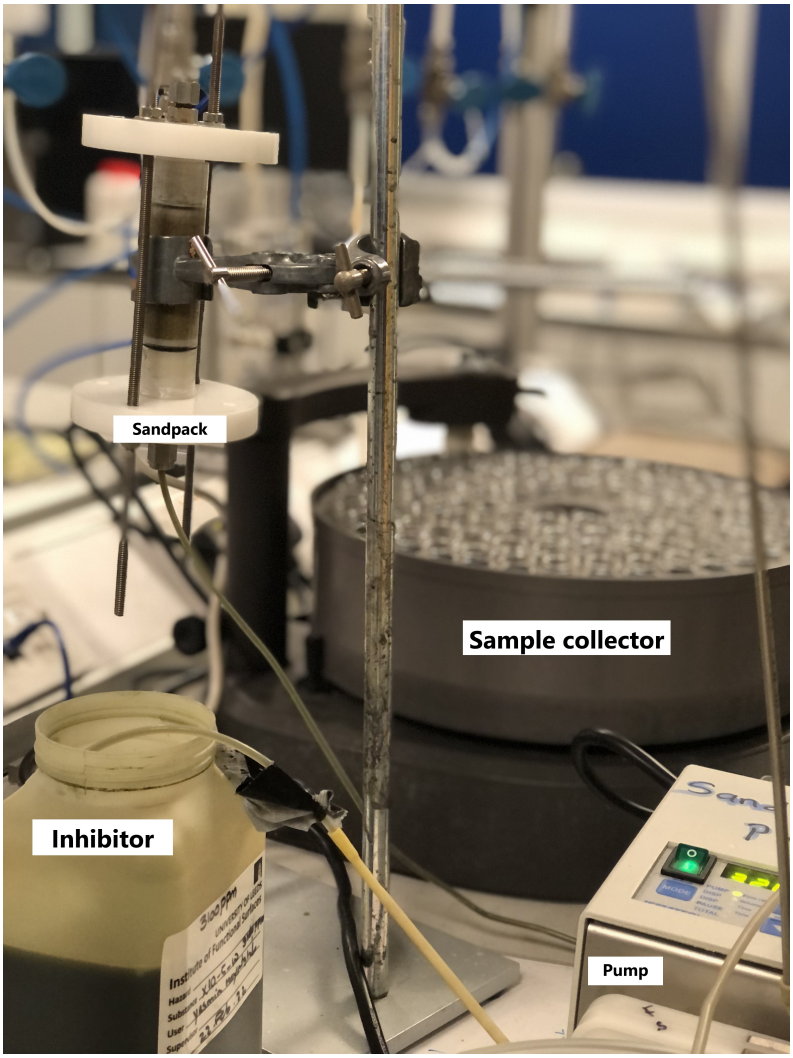

Figure 3.6: Sandpack setup

To precondition the sandpack for the main treatment, 10 PV of 1% NaCl brine was used at flow rate of Q = 150 ml/hour. The test was run for 3000 mg/L (active) FL1-DETA and X10-5 in the absence of H_2S gas to compare their retention behaviour in dynamic condition at room temperature with the flow rate of 20 ml/hour for both MT and PF. To replicate the squeeze treatment procedure as it is practised in the field, the first 35 PV of the initial PF stage was carried using SW. As a result, for the PF the synthetic SW with the composition listed in Table 3.5 was used. Studies [32] have shown the post flush with SW lasts 2.5 times less compared to the PF run by FW. This is mainly due to the absence of the complexing metal cations such as Ca^{2+} which helps with the precipitation absorption. After then, the brine was switched to CW to mimic the FW present in the field. However, to switch between the brines and avoid

the scaling reactions interfering the results, 10 PV of 1% NaCl followed by 8 hours of shutdown was used in between. The brine switch procedure was continuous after that and no shutdown periods were given in between 1% NaCl and CW.

Table 3.7: Sandpack column ID

25.02.22	Fine sand
PV (ml)	5.72
Length (cm)	5.8
Porosity	35.75%
DV+PV on 100 ml/hour	
Empty pack (g)	231.08
Dry sand pack (g)	25.02
wet sand pack (g)	263.74

03.03.22	Fine sand
PV (ml)	5.49
Length (cm)	5.1
Porosity	34.28%
DV+PV on 100 ml/hour	4 mins and 23 second
Empty pack (g)	230.72
Dry sand pack (g)	258.76
wet sand pack (g)	264.25

29.03.22	Fine sand
PV (ml)	5.54
Length (cm)	5.08
Porosity	34.73%
DV+PV on 100 ml/hour	4 mins and 23 second
Empty pack (g)	230.51
Dry sand pack (g)	257.68
wet sand pack (g)	263.22

30.03.22	Fine sand
PV (ml)	5.6
Length (cm)	5.5
Porosity	32.43%
DV+PV on 100 ml/hour	4 mins and 23 second
	51.52
Empty pack (g)	298.4
Dry sand pack (g)	328.4
wet sand pack (g)	334

3.4 Experimental setup and methodology in the presence of H_2S

For producing H_2S gas, pre-weighed amounts of $Na_2S.9H_2O$ were dissolved in AW stream just before the mixing. The CW stream was acidified by addition of HCl (1M) to the extent by which pH of 5.5 could be achieved as a consequence of mixing both streams together.

3.4.1 Static jar test

HTHP static test were conducted in the presence of excess H_2S gas (100 ppm) at 90°C in Huguette airtight tubes with a resealable stopper and aluminium crimp seals in the presence/absence of 10g sand. Separate AW and CW streams were heated in a water

bath for at least 2 hours and degassed with N_2. For controlled inhibitors contact time with all elements in the brine composition, 10 mg/L (active) of PANI-Co-Polymer was stored in a separate de-aerated tube. A mixing procedure was performed by injecting equal amounts of de-aerated and pre-heated solutions of CW followed by AW to the inhibitor containing tube with an airtight Luer-lock syringe via a resealable stopper. The total solution volume in each tube was set to minimise the head space for better H_2S dissolution in the brine. Figure 3.7 shows a schematic of this experimental setup.

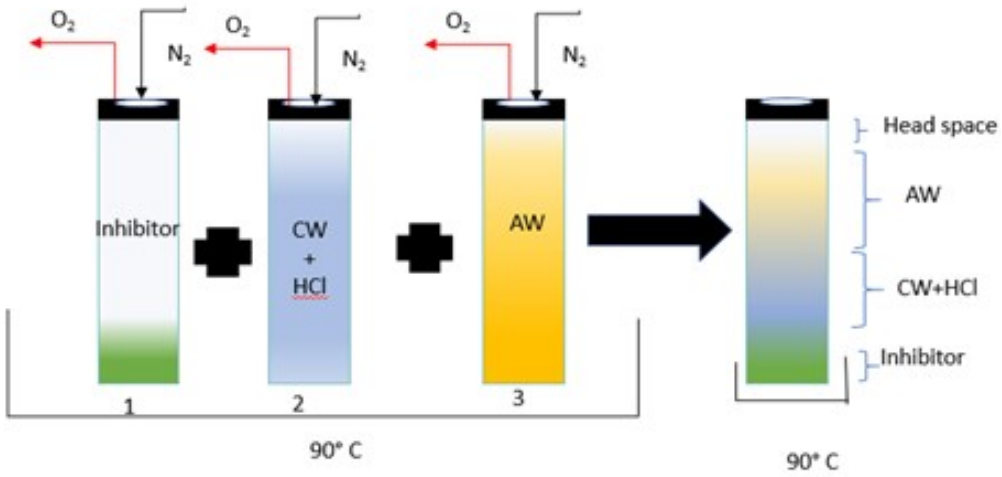

Figure 3.7: Schematic of Huguette airtight tube and the order of mixing procedure

3.4.2 Dynamic tube blocking test

Minimum effective dose (MED) is usually identified under dynamic conditions through tube blocking test. Even though static jar test can give useful information regarding the MIC, dynamic tube blocking test can provide more realistic MED results based on the dynamic nature of the production line and the field. The experiments were carried out with each brine composition listed in Table 3.4 for ZnS and PbS scale, separately. All TB tests were run at 635 psi and 125°C with brine 1 for ZnS to achieve saturation index of 5.24 and with brine 2 for PbS to achieve saturation index of 4.72. The CW* and AW* streams were co-injected through a 1,000 mm 1/16" outer diameter microborer coil, then through a 7-micron porous filter at a combined flow rate of 10 ml/ min. The scale inhibitor products were then added to the brine and differential pressure (dP) was monitored over a 1 hour time period to be compared with the blank conditions where no inhibitor was administered. The schematic of the rig is shown in Figure 3.8.

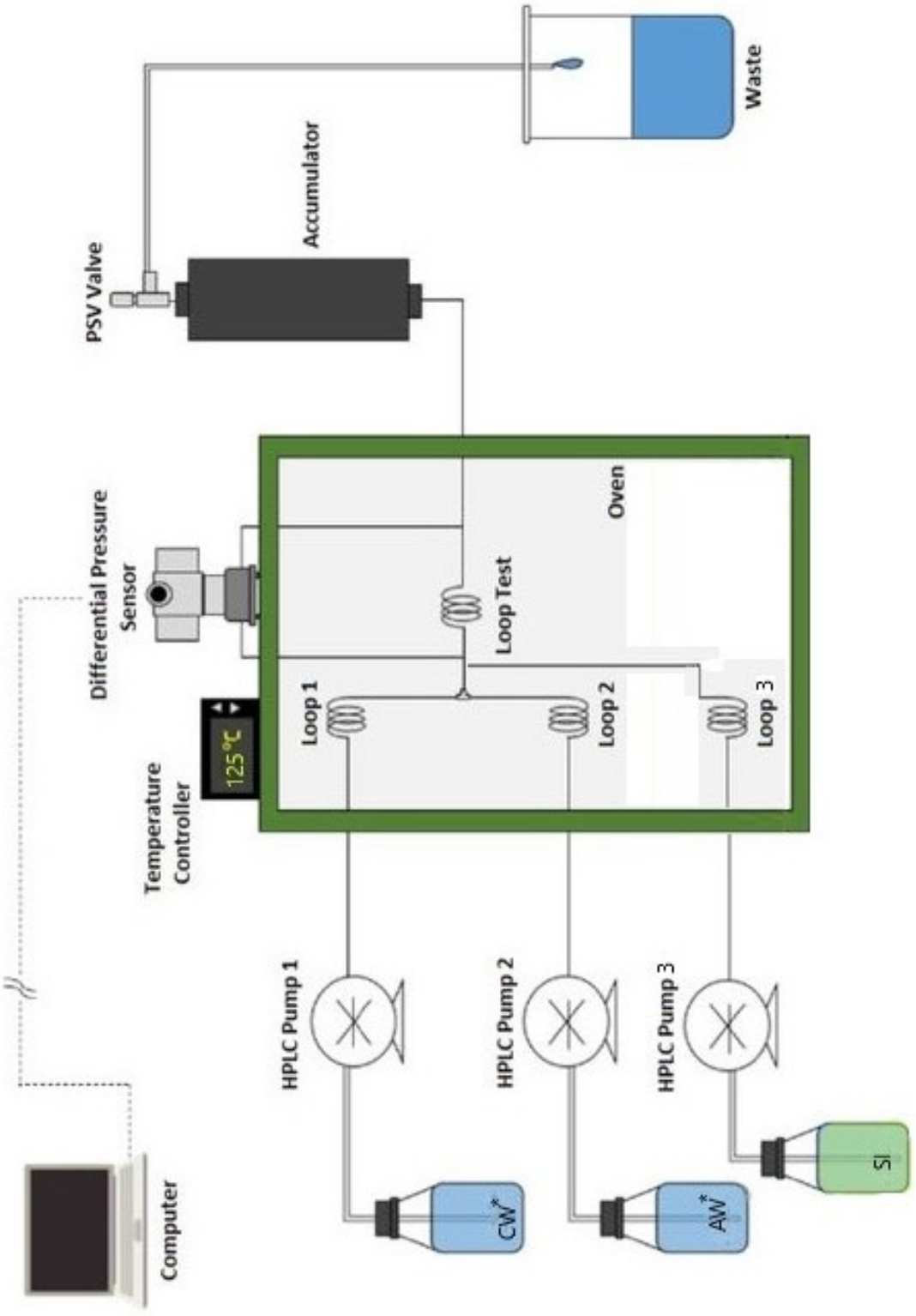

Figure 3.8: Scheme of the Dynamic tube blocking test [158].

CHAPTER 4

Basic characterisations

Introduction

FL1-DETA as a newly patented SI that is intended to cease or retard the formation of the ZnS and PbS scale has poor thermal and retention properties. Based on the aims and objectives provided in Chapter 1, the first stage of this thesis will focus to overcome the lack of information available on FL1 and FL1-DETA chemical structure and to characterise each participating fracture individually. This includes characterisation of both compounds and analysing their thermal stability, the characterisation on sandstone such as morphology, amount of nitrogen absorption (porosity) and analysing the composition. For basic understanding of the newly patented FL1-DETA scale inhibitor properties, all the experiments in this Chapter are conducted with 0 ppm H_2S, at room temperature and atmospheric pressure and not at elevated conditions, unless stated.

4.1 FL1-DETA basic characterisation

4.1.1 Functional groups: FTIR

To the identify the functional groups available on both FL1-and FL1-DETA, FTIR techniques explained in section 3.2.5 was used. As the functional groups of both FL1 and FL1-DETA were expected to be seen in the Mid-IR range, the analysis was carried out with the ATR accessory. These results are shown in Table 4.1 and Figure 4.1. The functional groups from the graphs for both FL1 and FL1-DETA, completely match the schematic of their structure provided in Figure 1.3. As expected, by doping FL1 with DETA, less -OH groups are available on the SI structure and -NH groups appear.

Table 4.1: ATR-FTIR results of FL1-DETA. FL1 and FL1 DETA functional groups

Material	$Wavenumber_1$ (nm)	$Wavenumber_2$ (nm)	Structure	Assignment
FL1	1300	1000	RCO-OH	
FL1	1100	1090	R_2CHOH	C-O Stretch
FL1	1160	1120	S=O	Second
FL1	1450	1350	S=O	
FL1	1561	1570	Alekens	C=C stretch
FL1	1700	1695	ARCHO	C=O stretch
FL1	3500	3200	AR-OH	
FL1	3400	2800	RCOOH	dimer
FL1-DETA	2873	2696	RHCO	Stretch
FL1-DETA	1705	1695	RCOHNHR	
FL1-DETA	1569	1640	RNH_2	NH_2 in plane bed
FL1-DETA	1450	1350		
FL1-DETA	1230	1030	R_2NH	C-N stretch
FL1-DETA	1230	1030	RNH_2	C-N stretch

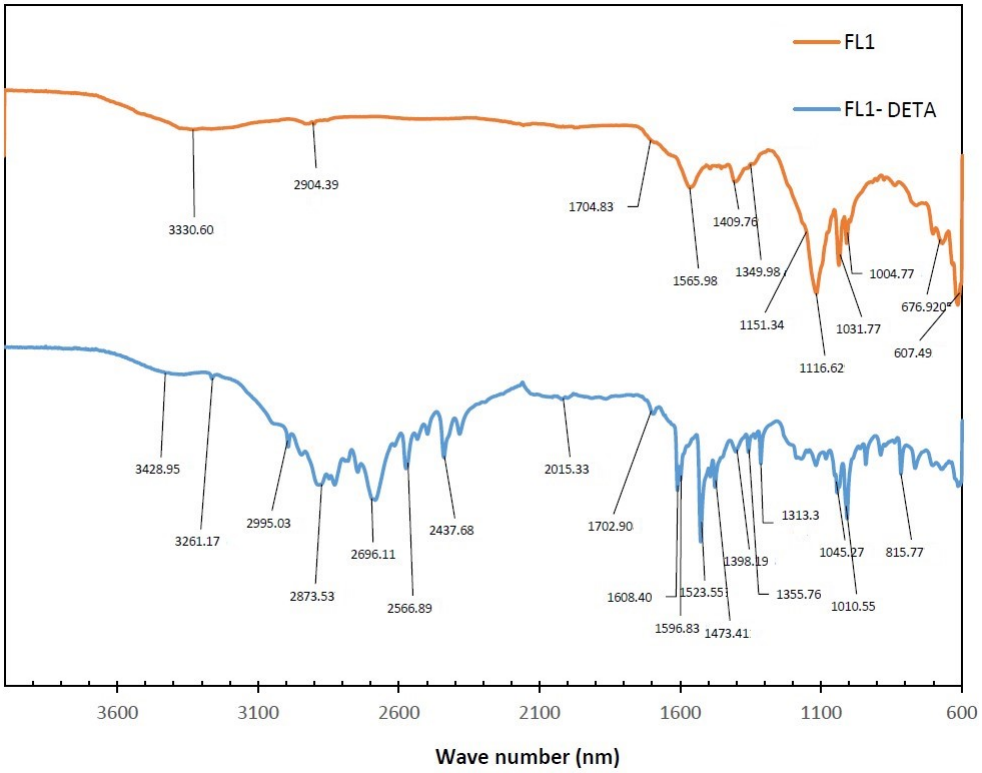

Figure 4.1: ATR-FTIR analysis. Results for FL1 and FL1-DETA.

4.1.2 Thermal stability: TGA

Using TGA techniques explained in section 3.2.6, the thermal stability of FL1 and FL1-DETA were investigated. As depicted in Figure 4.2, temperature ramp is in blue line whilst the orange lines represents the mass loss of the sample and the green line shows the derivative of the mass loss with respect to time. Based on the conducted TGA, FL1 is thermally stable until 250°C and the decomposition starts with a 4% mass loss at 250°C, probably by losing its carbonic acid functional groups. This continues to a major loss of 25% at 455 °C that is attributed to decomposition of the organic polymeric structure[159], finishing with total mass loss of 40% at 700°C.

In contrast, the TGA curve for FL1-DETA shows a delayed major mass loss at 340°C attributed to all the nitro (N-O) bonding that DETA have had formed in the structure of FL1-DETA [160]. The second mass loss at 434°C corresponded to main polymeric backbone. Although doping DETA on FL1 decreases the thermal stability of the whole material to a total mass loss of 90% at 700°C, however, it improves the thermal stability before 310°C, where the decomposition starts. For both materials the first mass loss at temperatures before 210°C is due to the loss of adsorbed water and hydrophilic sulfonyl groups [161]. As FL1-DETA is thermally stable until 300°C and

is on the threshold, improving the thermal stability of the compound is desirable for future plans.

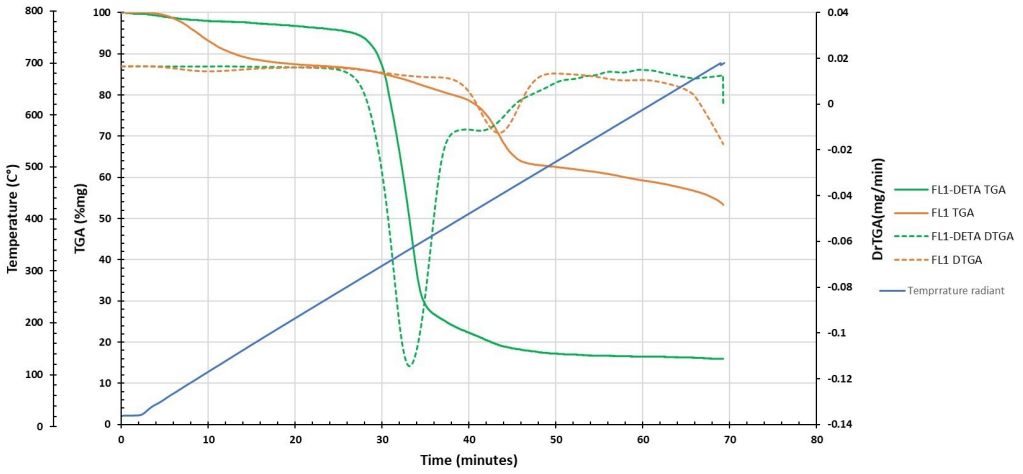

Figure 4.2: TGA results of FL1 and FL1-DETA scale inhibitor. The composition degrades at temperatures higher than 250°C.

4.1.3 Charge measurement: Zeta potential

Each sample measurements are repeated for three times. The average result showed that FL1 has negative zeta potential value of ξ=-15.03 ± 0.08 mV at its application pH, whilst by doping with DETA, the zeta potential increase to less negative values equal to ξ= -0.2 ± 0.05 mV. This can be mainly caused by the positive charge that ammonium-based functional groups carry at pH below 7 and their strong alkaline nature.

Based on the zeta potential measurements of the SI in the same pH region presented for sandstone, Figure 2.30, it can be deduced that the poor affinity of the SI to the sandstone reservoir, might be due to the negative values of of FL1 and FL1-DETA zeta potential with ξ= -15.02 ± 0.33 mV and ξ= -0.2 ± 0.50 mV respectively. However, zeta potential measurements on the SI presented are conducted through Electrokinetic phenomena through which and electric field is applied across the dispersion samples. During the zeta potential experiments, it was found that both samples lost their physical properties such as colour and dispersion stability and that FL1 and FL1-DETA are very sensitive to excessive electrical charges. FL1 and FL1-DETA are polyelectrolytes[1] with highly reactive structure of that exerting electric charge can cause a coagulation.

[1] AppendixB

Hence, the measurements for each set of sample could be run once and were not repeatable unless a fresh sample was used.

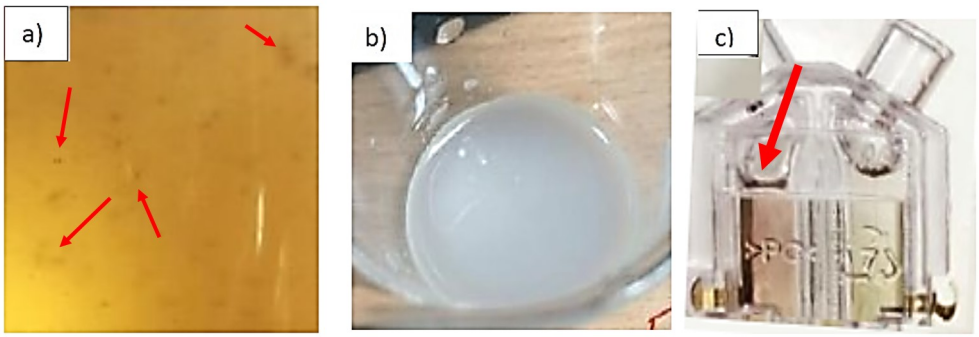

Figure 4.3: SI solutions appearance after Zeta potential measurements. a) FL1. Coagulation of the PSS-*co*-MA polymer can be seen as floating particles in the solution pointed by red arrows. b) FL1-DETA. The solution became cloudy and white after the Zeta potential measurement. c) FL1-DETA in zeta potential measurement cell. The solution became highly reactive during the experiment that corroded the PET cell and its gold electrode.This is pointed with the red arrow.

As high salinity brine have an affect on the conductivity of the solution and charge stability of dispersed particles, the effect of brine salinity and concentration was also investigated on the SI stability which will be present in the Chapter 5.

4.1.4 Spectrophotometry: UV-Vis

As a method of concentration measurement a UV-vis Spectrphotometer is used. The method is based on the direct relation between concentration of the SI and the intensity of the light adsorbed. To this end, calibration curves of FL1-DETA were made over a range of concentration. As the concentration decrease, samples lose their shade intensity i.e becoming less light absorbent when they are diluted.

The experiments were run at 150-700 nm range and the peak with highest intensity was chosen as a characteristic single wavelength attributed to certain concentration. Calibration curves for low concentration at 240 nm is graphed at Figure 4.4. Calibration curve for high concentrations at 320 nm is divided in two region 100-900 mg/l and 1000-5000 mg/l and both are graphed at Figure 4.5 and Figure 4.6, respectively. As it can be clearly seen, all three regions show a perfect linear regression fitting with $R^2 \geq 0.9$ whilst the slope of the fitted lines are non-identical. As a result, Uv-vis is used as a method of choice for further investigation on SI whilst is added to brine.

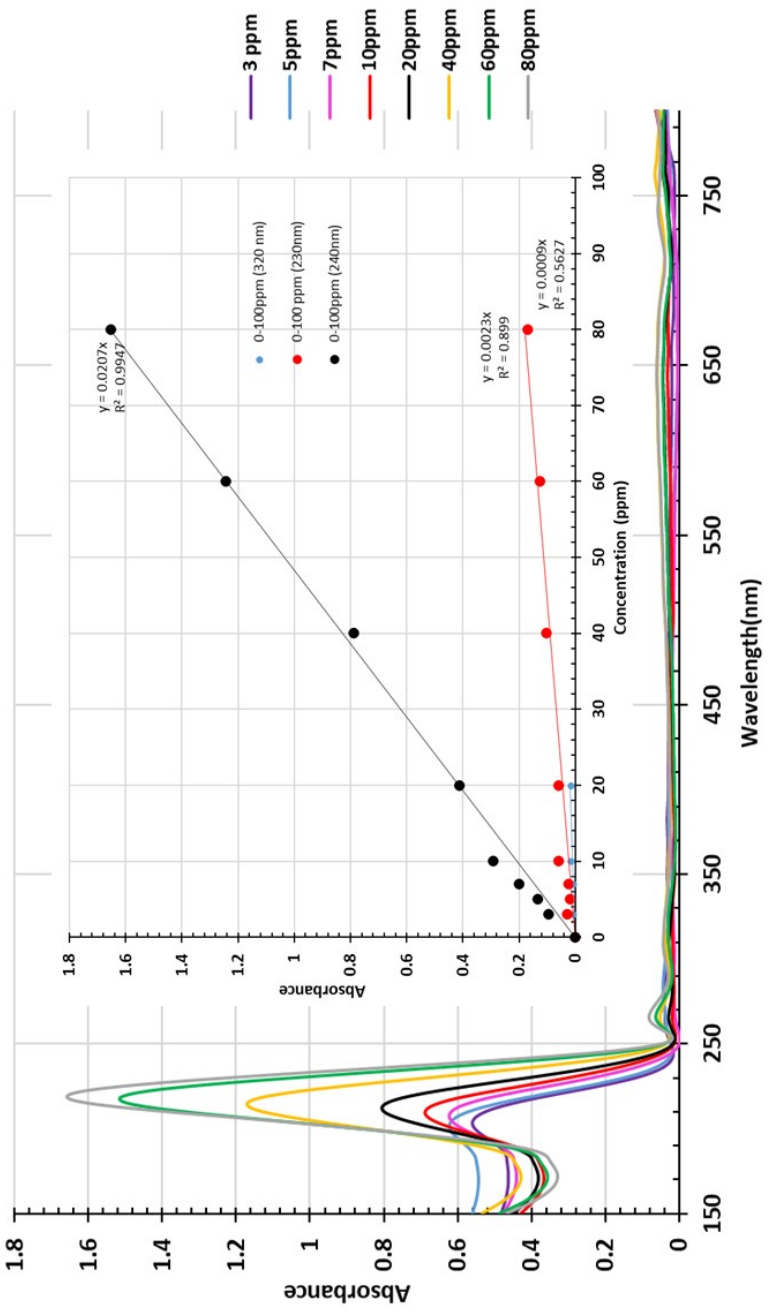

Figure 4.4: UV-Vis spectra of the FL1-DETA solution and corresponded calibration curve for 0-100 ppm sample solutions at 240 nm, 320 nm and 280 nm. 240 nm has the best fitting amongst all.

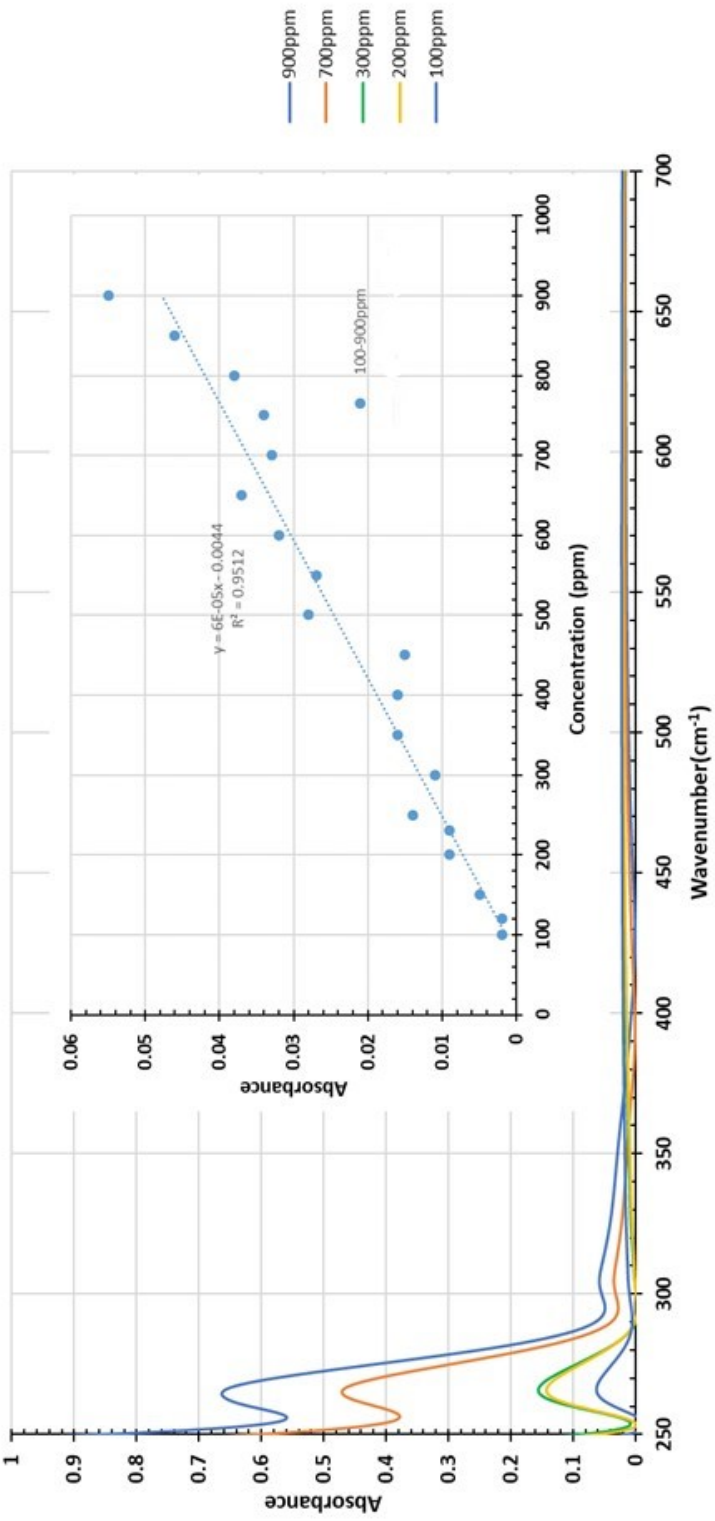

Figure 4.5: UV-Vis spectra of the FL1-DETA solution and corresponded calibration curve for 100-900 ppm sample solutions at 320 nm

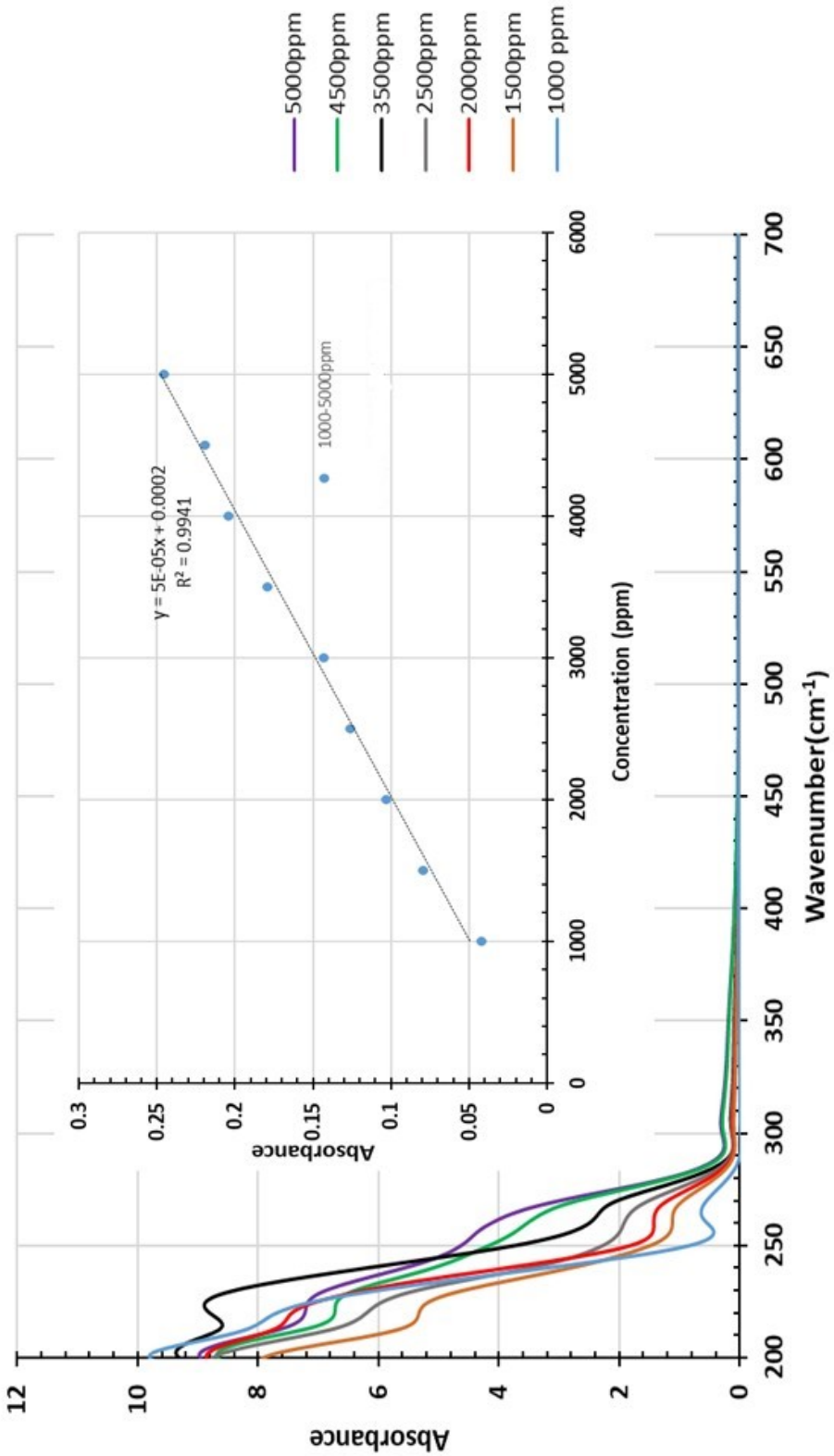

Figure 4.6: UV-Vis spectra of the FL1-DETA solution and corresponded calibration curve for 1000-5000 ppm sample solutions at 320 nm

4.2 Full brine characterisation

4.2.1 Characterisation: Scaling tendency

The scaling tendency of the brine composition listed in Table 3.2 was predicted with the Multiscale software. Table 4.2 and 4.3 and 4.4 show the calculated SR values of possible precipitates at two different conditions of ambient temperature/pressure and HTHP for 0.4% CO_2, 0% CO_2, 1% CO_2, respectively. 0.4% CO_2 is the amount of CO_2 in the atmosphere at ambient condition whereas 1% CO_2 is the amount of CO_2 that Multiscale software have the accuracy of prediction. As based on the information provided, no trace of dissolved CO_2 was reported in the production brine composition, 0% CO_2 was used as for the third form of calculations.

Table 4.2: SR value for predefined water composition 0.4% CO_2

1500 bar, 215 °C			
Salt	SR	Precipitation	With 34ppm H_2S in the system
		mmol/kg	SR
$FeCO_3$	0.96	0	-
$CaCO_3$	4.71	0	-
$BaSO_4$	16.46	0.26	2.63
$CaSO_4$ A [1]	1.08	0	-
$CaSO_4$ H [2]	2.12	0	-
$MgOH_2$	297.59	1.79	-
FeS	-	-	151.35
ZnS	-	-	660693
1 bar, 25 °C			
Salt	Init SR	Precipitation	With 34ppm H_2S in the system
		mmol/kg	SR
$FeCO_3$	193.88	0.59	524.80746
$CaCO_3$	268.06	0.66	588.84
$BaSO_4$	166.30	0.27	154.88
$BaCO_3$	2.94	0.08	-
$SrCO_3$	76.18	0.62	-
FeS	-	-	45708888.19
ZnS	-	-	3.17E+12

The highlighted columns in Table 4.2, Table 4.3 and Table 4.4 are the resulting SR when H_2S is added to the system. Another limitation of using this software is the scaling tendency prediction for Pb. Hence, calculations for PbS scaling are not listed in these tables. However, as explained in section 2.8 there will always be a

[1] Anhydrite,$CaSO_4$
[2] Hemihydrate,($CaSO_4$0.5H2O)

Table 4.3: SR value for predefined water composition 0%CO_2

1500 bar, 215 °C			
Salt	SR	Precipitation	With 34ppm H_2S in the system
		mmol/kg	SR
$BaSO_4$	16.49	0.26	21.28
$CaSO_4$ A	1.08	0	154.88
$CaSO_4$ H	2.12	0	-
$MgOH_2$	18104.73	1.98	-
ZnS	-	-	1659.58
1 bar, 25 °C			
Salt	SR	Precipitation	With 34ppm H_2S in the system
		mmol/kg	SR
$BaSO_4$	166.2681	0.2731	154.88
$MgOH_2$	12073.9914	1.9822	-
ZnS	-	-	1.99E+15

Table 4.4: SR value for predefined water composition 1%CO_2

1500 bar, 215 °C			
Salt	SR	Precipitation	With 34ppm H_2S in the system
		mmol/kg	SR
$BaSO_4$	16.23		12.63
$CaSO_4$ A	1.0665	0	-
$CaSO_4$ H	2.0906	0	-
FeS	-	-	15488.16
ZnS	-	-	354.813
1 bar, 25 °C			
Salt	SR	Precipitation	With 34ppm H_2S in the system
		mmol/kg	SR
$FeCO_3$	73.215	0	81.28
$CaCO_3$	101.07	1.0457	91.20
$BaSO_4$	166.11	0.27	154.88
$BaCO_3$	1.10	0	-
$SrCO_3$	28.64	0	-
FeS	-	-	3311.11
ZnS	-	-	2.69

cation replacement of FeS/ZnS to PbS in the presence of high concentrations of both metallic cations, therefore the formation of PbS should be expected. These data show, the scaling tendency of the brine increases in the presence of dissolved H_2S and that HTHP condition shows less severe scaling tendency comparing to ambient condition. This means that the scaling is mostly expected in the upstream of the production line.

4.2.2 Full brine turbidity test

As shown in Figure 4.7, the increase in turbidity for the uninhibited brine starts immediately after mixing of the two CW and AW brines. Based on the results the induction time is negligible due to high saturation levels of the brine. Hence, the the brine needs to be separated to two streams of CW and AW for storage purposes as defined in Table 3.3. Furthermore, the compatibility, sandpack test and other analysing experiments such as static jar tests needs to be run by separate streams. The turbidity value increases to a maximum of 74 FAU followed by a decrease which is caused by crystal settling after reaching a certain particle size due to the force of gravity. The observed plateau was observed after 2 hours indicates the equilibrium and the cease of crystal growth stage where the remaining formed crystals cannot grow any bigger in particle size to settle.

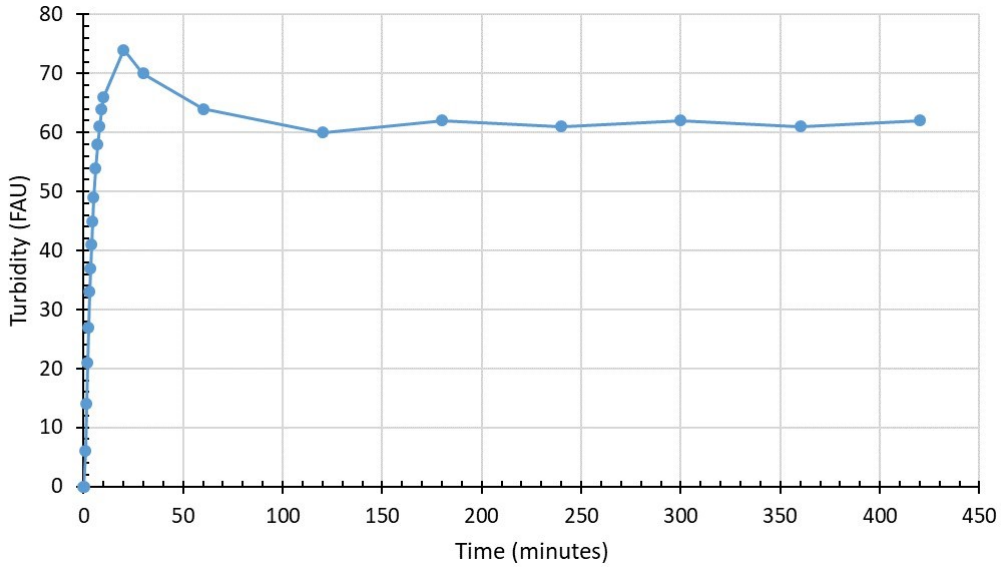

Figure 4.7: Brine turbidity measurement for CW+AW with 50/50 of volume ratio

4.3 Sand particle characterisations

4.3.1 Morphology and particle size analysis: SEM/EDS

In order to identify the morphology of the sandstone, SEM analysis was conducted through back scattering imaging. BSE with low voltage (5kV) was only used for non-conductive samples to eliminate the built-up charging effect and to avoid coating the samples, whereby, BSE at higher voltage (15kV) simply showed that every each of our samples were composed of one phase. The micrograph in Figure 4.8 shows the crushed sample has a porous morphology.

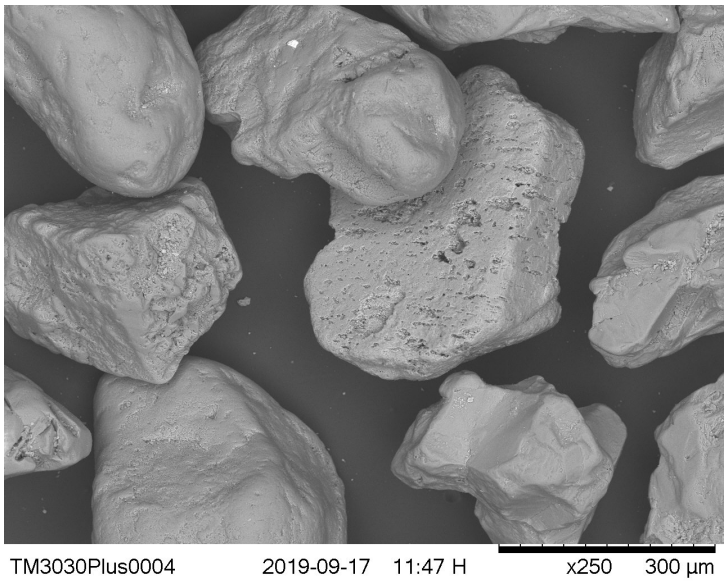

Figure 4.8: Sandstone characterisation. SEM micrograph with higher magnification on Sandstone particles. Particles show a porous structure.

To identify the elemental composition, samples were also mapped with EDS analysis. Results are presented in Table 4.5 and Figure 4.9. The sandstone sample mainly comprises silicon, oxygen, potassium and aluminium.

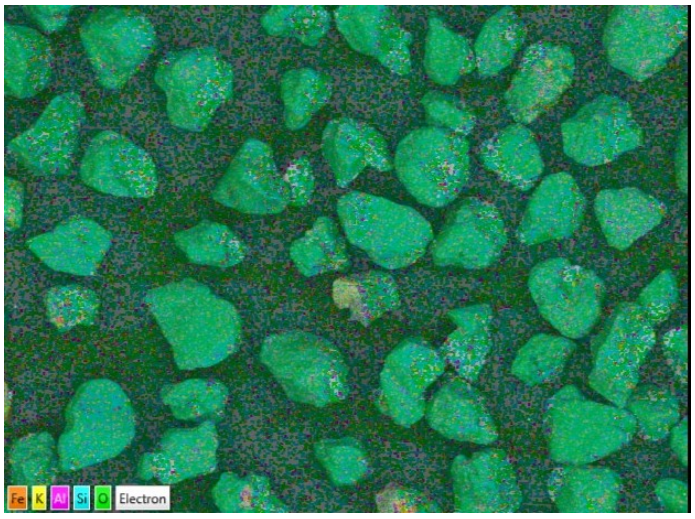

Figure 4.9: Mapping EDS results of crushed sandstone

The measured Sand particles size are listed in Table 4.10. Through five consistent

Table 4.5: EDS result.

Element	Weight%	Atomic%
O	57.63	70.65
Si	40.31	28.16
Fe	0.48	0.17
K	0.24	0.12
Ti	0.19	0.83
Al	1.15	0.83
Total	100	100

measurements, the prepared sand sample showed an average particle diameter of D_{50}= 0.2 mm (247μm) as shown in Figure 4.10.

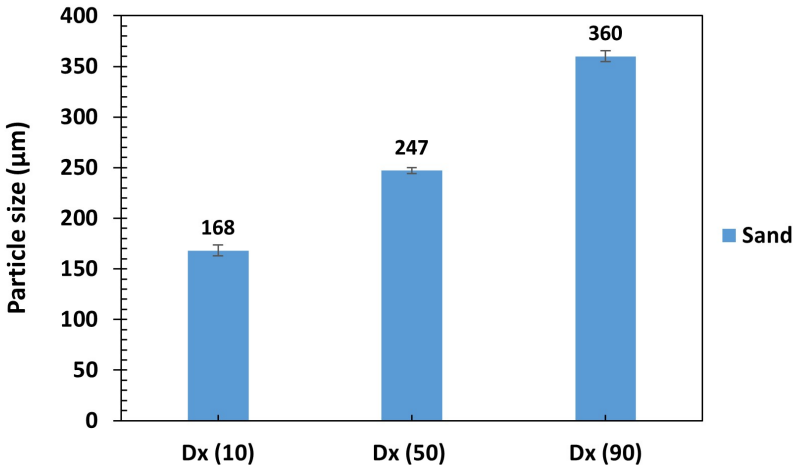

Figure 4.10: Sand particle initial particle size distribution

4.3.2 Crystallography analysis: XRD

The XRD pattern of the sandstone sample in Figure 4.11 presents its crystalline structure which was achieved through the method explained in Section 3.2.1. Peaks with highest intensity are highlighted with red lines and the complete list of peaks with corresponding Miller indices (hkl) is provided at Table 4.6. As it was expected, by comparing the results with reference RRUFF ID of R100134, the analysed sample completely matches a hexagonal Quartz and a Potassium Aluminium silicate with ICDD reference number of 00-049-0915 asserting the results from EDS analysis, Table 4.5.

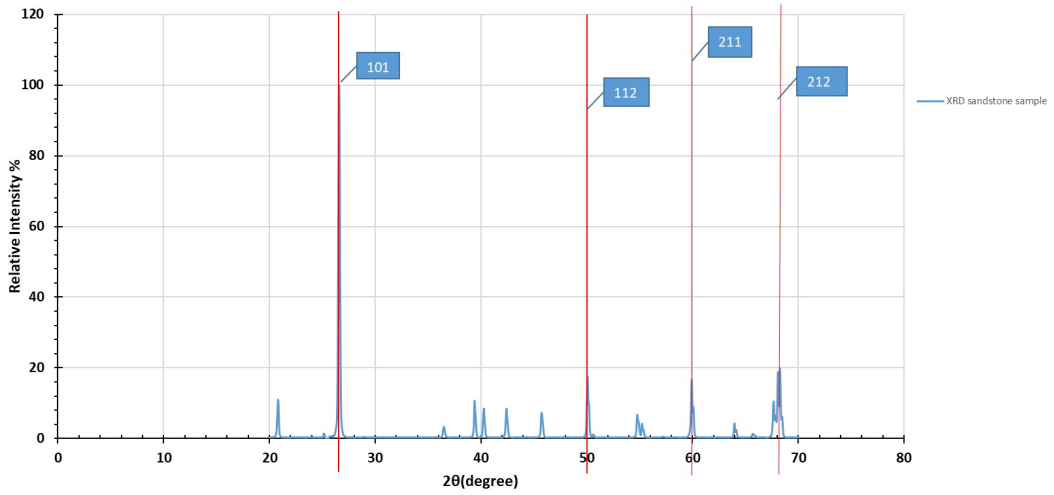

Figure 4.11: XRD pattern of the sandstone sample

Table 4.6: XRD of the sandstone sample

Peak centre°	d-spacing (A°)	h k l
20.88	4.26	100
26.56	3.35	101
36.4	2.465	110
39.39	2.284	102
42.39	2.129	200
45.73	1.98	201
50.07	1.819	112
54.79	1.54	211
64.02	1.45	113
67.64	1.38	212
65.75	1.418	300
20.78	4.26	100

4.3.3 Pore size evaluation: BET

As presented in SEM images Figure 4.8, sandstone particles have a porous structure. Therefore, Brunauer-Emmett-Teller (BET) technique explained in Section 3.2.4 is used to measure the average volume of the active surface area and the pores on the surface of sandstone particles. By using nitrogen as the adsorbate, the smallest detectable pore size is detected to be about 0.4 nm and the largest is approximately 300 nm. Figure 4.12 shows a schematic of how gas adsorption measures the pore size and pore volume while avoiding the voids between the particles themselves or in other words excluding the packing factor [162]. It is proven by Lyon *et.al* [163], that the packing of the powder would only effect the hysteresis shape at $P/P_0 > 0.75$. Since multipoint active surface

area calculation is calculated from $0.1 < P/P_0 < 0.5$ region and single point calculation is from $P/P_0 = 0.3$ region, powder packing factor will not affect the calculated results.

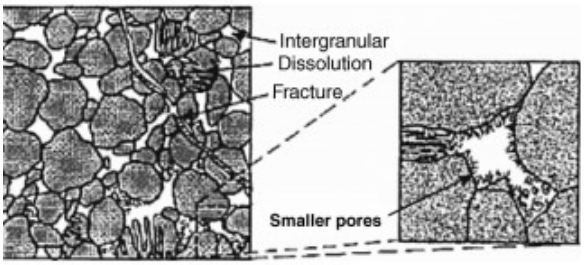

Figure 4.12: Schematic of gas adsorption on geological sandstone reservoirs [164].

Achieved adsorption/desorption isotherm in Figure 4.13, represents a type IV isotherm that is a mesoporous structure of a tight sandstone [165, 166]. The corresponding pore shapes are proposed based on literature [165].

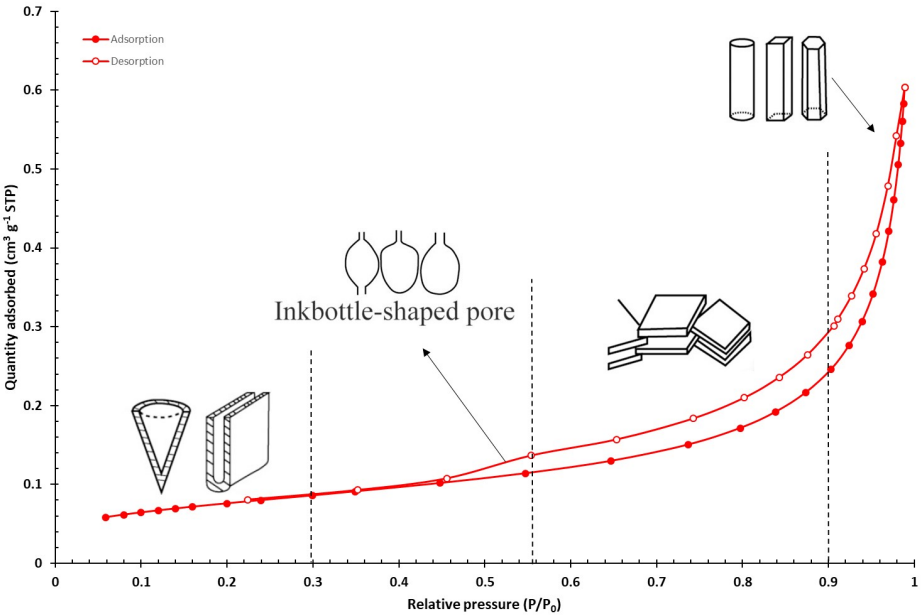

Figure 4.13: BET isotherm and corresponding pore shapes of sandstone particles

As the isotherm is not showing a sharp pore condensation step [165], a wide pore size distribution is expected. This asserts the results of the T-plot presented in Figure 4.14, that shows heterogeneity of pore structure and the existence of some micropores in addition to mesoporous structure. Statistical thickness is calculated based on

Herkin-Jura[1] equation:

$$Thickness = [13.99/(0.034 - log(P/P_o))]^{0.5} \tag{4.1}$$

The T-plot surface area, S_T, is calculated by multiplying the slope to the BET constant (15.47 m^2/g). If $S_T \neq S_{BET}$ then $S_T = S_{ext}$ and $S_{micropores}$ which is the surface area of micropores is calculated from below equation :

$$S_{micropores} = S_{BET} - S_{ext} \tag{4.2}$$

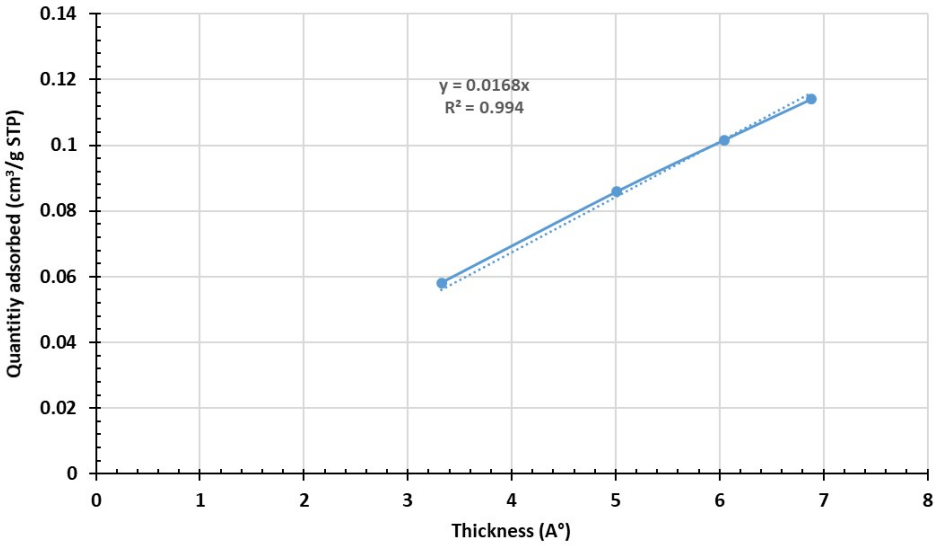

Figure 4.14: T-plot of sandstone particles, BET adsorption. The non-equality of active surface area calculated from t-plot slope and S_{BET} represents the presence of micropores.

Table 4.7 briefs the analysed data of BET measurement and shows that the active surface area of the particles is as low as 0.27 m^2/g with an average pore size of 12 nm, whilst the cumulative results define the pore volume as low as 0.824 mm^3/g.

From plotting the pore volume values versus pore diameter in Figure 4.15 and also the the very small difference between active surface area calculated by BJH and BET method (S_{BJH}-$S_{BET} \approx 0.0651 m^2/g$), it can be deduced that pores are relatively shallow with wide opening rather than deep, sharp and/ or narrow. This also confirms the

[1]For more information please refer to Appendix B
[1]Pore width
[2]Pore diameter

Table 4.7: Summary report of analysed BET data

Surface area	
S_{BET} single point	0.264 m^2/g
S_{BET} multipoint	0.274 m^2/g
S_{BJH} adsorption	0.230 m^2/g
t-plot micropores	0.259 m^2/g
Pore Volume	
V_{BET} single point	0.824 mm^3/g
V_{BJH} adsorption	0.922 mm^3/g
t-plot micropores	0.004 mm^3/g
Pore size	
W_{BET}[1]	12.01 nm
D_{BJH}[2]	16.01 nm

values for pore volume measurements and small differences between calculated V_{BJH} and V_{BET}. Furthermore, the 20 - 30 % difference between pore diameters calculated by BET and BJH, reconfirms the general mesoporous structure of sandstone particles [166].

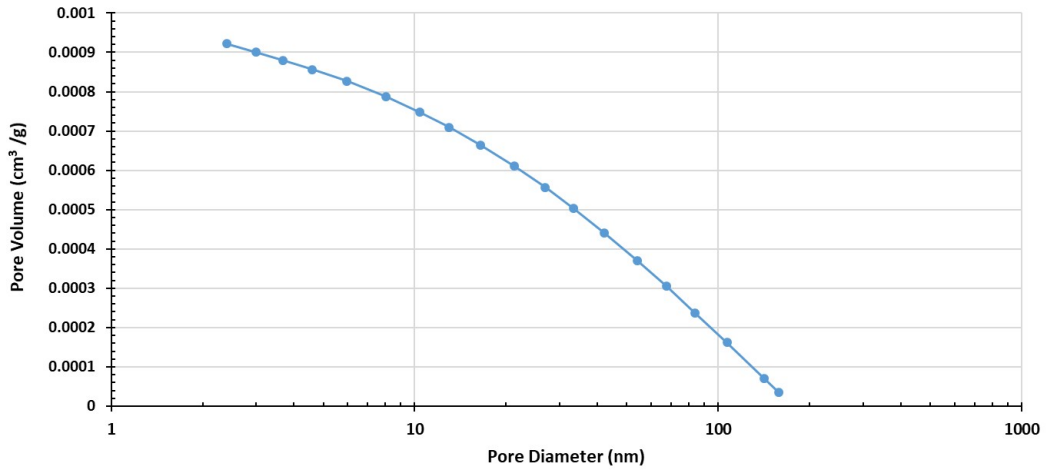

Figure 4.15: Pore volume Vs. Pore diameter of sandstone particles. As the diameter increase the pore volume decrease.

As it was explained earlier, BET technique measures the porosity and surface area of each individual sandstone particles and provides useful information regarding the absorbance capacity of sandstone particles when exposed to the adsorbents such as SI. However, it does not provide an accurate information on the porosity of sandstone rock and the spaces inside the rock where an SI can get trapped or precipitate. Hence, measurement of the entire formation is as important as individual particles. Therefore,

as a future work, Liquid Intrusion with mercury or Light, X-ray, and Neutron Scattering [162] of the actual core is suggested.

4.3.4 Charge measurement: Zeta potential

Zeta potential of the sandstone is measured at 25°C and pH 5.8 through Electroacoustic phenomena and colloid vibration current method in pure water. Colloid vibration current method is a dynamic method operating at high frequencies (megahertz) that allows measurements for microscale particles such as the sand. As was expected based on references [102], the average result of 10 measurements shows that the sand stone has negative values of zeta potential equals to ξ = -10.26 $\pm$ 0.21 mV in aforementioned conditions.

4.4 Summary

The aim of this PhD project is to improve retention properties of FL1-DETA on sandstone. In Chapter 4 we have provided individual qualitative and quantitative characterisation on the brine, initial scale inhibitor i.e. FL1-DETA and sandstone particles as an adsorbate. Considering that, all experiments conducted with the brine were at ambient temperature and pressure with no traces of H_2S and Fe^{2+} ions. Results indicated that FL1-DETA carries a net negative charge due to its —COOH and —SO_3H functional groups that can over come DETA. FL1-DETA showed high sensitivity to charge alteration caused by zeta potential measurements, whereas, it showed stability irrespective of ionic strength of the brine. The main reason for the instability was shown to be The PSS-*co*-MA being sensitive to be exposed into an electric field. However, the TGA results showed high thermal stability for both FL1 and FL1-DETA structure close to 250 °C.

Full production brine showed high scaling tendency especially at room temperature with no induction time. Therefore, for storage and testing purposes the production brine was divided to two separate streams of CW and AW.

The Scales produced from production water at 35 °C- 90 °C are expected to be:

1. $BaSO_4$
2. $CaCO_3$
3. FeS
4. ZnS
5. PbS

Sand particle sample was prepared in laboratory by mixing silica and kaolinite to replicate more realistic representation of sandstone rock. Sand sample initial D_{50}= 247 μm with shallow wide opening pores of $\leq$ 12 nm and ξ=10.26 mV at pH= 5.8.

CHAPTER 5

FL1-DETA behaviour in full brine without H_2S

Introduction

In this chapter, experimental designs for two factor (brine and SI) and three factor (brine, SI, sand) were explained. Where on the first stage the experiments will be conducted in the absence of H_2S. Despite the fact that these amended testing conditions significantly may affect the scaling outcome the brine, however, it can provide a good understanding of FL1-DETA and later the modified inhibitor X10-6 behaviour in future Chapters (Chapter 5 and 6) when two (brine and SI) or three factors (brine, SI and Sand) are included in the experimental setup. These step by step simplifications help to find the grounds for identification and improvement of the scale inhibitor adsorption and ultimately retention properties. Later in Chapter 7 H_2S as the final influencing factor will also be included in the experimental setup and SIs will be compared under full scaling scenario.

Two Influencing factor tests (SI, Brine)

5.1 Compatibility test

In this purely visual test, results are defined on a subjective scale as it is represented in Table 5.1. 0 denotes a clear solution; where in an increasing order, 1—4 denote a cloudy or hazy appearance and 5—7 denote higher observed levels of precipitation.

Table 5.1: Subjective Scale for the Precipitation of FL1-DETA in compatibility test

Solution condition	grade
Clear	0
Hazy/Cloudy	1, 2 ,3 ,4
Precipitate	5, 6 , 7

5.1.1 FL1-DETA in CW

In the first stage, compatibility of the FL1-DETA with the CW was investigated. The CW brine composition is listed in Table 3.3 and the SI sample solutions were prepared as explained in Section 3.3.1. Figure 5.1 shows samples appearance at the time of preparation (0 hr) and after 24 hours. The cross mark is made at the bottom of the beakers for better illustration of this visual test. As it can be seen, none of the samples had a clear appearance at the beginning of the experiment, which is the sign of incompatibility with the brine. The recorded pH and scale of cloudiness for each sample is reported at Table 5.2.

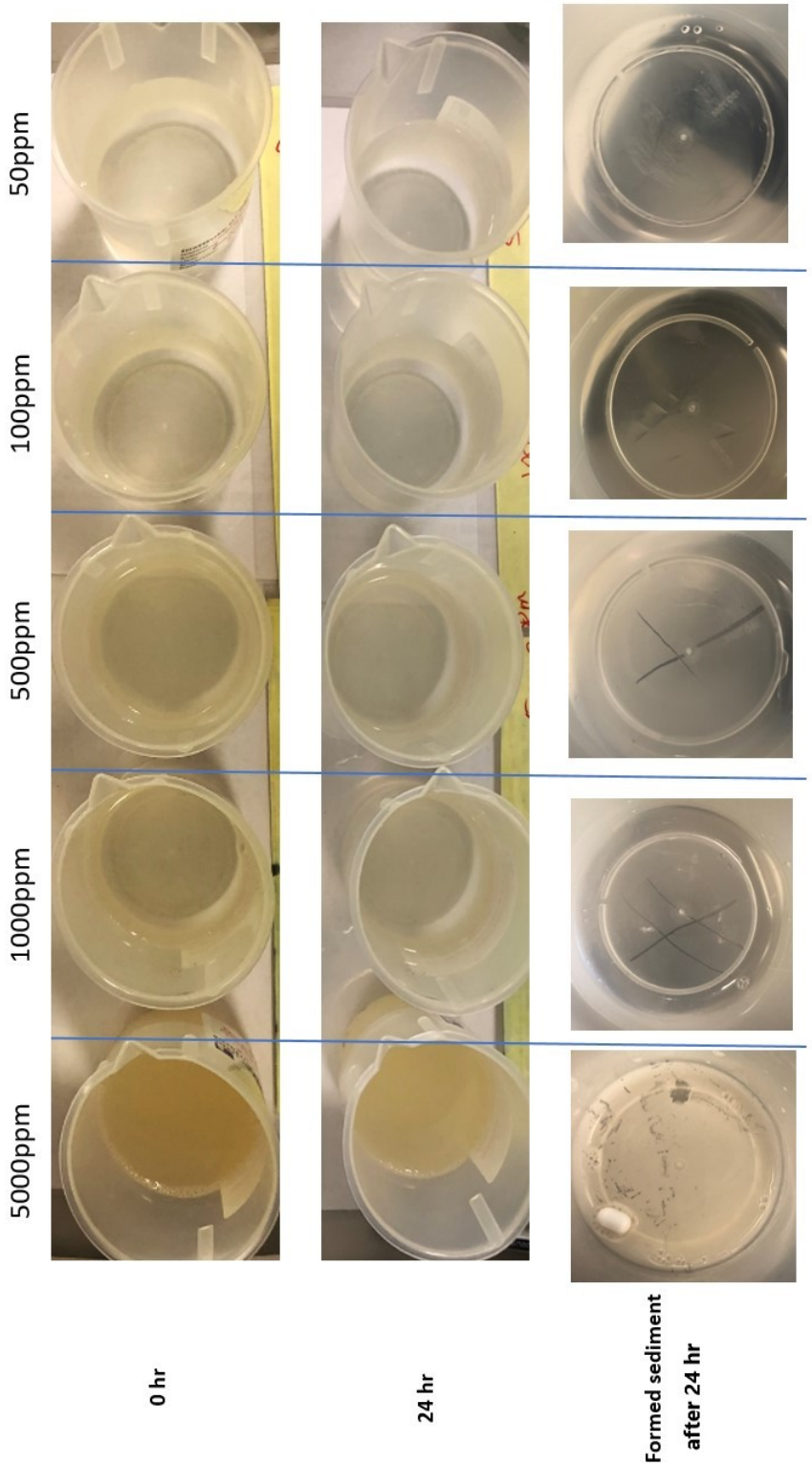

Figure 5.1: Compatibility test in CW at 23°C for different concentrations of FL1-DETA. Precipitation was observed at very early stages of this experiment for all the samples, except 100 ppm and 50 ppm.

Table 5.2: Results for compatibility test of SI in CW at 23°C

[FL1-DETA]	Initial pH	Initial condition	Final pH	Final condition
5000 ppm	5.32	7, 4	5.36	7, 3
2000 ppm	5.70	6, 4	5.42	7, 3
1000 ppm	5.76	5, 3	5.34	6, 2
500 ppm	5.96	5, 3	5.66	6, 2
100 ppm	6.08	-, 2	6.00	5, 1
50 ppm	6.11	-, 2	6.04	5, 1

The higher the [FL1-DETA], the more incompatibility was observed with the CW. Furthermore, a gel like precipitation was observed for all the samples in an escalating volume with the concentration increase. Precipitation from the 5000 ppm beaker was dried in oven at 73 °C overnight and the resulted powder was collected to be analysed with SEM/ EDX microscopy and X-ray diffraction.

5.1.2 FL1-DETA in diluted CW and NaCl 3.5%

FL1-DETA compatibility was also checked with diluted versions of CW. To this end, CW water was diluted 5 times with DI[1] and sample preparation was carried on as explained earlier in section 3.3.1 with the diluted brine. As Figure 5.2 shows, similar to a full concentration CW, extreme incompatibility was recorded.

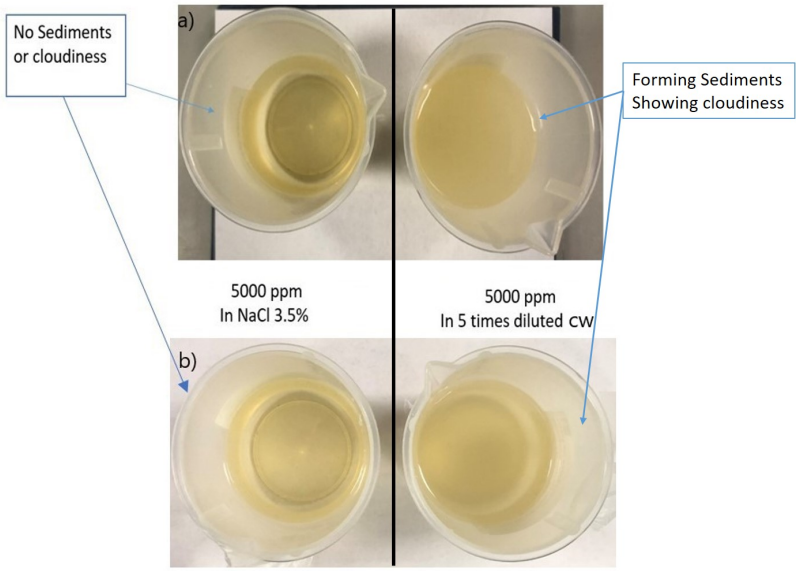

Figure 5.2: Compatibility of SI with diluted CW and NaCl 3.5%. a) at 0 hour b) After 24 hours

[1]Deionized water

Compatibility of the FL1-DETA was also investigated in NaCl 3.5% brine. As depicted in Figure 5.2, the SI showed a full compatibility with the brine solution in the whole duration of 24 hours without becoming cloudy or hazy and did not form any precipitation. Even though no clear phase separation was inspected, however, based on visual observation the solution had more viscosity close to the bottom of the beaker compare to the top. This means that FL1-DETA is incompatible to an element presented in CW and once the brine is replaced with a simple brine, FL1-DETA shows separation and swelling behaviour.

5.1.3 Responsible element for the incompatibility

As the formation water has a complex composition, in order to identify the responsible element for the FL1-DETA/CW incompatibility, tests are repeated for each salt component in CW brine (Table 3.3) separately, whilst they were dissolved in DI water with the exact defined concentration as proposed for CW. This set of experiments shows that the SI is compatible with the solution of all salts mentioned in Table 3.3 except the $BaCl_2$, Figure 5.3. Surprisingly, unlike most of the industrial scale inhibitors that are used in squeezed precipitation with high [Ca^{2+}] CW such as PPCA, FL1-DETA showed a total compatibility with Ca^{2+} no measured turbidity and did not form any visual sedimentation after 24 hours that could have been a sign of complex formation.

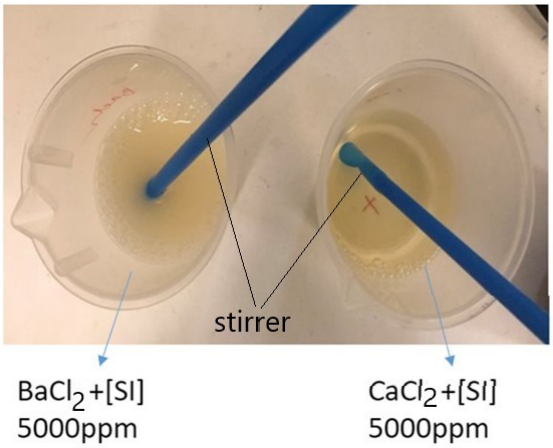

Figure 5.3: FL1-DETA compatibility with 4.37 g/L $BaCl_2$ (I=0.054 mol/L) and 64.9 g/L $CaCl_2$ (I=1.32 mol/L). The red cross at the bottom of the beaker should be visible for the compatible blend.

Further investigation on SI compatibility with CW is shown in Figure 5.4 where two CW brine were prepared without $BaCl_2$ and without $CaCl_2$, respectively. This would help to identify the synergetic effect of other salts in the composition and their ionic effect on various mixed concentrations of SI without the probable interfering element.

As can be seen, incompatibility occurred in the brine consisting $BaCl_2$ (labeled as CW with out $CaCl_2$). The red cross is placed on the surface beneath the beakers for better illustration on turbidity of the solutions. Compatibility on a full brine (CW+AW) was also investigated. As presented in Figure 5.4, in spite the presence of SI in the solution, the sample got turbid yet at lower degrees in comparison to other samples. Further analysis needed to identify the type of sediments formed in each beaker and to find the caused factor of turbidity in the full brine sample.

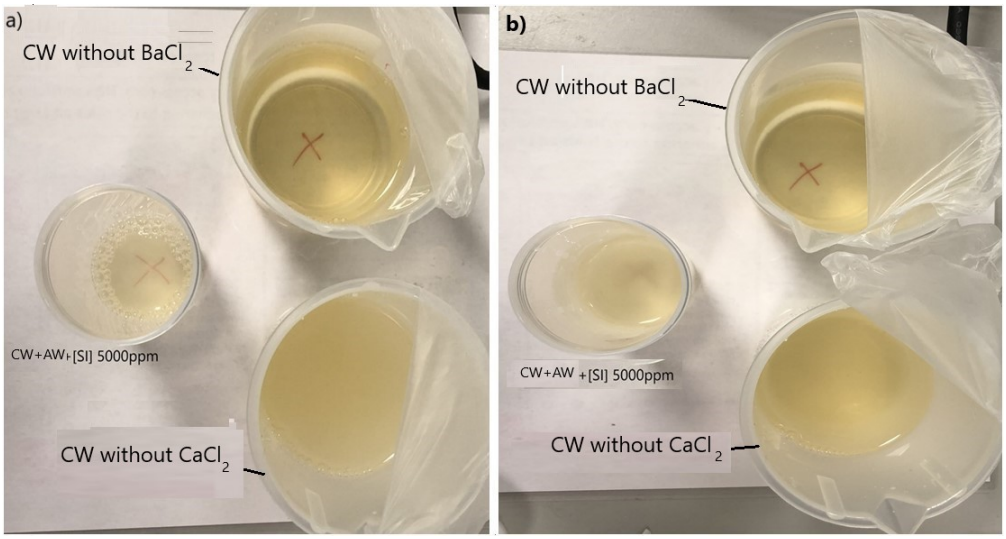

Figure 5.4: Compatibility test of FL1-DETA on full brine (AW+CW) and modified brine i.e CW without $BaCl_2$ and CW without $CaCl_2$. The red cross at the bottom of the beaker should be visible for the compatible blend. a) at 0 hour b) After 24 hours.

5.1.4 Characterisation of the FL1-DETA/CW precipitation

5.1.4.1 SEM/EDX

Dried powder of FL1-DETA/CW incompatibility sediment, was carbon coated and analysed by SEM/EDX microscopy. A carbon coating was sputtered on for capturing better resolution images from non-conductive samples. SEM Micrographs are presented in Figure 5.6 and 5.5. These SE pictures illustrate an amorphous structure like bead that have clustered together while drying whereby, their diameter is not exceeding a micron. The homogeneity of the samples are also analysed with BSE and no phase separation or structure was recognised.

EDX mapping results are presented in Figure 5.7, and it shows high concentrations of barium, sulphur and oxygen with traces of Cl where Sr and K are spotted. Interestingly, despite the amorphous morphology and jelly like sediment, carbon is not marked as bright as other elements in the sample mapping, suggesting presumably, carbon from

polymeric structure is embedded beneath barium and sulphur and that EDS can only detect the surface and not the core of the beads where the bulk is.

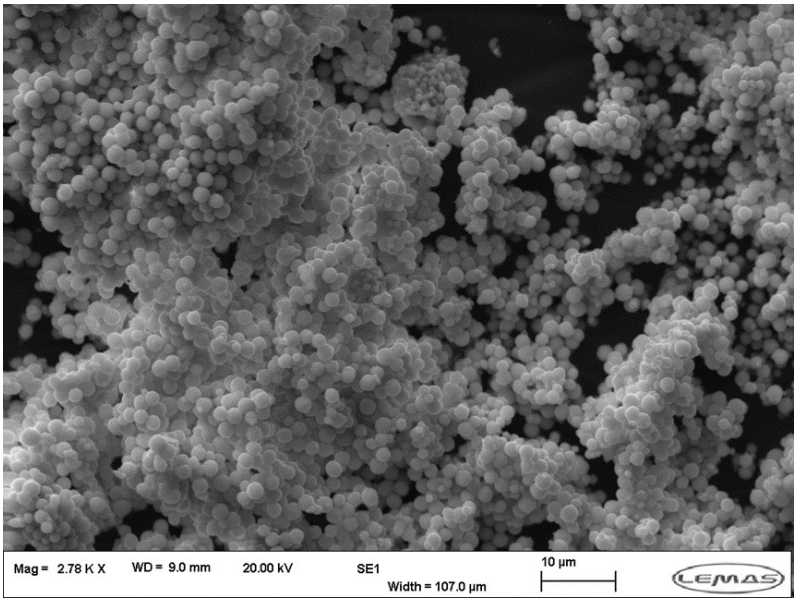

Figure 5.5: SEM of FL1-DETA/CW precipitation resulted from compatibility test. The SEM micrograph shows clusters of amorphous structure in bead shape morphology.

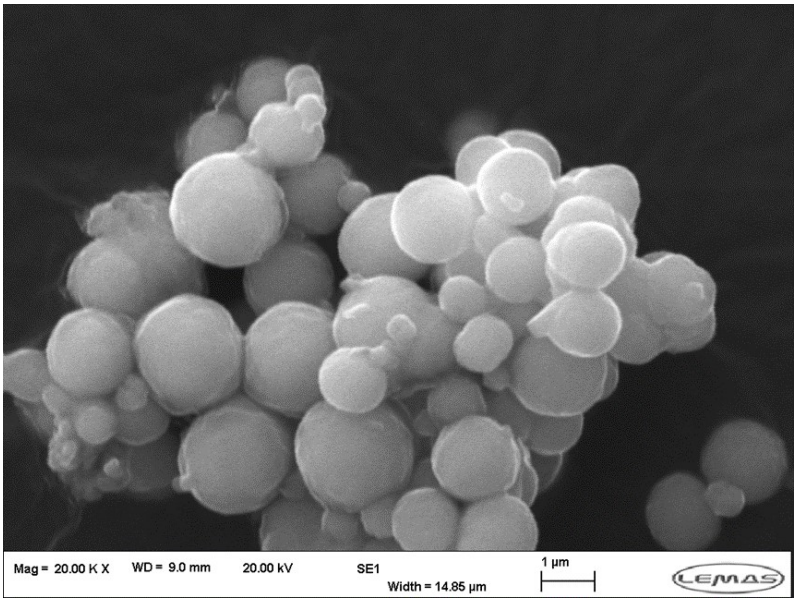

Figure 5.6: SEM micrograph of FL1-DETA/CW precipitation in higher magnification. The maximum diameter of single sphere/bead is $\approx 1\mu m$

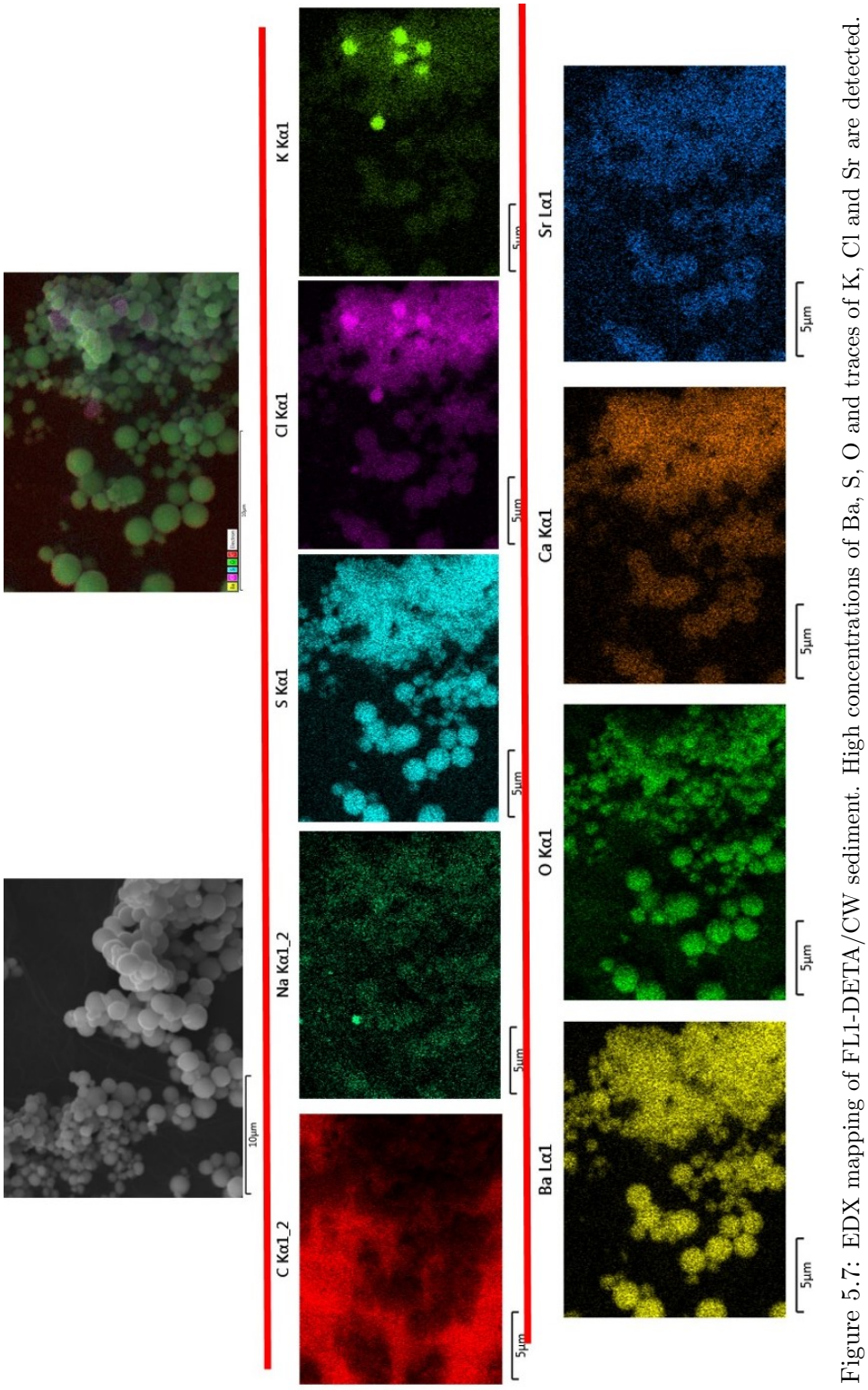

Figure 5.7: EDX mapping of FL1-DETA/CW sediment. High concentrations of Ba, S, O and traces of K, Cl and Sr are detected.

5.1.4.2 XRD analysis

The dried precipitated sample was also analysed with XRD. The achieved data is plotted in Figure 5.8 and the main peaks are labelled. Comparing the pattern with XRD of a standard $BaSO_4$ [167], peaks position completely match with a slight shift of less than 0.5 degree to the right, however, broadened.

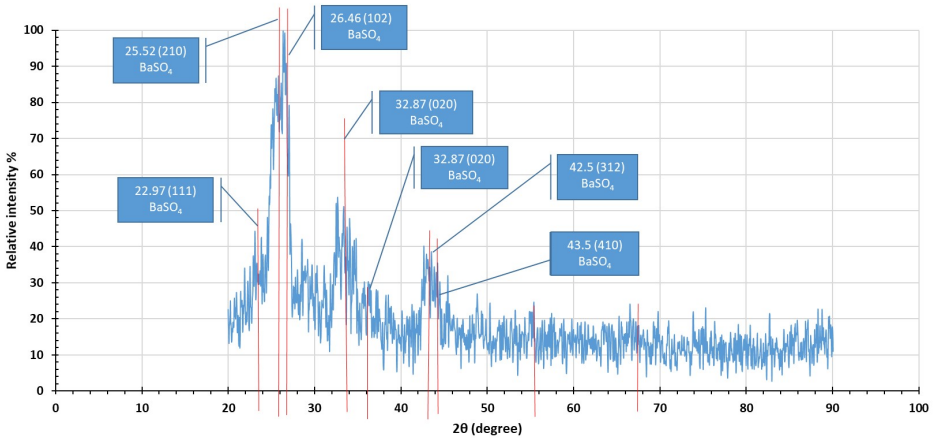

Figure 5.8: XRD pattern of precipitation from FL1-DETA—CW compatibility test

XRD peaks may shift due to internal stress caused by doping and crystal defects [168]. According to kinematic theory of scattering, X-ray diffraction peaks broaden either when crystallites become smaller than about a micrometer or if lattice defects are present in large enough abundance such as polymer intertwine [169]. In this case both theories are possible since the bead diameter is detected to be maximum 1 μm whilst it contains polymer chains. Furthermore, peaks belonging to KCl[170], $CaCl_2$ and $SrCl_2$ [171] are also visible in the achieved XRD pattern, mainly as the precipitated samples were not washed before being dried. Major peaks with their corresponding miller indices and matching crystalline material are highlighted with red line.

5.1.4.3 Re-dissolution of precipitation

The re-solubility of the fresh precipitate (without being dried) was investigated in both fresh CW and DI water at room temperature and 120°C. Figure 5.9 shows the re-dissolution attempt of the precipitate in a fresh DI water at 80°C. It appeared that the sediment is insoluble in all above stated conditions. Based on all characterisation results presented in this section i.e XRD, SEM/ EDX and re-dissolution observation, schematic Figure 5.10 is proposed. It is suggested Ba^{2+} ions form a complex with FL1-DETA through bonding with its SO_3^{2-} groups and forming a semi $BaSO_4$ structure where XRD peaks appears and an insoluble FL1-DETA—Ba^{2+} complex is created.

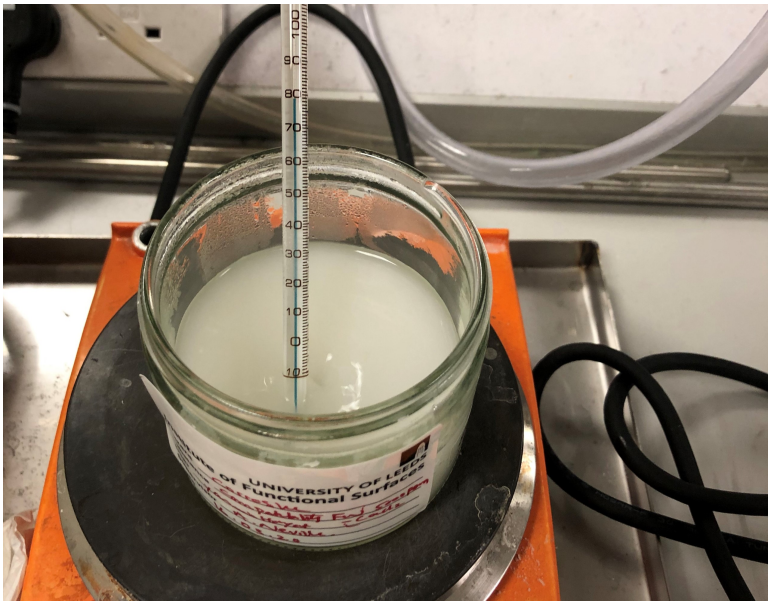

Figure 5.9: Qualitative analysis on fresh precipitate of FL1-DETA/CW blended with Fresh 100 ml of DI water. Sample is heated up to 80°C and still shows insolubility

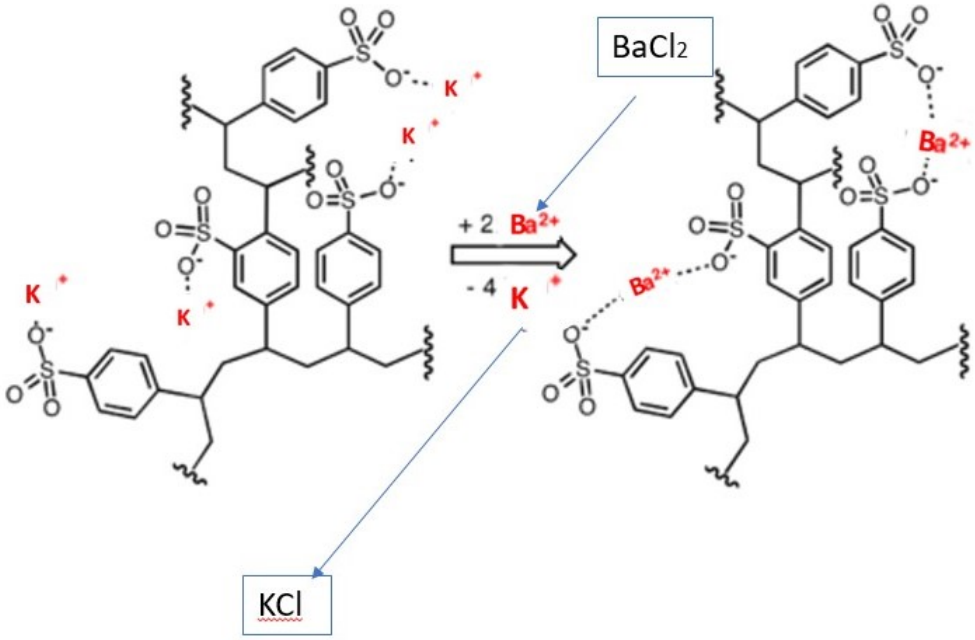

Figure 5.10: Schematic of Ba^{2+}—SI complex

Table 5.3: Relative selectivities of sulphonic resins for cations. Copied from reference[93]

	Degree of cross-linking, % DVB			
Cation	4	8	12	16
Monovalent				
H*	1.0	1.0	1.0	1.0
Li	0.90	0.85	0.81	0.74
Na	1.3	1.5	1.7	1.9
NH_4	1.6	1.95	2.3	2.5
K	1.75	2.5	3.05	3.35
Rb	1.9	2.6	3.1	3.4
Cs	2.0	2.7	3.2	3.45
Cu	3.2	5.3	9.5	14.5
Ag	6.0	7.6	12.0	17.0
Divalent				
Mn	2.2	2.35	2.5	2.7
Mg	2.4	2.5	2.6	2.8
Fe	2.4	2.55	2.7	2.9
Zn	2.6	2.7	2.8	3.0
Co	2.65	2.8	2.9	3.05
Cu	2.7	2.9	3.1	3.6
Cd	2.8	2.95	3.3	3.95
Ni	2.85	3.0	3.1	3.25
Ca	3.4	3.9	4.6	5.8
Sr	3.85	4.95	6.25	8.1
Hg	5.1	7.2	9.7	14.0
Pb	5.4	7.5	10.1	14.5
Ba	6.15	8.7	11.6	16.5

*Reference value

Table 5.4: Hydrated radius of some elements. Copied from reference[172]

Cation	Hydrated radius (nm)[a]	Ionic radius (nm)[b]	Hydration free energy (kJ mol^{-1})[b]
Na^+	0.358	0.102	-365
Ba^{2+}	0.404	0.136	-1250
Sr^{2+}	0.412	0.125	-1380
Ca^{2+}	0.412	0.100	-1505
Mg^{2+}	0.428	0.072	-1830

This theory also matches with ion exchange theory [93] that at primary stage, monovalent cation (K^+) can form an ionic bond with SO_3^{2-} group. However, they will

be exchanged with a divalent cation as they are very mobile. Furthermore, based on literature [173] SO_3^{2-} groups have very low/no affinity to Ca^{2+} in general. Dardel[93] explains that a sulphonic resin has a relative selectivity factor which differs for each pair of ions because the affinity of the resin for an ion is governed by the size of its hydrated form, Table 5.3. As an ion gets larger, the more the resin bead must expand to accommodate it, hence the selectivity number is bigger for Ba^{2+} compared to Ca^{2+} as it has smaller hydrated form. Some elements with corresponding hydrated radius are listed at Table 5.4. Another possible explanation can be that doping DETA to FL1 makes -COOH groups less accessible to Ba^{2+} and leaves it with only SO_3^{2-} groups to react. Therefore, as expected from any $BaSO_4$ complex and scale, the formed sediment does not dissolve in fresh CW/DI water at any temperature, due to its intrinsically low solubility constant. The dependence of $BaSO_4$ solubility with temperature was fully explained in Chapter 2, Section 2.2.3.

Three influencing factor tests (brine, SI, sand)

5.2 Coupled adsorption/precipitation static jar test

As explained in Chapter 2, two types of inhibitor squeeze treatment are routinely carried out where the intention is either:

- Adsorption Squeeze treatments where the aim is to adsorb the inhibitor by physic-chemical process onto the rock matrix; or
- Precipitation Squeeze treatments which is applied in order to extend the squeeze lifetime by precipitation (or phase separation) which is commonly carried out by adjusting the solution chemistry ($[Ca^{2+}]$, pH, temperature) of polymeric inhibitor

In the precipitation squeeze technique, the scale inhibitor reacts or is reacted to form an insoluble salt complex which precipitates in the pores in the formation rock. For instance, phosphonate scale inhibitors can be precipitated as calcium salts. Inhibitors such as phosphate esters are not suitable because of forming soluble calcium salts or salt complexes. In general, on adjusting the pH and increasing a calcium ion concentration, precipitation of scale inhibitor takes place within the pore spaces of the rock and extends the treatment lifetime [116]. As precipitation squeezes are usually superior to adsorption squeezes, thus, a chemical inhibitor whose calcium salt has a very low solubility should be a superior squeeze chemical [87].

These mechanisms – adsorption and precipitation – individually or working together are responsible for giving a long return curve of SI after a near-well SI squeeze treatment. To confirm which rock/scale inhibitor retention mechanism i.e. pure adsorption or coupled adsorption—precipitation is occurring, a number of different mass/volume ratios should be examined. As a result, in the static adsorption tests, experiments were performed using 3 masses of sand (m = 10g, 20g and 30g) at a constant volume of SI

solution (V = 0.08L). These experiments were carried out and compared directly with parallel static compatibility tests (no sand present) to evaluate the coupled adsorption—precipitation behaviour of FL1-DETA. FL1-DETA in different concentrations was blended with CW (or NaCl 3.5%) brine separately and poured on 10g, 20g or 30g of sand. Samples were settled at room temperature for 24 hours and the apparent adsorption was calculated via:

$$\Gamma_{app} = \frac{C_0 - C_{eq}}{m} \tag{5.1}$$

Whereas, m is the mass of the sand, C_0 is the initial concentration of SI (FL1-DETA) and C_{eq} is equilibrium concentration that is the residual concentration in the solution after 24 hours. All concentrations were measured through Uv-vis spectroscopy and fitted based on the calibration curves presented in Figures 4.4, 4.5 and 4.6. Γ_{app} shows the apparent adsorption as this formula would clearly be an over-estimation of the actual adsorption, since some of the SI would be precipitated. Kahrward *et. al* [114] with their modelling work, have proved that pure adsorption can be distinguished from coupled adsorption/precipitation by plotting Γ_{app} against C_{eq}, Figure 2.24. In this plot if :

- There is a clear region at lower concentrations where the "apparent adsorption" is clearly not a function of the (m/V) ratio, the region is showing a pure adsorption. (m is the mass of sand in static jar test and V is the volume of the brine used.)
- At higher concentrations, the "apparent adsorption" is clearly a function of the (m/V) and ratio with the adsorption seeming to increase as (m/V) decreases, that region is showing a coupled adsorption—precipitation

5.2.1 FL1-DETA in CW—sand

5.2.1.1 Apparent adsorption isotherm

The apparent adsorption isotherms of SI in CW brine at room temperature are depicted in Figure 5.11 for initial concentration values stated at Table 5.2. It can be seen that in general, the achieved H—type [1] isotherms are fully dependent on the (m/V) i.e. coupled adsorption—precipitation is the main governing factor.

In the achieved isotherms, all three start with a small region of pure strong adsorption (>0.4 mg/g, H—type) on the active sites available on the sand surface for concentrations less than 10 ppm. As the concentration increases, the remarkable dependence of (m/V) pronounces by showing different slopes for each curve after reaching a small insignificant plateau. Each plateau in an adsorption isotherm indicates saturation of the active sites available on the substrate that are completely occupied by the adsorbent [166, 174] suggesting that a single layer has formed into its maximum capacity. The small plateau region for all these three isotherms can be a sign of low affinity

[1] Isotherm classification is fully explained in Appendix B

of the SI to the sand and lack of bonding opportunities for SI—sand interaction or high SI—SI interaction. After the build up of the first monolayer, the isotherms show an increase trend that indicates the formation of a multilayer where SI—SI interactions are occurring. In current case as the steep slope of all three graphs (10 g, 20 g and 30 g) differs from one another, this can be a sign of aggregation and high interaction of SI—SI in the formed precipitation [166, 174]. Ultimately, the slope reduces to lower angles for all three curves.

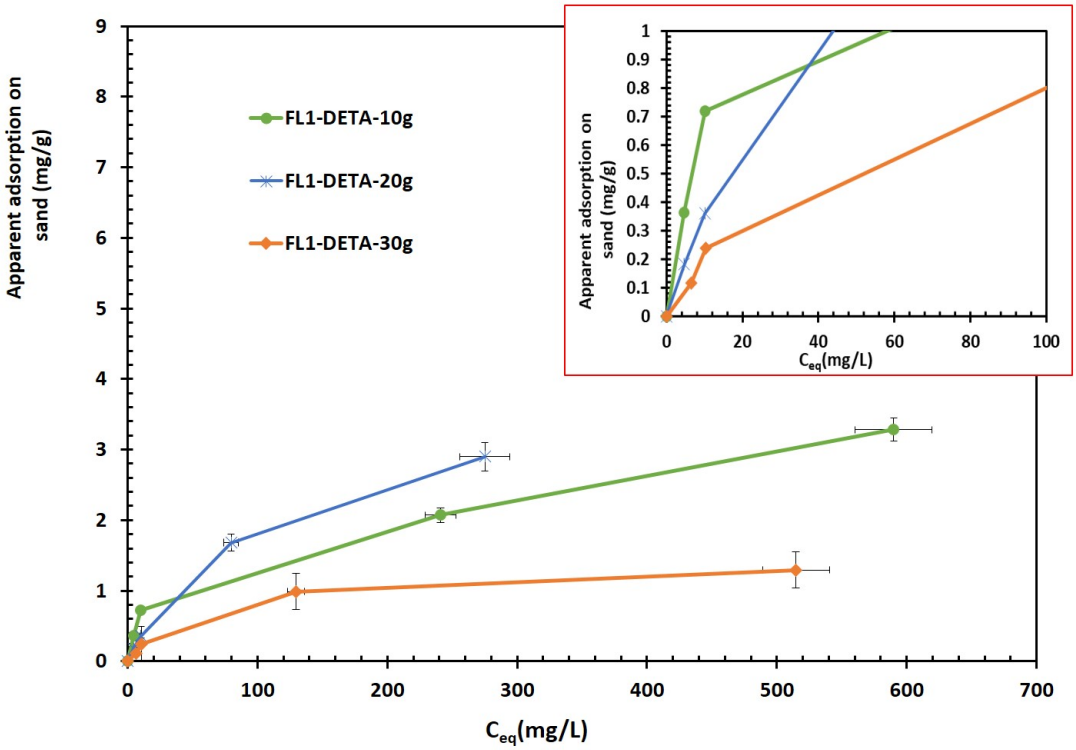

Figure 5.11: Apparent adsorption isotherm for FL1-DETA in CW. C_{eq} represents the concentration of the solution after 24 hours which is the FL1-DETA that is neither absorbed nor precipitated. $C_{initial}$ are 50 ppm, 100 ppm, 500 ppm, 1000 ppm that are marked on each graph in an increasing order.

Figure 5.12 shows the visual images of this experiment for FL1-DETA/CW—10 g sand where incompatibility of FL1-DETA/CW can be clearly seen in the very starting hour of the test. All samples got clear after 24 hours, however, samples with 5000 ppm and 2000 ppm FL1-DETA showed a turbid solution during the whole period of 24 hours.

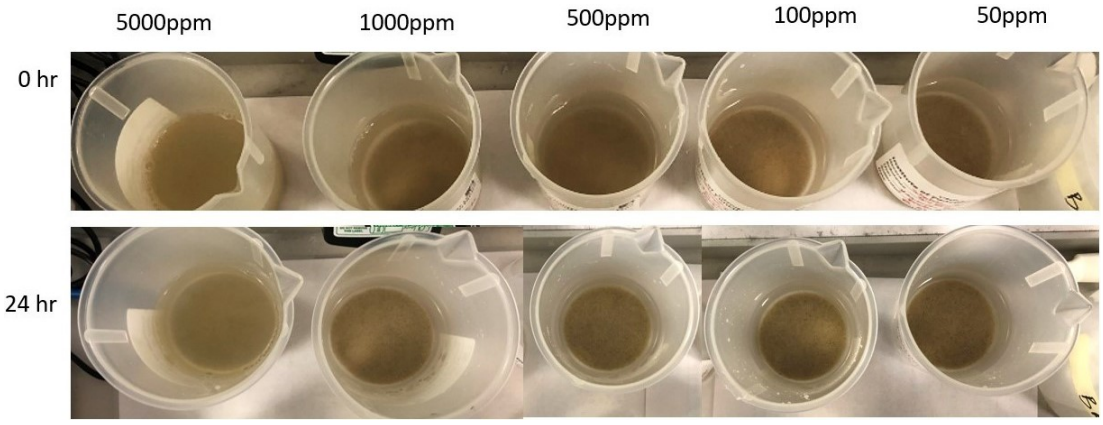

Figure 5.12: Coupled adsorption/precipitation static jar test for 10 g sand. Incompatibility of FL1-DETA/CW can be clearly seen in the starting of the experiment through the cloudiness of the supernatant which clears after 24 hours for most samples, due to precipitation. Samples with 5000 ppm FL1-DETA show a hazy solution for the whole duration of 24 hours.

5.2.1.2 Desorption measurements

For the next stage of the experiment the top solution was emptied and replaced with a fresh 80 ml of CW while keeping the formed precipitation for each beaker. The aim was to evaluate the amount of desorption from the adsorbed/precipitated FL1-DETA of the earlier set of experiments. Results are plotted in Figure 5.13, 5.14 and 5.15. As can be clearly seen from these graphs only few ppm of what was adsorbed/precipitated, desorbed.

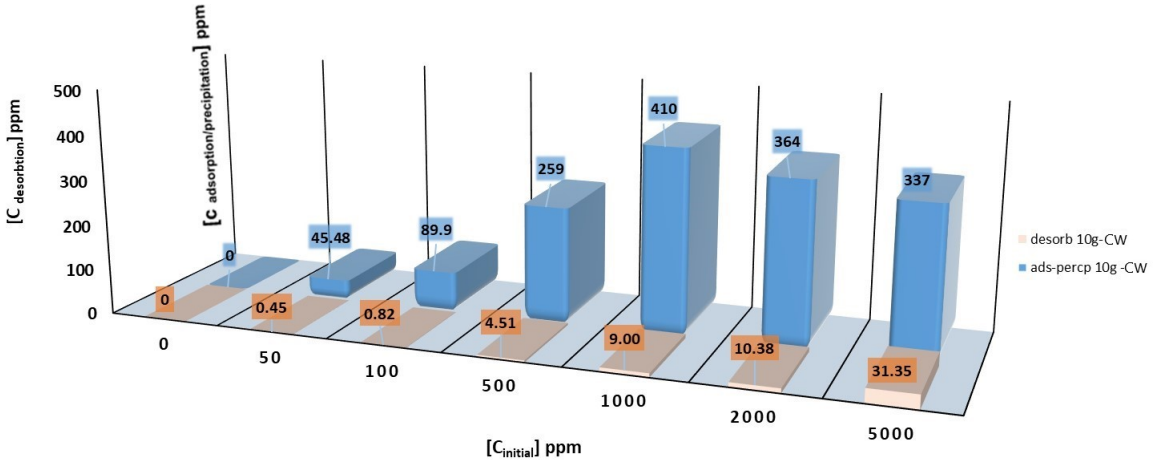

Figure 5.13: Desorption versus adsorption/precipitation for FL1-DETA/CW— 10g sand

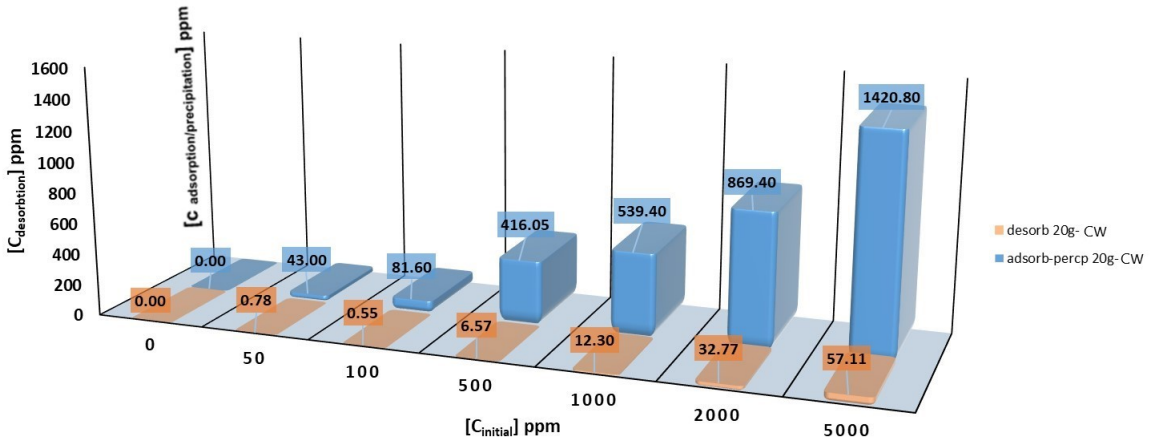

Figure 5.14: Desorption versus adsorption/precipitation for FL1-DETA/CW— 20g sand

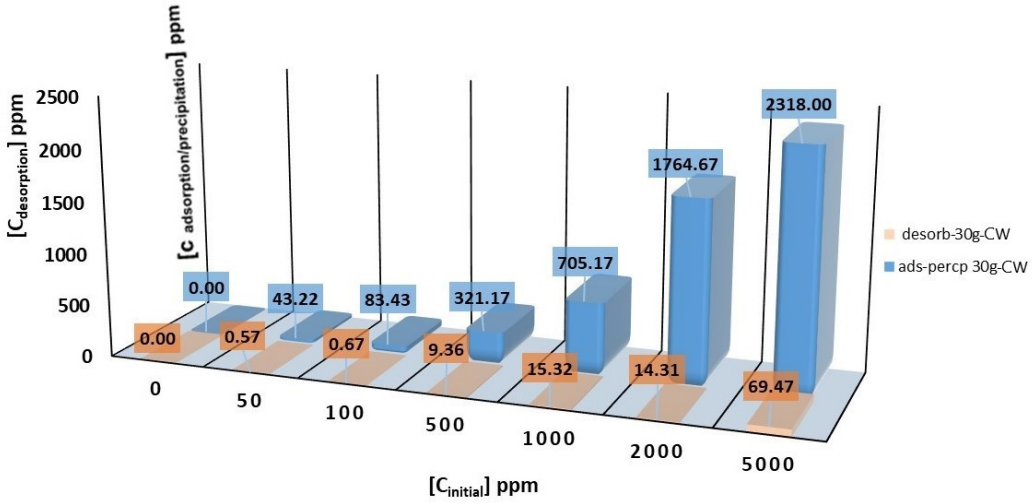

Figure 5.15: Desorption versus adsorption/precipitation for FL1-DETA/CW— 30g sand

For better comparison, Table 5.5 presents the results from concentration measurements for all mentioned experiments i.e. coupled adsorption—precipitation, desorption and compatibility test where pure precipitation is measured. It can be seen that very similar changes occur in the [FL1-DETA] in both cases of with and without sand. This means that the presence of sand for FL1-DETA does not make a very significant dif-

ference as compared to the changes in the [FL1-DETA] in the compatibility test. In another words, no significant adsorption on the sand particles can be justified. Using the equations 5.2 and 5.3, the pure adsorption is only about 3 ppm for 50 ppm and 100 ppm initial concentrations and not more than 20 ppm for $C_{initial} = 500$ ppm. This might rout to the fact that FL1-DETA acts as hydrogel and also forms an incompatible precipitate which will later be discussed in detail at section 5.2.2.

Table 5.5: Result of concentrations measurement for FL1-DETA/CW static jar tests

	10 g	20 g	30 g	Compatibility test	10 g	20 g	30 g
$C_{initial}$ (ppm)	$C_{adsorption/precipitation}$ (ppm)			$C_{pureprecipitation}$ (ppm)	$C_{desorption}$ (ppm)		
50	40.5	44.2	43.3	43.2	0.4	0.8	0.6
100	83.2	85.8	86.5	88.9	0.8	0.5	0.7
500	266.5	418.1	345.7	296.7	4.5	6.6	9.4
1000	429.9	630.1	595.2	-	9	12.3	15.3
2000	362	442.7	1182.8	-	10.4	32.8	14.3
5000	261.7	108.4	1587.5	-	31.3	57.1	69.5

As Table 5.5 indicates for $C_{initial} = 100$ ppm, despite the fact that all three masses of sand show the same amount of $C_{adsorption/precipitation}$, pure precipitation results from compatibility test reveals that the average amount of $C_{adsorption/precipitation}$= 85ppm is mostly precipitation and only 6ppm of this amount is adsorbed. The calculated pure adsorption is equal for both $C_{initial} = 100$ ppm and 50 ppm. Regarding the desorption results show that, for all values of initial concentrations, less than 1.2% of adsorbed/precipitated FL1-DETA was released and detected at desorption test. In other words, irrespective to the initial concentration, only less than average amount of 10 ppm of [FL1-DETA] shows a pure adsorption on the sand that is irreversible and the rest is coupled with precipitation that does not show a high solubility under static conditions during 24 hours.

$$C_{adsorption/precipitation} = C_{initial} - C_{eq} \tag{5.2}$$

$$C_{pureadsorption} = C_{adsorption/precipitation} - C_{pureprecipitation} \tag{5.3}$$

5.2.2 FL1-DETA in NaCl 3.5%—sand

The apparent adsorption isotherms of SI in NaCl 3.5% brine at room temperature are plotted in Figure 5.16 for initial concentration values stated in Table 5.2. Figure 5.16 divides into two parts of $C_{initial} \leq 1000ppm$ and $C_{initial} \geq 1000ppm$. For

$C_{initial} \leq 1000ppm$ a clear pure adsorption region of more than $>$ 4 mg/g can be seen, whereas after that at $C_{initial} \geq 1000ppm$ coupled precipitation/adsorption governs.

The same explanations as for FL1-DETA/CW—sand isotherms in previous section, are applicable for the H—type isotherms of FL1-DETA/NaCl 3.5%—10 g and 20 g. However, FL1-DETA/NaCl 3.5%— 30 g is an S-type curve. All three isotherms belong to sub class 4, nevertheless, FL1-DETA/NaCl 3.5%—20 g belongs to mx subclass. All three FL1-DETA/NaCl 3.5%—sand isotherms (10 g, 20 g and 30 g), start with a slightly bigger region of pure strong adsorption(>0.4 mg/g) as compared to FL1-DETA/CW—sand. Based on research by Kahward[114], this pure adsorption region can be clearly seen for 20 g and 30 g sand isotherms for up to $C_{initial}$ = 1000 ppm.

As the concentration increases, the dependence of (m/V) appears by showing different slopes for each curve that eventually reach a significant plateau indicating the formation of a multilayer or SI—SI interaction into its maximum capacity. In the current case, as the steep slope of all three graphs (10 g, 20 g and 30 g) differs from one another, this can be a sign of aggregation and high interaction of SI—SI in the formed layers as the isotherm is governed by precipitation[114]. Interestingly, FL1-DETA/NaCl 3.5%—30 g shows an S-type shape isotherm which indicates a vertical orientation tendency of the FL1-DETA chains in a higher concentration, if adsorbed on the sand this provides more available sites on the sand for adsorption [174], otherwise it can be interpreted as aggregation of the SI.

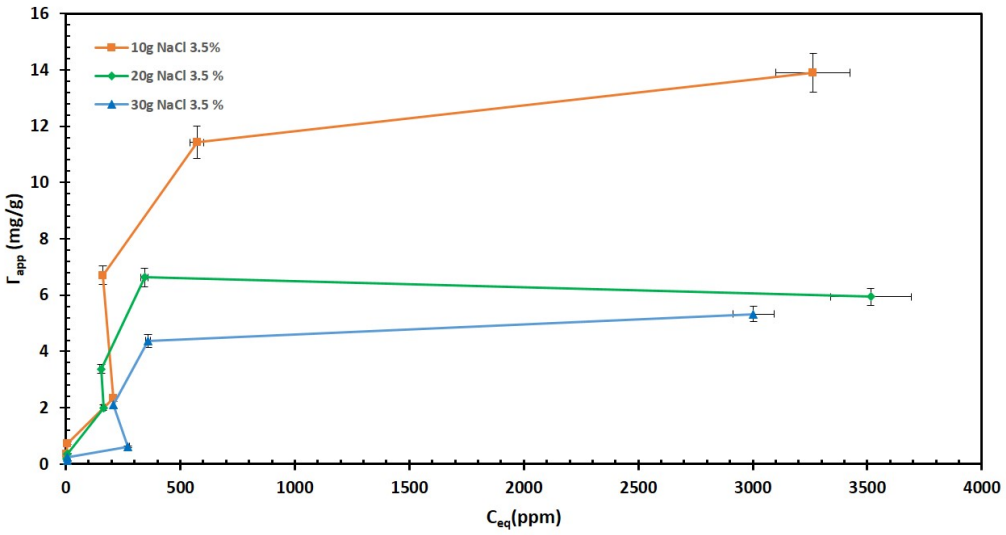

Figure 5.16: Apparent adsorption isotherm for FL1-DETA in NaCl 3.5%. C_{eq} represents the concentration of the solution after 24 hours which is the FL1-DETA that is neither absorbed nor precipitated. $C_{initial}$ are 50 ppm, 100 ppm, 500 ppm, 1000 ppm, 2000 ppm and 5000 ppm that are marked on each graph in an increasing order

It is worth noting that in the compatibility test of SI with NaCl 3.5%, no visual precipitation like as the one for FL1-DETA/CW was seen section 5.1.2. It was explained earlier in Chapter 4, that FL1-DETA is a water soluble polymer and schematic of its 3-dimensional structure was presented in Figure 1.3. Referring to the literature presented in Appendix A.4, water soluble polymers could create a hydrogel structure, especially, if they possess or achieve a 3-dimensional structure. A physically cross-linked nanostructured hydrogel can be prepared by varying :

1. pH
2. Using additional molecule to increase the polymer-polymer interaction like as:
    - Hydrogen bonding
    - Complex coacervation [1]
    - Ionic interaction

Hydrogen bonding is provided by DETA in the structure of FL1-DETA and in case of FL1-DETA/CW precipitation, complex coacervation could be possible through bonding with Ba^{2+} that is appearing as hydrogel (gel-like polymer) sinking in the bottom of the beaker due to the increase in density caused by Ba^{2+} cations. The formed hydrogel has a white colour that might be caused by Ba^{2+} bonding with SO_3^{2-} groups and as was explained forming $BaSO_4$ structure that cause a visible precipitation. In the case of FL1-DETA/NaCl 3.5%, there are no opposite charge cations bonding with the SI structure whereas as explained, the 3D structure itself could help with trapping the water molecules which is intensified by the ionic interactions in the solution. As there are no foreign elements intruding the FL1-DETA structure, the hydrogel might be formed with the same colour of the solution while floating and not sinking properly at the bottom of the beaker due to the lack of increase in density. Thus, the formed hydrogel that was not visible to the bare eyes, is detected by coupled adsorption/precipitation test.

5.2.2.1 Desorption measurements

Desorption tests were conducted in the same procedure as FL1-DETA/CW—sand. Results are graphed in Figure 5.17, 5.18 and 5.19. As can be clearly seen from these graphs only few ppm of what was adsorbed/precipitated, desorbed. For better comparison, Table 5.6 presents the results from concentration measurements for all mentioned experiments i.e. coupled adsorption/precipitation, desorption. It is clear that all three sand samples (10 g, 20 g and 30 g) are showing the same values of $C_{adsorption/precipitation}$.

[1] Complex coacervation can be formed when ionic polymers cross-link by the addition of a multivalent ion of opposite charges to a polyelectrolyte solution [175]

5. FL1-DETA BEHAVIOUR IN FULL BRINE WITHOUT H_2S

Regarding the low quantities detected in the desorption column, there is a high possibility that the floating pre-explained hydrogel was removed from the beaker while sample preparation as it did not sediment properly nor adsorbed, hence, very low amounts of FL1-DETA are traced for each beaker.

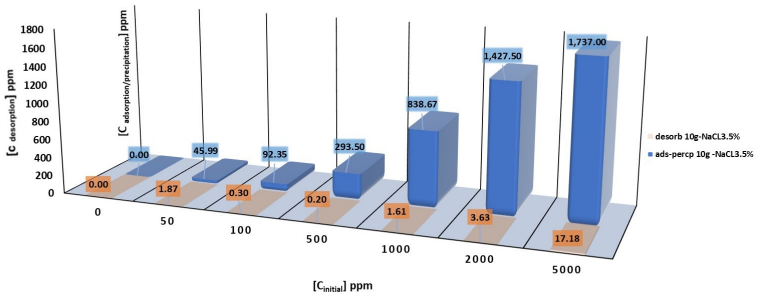

Figure 5.17: Desorption versus adsorption/precipitation for FL1-DETA/NaCl 3.5%— 10 g

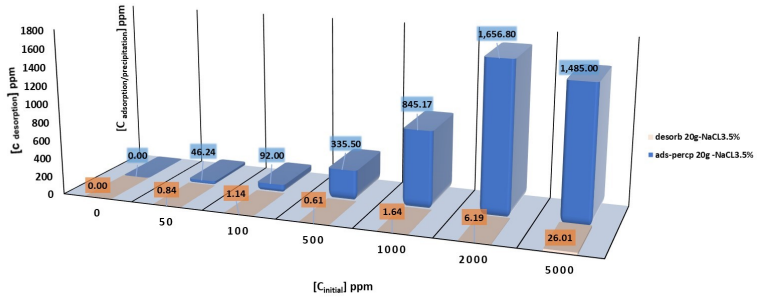

Figure 5.18: Desorption versus adsorption/precipitation for FL1-DETA/NaCl 3.5%— 20 g

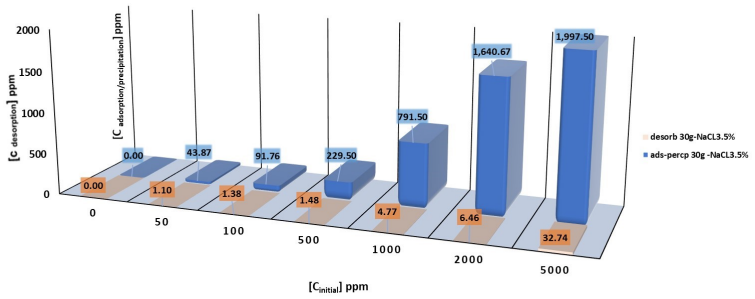

Figure 5.19: Desorption versus adsorption/precipitation for FL1-DETA/NaCl 3.5%— 30 g

Table 5.6: Result of concentrations measurement for FL1-DETA/NaCl 3.5% static jar tests

	10 g	20 g	30 g	10 g	20 g	30 g
$C_{initial}$(ppm)	$C_{adsorption/precipitation}$(ppm)			$C_{desorption}$(ppm)		
50	46.2	46	43.9	0.8	1.9	1.0
100	92.00	92.3	91.8	1.1	0.3	1.4
500	335	293.5	229.5	0.6	0.2	1.5
1000	845	838.7	791.5	1.6	1.6	4.8
2000	1656	1427	1640	6.2	3.6	6.4
5000	1485	1737	1997	26.0	17.2	32.7

5.3 Summary

FL1-DETA has showed a positive outcome in ageing tests above at 250 °C and tube blocking tests based on the provided patent [12] whilst it was tested at concentrations below 30 ppm. Results from Chapter 5 shows that FL1-DETA is concentration sensitive, and by increase in the concentration the incompatibility with CW stream becomes a remarkable feature of FL1-DETA. This has paramount importance as typically the SI concentration in the injection stage of a squeeze treatment is ≈ 5000 ppm or more.

Furthermore, it is shown that this incompatibility affects the release of the scale inhibitor in duration of 24 hours as it is forming a dissoluble/low soluble complex with the cations available in the CW composition. Based on observations, an assumption is proposed that the FL1-DETA is building a complex with Ba^{2+} forming a precipitation with morphology of sphere bead shapes. The beads have diameter of less than 1 micron that leads to a hypothesis of nano structured $BaSO_4$ configurations that are wrapped within the organic polymer, whereby, the XRD graph of this precipitation shows a strong resemblance to the nano structure $BaSO_4$ published by Meagher *et.al* [167]. However, this is only an assumption which needs further investigation specially

as the FL1-DETA/NaCl 3.5% samples show more or less the same amounts of coupled adsorption—precipitation as FL1-DETA/CW. SI/NaCl 3.5% samples represent lower amounts of dissolution in 24 hours time frame compared to which recorded for FL1-DETA/CW where interestingly there are no cations in the system to cause any kinds of complex formation. Hence, it is believed that there maybe a synergistic outcome of different factors such as hydrogel formation, polymer nature and complex formation resulting in poor retention behaviour of FL1-DETA.

CHAPTER 6

Overcoming the incompatibility

Introduction

Results from Chapter 5 indicates that possible causes for FL1-DETA showing low adsorptions on sand particles routs to:

1. Ba^{2+}—complex formation (incompatibility with the brine)
2. Hydrogel formation (incompatibility with the brine)
3. Polymer nature (possessing many negative functional groups)

As explained in Chapter 5, 3-D structure of FL1-DETA caused by short chains of DETA is responsible for hydrogel formation. Since FL1-DETA is constructed from two separate sites i.e. FL1 and DETA, the SI was deconstructed and DETA part as short cross linking chains was removed whilst FL1 as the main structure was retained. By this means, FL1 will only be simple polyelectrolyte possessing negatively charged functional groups of —COOH and —SO_3H with no hydrogel formation issue.

Based on previous research works, for FL1 adsorption on sand particles, positively charged functional groups are also needed. Hence, in this Chapter, the aimed are:

- Find a solution to the incompatibility of the SI with the main production brine.
- Modify the structure for better adsorption properties on sand samples by adding positively charged functional groups.

6.1 FL1 compatibility with production water components

FL1 on its own, shows good thermal stability until 200°C and can inhibit ZnS formation to some extent by dispersing the scale through repulsion[1] [12]. However, this co-polymer has a very low affinity to sandstone due to its intrinsic negative zeta potential. As was expected from the chemical structure, FL1 showed a significant incompatibility whilst mixed with the saline production brine. This finding is also in line with FL1-DETA incompatibility with CW that is caused by Ba^{2+} and —SO_3H complex formation that was explained in Chapter 5. By possessing a sulfonyl acid group on its structure, FL1 at concentrations above 30 ppm complexes with the Ba^{2+} present in CW and forms an insoluble deposit. Nevertheless, deposits are less jelly-like as no hydrogel is formed due to the absence of DETA. Figure 6.1 (a) and (b), show the compatibility test of FL1 on its squeeze concentration of 1000 ppm in full CW at room and elevated temperature, respectively. Figure 6.1 (c) and (d) show its compatibility with sea water(SW) and CW containing no Ba^{2+} concentrations.

[1] Please refer to Chapter 1 for the explanation

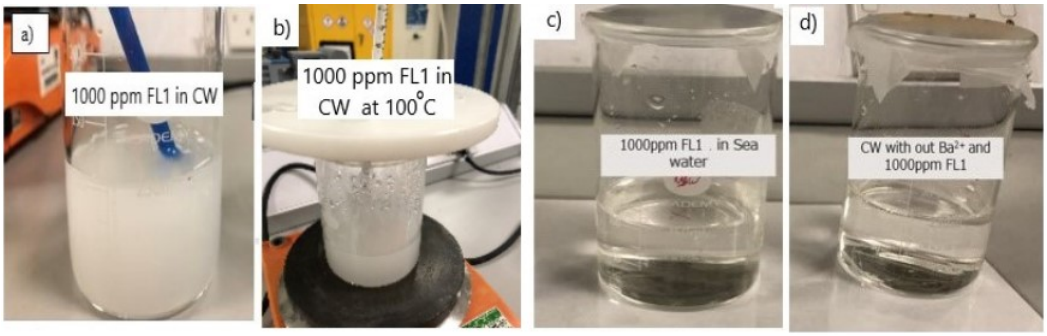

Figure 6.1: Incompatibility of 1000 ppm FL1 with CW. a) Room temperature, b) at 100°C, c) FL1 in SW, d) FL1 in CW without [Ba^{2+}]

6.2 Finding a threshold for barium

As FL1 shows complete compatibility with other cations present in CW composition with the exception of Ba^{2+}, [Ba^{2+}] was reduced step wise to identify a threshold value for compatibility. Results indicate, any small amount of [Ba^{2+}] leads to incompatibility of FL1 with the brine at concentrations above 1000 ppm, whereby the highest [Ba^{2+}] compatible with 1000 ppm FL1 was found to be 2.454 mg/L i.e. 1000 times less than actual amount of [Ba^{2+}] present in CW. Photographs of this visual comparison is presented in Figure 6.2.

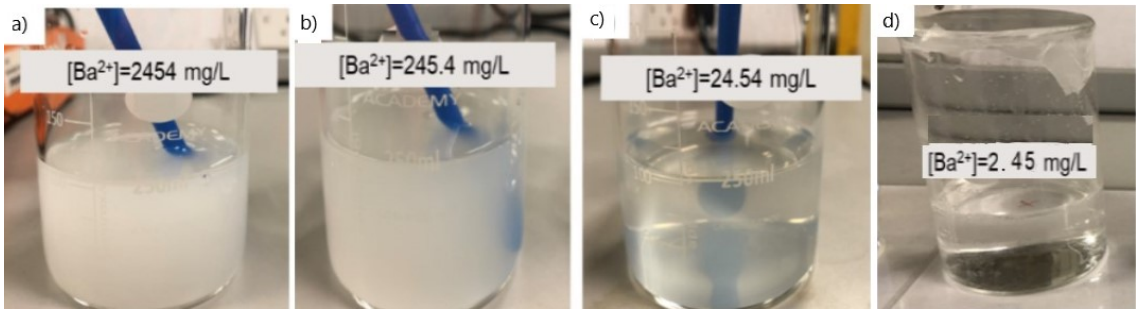

Figure 6.2: Sourcing incompatibility at 1000 mg /L FL1-DETA FL1-DETA in CW with reduced [Ba^{2+}] a) 2454mg/L, b) 245.4 mg/L, c) 24.54 mg/L, d) 2.454 mg/L.

6.3 Making blends of FL1 with other industrial SI

Based on Shaw *et.al* [176] blend of organic polymers and phosphonate inhibitors, can perform as synergistic inhibition outcome. Such inhibitors are referred to as blended scale inhibitors which exhibit better behaviour compared to single inhibitor [87]. Therefore, numerous attempts were made to control the incompatibility caused by barium complex formation through this method, i.e. blends of inhibitors. The initial idea

was to entrap the barium with other chemicals that are routinely used in industry for $BaSO_4$ inhibition [173]. To this end, PPCA and DETPMP were used in different concentrations with FL1 as a mixture. It is worth noting that PPCA does not have a high thermal stability to be applied at HTHP conditions as it cannot withstand high temperatures such as 196°C, as it decomposes.

6.3.1 FL1 blended with DETPMP

DETPMP inhibitor showed severe incompatibility with high saline CW on its pure concentration. Similar to FL1 behaviour, DETPMP turned the CW cloudy at any concentrations. Figure 6.3 depicts this incompatibility. Hence, blending and mixing DETPMP with FL1 was not proceeded any further.

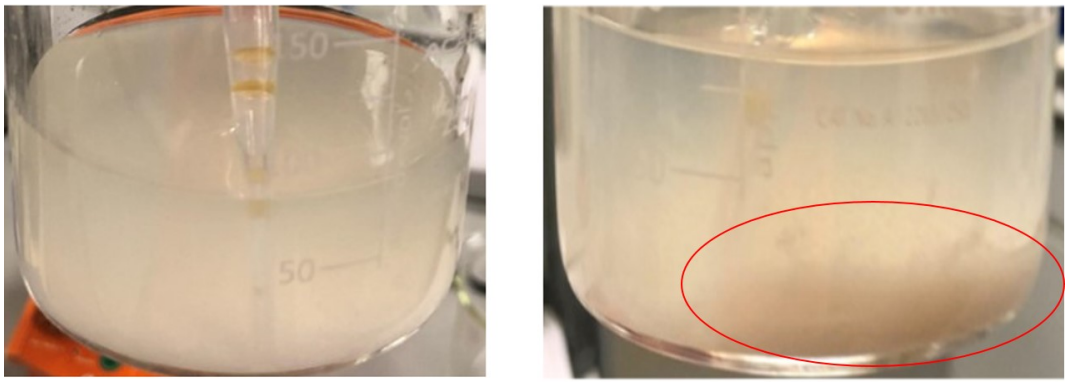

Figure 6.3: 1000 ppm DETPMP in CW. The mixture showed pure incompatibility by getting cloudy and forming deposits.

6.3.2 FL1 blended with PPCA

Figure 6.4 (a) shows the compatibility test for PPCA with full CW, whereas Figure 6.4(b) presents a 1000 ppm PPCA in 2.4 mg/L $BaCl_2$ solution. These results do not indicate compatibility nor incompatibility. In fact, the inhibitor has contracted and deposited at the bottom of the beaker due to the high salinity and has become ineffective.

By 4 times reducing the salinity of the solution, PPCA showed complete compatibility with CW. Therefore, for making a compatible blends of FL1 with PPCA two separate test methods were suggested:

1. Pre-mixing 1000 ppm PPCA with 5000 ppm FL1 in a separate beaker followed by adding the mixture to CW.

2. Introducing 1000 ppm PPCA in 4 times diluted CW and adding 1000 ppm FL1 afterwards.

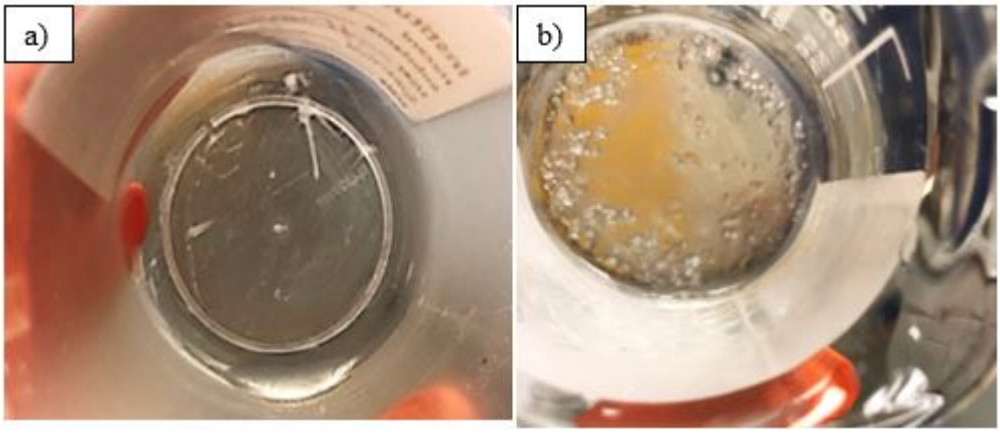

Figure 6.4: PPCA compatibility test with CW. a) 1000 ppm PPCA in CW contracted at the bottom of beaker, b) PPCA in 2.4 g/L $BaCl_2$, forming salt complexes.

Both methods of preparation were unsuccessful as none of the above test methods showed compatibility with the brine. Figure 6.5(a) shows the compatibility test results of method 1, where the blended chemical curdled as soon as was introduced to the full CW, even though it was premixed stage was prolonged for 30 minutes.

Figure 6.5 (b) shows the results from the second method. The clear solution of diluted CW and PPCA gradually got cloudy after adding the PSS-*co*-MA in less than 10 minutes and formed deposits. Considering the incompatibility results, the PPCA low thermal stability and the diluted CW which would be far away from the reality, the idea of making blends with other scale inhibitor was found to be unsuccessful.

6.4 Development and characterisation of PSS-*co*-MA—PANI composite

Working at Ba^{2+} threshold could only solve the FL1- CW compatibility for laboratory tests and not in the actual field, furthermore, the low affinity of FL1 to the sandstone is still remained. Thus, structural modification of FL1 is needed.

To this end, the number of sulfonyl acid groups on PSS-co-MA structure should be minimised whilst properties such as thermal stability and water solubility be considered. Hence, FL1 was replaced with FL1b that has the same chemical composition, however, with equimolar ratio of carboxylic acid and sulfonyl groups. Replacing FL1 with FL1b helps to reduce the amount of sulfonyl groups and increasing the -COOH groups that are responsible for inhibiting scale. Furthermore, by having less $-H_2SO_3^-$ functional groups on the structure, there will be fewer active sites available for barium to form an insoluble complex with. On the next step, FL1b was doped with PANI. This

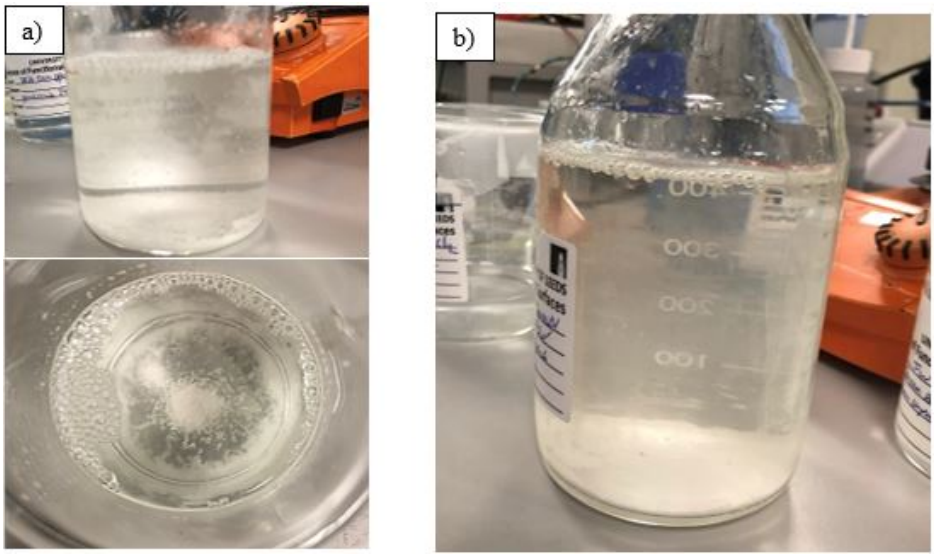

Figure 6.5: Compatibility test of PPCA-FL1 blend with CW. a) Method 1, b) Method 2. Both methods showed incompatibility in less than 24 hours.

will add positive charges to the structure of the SI and improves its thermal stability as well as affinity to the sandstone. Furthermore, PANI contains spacious benzene rings which would also constrain barium approaching sulfonic acid groups through hindrance effects.

However, PANI in its positively charged state (Emraldine slat) is not soluble in water and in best scenarios only forms a dispersion which is not stable for more than a couple of hours. Many attempts have focused on the improvement of PANI processability in the past severeal years, such as substitution of the aromatic ring of polyaniline with methyl (-CH_3) [177], methoxy(-OCH_3), sulphonate (-SO_3) [178], or long alkyl chain [178] which were found to lead to a higher solubility in organic solvents and even in water. However, while the addition of side-groups enhances PANI solubility and processability, the electrical conductivity is reduced because of steric hindrance, increase of interchain length and decreased conjugated length [179, 120]. Using sulphonation methods, Yang et al. [180] reported the synthesis and characterisation of cytocompatible sulfonated polyaniline (SPANI) copolymers with different sulphonation degrees. It was observed that the synthesised SPANIs were insoluble in water as well as chloromethane (CH_3Cl), and toluene. However, they could be dissolved in dimethylformamide, dimethyl sulfoxide, and N-Methyl-2-pyrrolidone (NMP), with NMP as the best solvent for all aforementioned [180]. Later, Meriga *et.al* [181] improved the water solubility of SPANI by forming a composite with reduced graphene oxide which increased the charge storage capacity of SPANI, however, this means that for making PANI soluble SPANI firstly should be synthesised, and such a procedure is lengthy/time consuming. Other sulphunation techniques like externally doped sulfonated polyaniline

(ED-SPANI) [182, 183], also showed high solubility in water but very low conductivity properties. Liu and coworkers [184, 185] produced a water soluble PANI polyelectrolyte by using polystyrenesulphonate (PSS) linear template, through a complicated enzyme polymerisation method. However, the highest conductivity of 10^{-2} S/cm^{-2} was only achievable at high temperatures (120-150°C) or with additional HCl doping. Interestingly, the same complex prepared through oxidation polymerisation was not soluble in water [186].

This work describes the synthesis of a sulphonated PANI composite that remains actively conductive without extra HCl doping at ambient conditions. Most of the previous publications have either neglected to discuss the thermal stability of the final product or sacrificed it [181, 187] for more conductive and soluble end product. However, in this work, we are proposing a simple oxidation polymerisation of PANI at room temperature doped with (sulphonated polystyrene-co-maleic acid) PSS-*co*-MA that results in a water soluble composite up to 2.5 g/L, with high thermal stability and medium conductivity properties (0.3-0.7 s/cm at 3000 ppm and room temperature), at both acidic and neutral pH range pH = 2-7. It will be shown that, forming a composite of PANI with PSS-co-MA, helps PANI to stably disperse in aquas medium due to the presence of -$H_2SO_3^-$ groups.

All samples prepared were compared through:

- ICP/OES and AAS analysis: to measure the amount of cation concentration, especially Zn and Pb entrapment by the modified inhibitor.
- SEM /EDX: To identify the morphology of the synthesised PSS-*co*-MA—PANI composite and the adsorption/retention of the SI on the sandstone
- FTIR: Characterisation method for identification of the functional groups on the modified SI structure.
- UV-vis: As characterisation method for PANI as well as concentration measurement for adsorption/desorption process.
- TGA analysis: To measure the thermal stability of the modified SI.

.

Characterisation of PSS-*co*-MA—PANI samples

6.4.1 Morphological Analysis

SEM image of pure PANI produced based on Table 3.1 specification is shown in Figure 6.6 (a). There are multiple factors that can affect the morphology of oxidative polymerised PANI, such as temperature, time, [Aniline], [APS], [acid], pH, type of acid and even stirring speed [186, 188, 189, 190, 191, 192, 193]. As a result, all above factors were considered through synthesis of PSS-*co*-MA—PANI.

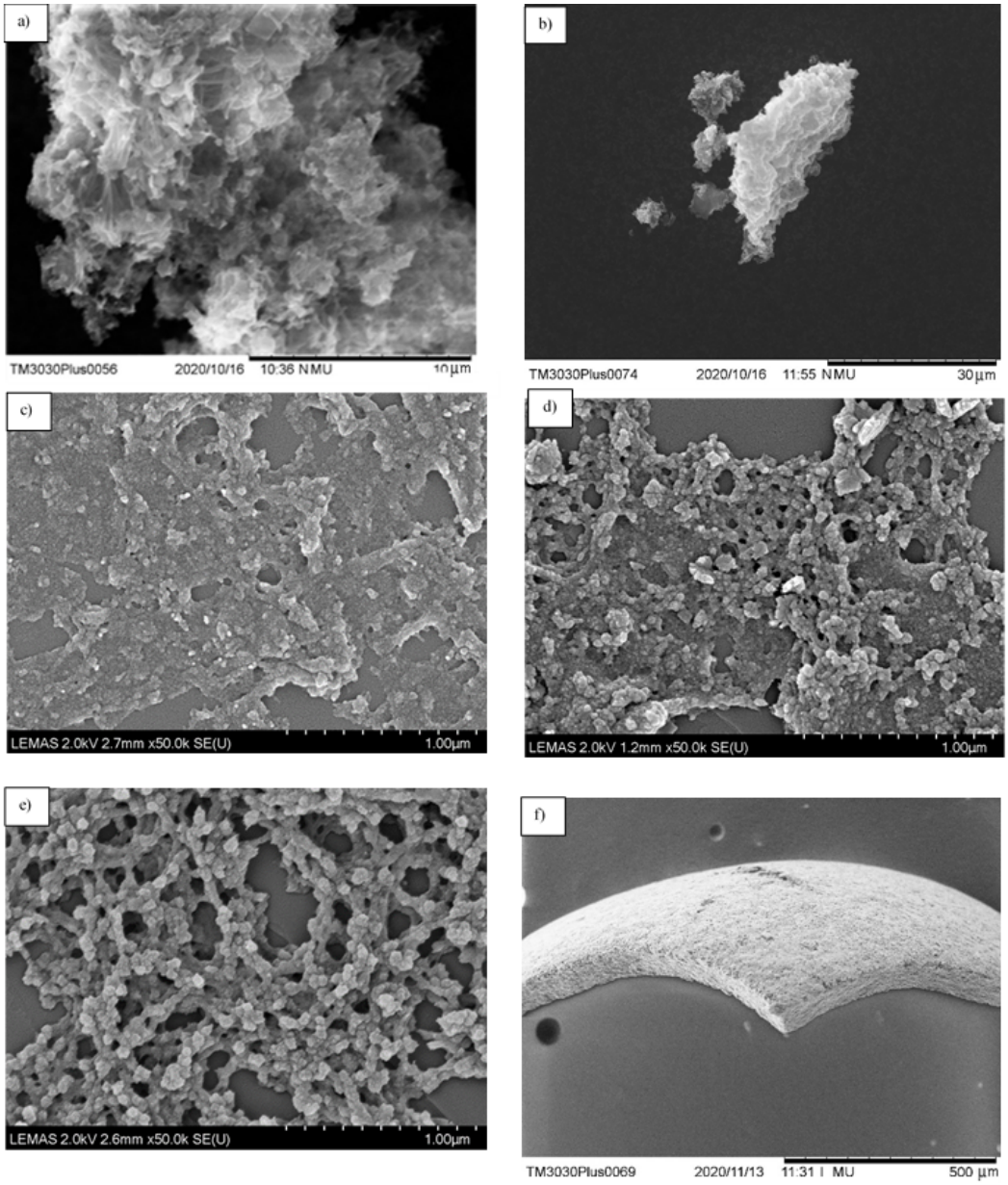

Figure 6.6: SEM micrographs of PSS-*co*-MA—PANI with different acid ratios. a) PANI, b) X/5-5, c) X5-5, d) X10-5, e) X10-6, and f) X10-20

For successful doping of FL1b (PSS-*co*-MA) on PANI structure, different mixing sequences of FL1b with polyaniline were tested and the effect on morphology was investigated. Figure 6.7, shows SEM images of sample P(Anilne + FL1b) where aniline monomer was mixed with PSS-*co*-MA in 20 ml of HCL (1M) before APS was added to the mixture. Even though protonated aniline monomers were firstly in contact with

PSS-*co*-MA and were later polymerised, BSE micrographs show two separate polymeric phase that are randomly dispersed and not blended evenly.

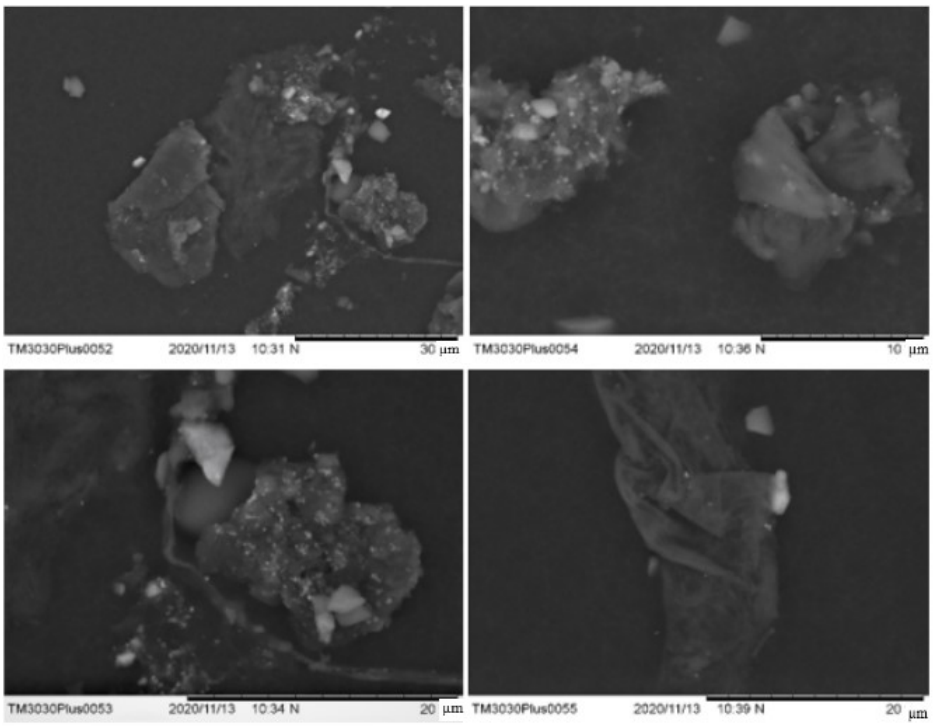

Figure 6.7: Back scattered SEM images of P(Aniline+FL1b). The Two polymers formed randomly dispersed separate phases

Figure 6.8, shows SEM images of sample PANI→ FL1b. For this sample, as a pre-step PANI was fully polymerised and later was mixed with FL1b for 20 minutes on a medium speed at room temperature. As it can be seen in Figure 6.8, SEM images indicates not much of a difference compared to the previous sample, i.e. random dispersion of two polymeric phase.

However, for samples labelled with X and AA, LBL (Layer-by-Layer) polymerisation assembly method was used, whereby, FL1b is introduced to the mixture couple of minutes after EB- PANI is formed, yet PANI was not fully polymerised [136]. By this means, PANI will use the 2D structure of FL1b as a template [194] and layers on top whilst polymerising, forming a PSS-*co*-MA—PANI composite which is an LBL assembled film. Effect of Aniline/APS, Aniline/FL1 and HCl/Water ratio on morphology of these LBL films were also analysed by SEM. In general, the thickness of these formed thin films varies with the amount Aniline/APS ratio. By decreasing the amount of APS, less Aniline would be oxidised to form polyaniline which leads to thinner and shorter PANI fibres and thinner PSS-*co*-MA—PANI films, Figure 6.9.

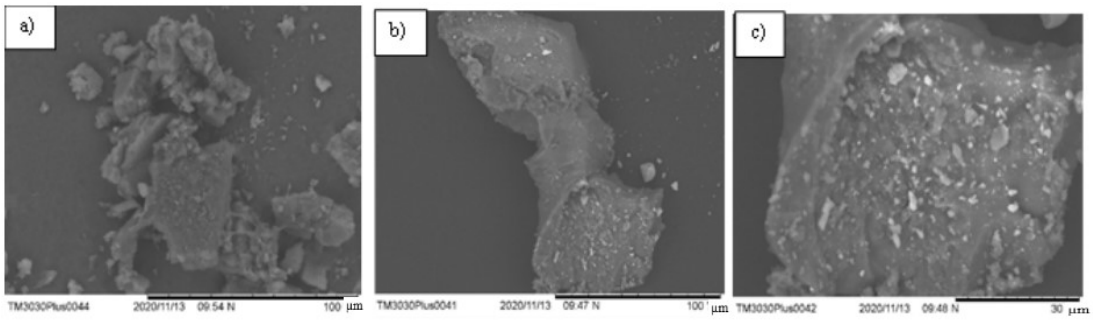

Figure 6.8: SEM images of PANI→FL1b. a) SE, b) BSE, c) BSE at higher magnification

Figure 6.6 (b) shows the morphology of X/5-5 sample. Compared to pure PANI, it is clear that in X/5-5 sample, PANI has benefited from PSS-*co*-MA as a template and polymerised chains have grown in a 2D direction along with the template [194] forming a LBL PSS-*co*-MA—PANI composite. This effect becomes more pronounce as the Aniline:PSS-*co*-MA ratio increases.

As depicted in Figure 6.6 (b-d), increasing the amount of PSS-*co*-MA, resulted in more available smooth 2D template structures for aniline monomers leading to organised and polymerised PANI. The Aniline/ HCl ratio effect on the morphology of PSS-*co*-MA—PANI composite is more delicate. HCL, in aniline polymerisation, is responsible for protonation of aniline that could be later oxidised with APS. On the other hand, HCl affects pH and dissociate the sulfonyl groups located on PSS-*co*-MA polyelectrolyte (pKa$<3 = 0.7$). This means that for forming an LBL composite, an optimal amount of HCl would be needed to help with the proper arrangements of the functional groups on either of the two focusing polymers, otherwise the chances for crosslinking would increase as it is shown for X10-6 Figure 6.6 (e). Furthermore, the micrographs show that this could also occur by increasing the amount of the dopant (PSS-*co*-MA). As a result, X10-5 PSS-*co*-MA—PANI composite, Figure 6.6(d) has less continuous morphology spread along the substrate, forming a web shape structure with voids as compared to X5-5 Figure 6.6 (c). This could be interpreted by the total amount of available acidic functional groups in the reaction media as PSS-*co*-MA itself has acidic functional groups on its structure that could compensate for the lack of enough HCl for the synthesis to protonate the nitrogen containing backbone of PANI whilst doping. Figure 6.6 (f) shows the compacted morphology of X10-20 caused by excess HCl and corsslinking. As it will be shown in both FTIR and stability sections, an increase in the amount of HCl will, not only have a direct effect on water dispersion of the samples, but would also change the FTIR spectra. This is mainly due to the fact that the carboxylic acid and sulfonyl acid groups of PSS-*co*-MA, that could form hydrogen bonds with the water, are occupied and cross linked to the already activated nitrogen atoms on PANI structure.

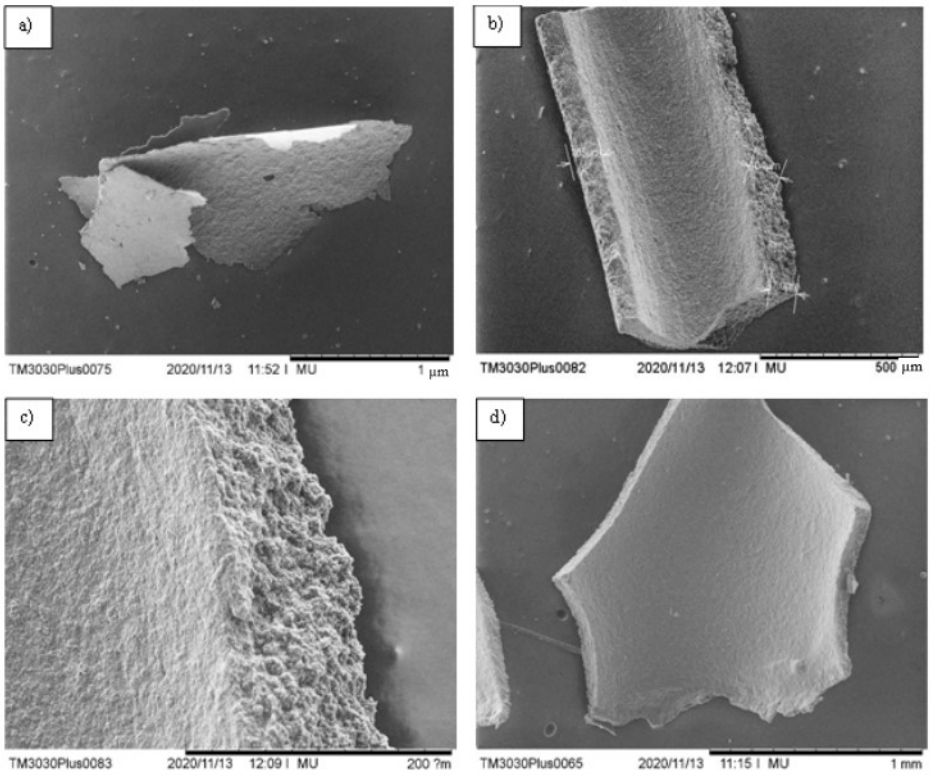

Figure 6.9: SEM micrographs FL1b-PANI with different ratios of Aniline/APS. a) AA-2, b) AA-3, c) AA-3, d) AA-4

6.4.2 FTIR

FTIR analysis of PSS-*co*-MA—PANI, pure PANI and PSS-*co*-MA samples are presented in Figures 6.10 and 6.11. The FT-IR spectra of PANI depicts the vibrational peaks around 3400–3200 cm^{-1} corresponding to N-H stretching vibrations, with C-H stretching vibrations observed around 3100–2800 cm^{-1} [136]. The broad band in the region 2800–2300 cm^{-1} interspersed with several small vibrational peaks indicates the presence of iminium sites with dopant ions on PANI matrix [195, 196].

PSS-*co*-MA has its own distinctive bands at 3380 cm^{-1} and 1010-1030 cm^{-1} for the–SO_3^- group and 3120, 2720-2350 cm^{-1} and 1910-1760 cm^{-1} for the –C=O group [197]. The peak at 1600 cm^{-1} represents C=C within the aromatic benzene ring, whereas 1310-1240 cm^{-1} is attributed to the bending stretches of –SO_3^- and –COOH [197]. In the lower frequency regions, the peaks around 1100– 1160 cm^{-1} are attributed to the aromatic C-H in-plane deformation [188] which for the case of X10-5 and X5-5

(Figure 6.11), are merged with $-SO_3^-$ bands at 1190-1030 cm^{-1}. The broad intense band at this region is described as the "electronic-like band" [198] and is considered to be a measure of the degree of de-localisation of electrons. In general, for all composite samples, a shift of 200 cm^{-1} to higher wavenumbers is observed for peaks at 1380, 1550 and 1100 cm^{-1}, showing hydrogen bonding of $-SO_3^-$ and –COOH groups with nitrogen on the PANI structure [199]. The characteristic vibrations around 1590–1560 cm^{-1} and 1500–1490 cm^{-1} indicated the signatures of the PANI backbone, arising due to the stretching modes of the quinoid and the benzenoid rings [195, 200]. The peaks around 1300 cm^{-1} are due to the strong aromatic C-N stretching vibrations in PANI [201, 202]. Furthermore, the stretching and bending vibrations around 1600–1500 cm^{-1} in X10-5 are red shifted compared to pure PANI, implying the removal of chloride ions by PSS-*co*-MA from the PANI matrix [189] and the peak at 1708 cm^{-1} in both X10-5 and X5-5 corresponds to the C=O stretching of the dopant PSS-*co*-MA acid.

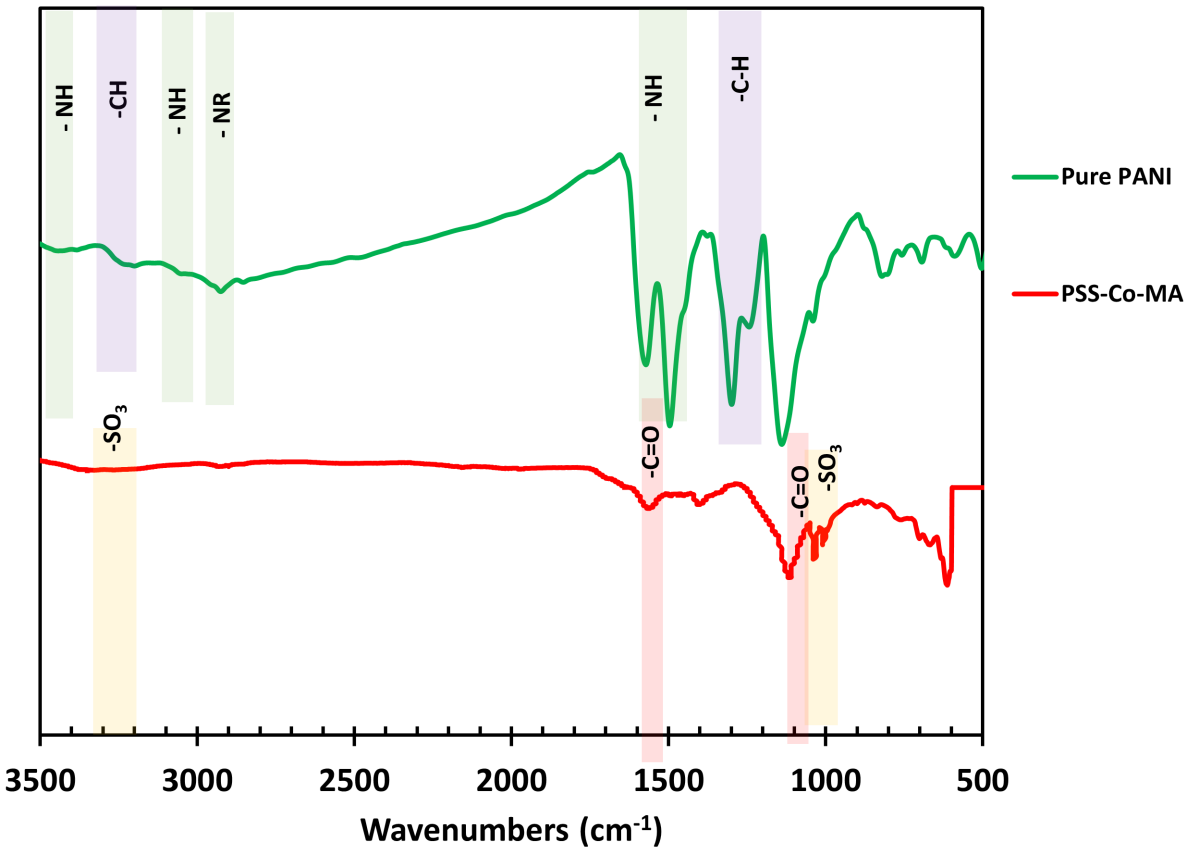

Figure 6.10: FTIR spectra of pure PANI in green and PSS-*co*-MA in red.

Figure 6.11 depicts a clear comparison on FTIR spectra of the samples based on

Aniline:PSS-*co*-MA(dopant) ratio and Aniline:HCl; (acid ratio). It can be clearly seen that for the same Aniline:HCl (wt/ml), the Aniline:PSS-*co*-MA (wt/wt) will not affect the FTIR spectra (sample X5-5 and X10-5), however, for the same Aniline:PSS-*co*-MA (wt/wt) with different Aniline:HCl (wt/ml) that would not be the case and FTIR spectra completely changes, between 2500-1850 cm^{-1}, where the bands broadened for samples X5-5 and X5-20. This can be explained by the extra amount of HCl that can protonate PANI's backbone by forming more positively charged nitrogen [189]. The charged nitrogen presents sites for negatively charged $-SO_3^-$ and –COOH groups to dope with. As a result, the C=O band at 1708 cm^{-1} increases and also shifts slightly to higher wavenumbers due to the electronegativity of N [199]. Bands between 2500-1850 cm^{-1} and at 1100 cm^{-1} broaden, whilst wide bands at 3000 cm^{-1} and 1600-1500 cm^{-1}, which belong to -NH out of plane stretches, start to fade, leading to complete chemisorption of PSS-*co*-MA on PANI backbone.

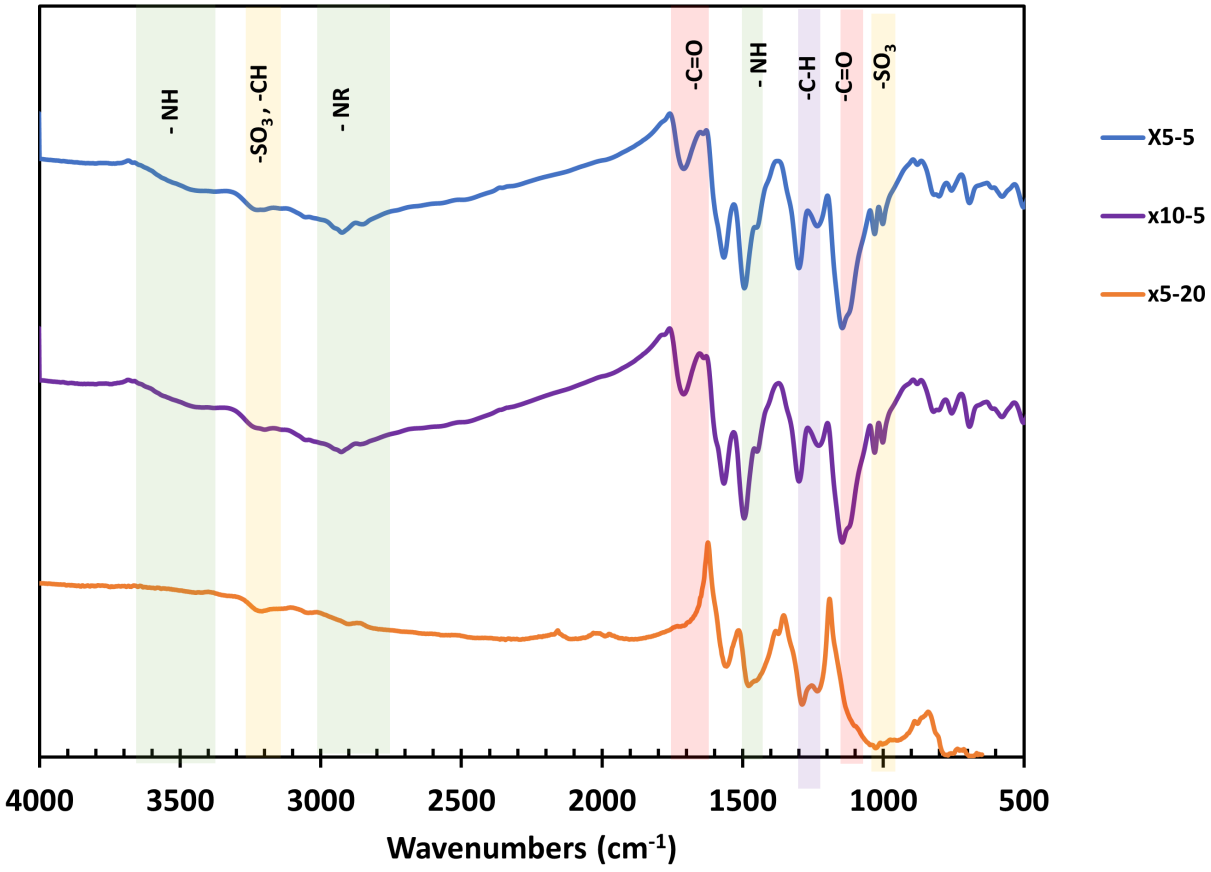

Figure 6.11: FTIR spectra of the samples based on Aniline: PSS-*co*-MA(dopant) ratio and Aniline: HCl, (acid ratio).

Figure 6.12, depicts the effect of Aniline/ APS. Same explanation of the previous samples applies to here which means there is a possibility that PSS-*co*-MA has doped with PANI through its $-SO_3^-$ or COOH groups, hence, the NO_2 stretching vibrations are merged with the C-N stretching band of PANI and bands representing $-SO_3^-$ at 3580 cm^{-1} is missing the OH stretch. Whilst vibrations around 1590 –1560 cm^{-1}1and 1500–1490 cm^{-1} correspond to PANI backbone are broadened [197], the broad peak belonging to PANI at 3000 cm^{-1} can not be seen in any of the AA samples. This might be due to the incomplete polymerisation of Aniline monomer.

FTIR results of composites with Aniline/ HCl = 0.12 and Aniline/APS = 0.2 suggests possible reactions of FL1b on PANI with a possible chemical structure as depicted in Figure 6.13 (a), whereby all crucial functional groups for inhibition are preserved and the structure forms a stable dispersion in aquas medium with high thermal stability. However, for other lower Aniline/HCl or Aniline/APS, the end product will be a resultant if FL1b chemisorption on PANI with more complicated chemical structures such as ones presented at Figure 6.13 (b).

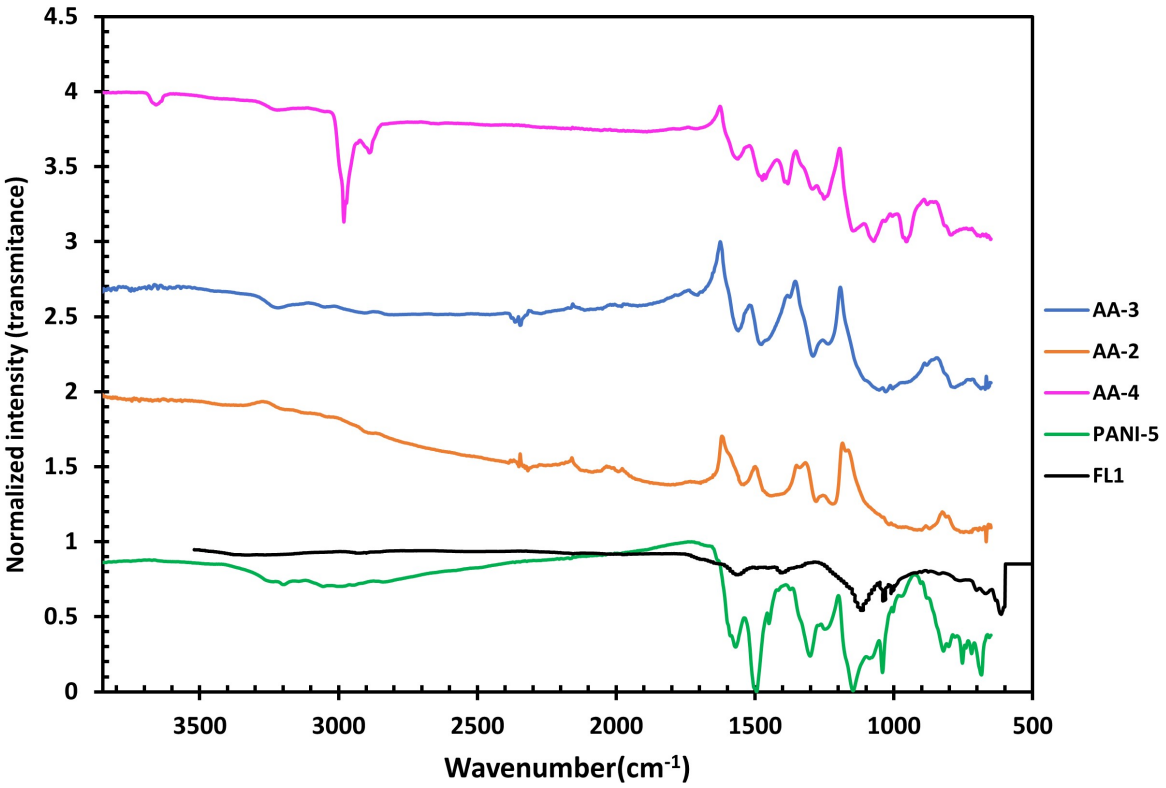

Figure 6.12: FTIR spectra of PSS-*co*-MA—PANI samples for AA series compared to PSS-*co*-MA and pure PANI, effect of Aniline/APS

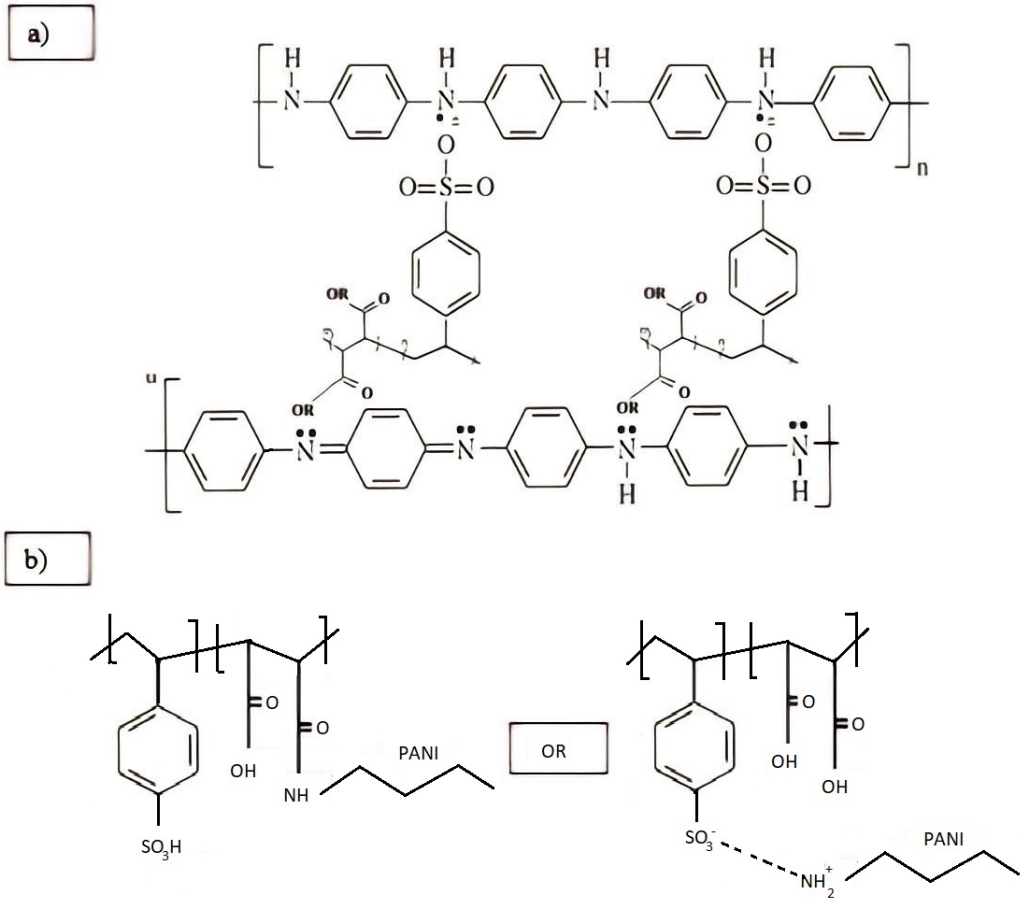

Figure 6.13: Probable chemical structure for a) physiosorbed, b)chemisorbed FL1b-PANI composite.

6.4.3 UV-vis.

The UV–Visible absorption spectra of PANIs generally depend on the level of doping, extent of conjugation, nature of the polymer and solvent. PANI(EB) exhibits two bands around 330–360 nm (B peak) and 600 nm (Q peak) characteristic of two chromophores, representing emeraldine oxidation states. The absorption peaks around 330–360 nm is attributed to the π–π^* transitions in the aromatic rings [203]. However, the absorption bands around 600–650 nm correspond to the intramolecular electronic transitions between quinoid and benzenoid units representing both inter and intra chain interactions which intensity and wavelength can easily be affected by various factors such as molecular mass (MW), solvent, solubility and oxidation level [203]. As a result, in all the PANI salts, the free electron absorption tail is observed in the region of 800–1100 nm that is a characteristic for highly conductive substances [204]. When PANI is doped

with acids, i.e., HCl for pure PANI and PSS-*co*-MA for the composites samples, the quinoid bands exhibit hypochromism as seen in Figure 6.14. This indicates the presence of a random coil configuration in PANI salts (ES) [205]. This shift shows some characteristic low wavelength polaron bands around 400–440 nm that are due to the conductive form of PANIs and this can only be observed with PANI salts. Hence, the effect of PSS-*co*-MA presence in the PSS-*co*-MA—PANI composites, can be correlated with the increase of light absorption around 500nm, the hypochromic effect of 350nm band to 450nm and the tail re-appearance at 800 nm.

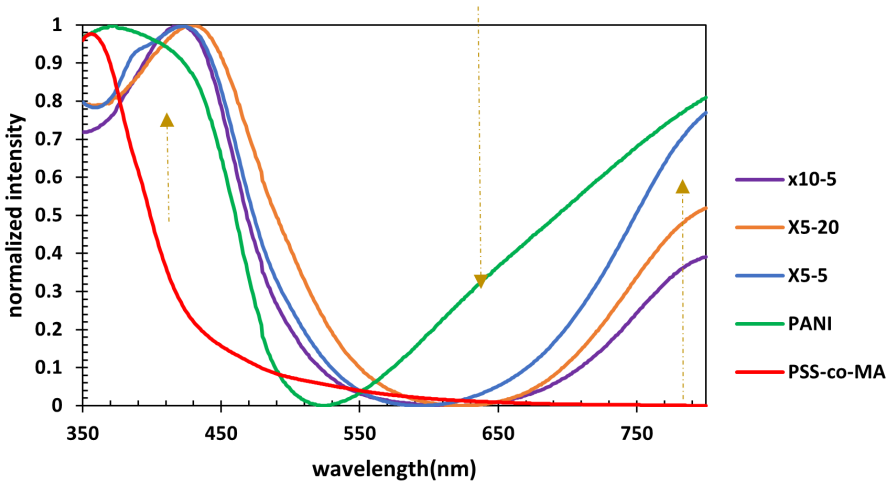

Figure 6.14: Uv-vis spectra of PSS-*co*-MA—PANI composites and PANI. Spectra's trend show the hypochromic effect if PANI rod shape peak from 350nm to 450nm

6.4.4 Aqueous Solution Stability and Conductivity

Although PANI-ES is an interesting conductive polymer with many applications, it does not dissolve in aqueous media. However, through a series of experiments, it was found that by proper design, PSS-*co*-MA—PANI can have a stable dispersion of the composite in DI water for months and still be conductive. Figure 6.15 shows the stability state of dispersed composites in DI water after seven days indicating that samples with 5-6 ml of HCl in their reaction ingredients such as X5-5, X10-5 and X10-6, have the highest periods of stable dispersibility in water up to 2.5 g/L. All samples were also analysed for their conductivity properties. By measuring the conductivity for X5 and X/5 series samples, which only differ with the volume of HCl used, it appears that the conductivity values increase in parallel with the amount of acid used, as depicted in Figure 6.16(a).

Combining stability data and conductivity in Figure 6.16 (b) for pure PANI, X/5-5 as non-dispersible samples in water and X5-5, X10-5 as dispersible samples in water, showed that optimal amount of conductivity, (positive charges) would be needed for

a composite to be stably dispersible in a polar solvent such as water. In fact, it was revealed that having an optimal amount of acid ratio plays a crucial role for dispersing PANI in an aqueous medium, whereas Aniline/APS and Aniline:PSS-*co*-MA help with the formation of composite films through its structure, morphology and conductivity.

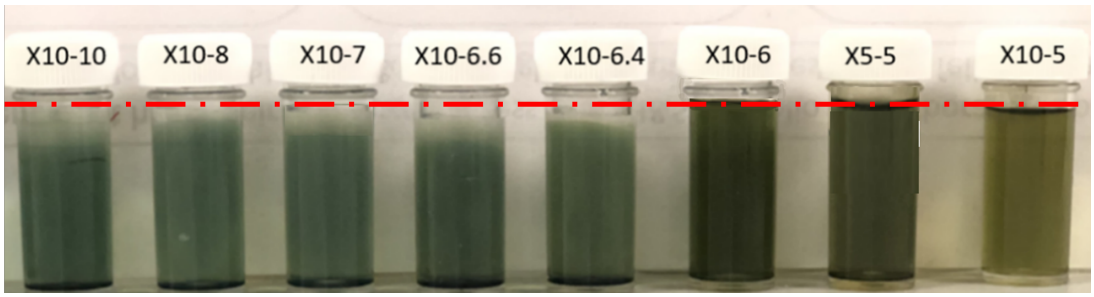

Figure 6.15: Effect of acid ratio on the dispersibility of final product in a one week time frame. X10-5 and X10-6 have the highest stability. The red dashed line is showing the top of the meniscus for all samples.

Previous research has shown that a linear and highly conjugated structure will lead to more conductive forms of PANI. To achieve this, soft [206, 207, 208, 141] or hard templates [209, 210, 211] can be used in the process of PANI polymerisation. To create a guided polymerisation based on soft template configuration, big molecules [179, 212, 184] or polyacids [186] are needed to aggregate and form micelles above a critical concentration whereas small molecules [194], without the ability to form head to tail templates have shown that cannot form a highly conductive PANI. Hence, in order to maintain PANI's electrochemical properties whilst increasing its dispersibility in water, an aggregation of anionic doping species is essential to be used as a template for aligning monomers [213] that can also introduce protonating dopants with dispersibility properties on the structure [165] such as polyacids [186]. A sufficient concentration of HCl improves the positive charge on the PANI backbone by protonating it and helps PSS-*co*-MA to form a template for the 2D PANI sheet. Through polymerisation process at acidic pH, sulfonyl acid and aniline are charged negatively and positively respectively and they form a complex due to the established electrostatic interactions as explained by their respective pKa values of 0.70 and 4.63. As aniline monomers become more ordered and the para-directed reaction is favoured, a linear and highly conjugated structure is produced [184, 213, 178], resulting in conductive and soluble PSS-*co*-MA—PANI composites. On the other hand PSS-*co*-MA free $-SO_3^-$ and carbonyl groups help with the composite dispersibility as a surfactant for the 2D polymerised PANI sheets, along with aligning PANI polymer chains by establishing hydrogen bonds with water molecules. The change in conductivity data between samples X5-5, X10-5 and X5/5 could be explained by the optimal amount of PSS-*co*-MA in X5-5 which helps structural linearisation without extra crosslinkings through functional groups like X10-5. As a rule of thumb, for dispersion of these composite in water, a

minimum conductivity of 2800 μs/cm would be needed, unless the Aniline:PSS-*co*-MA (wt/wt) ratio $\leq$ 0.2.

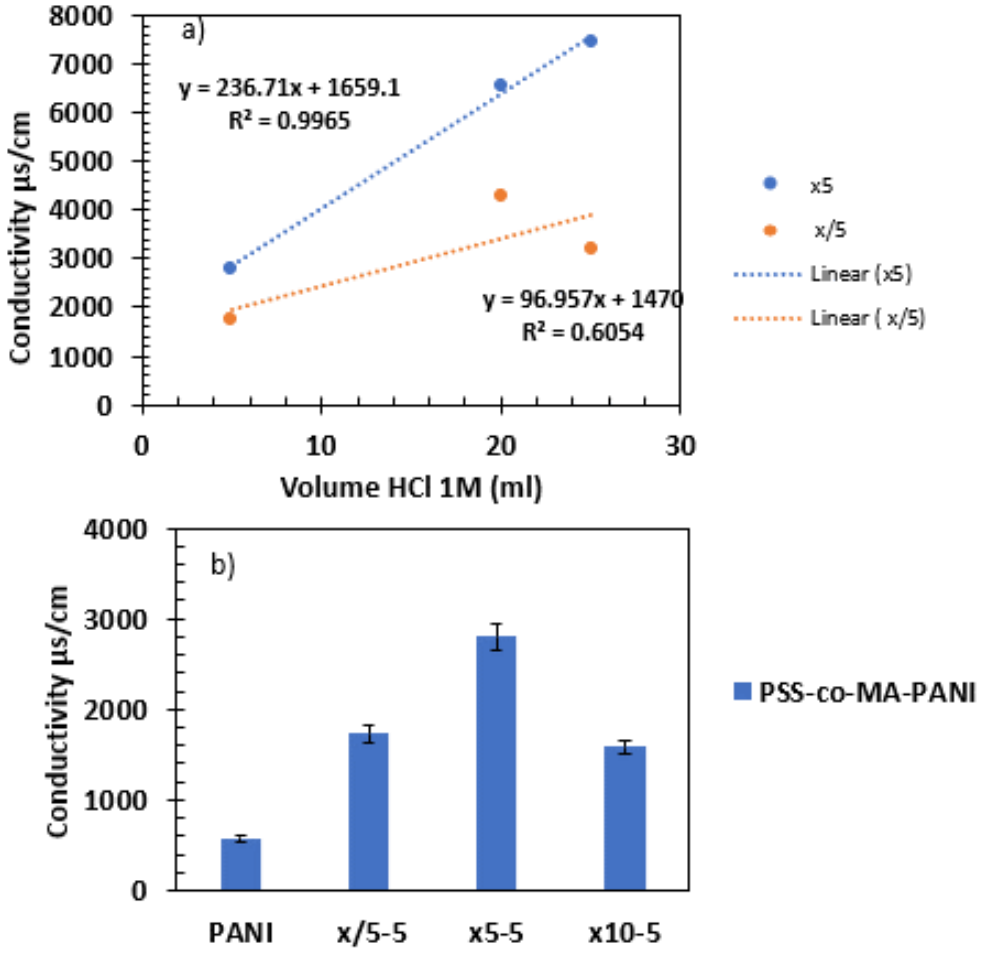

Figure 6.16: Conductivity measurements for PSS-*co*-MA—PANI composites at 3000 ppm. a) Effect of dopant (PSS-*co*-MA), b) effect of Aniline:HCl

6.4.5 Concentration based calibration curve

Stability of dissolved X10-5, X10-6 and X5-5 in water will not only help with their administration through injection/production line as inhibiting chemicals but also will allow the user to build an easy concentration based calibration curve to control the amount of the inhibitor in the field. As explained in Chapter 3, UV-vis spectrophotometry can be used as a method of concentration measurement for chemicals which have a visual colour or peak intensity in the range of 200-800 nm wavelength based on the direct relation between concentration and intensity of the light adsorbed by the

detector. Figure 6.17 shows the Uv-vis spectra collected from sample X10-6 at different concentration.

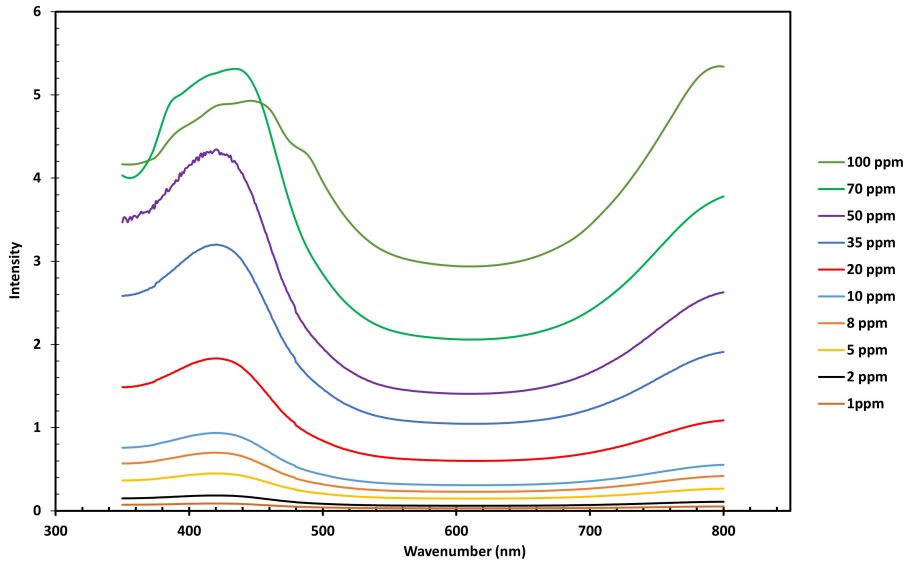

Figure 6.17: UV-Vis spectra of the PSS-*co*-MA—PANI solution for 0-100 ppm

As can be seen in Figure 6.17, there are two major peaks detected for PSS-*co*-MA—PANI composite; one at 420 nm and the other one at 800 nm. These peaks and their meaning were explained earlier in Section 6.4.3 of this chapter. Figure 6.17 shows that the peak at 800 nm is the peak that shows linear relation between its intensity and concentration of the chemical. As a result corresponded peaks to each concentration listed in Table 6.1 are graphed in the Figure 6.18 to produce the calibration curve. The equation derived will be later used to measure the unknown concentration of static jar for PSS-*co*-MA—PANI samples.

Table 6.1: Uv-vis intensity detected at 800 nm for X10-6 PSS-*co*-MA—PANI

Concentration (ppm)	Intensity
100	5.34
70	3.77
50	2.62
35	1.909
20	1.088
10	0.553
8	0.419
5	0.266
2	0.109
1	0.052

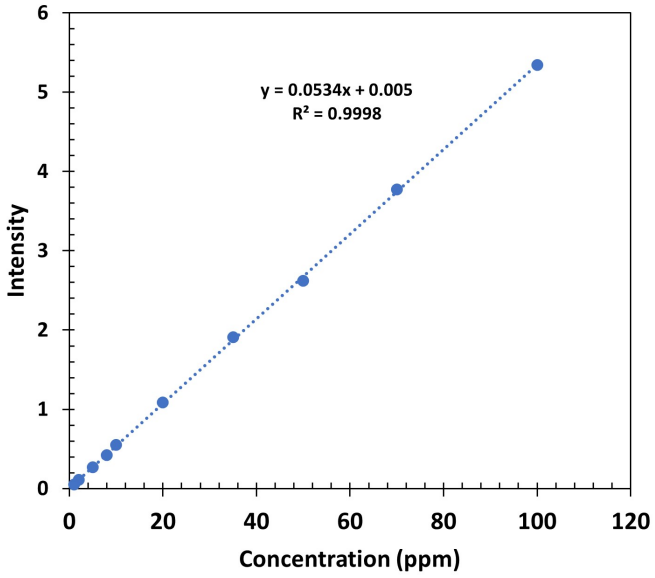

Figure 6.18: Calibration curve for 0-100 ppm sample solutions of PSS-*co*-MA—PANI at 800 nm

6.4.6 Thermogravimetric analysis (TGA/DTG)

As the results in Figure 6.19 (a) show, by introducing PANI, the thermal stability of PSS-*co*-MA increases and in fact an optimal combination of both polymers in X10-5 composite, can withstand temperatures up to 358 °C before any decomposition starts. For better interpretation, DTG results are presented in Figure 6.19 (b). In this graph, PSS-*co*-MA thermal stability is shown on a secondary Y-axis on the right hand side in red, separate from the other 3 samples as it shows 10 times more mass loss than Pure PANI and PSS-*co*-MA—PANI composites.

In general, PSS-*co*-MA and X10-5 show 4 major mass losses, whilst X5-5 and PANI samples are showing 5 stages. For all these samples, the first stage of loss from 73-150 °C refers to H_2O evaporation [141]. This can be seen more significantly for PSS-*co*-MA as it adsorbs more water due to its hydrophilic nature. For pure PANI and PSS-*co*-MA—PANI composites, the second stage of loss takes place at 150-250 °C which corresponds to the release of loose dopants like HCl [136]. This is more significant for pure PANI as for composite samples, considerable amount of HCl were replaced by successful doping of PSS-*co*-MA to the PANI structure. PSS-*co*-MA experienced its second stage of loss through losing its –COOH groups at 240 °C. However, as a result of PANI presence in X5-5 structure, –COOH groups started to decompose at higher temperatures i.e. 300 °C as well as partially merging with $-SO_3^-$ mass loss between

358-480 °C [187]. Interestingly, X10-5 did not show any early stages of mass loss corresponding to HCl dopants or –COOH, instead –COOH functional group might have completely decomposed at a later time along with $-SO_3^-$ groups showing a more intense peak at 400 °C. This interpretation is mainly based on the widened $-SO_3^-$ peak for all of these three samples compared to PSS-*co*-MA that loses $-SO_3^-$ groups between 385-500 °C with a sharp peak at 440 °C. In general, PANI composites showed higher thermal stability and a maximum decomposition of 40% up to 700 °C, whereas pure PSS-*co*-MA decomposed at this temperature.

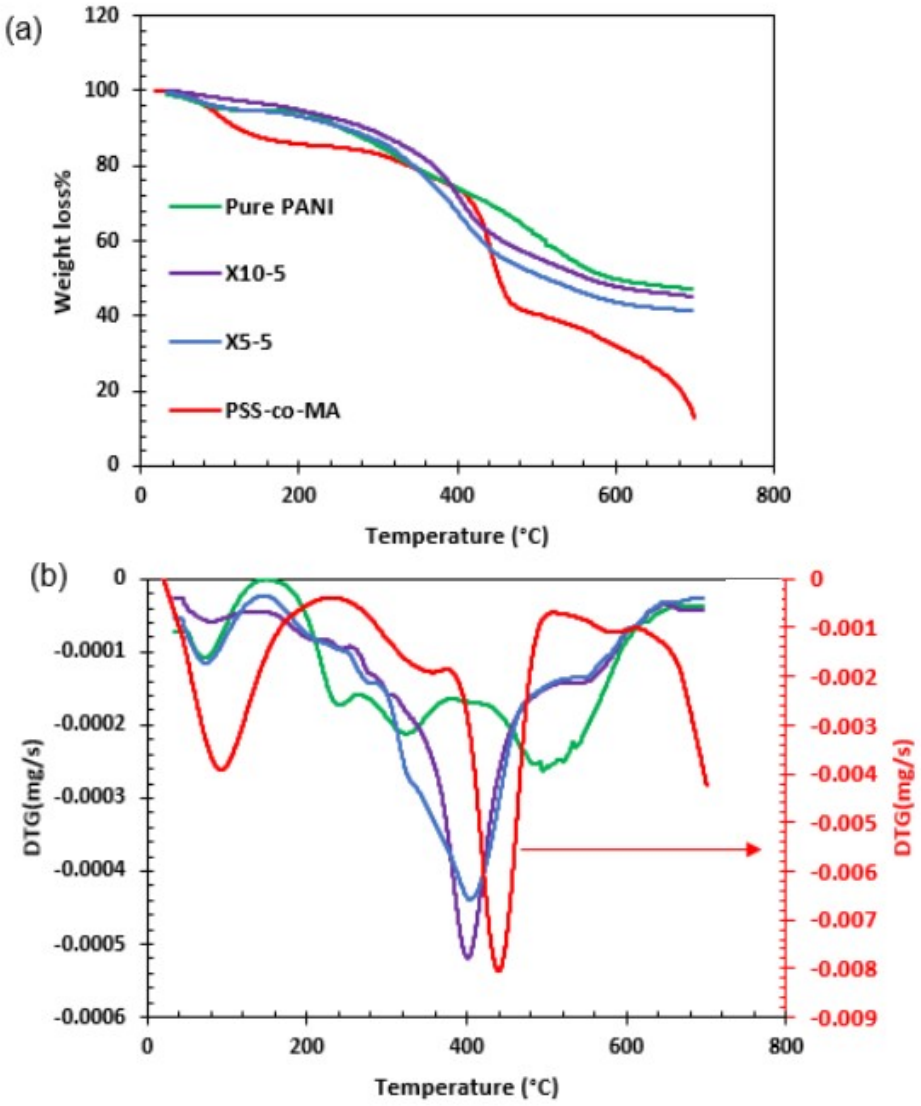

Figure 6.19: TGA (a) and DTG (b) results of PSS-*co*-MA—PANI samples vs. Pure PANI and PSS-*co*-MA that shows the increase of thermal stability around 200 °C

6.5 Summary

In this Chapter it was firstly aimed to resolve the incompatibility issue of FL1-DETA though simple modification, avoiding complications accompanied by designing a new chemical structure. Such as:

1. Breaking down the FL1-DETA structure to FL1 solely
2. Finding a threshold for Ba^{2+} to resolve incompatibility
3. Blending industrial $BaSO_4$ scale inhibitors with FL1-DETA to avoid the formation of Ba^{2+}—SI insoluble composite.

However, none of the above mentioned methods were successful. As a result, FL1-DETA scale inhibitor was modified through replacing FL1 with FL1b that has reduced sulfonic acid groups. The structure was then doped with PANI. Produced PSS-*co*-MA—PANI composite were then characterised with different techniques and the samples were narrowed down to X10-5, X10-6 and X5-5 based on their, morphology, availability of functional groups, dispersiblity in water as well as thermal stability and conductivity. PSS-*co*-MA—PANI's modified structure is thermally stable up to 385 °C.

In the next Chapter, the newly formed PSS-*co*-MA—PANI composite will be tested under full scaling scenario and their behaviour would be analysed and compared with FL1-DETA in both static and dynamic tests.

CHAPTER 7

Comparison of FL1-DETA and PSS-*co*-MA—PANI

Introduction

In this Chapter FL1-DETA and the modified PSS-*co*-MA—PANI composites will be compared as SI against routine and sulphide scales (ZnS and PbS). The newly developed inhibitor compatibility with HS Elgin brine composition and its adsorption properties on the sand particles will be evaluated. The performance of both inhibitors will be investigated thoroughly through Static and dynamic scaling tests. At the end of the Chapter, the improved retention properties of X10-5 as a PSS-*co*-MA—PANI composite will be confirmed versus FL1-DETA.

7.1 Static jar test: Full brine

7.1.1 Compatibility with CW

Newly formed composites were all tested for compatibility with CW. Results as presented in Figure 7.1, shows that by introducing PANI to the inhibitor structure, the compatibility with CW significantly improves.

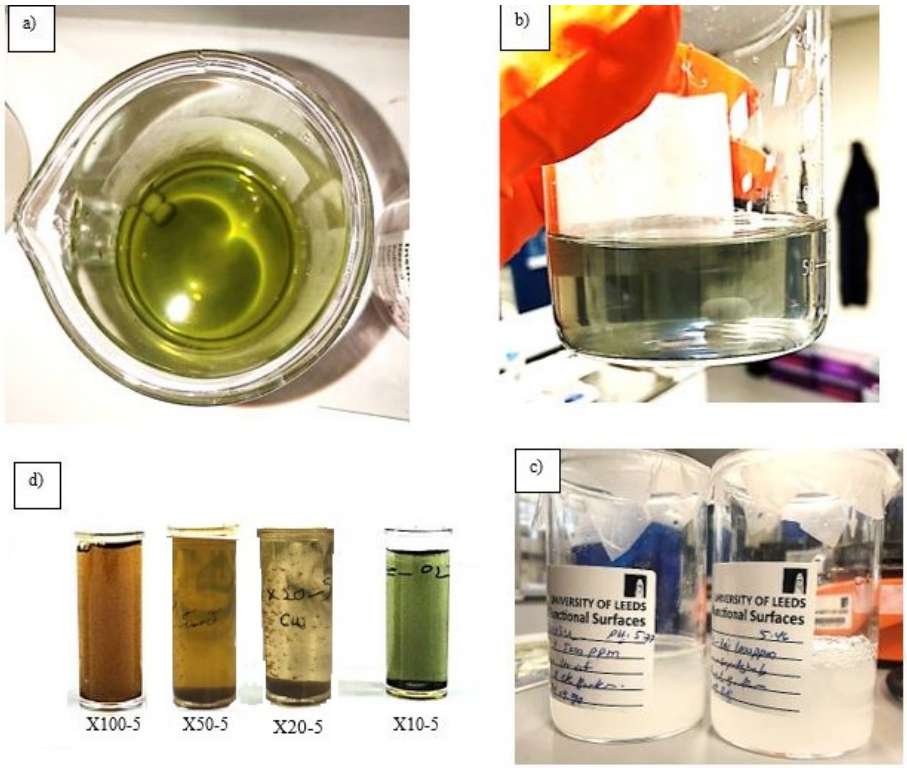

Figure 7.1: Compatibility test with CW. a) X5-5, b) X/5-5 c) FL1b d) X100-5, X50-5, X20-5 and X10-5. The incompatibility can be easily seen though comparing the blurriness of the cross sign on the bottles

Even though having high fractions of FL1b improves the solubility of the composites, for having a compatible inhibitor with CW, a sufficient amount of PANI is needed. Hence, as it can be seen in Figure 7.1 (c) AA-5, X50-5, X20-5 and X100-5 showed incompatibility with the CW due to the lack of enough PANI that blocks Ba^{2+} access to $-SO_3^-$ groups, whereas X/5, X5 and X10 series showed complete compatibility. However, as explained in Section 6.4.4, X/5 samples did not show enough storage stability and dispersibility in its own solution to meet industrial and squeeze treatment application requirements. As a result, for further scale and flow assurance tests, samples were ultimately narrowed down to X10-6, X10-5 and X5-5 based on their resultant properties such as thermal and solution stability, conductivity as well as compatibility with CW.

7.1.2 Coupled adsorption/precipitation

The adsorption/desorption ability of the stable modified structures i.e X10-6, X10-5 and X5-5 and the FL1-DETA were investigated through static tests on 30 g sand particles at room temperature with full production brine as listed in Table 3.2 without scaling ions. The adsorption data in Figure 7.2 were computed by subtracting the residual concentration (C_{eq}) in CW from the initial value ($C_{initial}$) after 24 hours which was then normalised by the mass of sand as the adsorbate. The static adsorption test and procedure is explained previously in Chapter 3. Results showed that the modification of the PSS-*co*-MA (FL1b) structure with aniline functional groups has a remarkable impact on the SI adsorption and desorption ability on sandstone particles. As it can be observed in Figure 7.2, X10-6 with lowest adsorption of all modified PSS-*co*-MA—PANI composites, shows more than 60% improved apparent adsorption for range of concentration as compared to FL1-DETA and 25% less desorption over 24 hours. To identify the adsorption mechanism of PSS-*co*-MA—PANI composites on sandstone, static jar test was carried for three different masses of 10 g, 20 g and 30 g of sand. The isotherm associated with X10-6 and FL1-DETA are provided in Figure 7.3 and Figure 7.4, respectively. Figure 7.3 demonstrates a pure adsorption for the X10-6 for initial concentrations below 500 mg/L and a coupled precipitation adsorption mechanism for higher concentrations where the slope for three different masses of sand deviates [114]. However, as can be seen in Figure 7.4, the pure adsorption region for FL1-DETA only exists for initial concentrations below 50 ppm as above this concentration all three graphs deviates due to precipitation caused by incompatibility.

X10-6 produced isotherms were then fitted by different adsorption theories [214]. Langmuir and Freundlich showed the best fit for low (10 g) and high (20 g and 30 g) masses of sand, respectively and the parameters are listed in Table 7.1. In L-type and H-type isotherms, as the concentration of chemical under investigation increases, the relative adsorption decreases[1]. This is mainly due to the saturation of adsorption sites available to the chemical resulting in relatively less adsorption. For the FL1-DETA, this implies the poor affinity of this inhibitor to the sandstone particles whilst the S-type isotherm of X10-6, shows intermolecular interaction and high affinity of the modified

[1]Please refer to Appendix B for more information

SI to the sandstone. The Freundlich fitted n<1 and the shape of the isotherms for X10-6 confirms that, the SI has an "S-Type " isotherm. The corresponding parameters of this fitting are listed in Table 7.1. The S-type isotherm suggested for PANI-Co-Polymer composites shows, the modified SI high affinity to this adsorbate particles. The fact that the isotherms are not followed by a plateau at high concentration shows that PANI-Co-Polymer has a tendency to vertically orientate at higher concentration to make more sites available for adsorption of SI onto sand particles [174]. This is schematically shown in Figure 7.5.

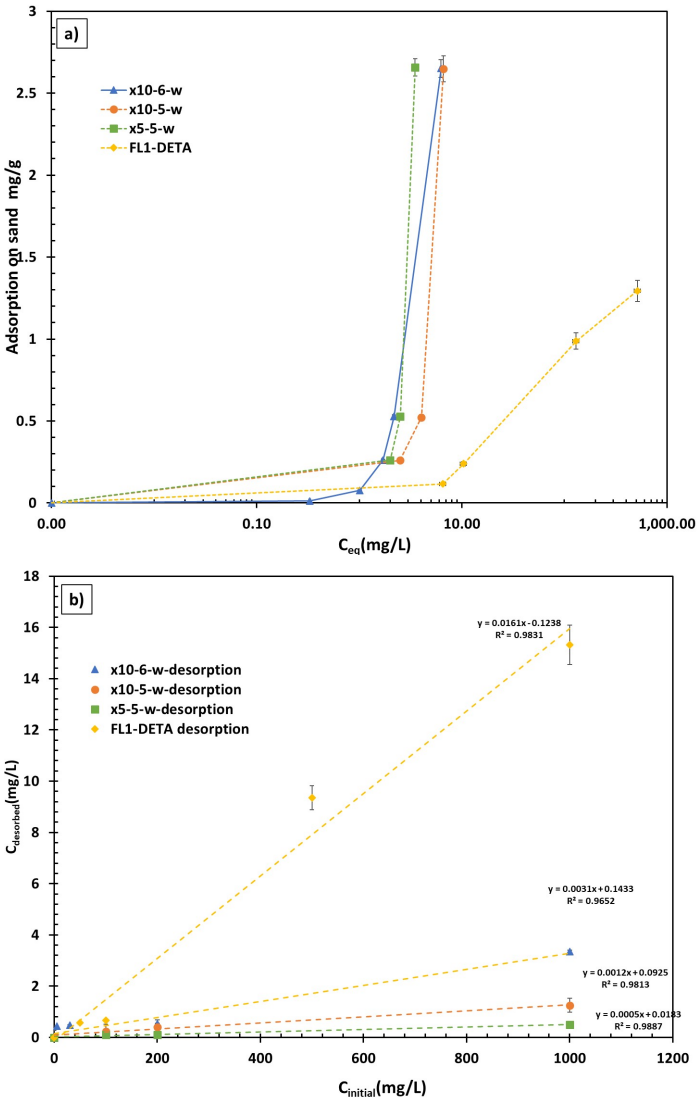

Figure 7.2: Comparison of a) adsorption b) desorption ability of PSS-*co*-MA—PANI (X10-6, X10-5, X5-5) Vs. FL1-DETA. The initial concentrations for both chemical were 5, 30, 100, 200, 500 and 1000 mg/L which was added to 80 ml of CW and 30 g of sand as the adsorbate.

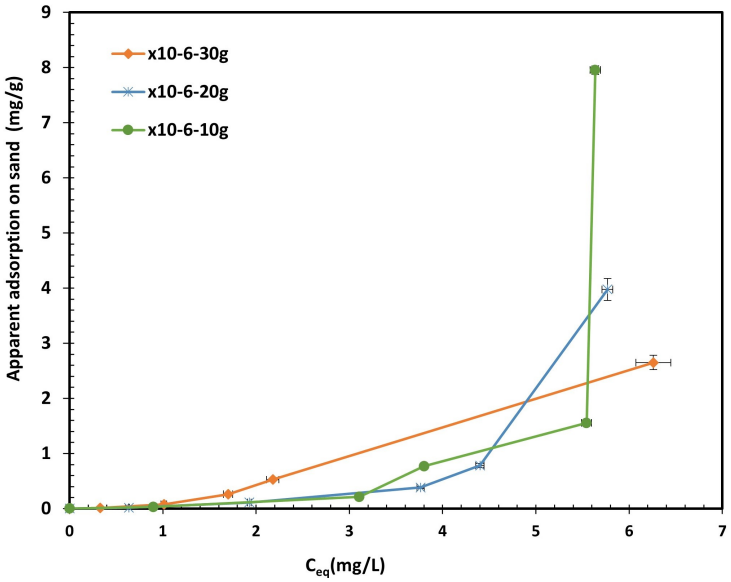

Figure 7.3: Adsorption isotherms for X10-6 in CW on sand particles.

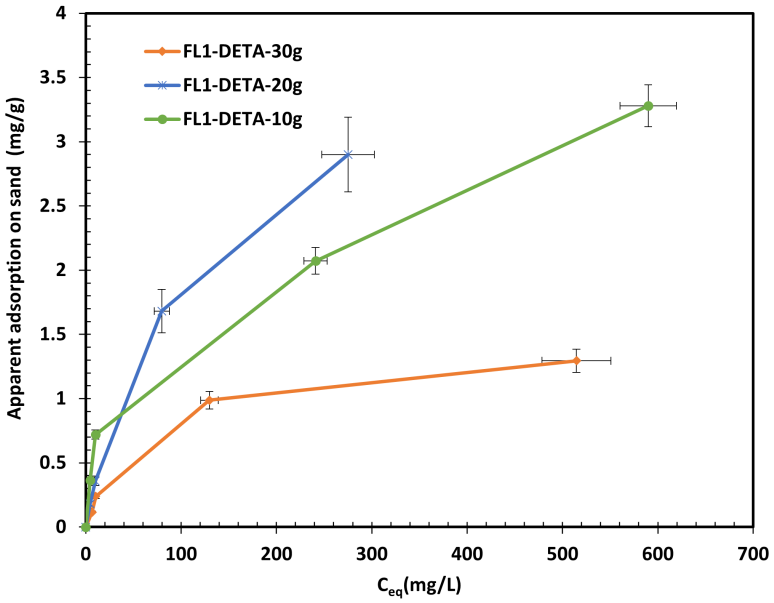

Figure 7.4: Adsorption isotherms for FL1-DETA in CW on sand particles.

Table 7.1: Isotherm Parameters for X10-6 in CW on Sand

Model	Parameter	10 g	20 g	30 g
Langmuir	K_{L} mg/L	0.175	0.182	0.170
	R^2	0.92	0.90	0.49
Freundlich	n	0.39	0.44	0.0
	K_{f} mg/L	0.030	0.035	0.530
	R^2	0.85	0.92	0.99
D—R	E kJ/mol	$7X10^2$	$7.9X10^2$	$5X10^{-4}$
	β_D mol^2/kJ^2	10^{-6}	$8X10^{-7}$	$2X10^6$
	q_m mg/g	1.76	1.10	N/A
	R^2	0.68	0.72	0.78
Temkin	A	0.75	0.94	1.52
	b_T	1014.9	2075.6	2912.5
	B	2.41	1.80	0.85
	R^2	0.92	0.39	0.68
Herkin	A	0.0008	0.0003	0.0002
Jura	B	0.66	0.61	0.45
	R^2	0.89	0.80	0.63
Jovanic	K_J	-1.016	-0.099	-0.077
	R^2	0.92	0.98	0.78

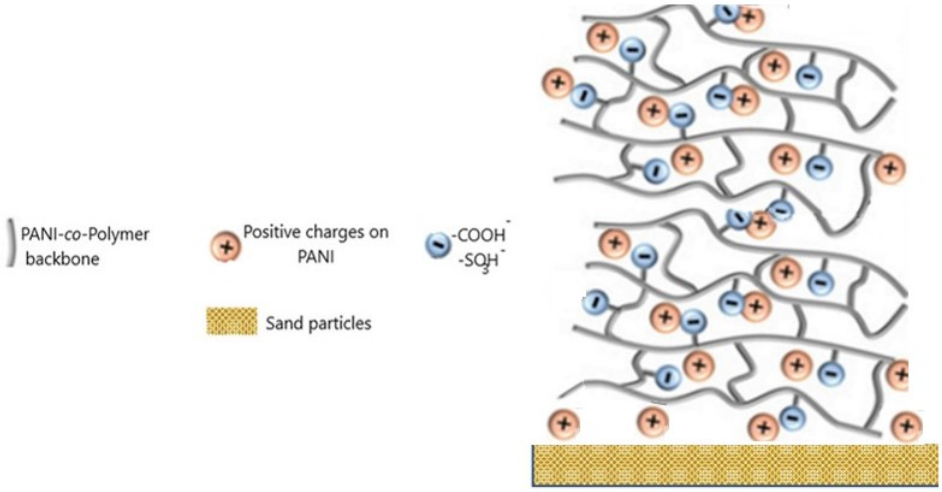

Figure 7.5: Probable schematic of PSs-*co*-MA-PANI adsorption on the sand particles

Three Influencing Factor tests (Full Brine, SI, H_2S)

7.1.3 Scaling tests: Bulk test (full brine)

The scaling tendency of the full production brine was estimated through Multiscale software by calculating the saturation ratio for 1 bar and 90°C[1], respectively. To assess the effect of modified SIs (X10-6, X10-5, X5-5) on scale formation tendency and co-precipitation of different scales in the presence of dissolved H_2S, the static jar test was conveyed in Huguette airtight tubes. All tubes were incubated at 90°C and for simpler analysis, no sand particles were added to the tubes at this stage. The test was stopped after 24 hours by removing and neutralising the unreacted H_2S gas in each tube into 10% NaOH solution through purging nitrogen for 20 minutes. Figure 7.6 is showing these tubes after 24 hours. The Blank sample is uninhibited tube with no scale inhibitor inside. As it can be seen the deposit in PSS-*co*-MA—PANI tubes discoloured to the green shade of the inhibitor where as the actual blank and FL1-DETA sample showed yellowish deposit.

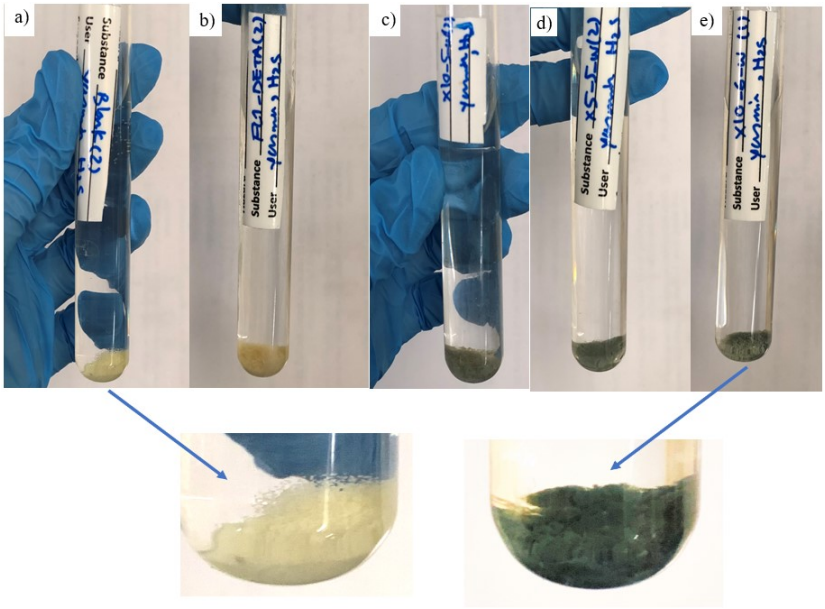

Figure 7.6: Bulk static test for PSS-*co*-MA—PANI in full brine in an airtight tube including full brine and H_2S for 10 mg/L active a) Blank, b)FL1-DETA, c) X10-5, d)X5-5, e)X10-6. Blank sample is the full brine without inhibitor

Table 7.2 shows the remaining $[Zn^{2+}]$ and $[Pb^{2+}]$ as well as the final pH in each tube test. It is worth mentioning that all tube cells had equal initial pH of 5.8, therefore, final results are showing dramatic pH decrease in pH after 24 hours of test duration. This is more severe for the tube with no inhibition i.e. the blank sample. This is mainly

[1]Please refer to Chapter 4. Based on the prediction, the severe formation of ZnS, PbS, $CaCO_3$ and $BaSO_4$ is expected in these conditions with saturation ratio of 2.69, 2.35, 91.2 and 154.88, Section 4.2.1

because of the absence of buffer in the system and decrease of the pH in the closed system. The use of buffer was avoided intentionally to keep the affect of interfering elements as minimal as possible in the system. Another factor is the absence of CO_2 in the tubes. CO_2 induces the formation of carbonated scales which moderate the acidity of the closed system. The effect of this pH drop on the formed deposit and scales will be discussed later in this section.

Table 7.2: AAS and pH results of the bulk static test of the supernatant in the presence of 100 mg/L dissolved H_2S

Sample	Concentration mg/L	$[Zn^{2+}]$ mg/L	$[Pb^{2+}]$ mg/L	Final pH
Blank	0	0.9	-0.02	3.94
FL1-DETA	10	0.7	-0.07	5.29
X10-6	10	0.6	-0.09	4.29
X10-5	10	0.8	-0.04	4.03
X5-5	10	0.7	-0.04	3.29
CW[1]	with out H_2S	79.4	7.31	5.5

Each solution was then filtered under a fume hood equipped with H_2S gas sensor with the sensitivity of < 5 ppm and the bulk formed deposition was separately collected on fibreglass filter paper. Figures 7.8, 7.10, 7.9, 7.11 present the SEM micrographs and EDX results of the bulk deposition formed in each tube in the presence of 10 mg/l active FL1-DETA and X10-6, X10-5 and X5-5, respectively.

On the other hand Figure 7.7 shows the deposits from the blank tube. As it can be seen, none of the tubes showed $CaCO_3$ scale formation. This is mainly due to the absence of CO_2 and dropped pH which dissolves any forming $CaCO_3$[2]. EDX analysis of all tubes proves the presence of sulphide scales (ZnS, PbS) as smooth morphology on the SEM images of filter papers. The formation of sulphide scales was also confirmed by AAS analysis on quenched supernatant with 5% Nitric acid showing the consumption of zinc element to more than 60% for all inhibited tubes. This indicates that none of these SI chemicals suppressed the formation of the ZnS/PbS scale. Figure 7.8 shows the deposit collected from the FL1-DETA tube with pure depositions of sulphide scale (ZnS, PbS) as well as interesting $BaSO_4$ crystals that their morphology is affected by co-precipitation with sulphide scales as compared to the blank sample in Figure 7.7. This means that for FL1-DETA the deposit formed showed crystals are in the micron-cale size. However, results from X10-6 in Figure 7.10, show complete inhibition of $BaSO_4$ crystals and X10-5 and X5-5 show disturbed and defected crystals of $BaSO_4$. Last but not least, inhibited samples showed higher final pH values as compared to the blank samples, whereby FL1-DETA showed the highest value of them all. It is worth mentioning that the initial pH value of all inhibitors was set at 4.5 before and prior to injection into the tubes.

[1]Check Table3.2 for the composition

[2]The effect of pH on $CaCO_3$ solubility is discussed in Chapter 2, Section 2.2.5

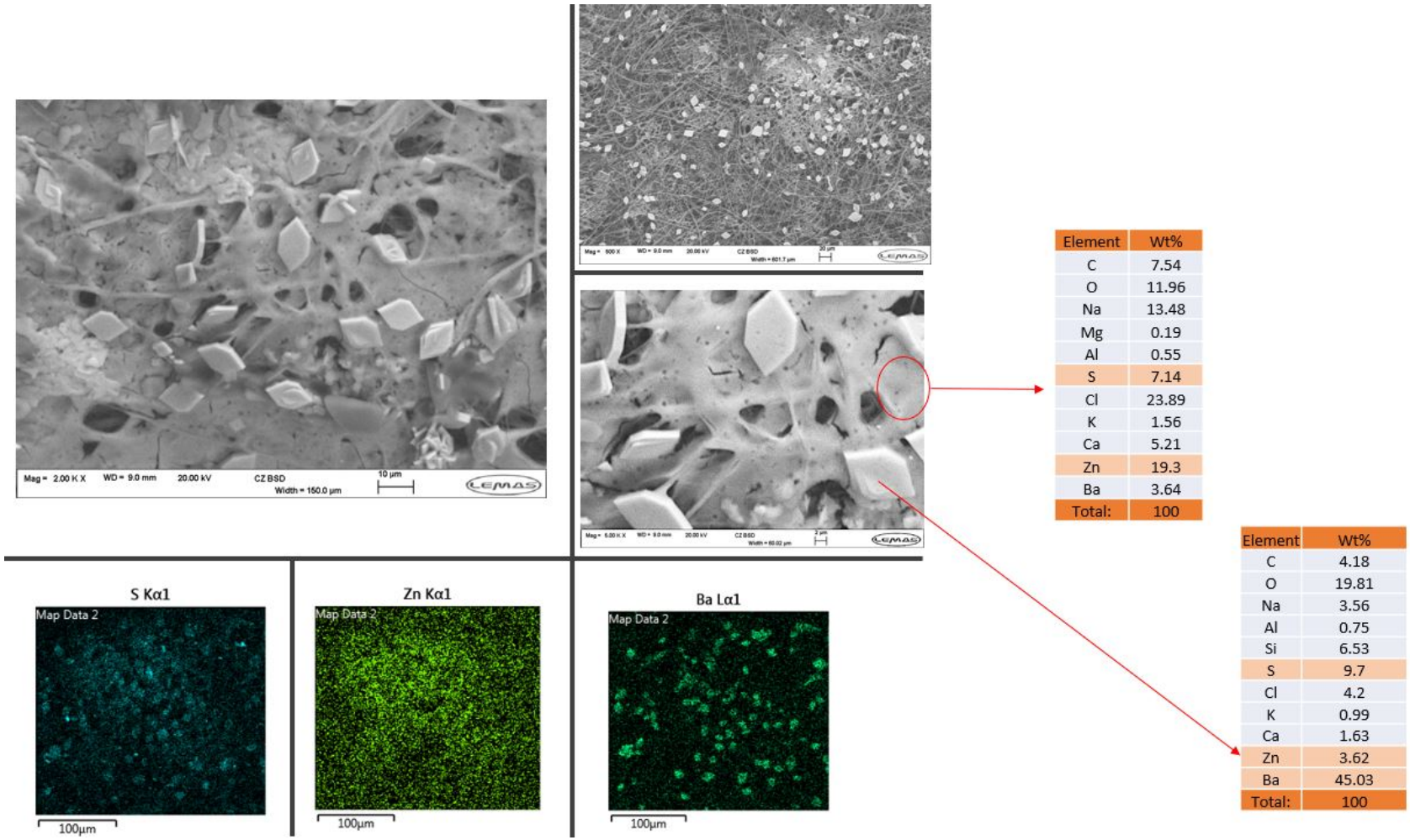

Element	Wt%
C	7.54
O	11.96
Na	13.48
Mg	0.19
Al	0.55
S	7.14
Cl	23.89
K	1.56
Ca	5.21
Zn	19.3
Ba	3.64
Total:	100

Element	Wt%
C	4.18
O	19.81
Na	3.56
Al	0.75
Si	6.53
S	9.7
Cl	4.2
K	0.99
Ca	1.63
Zn	3.62
Ba	45.03
Total:	100

Figure 7.7: SEM/EDX of bulk test deposition on filter paper for Blank sample.SEM and EDX results reveal the formation of ZnS and $BaSO_4$.

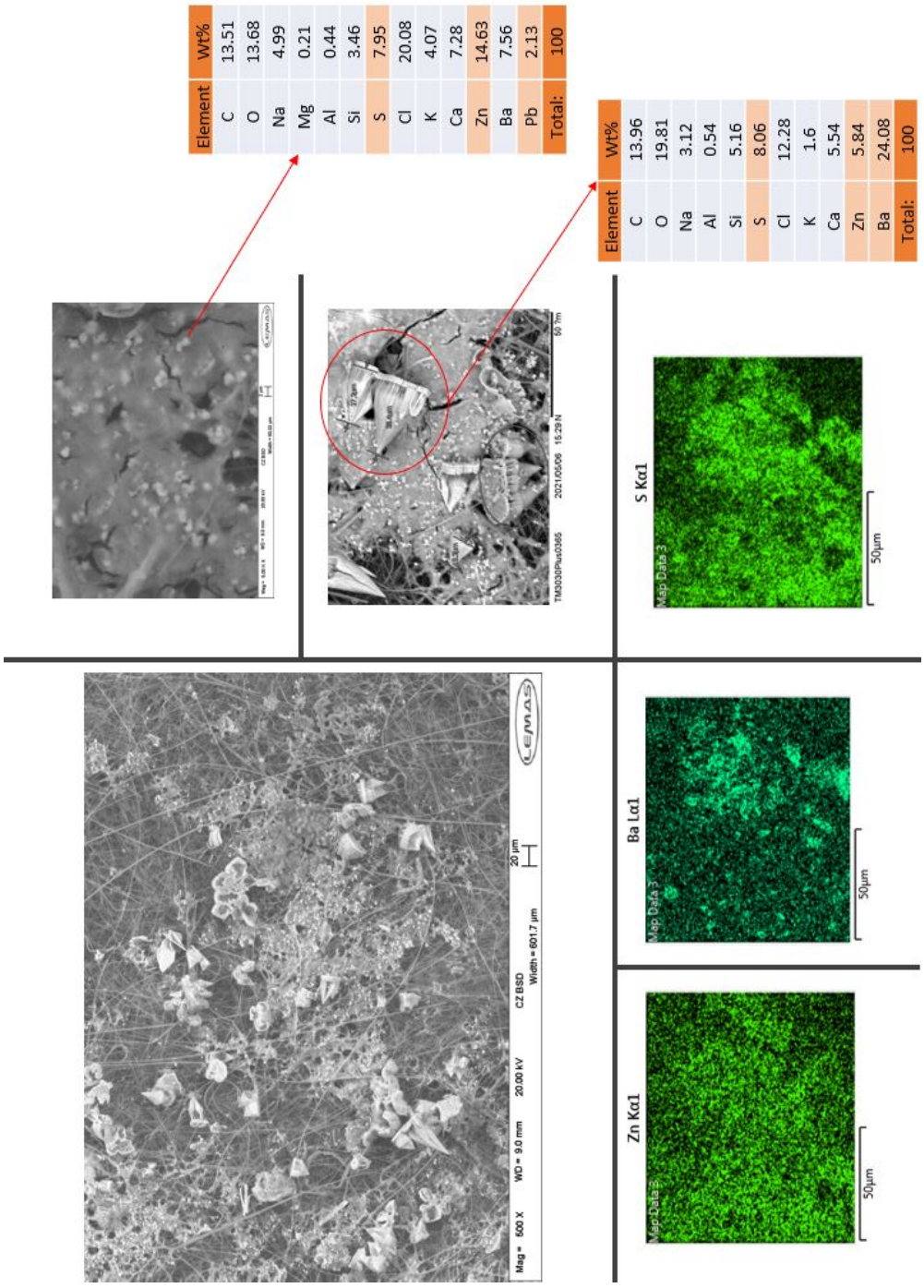

Figure 7.8: SEM/EDX of bulk test deposition on filter paper for FL1-DETA sample. SEM and EDX results reveal the formation of ZnS and $BaSO_4$ disrespect of inhibitor presence.

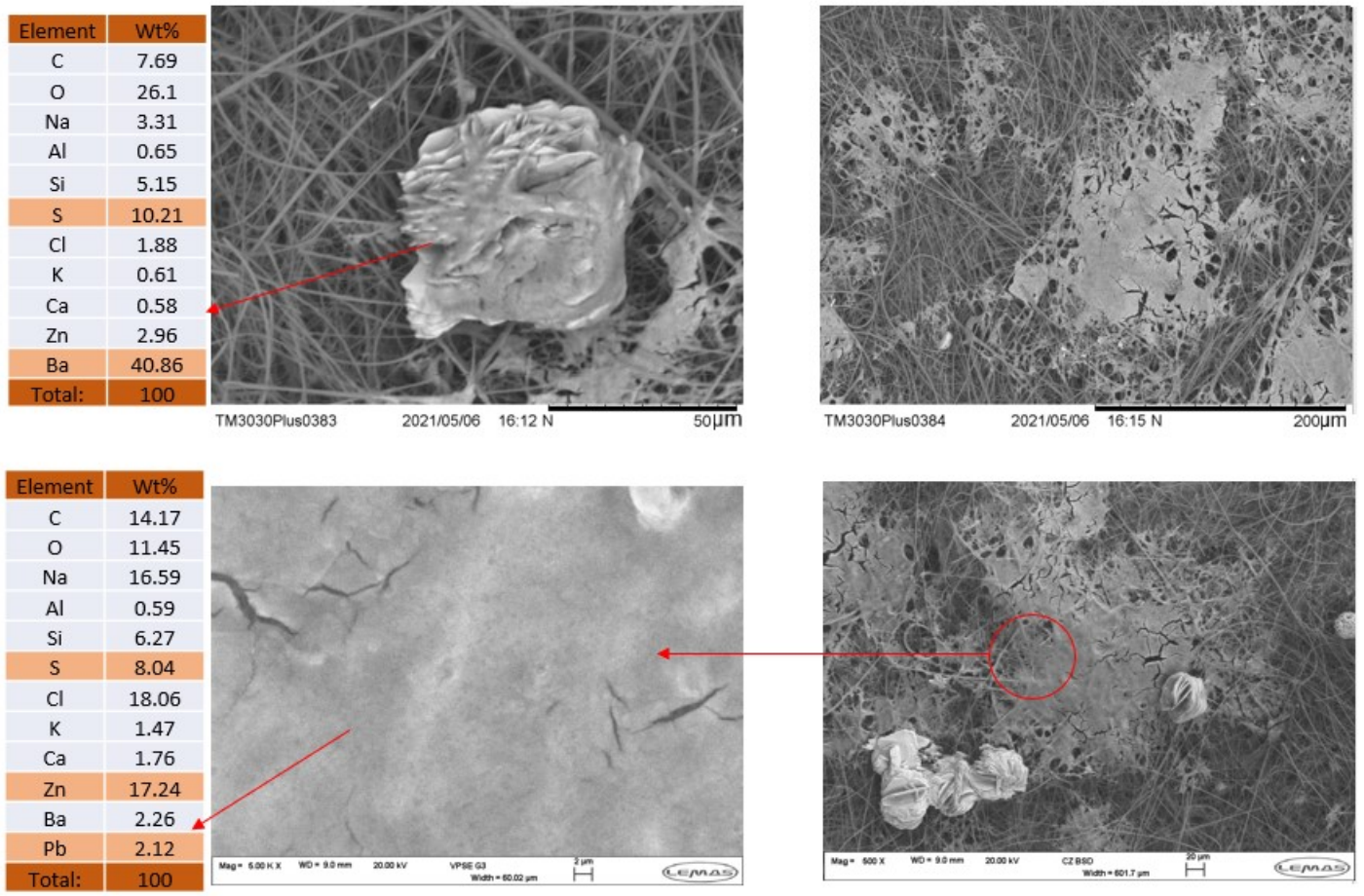

Figure 7.9: SEM/EDX of bulk test deposition on filter paper for X10-5 sample.SEM and EDX results reveal the formation of ZnS and disrupted $BaSO_4$ crystals.

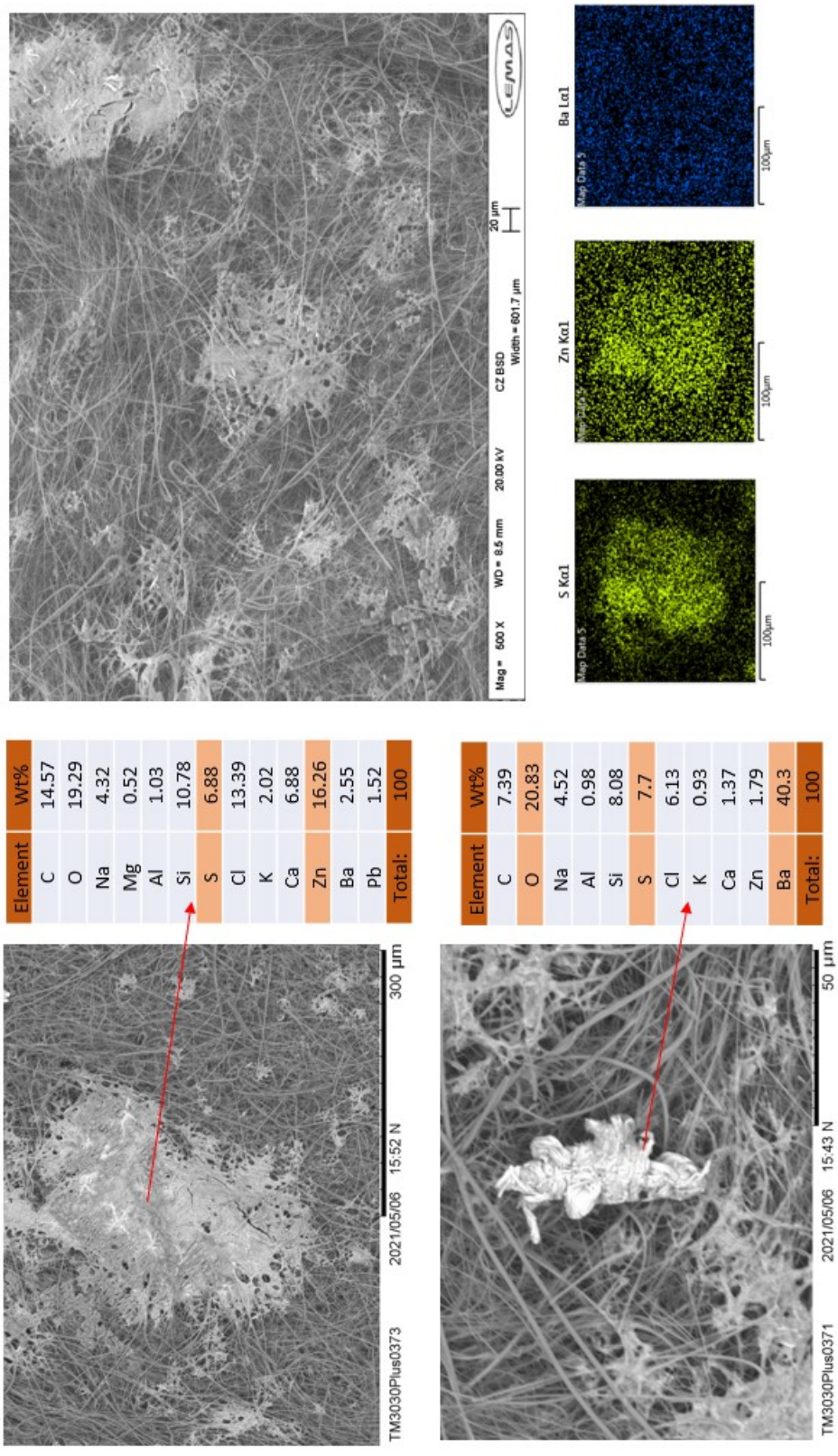

Figure 7.10: SEM/EDX of bulk test deposition on filter paper for X10-6 sample. SEM and EDX results reveal the formation of ZnS solely.

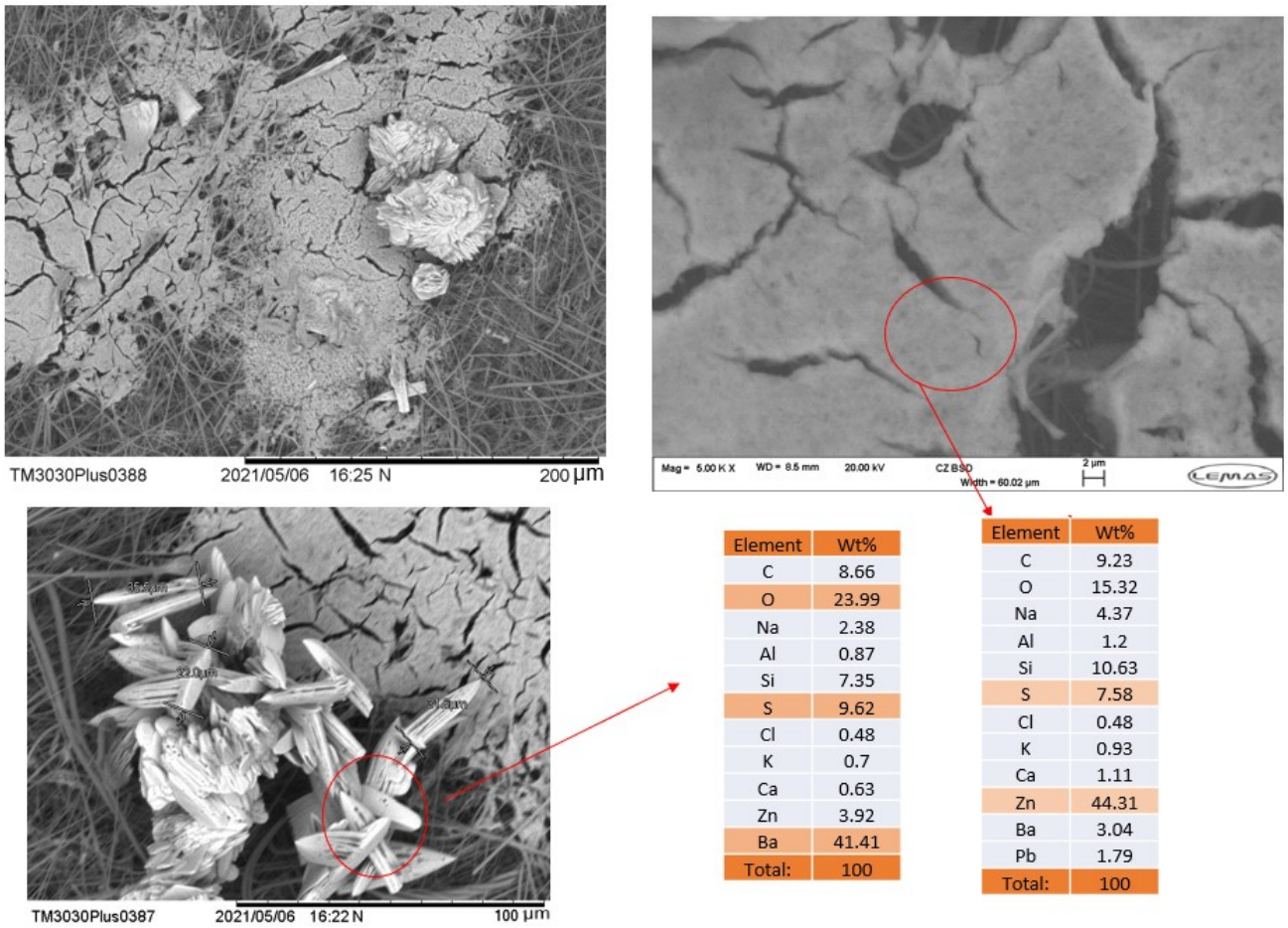

Element	Wt%
C	8.66
O	23.99
Na	2.38
Al	0.87
Si	7.35
S	9.62
Cl	0.48
K	0.7
Ca	0.63
Zn	3.92
Ba	41.41
Total:	100

Element	Wt%
C	9.23
O	15.32
Na	4.37
Al	1.2
Si	10.63
S	7.58
Cl	0.48
K	0.93
Ca	1.11
Zn	44.31
Ba	3.04
Pb	1.79
Total:	100

Figure 7.11: SEM/EDX of bulk test deposition on filter paper for X5-5 sample. SEM and EDX results reveal the formation of ZnS and $BaSO_4$ disrespect of inhibitor presence.

Four Influencing Factor tests (Full Brine, SI, H_2S, Sand)

7.1.4 Scaling test: on sand

The H_2S containing static test was repeated for all inhibitors at 90°C by introducing 10 g of sand in the Huguette airtight tubes before sealing. Later, the tubes were degassed and 10 mg/L active of each inhibitor was added to the tubes. For better adsorption of the inhibitors and replicating the squeeze treatment procedure, tubes were left intact for 4 hours at 90°C. After that, the brine was added to each tube through the mixing procedure as described in the experimental method section of Chapter 3. Tubes were incubated for another 24 hours and degassed and neutralised from unreacted H_2S gas at the end. In general Figure 7.12 shows all scale inhibitors, decreased the amount of formed deposit compared to the blank sample where brine chemistry experienced scaling in the absence of inhibitor.

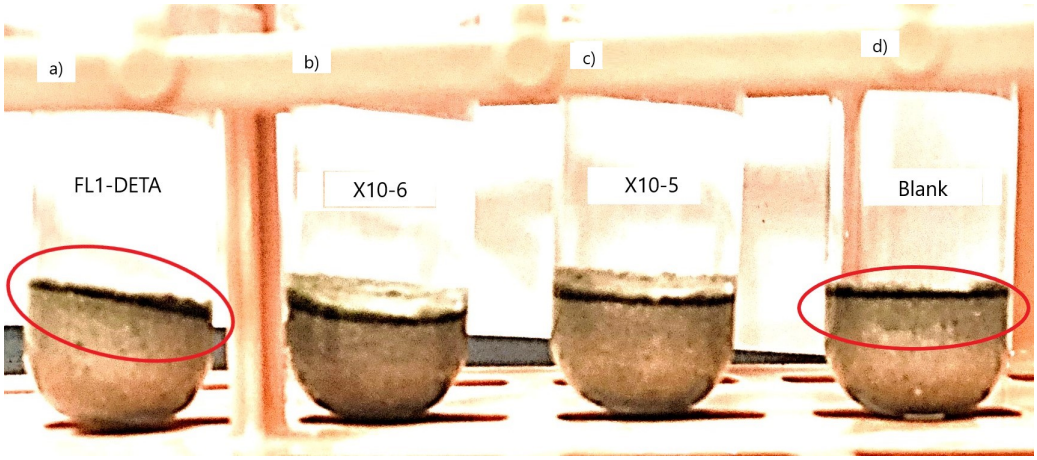

Figure 7.12: Static jar test in an airtight tube in presence of sand, full brine and H_2S for 10 mg/L active a) FL1-DETA, b) X10-6, c) X10-5, d) Blank sample of full brine without inhibitor

By analysing the quenched supernatant with ICP, it was found that none of these chemicals could have suppressed sulphide scales formation. Figure 7.13 shows these ICP results for Zn^{2+}, Pb^{2+}, Ca^{2+} and Ba^{2+}. Based on the analysis more than 70% Zn^{2+} cations were consumed in the presence or absence of any inhibitors. In the case of Pb^{2+}, the FL1-DETA tube and the blank sample show total consumption, whereas for the X10-6 tube approximate 10% inhibition was measured.

Later, sand particles from each tube were collected, gently rinsed with DI water and dried for further analysis with SEM/EDX. Figure 7.14 (a) shows the sand particle and the formed scale in absence of scale inhibitor i.e. blank sample. In general, both types of scale inhibitors helped to decrease the amount of scale deposition on sand parti-

cles. Figure 7.14(c),(d) reveal that, unlike most expectations, even though FL1-DETA showed reduced visual deposit formation in its tube, sand particle micrographs are covered with deposits of sulphide scale (ZnS/PbS) and crystals of $BaSO_4$. In Figure 7.14, $BaSO_4$ crystals are shown with red ovals and sulphide scale layer with red squares for all samples. This could also be visually seen in Figure7.12 as darkened sand particles that are shown with a red circle. Nevertheless, for X10-6 and X10-5 sand particles, this darkened layer of sand could not be observed and based on SEM micrographs, the only deposit formed was flaky the ZnS/PbS scale with disrupted morphology and no signs of any $BaSO_4$ formation. These micrographs for the X10-6 sample are shown in Figure 7.14(f),(g).

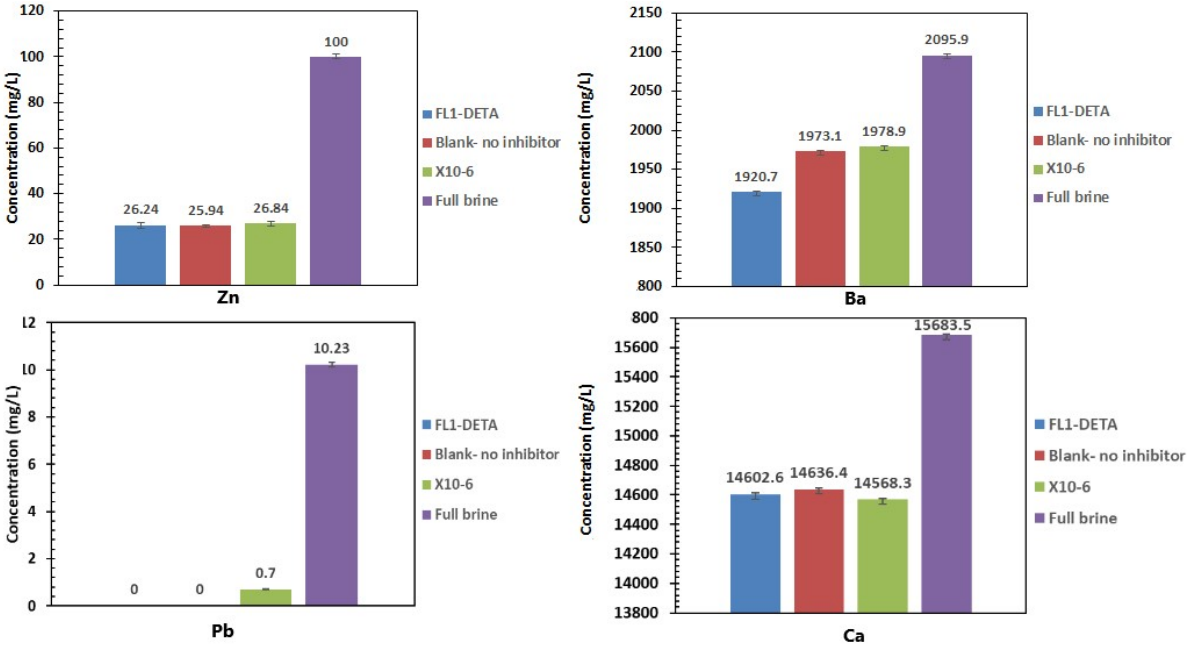

Figure 7.13: ICP results of full brine without scaling element (Purple), FL1-DETA (blue), blank sample i.e. scaled brine with no inhibitor (red) and X10-6 (green).

On the second stage of this analysis, the scaled sand particles were furtherly washed with DI water through stirring in a beaker for 5 minutes. These sand samples were dried and imaged through SEM and micrographs in Figure 7.14 labelled as (b), (e) and (h) were achieved. These micrographs show the clear difference between the two scale inhibitor chemistries and the remarkable effect of PSS-*co*-MA—PANI on all ranges of forming scales.

Figure 7.14 (b) presents the blank sample after dynamic washing which shows clear persistence of the formed scale on sand particles. Even though both scale inhibitors helped to decrease the amount of scale deposition on sand particles after the dynamic washing procedure, however, Fl1-DETA micrographs show persistent depositions of

sulphide and $BaSO_4$ scales after this stage. Nevertheless, in the same scenario and after the dynamic washing procedure, the only adsorbed layer on X10-6 sand particles was the unreacted modified polymeric inhibitor. Meaning that the flaky deposit of sulphide scale was being washed away. Other PSS-*co*-MA—PANI samples such as X10-5 and X5-5 showed the exact same behaviour as X10-6 towards sulphide scales and disturbed the morphology of formed crystals. Therefore, it is anticipated that PSS-*co*-MA—PANI composites are capable of protecting sand particles from built-up layers of scales by disrupting their crystals and affecting their adherence to the substrate. This type of scale inhibitor and their mechanism of action as adherence inhibition was explained in the literature review at Section 2.4.1.1 of this thesis. It is worth noting that the bead shape morphology in the FL1-DETA micro-images is the same incompatible morphology that was observed for SEM images of incompatible deposits in Figure 5.7. The incompatible inhibitor is highlighted with an arrow in Figure 7.14 (d) and (e). This means that FL1-DETA is leaving an extra insoluble and persistent deposit behind on the sand which at bigger scales of injection concentrations, might increase the risk of formation damage in the field.

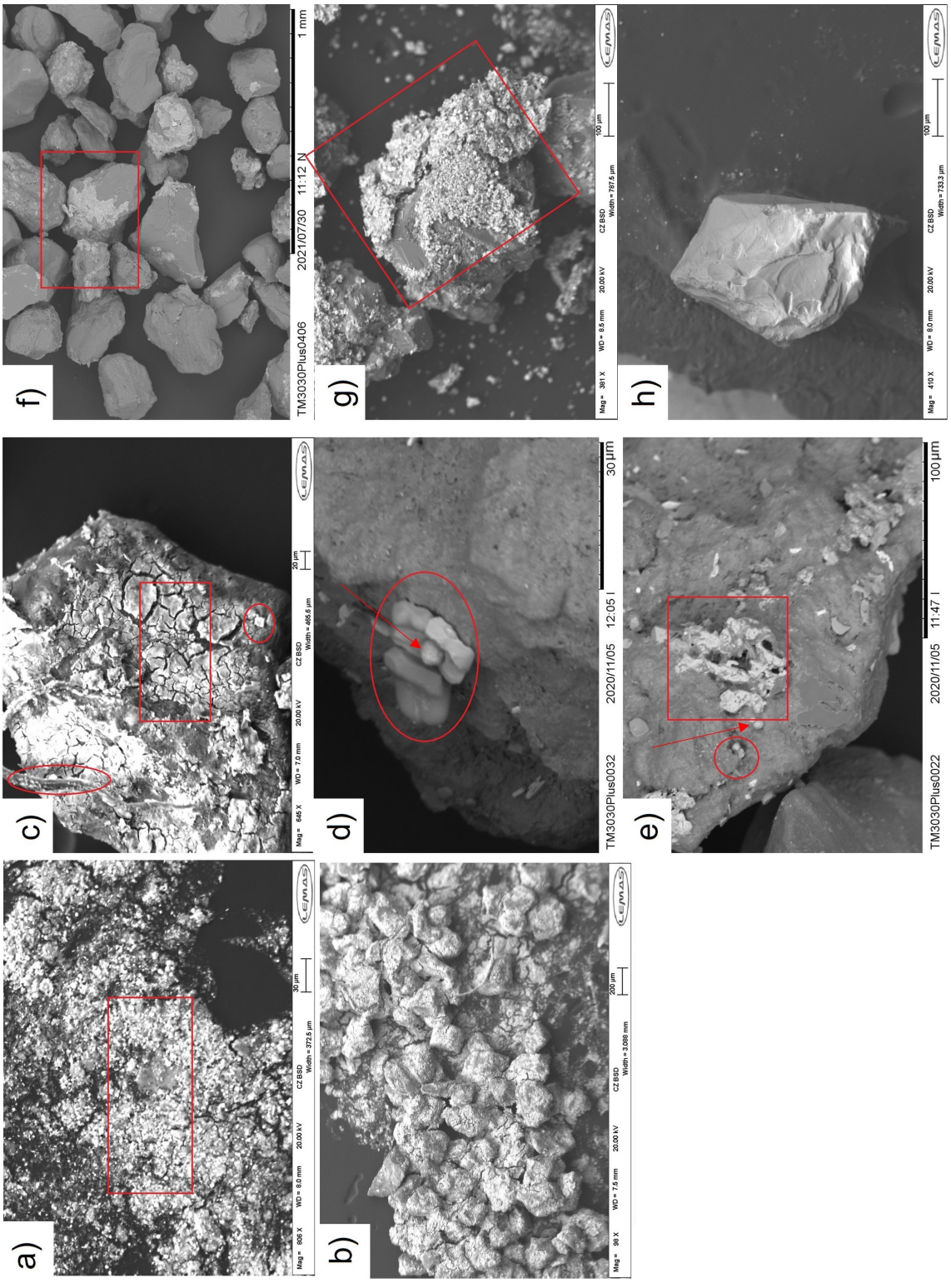

Figure 7.14: SEM images showing the effect of adsorbed X10-6 and the PSS based SI on sandstone (a)-(b) Blank, (c)-(e) FL1-DETA, (f)-(h) X10-6.

7.2 Static jar test: Simplified brine

Based on the saturation ratios presented in Chapter 3 Section 4.2.1, the full brine composition listed in Table 3.2, tends to form other scales such as $BaSO_4$ and $CaCO_3$ along with PbS and ZnS. To identify PSS-*co*-MA—PANI SIs and FL1-DETA mechanism of action on sulphide scale solely, the number of influencing factors on SI to scale interaction were reduced by simplifying the brine to single scaling component in the Table 3.4, whilst maintaining their concentration. Afterwards, both sets of static jar tests were conducted in the presence and absence of sand particles. Brine simplification would help with the impact analysis of the inhibitor on ZnS formation solely whilst the micro and nanoscale imaging by SEM, TEM and the SAED could be collected without the interference of other scaling species like $BaSO_4$ and $CaCO_3$.

7.2.1 Scaling test: bulk and sand

Figure 7.15 shows the visual comparison of bulk static test between the uninhibited (blank) and inhibited samples mixed in Table 3.4 brine 1 composition where Zn^{2+} is the only scaling cation, (i.e no Pb^{2+}). The main purpose of this experiment, was to qualify the performance of each inhibitor against the ZnS scale, solely. For better replication of squeeze treatment procedure, the testing SI was added to the sand containing tube 24 hours in advance of the mixing procedure and was degassed.

As it is shown in Figure 7.15 (a_1 and b_1), based on the visual comparison, both static tests i.e. bulk and in the presence of sand, showed white dusty deposition for the blank tube. For both modified SI test tubes i.e. X10-5 and X10-6, the amount of visual deposits was significantly reduced compared to the blank sample at both test types. Nevertheless, as shown in Figure 7.15 (a_2, b_2 and a_3, b_3) all formed deposits were discoloured to green in these tubes. Interestingly, unlike the bulk test shown in Figure 7.15 (a_4) and the full brine experiment shown in Figure 7.12, in the presence of sand, FL1-DETA containing tube at Figure 7.15 (b_4) was cloudy with no visual deposits. Whereas X10-5 and X10-6 tubes contained a clear supernatant with a small amount of discoloured green deposition as shown in Figure 7.15 (b_2) and (b_3), respectively. This means that the FL1-DETA acted as a successful dispersant, however, modified inhibitors presumably, adsorbed on the deposit's surface and discoloured the white formed deposit to green. It also shows that FL1-DETA dispersibility properties toward ZnS will be ineffective in the presence of PbS and other mineral scales.

Supernatant of Figure 7.15 (b_1, b_2,b_3 and b_4) samples were compared by AAS for the residual Zn^{2+} concentration. These results and the final pH are listed in Table 7.3 whereby shows that even though X10-5 and X10-6 did not fully suppress the consumption of Zn^{2+} cations in the brine, but were able to reduce its consumption significantly. Due to the observed deposit discolouration for modified SI, both bulk deposit and sand samples of all tubes were analysed and compared through SEM/EDX analysis.

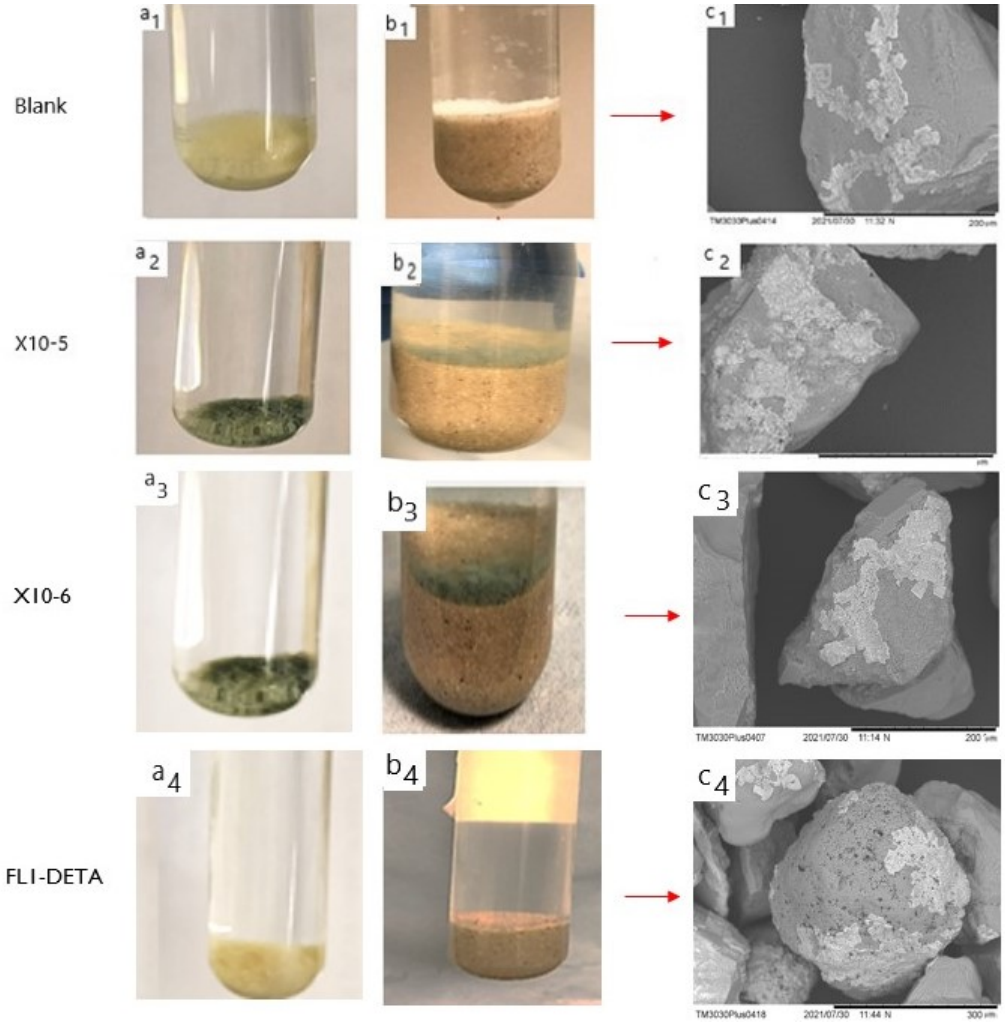

Figure 7.15: Static jar test for bulk (a_1-a_4) and in the presence of sand particles (b_1-b_4) for simplified brine composition including Zn^{2+}, and SEM micrographs from sand particles (c_1-c_4) of blank (1), X10-5 (2), X10-6 (3), and FL1-DETA (4), samples.

Table 7.3: AAS results of the Blank and X10-5 bulk static test supernatant

Sample	Concentration (mg/L)	H_2S (mg/L)	Time (hour)	$[Zn^{2+}]$ (mg/L)	$pH_{Initial}$	pH_{Final}
Blank	0	100	24	4± 0.2	5.5	4.02
X10-5	10	100	24	67.8± 0.5	5.5	3.43
X10-6	10	100	24	51.4± 0.5	5.5	4.23
FL1-DETA	10	100	24	43 ± 0.8	5.5	4.81

7.2.1.1 SEM and EDX analysis

Deposits of all tubes in Figure 7.15 were collected and analysed with SEM. Micrographs are shown in Figure 7.16 for bulk and top loose layer deposit on sand. Sand particles were also dried after rinsing with DI water, and analysed with SEM which the micrographs are shown in Figure 7.15 (c_1, c_2, c_3 and c_4).

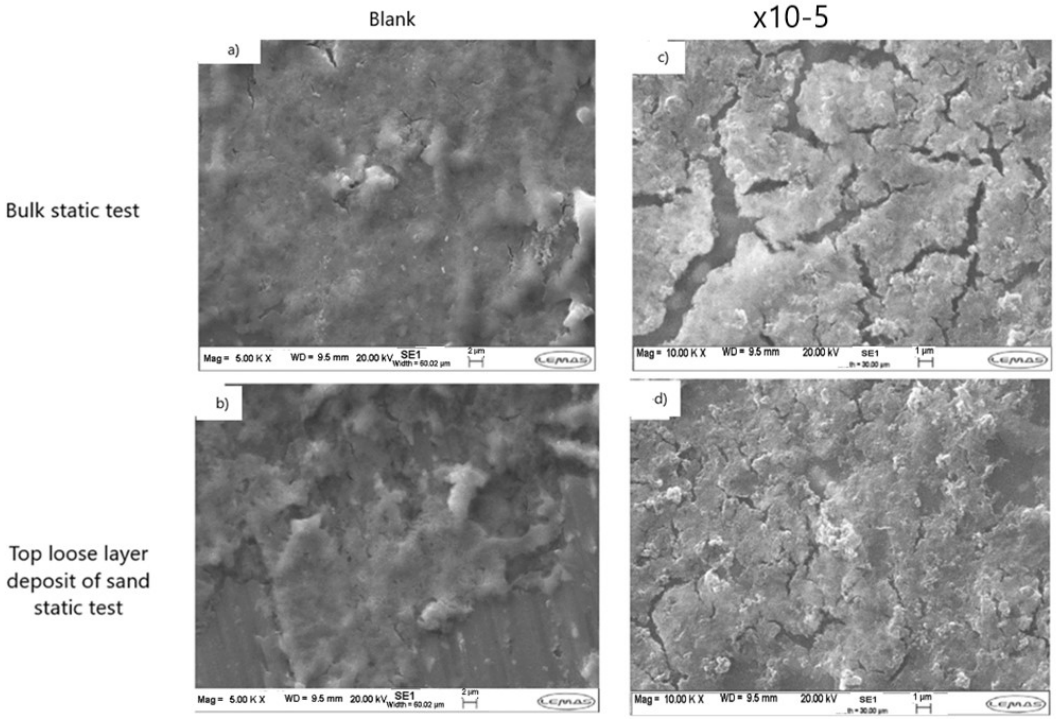

Figure 7.16: SEM micrographs for static jar deposition in bulk (a,c), and sand top layer (b,d) for blank (a-b) and X10-5 (c-d) sample

In general, for both sets of tests (bulk and sand static), SEM micrographs of top loose deposit layers on the sand and bulk tests resembled in morphology, yet they were completely dissimilar to the morphology of the scale grew on sand particle samples. As for the blank sample, the deposit in Figure 7.16 (b) showed a completely smooth and snow dust shape morphology very similar to Figure 7.16 (a). Nevertheless, micrographs from Figure 7.15 (c_1) sand particles showed clear growth of cubic ZnS crystals on the surface for the blank sample. Likewise, with the SI included tube, the dense smooth morphology in the bulk static jar test only resembled the morphology to the loose deposit from the sand top layer, Figure 7.16 (c) and (d), respectively. This shows the change of dusty ZnS scale's morphology, once it adsorbs and grows on the surface of the sand particles. Micrographs of sand particles from the SI included tube, are shown in Figure 7.15 (c_2, c_3 and c_4). Compared to Figure 7.15 (c_1), Figure 7.15 (c_2 and c_3) shows flaky deposition grew on the sand particle with no clear edge or crystal shapes of ZnS. This indicates the successful adsorption of X10-5 and X10-6 on ZnS scales and the

disruption of their crystal growth stage. For the FL1-DETA sample, the ZnS formed on the sand showed more compact and smaller crystals, however, with clear edges similar to the blank sample. This means that FL1-DETA also affects the growth stage of ZnS to some extent.

Unfortunately, the SEM images from formed deposits of either bulk or sand static test did not show any conclusive data on the colour change of the PSS-*co*-MA—PANI formed deposit in green, hence, all samples from the bulk test were compared through TEM and SAED technique.

7.2.1.2 TEM and SAED analysis

For further investigation on the discolouration of X10-5 and X10-6 compared to blank and FL1-DETA deposits, samples were all compared through TEM analysis where the corresponded nanographs are presented in Figure 7.17 (a-d) in the absence and (e-h) in the presence of X10-6. X10-5 and FL1-DETA TEM/SAED nanograph and SEM micrographs are shown separately in Figure 7.18 and 7.19, respectively.

TEM images reveal that all smooth areas observed on lower magnification SEM micrographs, consist of numerous nanoscale ZnS crystals for both blank and inhibited samples. Figure 7.17 (d) confirms the formation of ZnS crystals by presenting the measured d-spacing of blank ZnS crystals at $\overline{(100)}$ and $\overline{(101)}$ plane. SAED and FFT[1] of all samples are included in Figure 7.17, Figure 7.19 and Figure 7.18. Interestingly TEM, SAED and corresponded d-spacing and FFT images of both blank and FL1-DETA deposits were similar. However, this was not the case for X10-6 and X10-5 samples. This means that even though FL1-DETA affect the crystal size of ZnS through growth inhibition it does not affect its lattice.

Table 7.4: D-spacing of ZnS crystals in the presence and absence of inhibitor with their corresponding miller indices.

Blank d-spacing (A°)	X10-6 d-spacing (A°)	X10-5 d-spacing (A°)	FL1-DETA d-spacing (A°)	(h k l)
3.22	4.9	4.91	4.9	100
3.16	3.06	3.02	3.09	002
3.07	2.89	2.85	2.91	101
1.89	1.86	1.84	1.88	110
1.80	1.78	1.76	1.80	103
1.58	1.56	1.55	1.57	112

[1]Fast Fourier transformation

In general, SAED is a collective effect of electron interaction from the bulk and the surface of the analysed sample, whereas FFT is only the electron diffraction from the surface in the selected area (the red rectangle). Blank sample's SAED in Figure 7.17 (a) and FFT in Figure 7.17 (b) depict similar clear diffraction rings. This shows that both the bulk and surface of the blank sample have similar polycrystalline nature. However, for X10-6 green deposits, there was a discrepancy between the collected SAED from the bulk as shown in Figure 7.17 (e) and the FFT analysis of the surface as shown in Figure 7.17 (f). Whereby, the SAED shows a polycrystalline structure for the bulk, whereas, FFT confirms an amorphous surface. Furthermore, collected diffraction rings in Figure 7.17 (e) of the X10-6 deposit, does not show similar intense signals as for the blank sample in Figure 7.17 (a). The same explanation applies for X10-5 which its TEM nanographs, SAED and FFT are shown in Figure 7.18. The discrepancy between SAED and FFT for these samples shows the dissimilarity of the bulk nature and its structure, to the surface of individual ZnS crystals in green shaded deposits.

It is worth to note that based on the patent suggested mechanism for FL1-DETA inhibition [12], sulphide scales (ZnS, PbS and FeS) inhibition, occurs due to the existence of the non-paired active electrons that are located on the DETA (nitrogen) structure that react with Zn^{2+}, Fe^{2+} and Pb^{2+}. However, based on coordination chemistry theories [215], non-paired electrons located on nitrogen can only chelate cations from the transition metal group. Although Fe is from this group, Zn belongs to post transition metal group as it has the electronic configuration of $d_{10}s_2$ with no incomplete d shell, while Pb is not associated with any of the groups mentioned. Hence, formation of a coordination compound as a mechanism of inhibition should only be expected for Fe and high concentrations of Zn. Therefore, the poor performance of FL1-DETA against PbS as well as the TEM images achieved from FL1-DETA in the presence of ZnS can be explained.

Comparing SAED with FFT and considering the nanographs, it was revealed that PSS-*co*-MA—PANI composites have the ability to wrap around ZnS nano-crystals thus changing the d-spacing, as listed in Table 7.4. As explained, even though the none paired electrons can contribute to chelateing Zn^{2+} to some extent, however, the wrapping is most probably due to the positive charges located on the PSS-*co*-MA—PANI structure through electrostatic interaction with the negatively charged ZnS and PbS [216]. As a result of wrapping, the formed deposit changes colour to green shade of PSS-*co*-MA—PANI composites. The benefit of this behaviour can clearly be observed where the crystal growth and nucleation of the ZnS scale are disturbed on sand particles in Figure 7.15 (c_2 and c_3).

Figure 7.17: TEM analysis of aggregated ZnS crystals formed in bulk for blank sample (a-d) and secluded ZnS crystals wrapped in X10-6 for inhibited sample (e-h). TEM nanographs: (c-d, g-h); SAED: (a),(e) and FFT: (b),(f) of the selected area in red square. The amorphous FFT signal from inhibited sample shows the surface of the ZnS crystals are covered with the polymer.

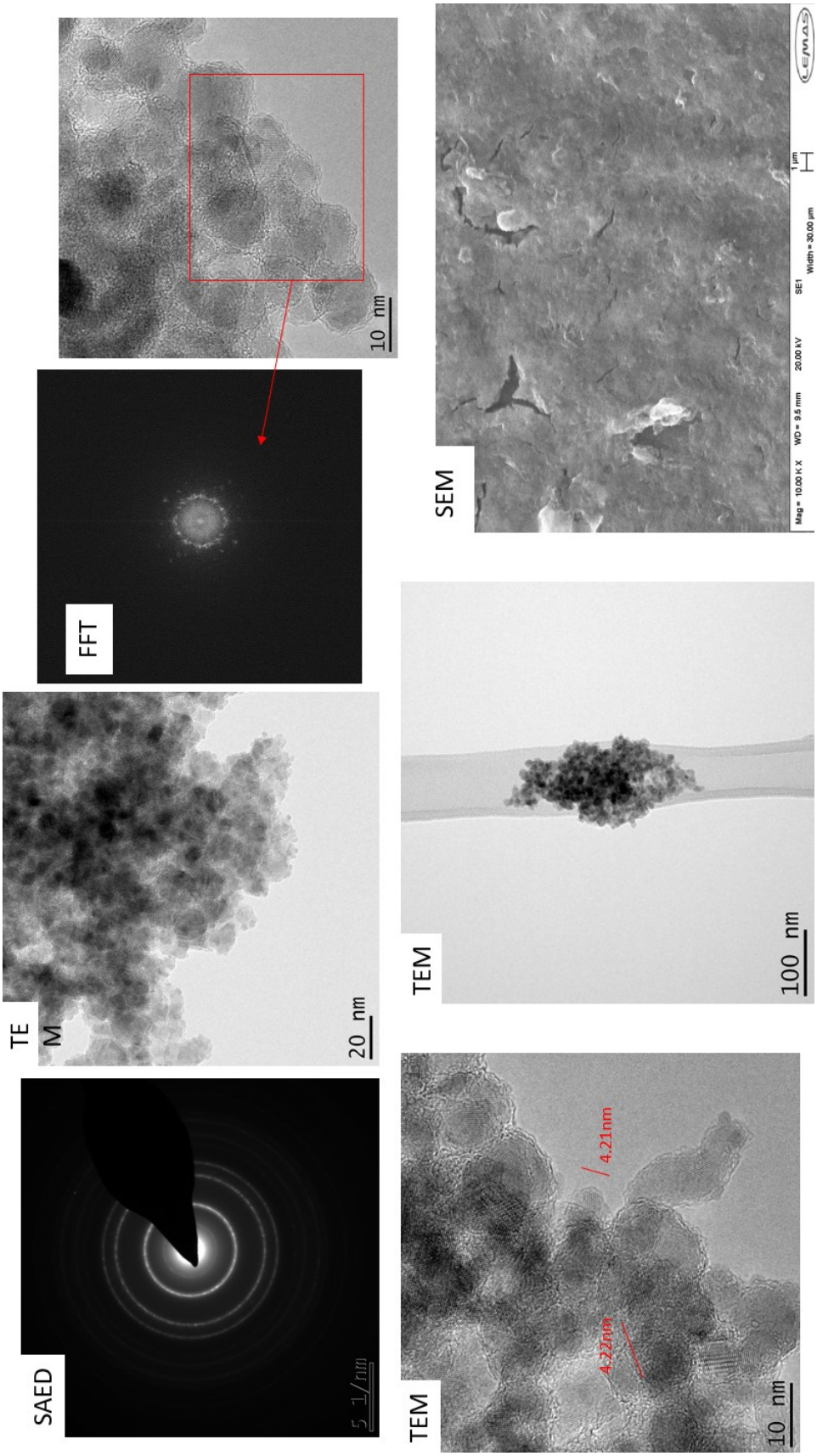

Figure 7.18: SEM micrograph and TEM nanographs of secluded ZnS crystals in the presence of X10-5 wrapped in inhibitor. Both SEM and TEM images are from the bulk static test in simple brine and the absence of sand particles.The amorphous signal FFT from inhibited sample shows the surface of the ZnS crystals are covered with the polymer.

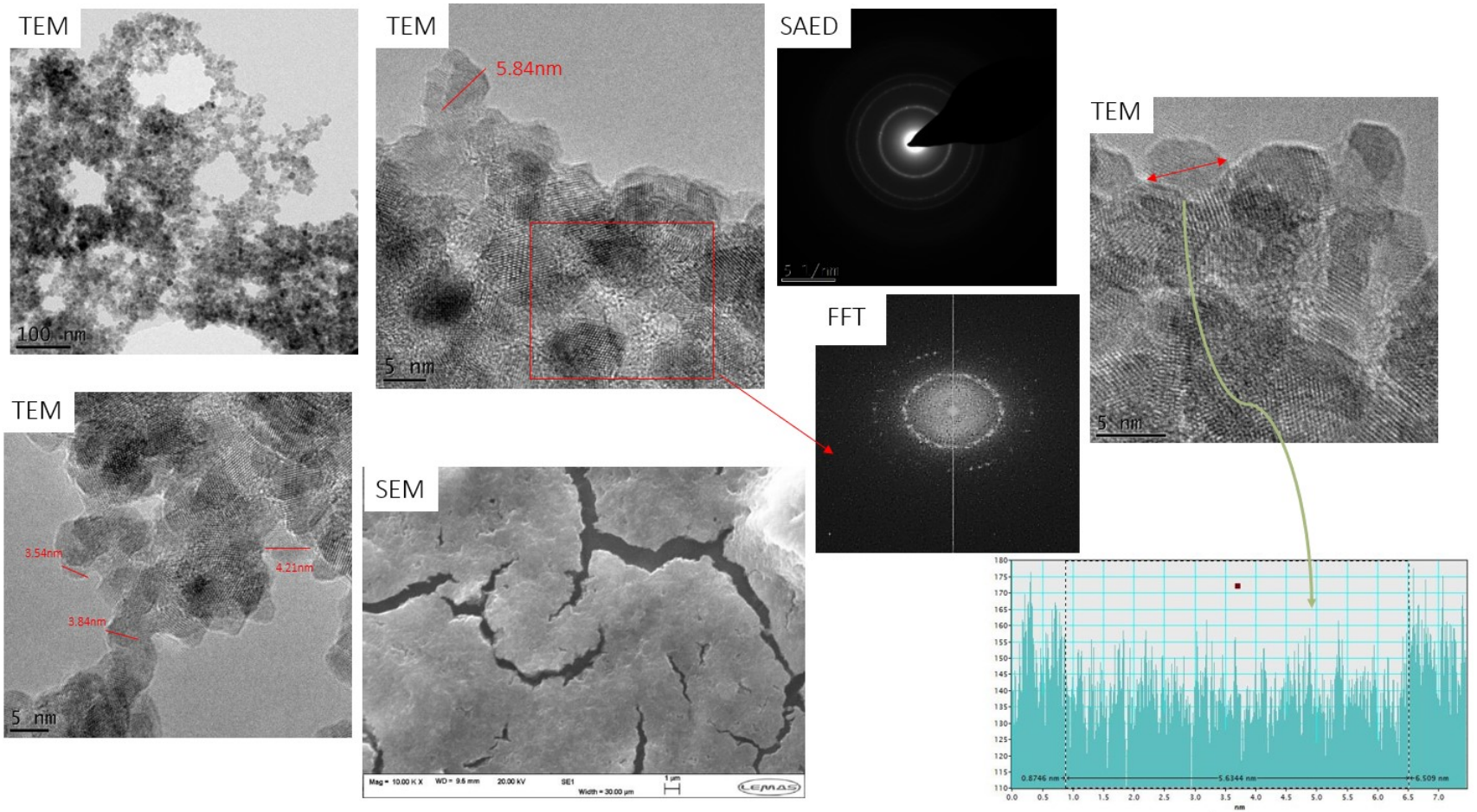

Figure 7.19: SEM micrograph and TEM nanographs of aggregated ZnS crystals in the presence of FL1-DETA inhibitor. Both SEM and TEM images are from the bulk static test in simple brine and the absence of sand particles. The polycrystalline FFT signal from inhibited sample shows the surface of the ZnS crystals are not covered with the polymer, hence the ZnS crystal sizes are bigger in size compared to PANI samples and aggregate.

7.3 Dynamic tests

7.3.1 Tube blocking test for ZnS

The tube blocking[1] test was conducted in the presence of 5 ppm H_2S where the saturation index of ZnS is calculated to be 5.24. The pH was adjusted to 4.6 for the whole duration of the test, using an acetic acid-acetate buffer. Due to the special morphology of the sulphide scales, it is conventional for easier interpretation of results, to use a filter at the end of the line to collect the formed deposit and receive a measurable pressure difference (dP). As a result, dP was measured for both coil and in the presence of the 7-micron filter. An increase of pressure through the line will be a sign of blockage caused by scale formation i.e. ZnS as it will narrow the coil tube or block the filter.

Different inhibitors were added individually, one at a time in different concentrations and the dP was recorded over an hour period. Later, to determine the type and abundance of deposits collected on the in-line filter after each run, the filter was cleaned with Reverse Osmosis (RO) water and analysed by SEM/EDX. The SEM/EDX micrographs are shown in Figure 7.20 for blank (uninhibited) sample, Figure 7.21 for FL1-DETA, Figure 7.22 for X10-6 and Figure 7.23 for X10-5 and Figure 7.24 for X5-5. These results are summarised in Table 7.5.

Table 7.5: Summary of results for ZnS tube blocking dynamic test

Scale Inhibitor	Active Concentration (mg/l)	Increase in dP (psi) (after 1 hour)		SEM	Appendix B Image No.	MED (mg/l) Weighted On SEM/EDX
		Coil	Filter			
Blank / Optimisation	0	0.0 0.1	2.0 1.5	High ZnS	1 - 2	
FL1-Deta	0	0.1	1.5	High ZnS	3	≤ 1 mg/l
	1	0.1	0	Trace ZnS	4	
	3	0.0	0	Trace ZnS	5	
	5	0.0	0	Trace ZnS	6	
X5-5-W	0	0.0	1.0	High ZnS	7	5 – 10 mg/l
	5	0.1	3.1	Moderate ZnS	8	
	10	0.1	0.5	Trace ZnS	9	
	30	0.0	17.0	Trace ZnS	10	
X10-5-W	0	0.0	1.5	High ZnS	11	≤ 5 mg/l
	5	0.0	0.3	Trace ZnS	12	
	10	0.0	7.6	Trace ZnS	13	
	30	0.0	0.5	Trace ZnS	14	
X10-6-W	0	0.1	1.4	High ZnS*	15	≤ 5 mg/l
	5	0.0	0.2	Trace ZnS	16	
	10	0.3	2.1	Trace ZnS	17	
	30	0.0	0.2	Trace ZnS	18	

[1]These tests were run by a third party, arranged through the sponsor of the project

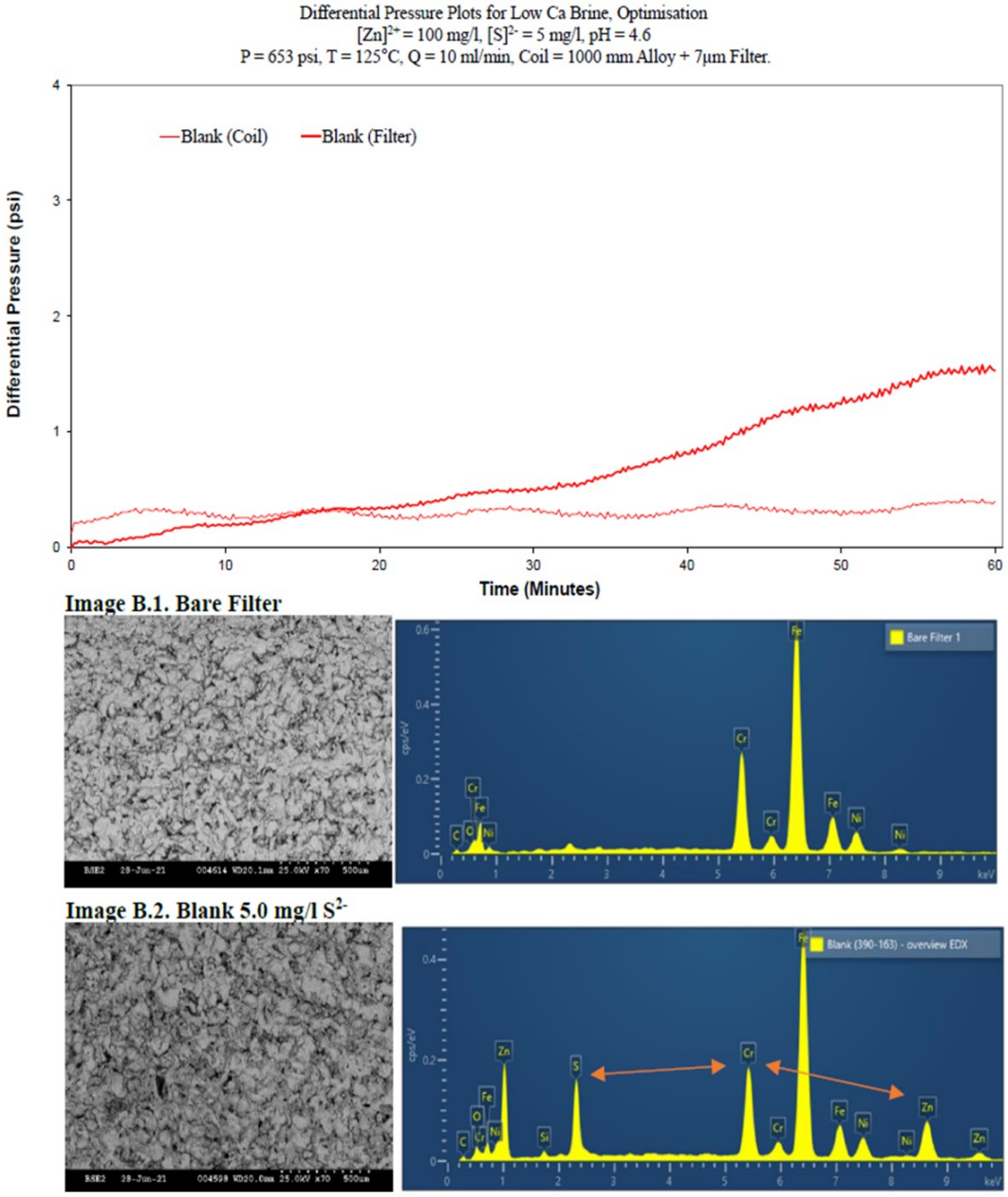

Figure 7.20: Tube blocking test for ZnS scaling in the absence of inhibitor. SEM/EDX images results of the filter shows decreased signal for zinc element in respect to chromium as a reference peak

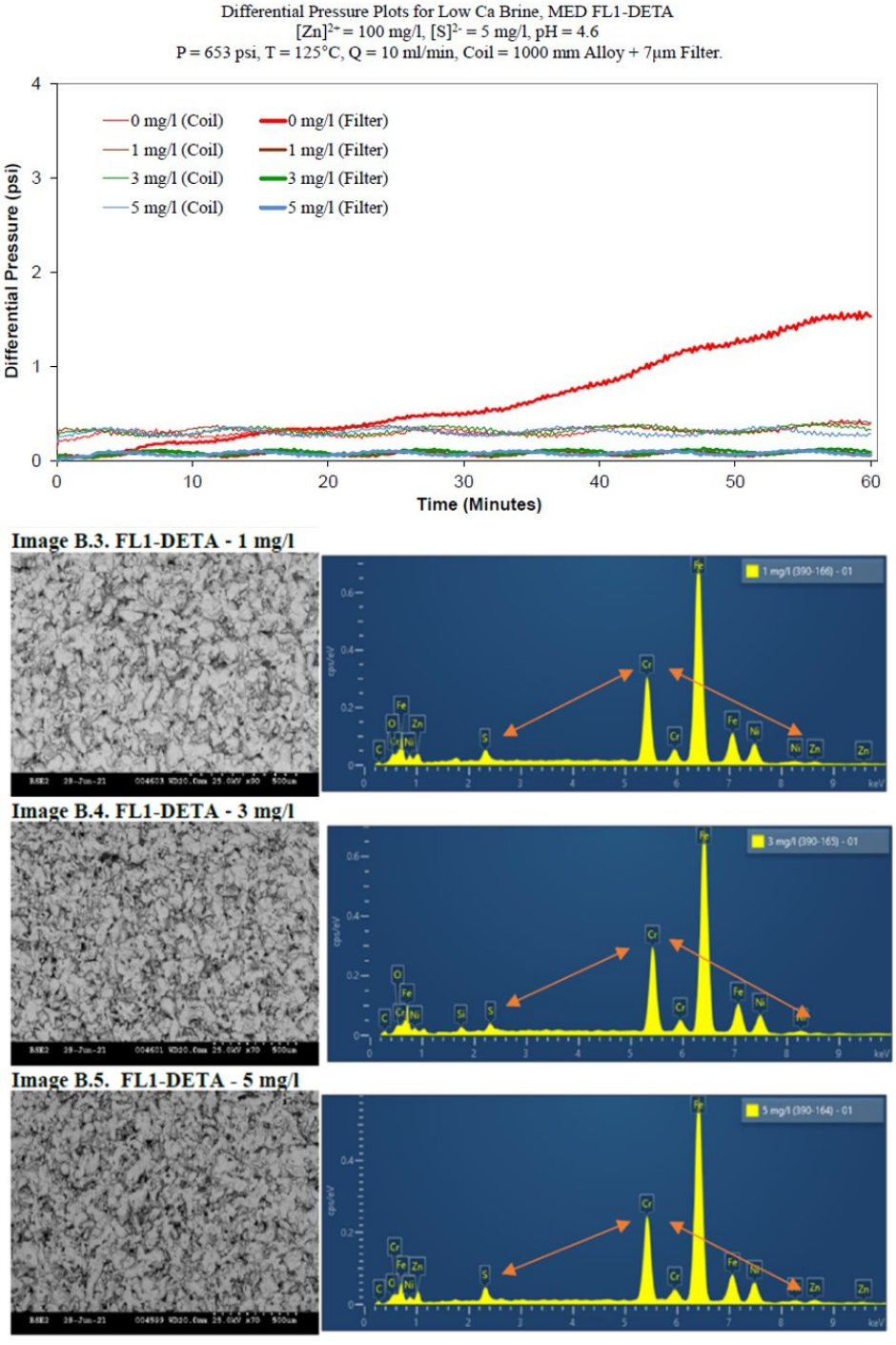

Figure 7.21: Tube blocking test for ZnS scaling in the presence of different FL1-DETA concentration. SEM/EDx images results of the filter shows decreased signal for zinc element in respect to chromium as a reference peak

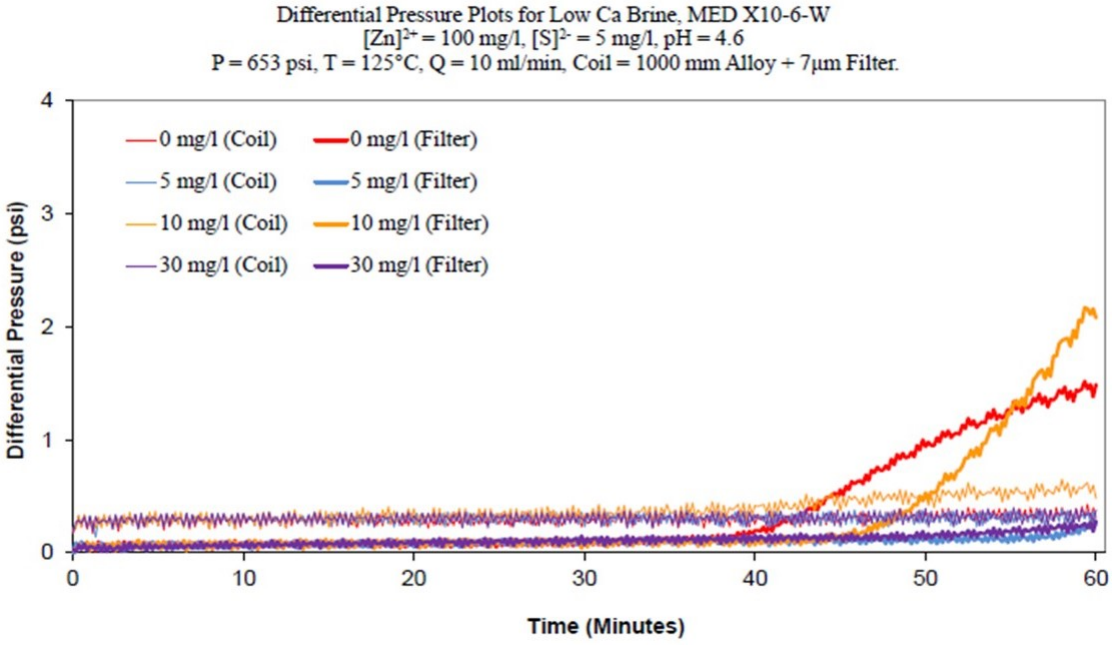

Image B.15. X10-6-W - 5 mg/l

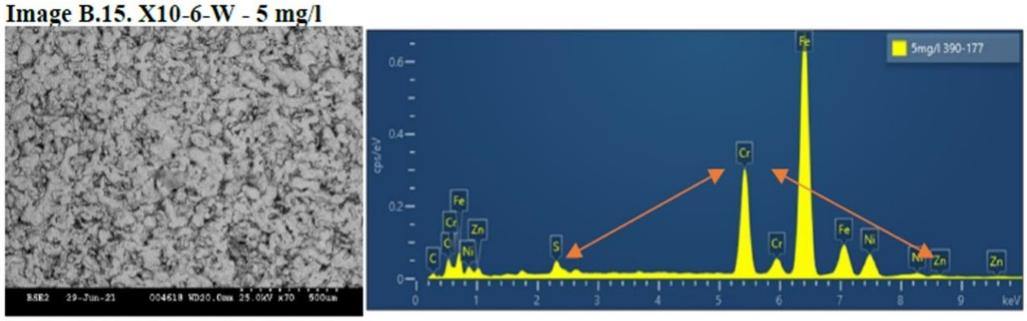

Image B.16. X10-6-W - 10 mg/l

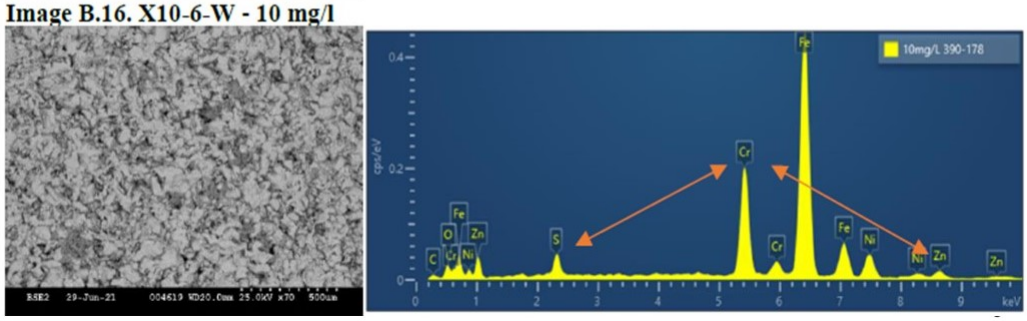

Figure 7.22: Tube blocking test for ZnS scaling in the presence of different X10-6 concentration. SEM/EDx images results of the filter shows decreased signal for zinc element in respect to chromium as a reference peak

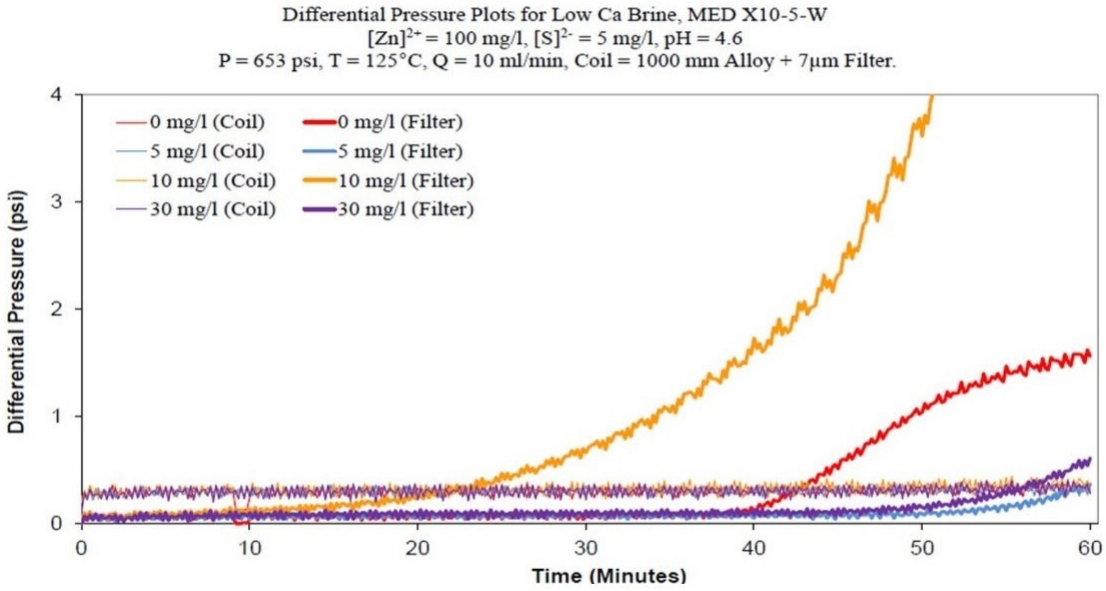

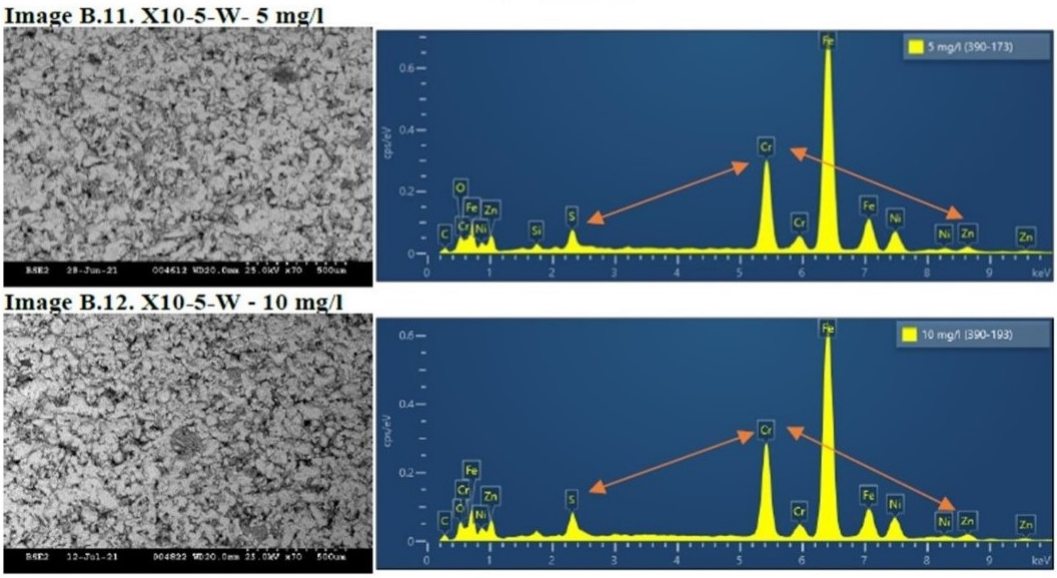

Figure 7.23: Tube blocking test for ZnS scaling in the presence of different X10-5 concentration. SEM/EDx images results of the filter shows decreased signal for zinc element in respect to chromium as a reference peak

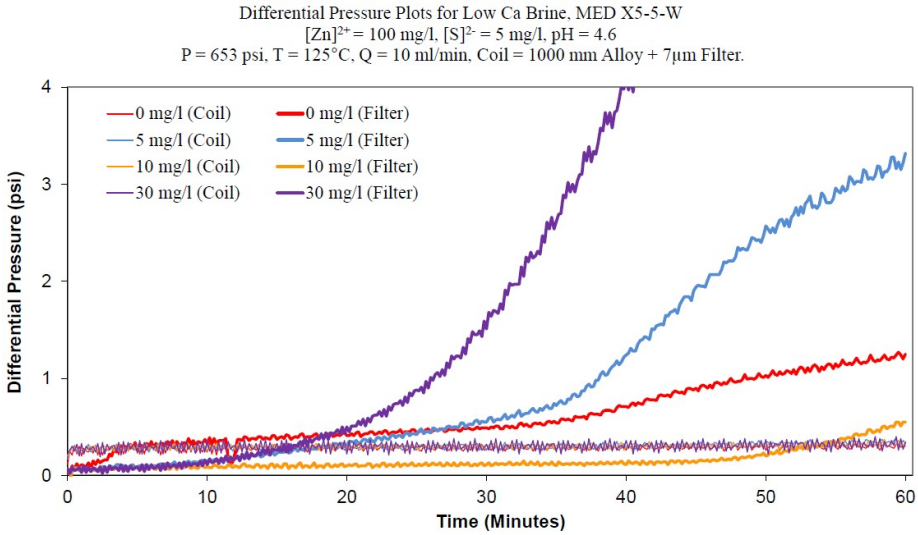

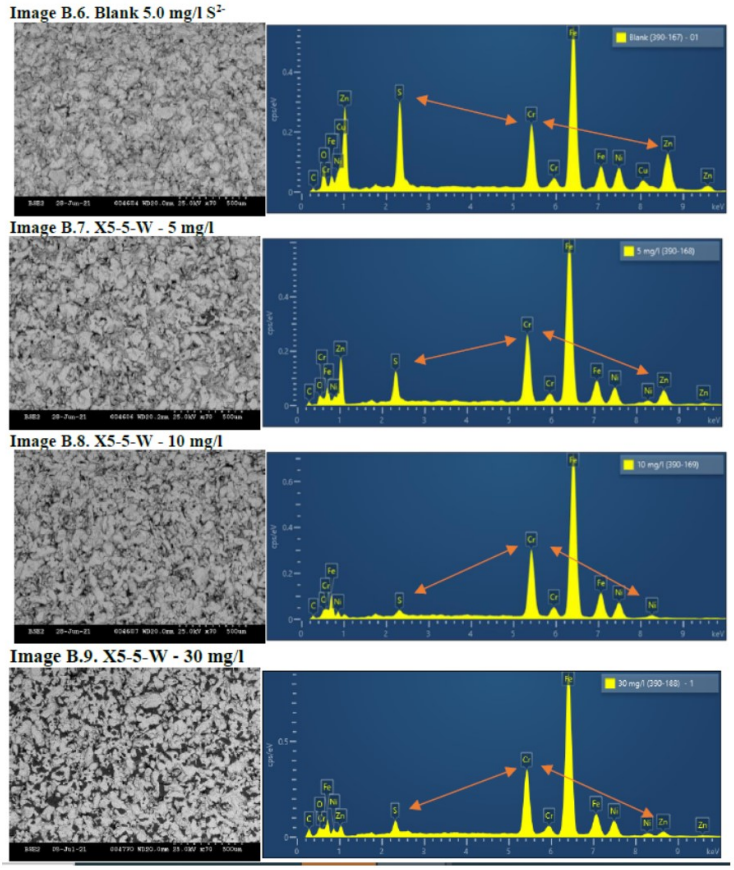

Figure 7.24: Tube blocking test for ZnS scaling in the presence of different X5-5 concentration. SEM/EDx images results of the filter shows decreased signal for zinc element in respect to chromium as a reference peak

The blank test in Figure 7.20 demonstrated scaling in the coil with an average dP increase of ≤ 0.1 psi in 60 minutes and dP increase of 2 to 1.5 psi across the 7 μm filter. In general, for PSS-*co*-MA—PANI and FL1-DETA samples the increase in dP across the coil was consistently less, compared to the blank run (in red) on the same day. However, unlike FL1-DETA results provided in Figure 7.21, higher dP's were occasionally observed across the filter in the presence of the all PSS-*co*-MA—PANI samples i.e. Figure 7.22 for X10-6 and Figure 7.23 and Figure 7.24 for X10-5 and X5-5, respectively. This could be due to the PSS-*co*-MA—PANIs web shape morphology which were shown in Figure 6.6 and long chains of PANI that can coil up or get tangled at certain concentrations. Due to the presence of positive charges on the backbone of PANI causing repulsion, the formed coils will be loosely tangled [217]. The coiling effect can also be reduced by the addition of side branches on the polymeric structure [218]. As a result, the effect of dP fluctuation is mostly seen for X5-5 with the least amount of voids on its morphology and least number of side branches of PSS-*co*-MA on its structure. The effect becomes less stronger for X10-5 and afterwards, X10-6 with increasing amount of PSS-*co*-MA as side branches which avoid the entanglement of the polymeric chains through steric hindrance effect [218].

On the other hand, at low concentrations, the tangled chains of PSS-*co*-MA—PANI polymers will still be able to pass through the filter as there will be few loosely formed coils [219]. However, as the concentration increases to 10 mg/L there are more numbers of grew coils with increased possibility to block the filter [219]. Nonetheless, as the concentration increases even more i.e. 30 mg/L and above, polymeric chains have less freedom of movement due the increased number of polymers in the media, considering the positively charged structure, PSS-*co*-MA—PANI chains re-orientate themselves with the flow in the pipe and become parallelly aligned. As a result, the filter at the end of line will not get blocked at higher concentrations of X10-5 and X10-6.

To identify the elemental composition of the formed deposit on each filter, EDX analysis was utilised. As a method of assessment, Cr (chromium element) peak intensity, was set as the reference in each EDX analysis. Comparing SEM/EDX images in Figure 7.21 (B.3) for FL1-DETA, Figure 7.22 (B.15) for X10-6 and Figure 7.23 (B.11) for X10-5 with blank's run in Figure 7.20 (B.2) and the bare filter (B.1), it was revealed that the formed deposits for all inhibitors, i.e. PSS-*co*-MA—PANI experiments and FL1-DETA, only contained small traces of ZnS after one hour duration of the test. Whereas, this was an intense peak for the blank run in the absence of any SI, forming deposits characterised as mainly ZnS. Considering minimal dP increase in the filter and no increased dP in the coil setup for X10-6 and X10-5 runs, as well as SEM/EDX results, the minimum effective dose (MED) of administration of both SIs was identified as 3-5 mg/L.

Nonetheless, FL1-DETA showed the best performance amongst all inhibitors, producing minimal dP increase over coil and in-line filter as well as reduced ZnS deposition on the filter. The MED for the FL1-DETA sample was identified as 1 mg/L, 2-3 mg/L

less than PSS-*co*-MA—PANI samples. This results show that the modified SI, PSS-*co*-MA—PANI, similar to its original SI structure, FL1-DETA can inhibit the excess formation of ZnS scale, however, with improved properties.

Even though X5-5 showed inhibition performance toward ZnS deposition based on its Edx results, the sample was disregarded for future experiments as it caused extreme dP increase across the filter, Figure 7.24.

7.3.2 Tube blocking test for PbS

To identify the MED and performance of each scale inhibitor against the PbS scale, tube blocking tests with the same condition as stated in the section 7.3.1 were carried with the simplified brine 2 as listed in Table 3.4. The brine has a saturation index of 4.29 for PbS at 125 °C and 653 psi with buffered pH at 4.5. dP in the rig was measured for both coil and in the presence of the 7-micron filter over 60 minutes. The variation of dP over time as well as SEM/EDX micrographs of each sample are shown in Figure 7.25 for blank (uninhibited) sample, Figure 7.26 for FL1-DETA, Figure 7.27 for X10-6 and Figure 7.28 for X10-5. These results are summarised in Table 7.6. In all EDX data, Fe peak intensity was set as reference peak in all EDX spectra to be compared to Pb signal.

Table 7.6: Summary of results for lead Sulphide tube blocking dynamic test

Scale Inhibitor	Active Concentration (mg/l)	Increase in dP (psi) (after 1 hour)		SEM	Appendix G Image No.	MED** (mg/l) Weighted On SEM/EDX
		Coil*	Filter			
Blank / Optimisation	0	0.6	0.9	High PbS	1 - 2	NA
FL1-Deta	0	0.3	0.9	High PbS	3	> 100
	30	0.1	1.9	High PbS	4	
	50	0.2	2.2	High PbS	5	
	100	0.1	2.5	High PbS	6	
X5-5-W	0	0.2	0.9	High PbS	7	> 100
	30	0.1	1.9	High PbS	8	
	50	0.0	2.9	High PbS	9	
	100	0.0	13.9	High PbS	10	
X10-5-W	0	1.0	1.1	High PbS	11	> 100
	30	0.1	3.1	High PbS	12	
	50	0.0	6.2	High PbS	13	
	100	0.0	41.4	Reduced PbS	14	
X10-6-W	0	0.3	0.9	High PbS	15	> 100
	30	0.1	2.8	High PbS	16	
	50	0.0	4.2	High PbS	17	
	100	0.1	11.1	Reduced PbS	18	

As Figure 7.25 shows, in the absence of scale inhibitors i.e. blank sample, the dP behaviour for the coil shows spikes of blockage after 40 minutes, whilst the effect shows

itself much more quickly with the filter in place, after 10 minutes. The comparison of the SEM micrograph in Figure7.25 of the blank sample with the bare filter shows the full coverage of the filter with a smooth layer of deposit/scale. EDX analysis of the filter shows strong signals of Pb and sulphur which represent the PbS scale. FL1-DETA results showed more or less the same behaviour as blank with the difference in higher dPs in the presence of filter and increase of [SI] up to 50 mg/L. As SEM micrographs in Figure 7.26 show, the filter was completely covered with the PbS scale. As a result, FL1-DETA did not show any performance against the PbS scale thus no MED was assigned to it. Likewise, X5-5 did not show any performance against the PbS scale. This could be due to the X5-5 nature that is more similar to FL1-DETA based on its FL1 to PANI ratio during its synthesis procedure.

On the other hand, the other two PSS-*co*-MA—PANI samples, X10-6 and X10-5, both reduced the amount of PbS scale on the filter at concentrations above 50 mg/L. They both showed lower dPs in the coil compared to the uninhibited (blank) test on the same day test, however, the filter dP results were significantly higher. This side effect was previously explained in section 7.3.1. Based on these results, the MED for both X10-5 and X10-6 was identified as 100 mg/L. The performance of PSS-*co*-MA—PANI composites with the increased level of PANI could be due to none paired electrons available on PANI surface forming legands with Pb or due to the positive charges available on the structure. These possible mechanisms were all explained in Chapter 2. As x10-5 showed, stronger performance against PbS as compared to X10-6, the sandpack test in section 7.3.3 was carried with this formula.

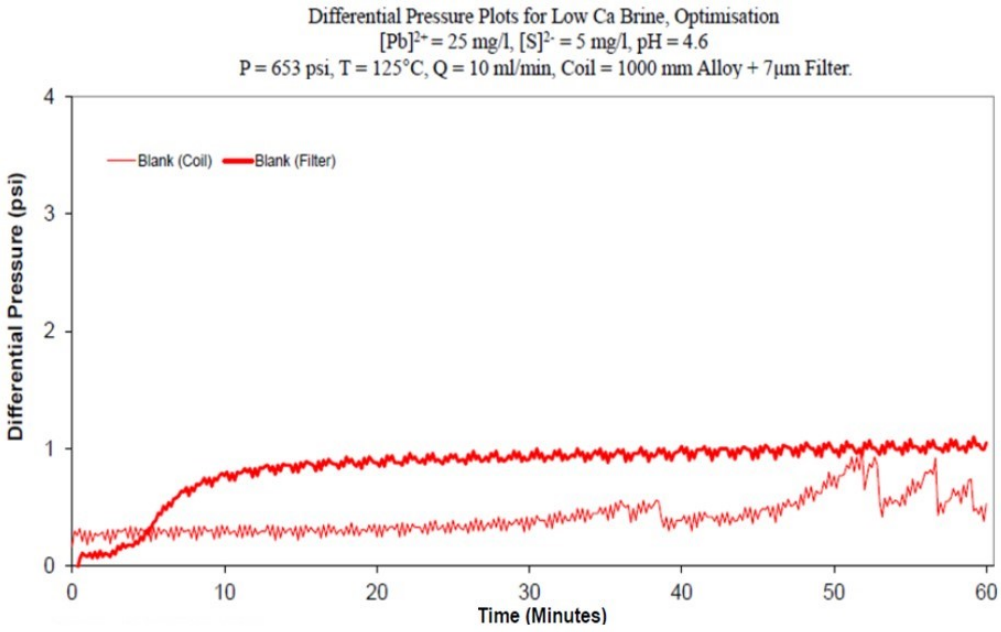

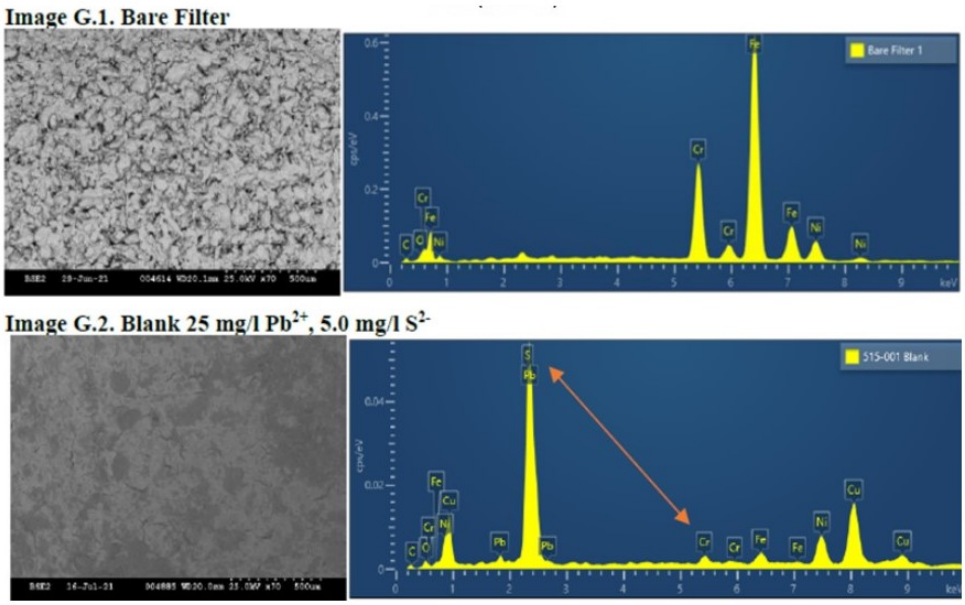

Figure 7.25: Tube blocking test for PbS scaling in the presence of different X10-6 concentration. SEM/EDx images results of the filter shows decreased signal for lead element in respect to chromium as a reference peak

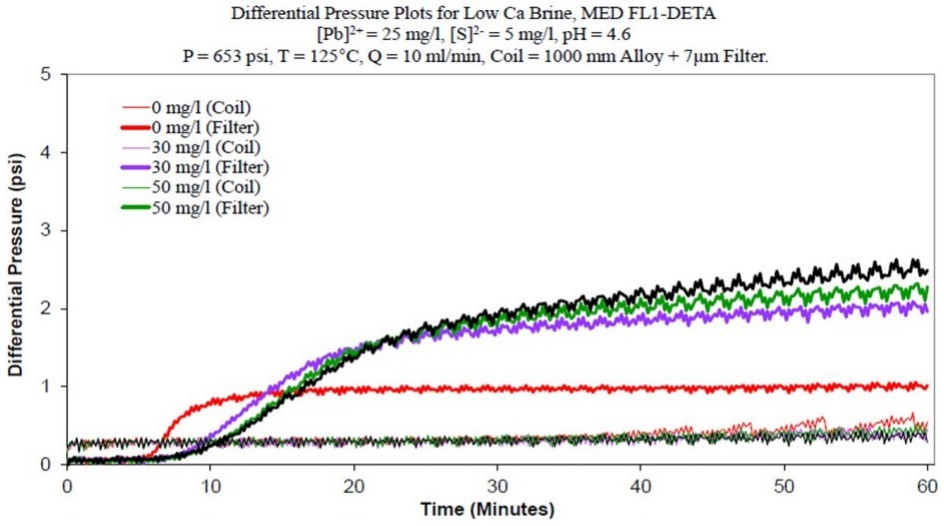

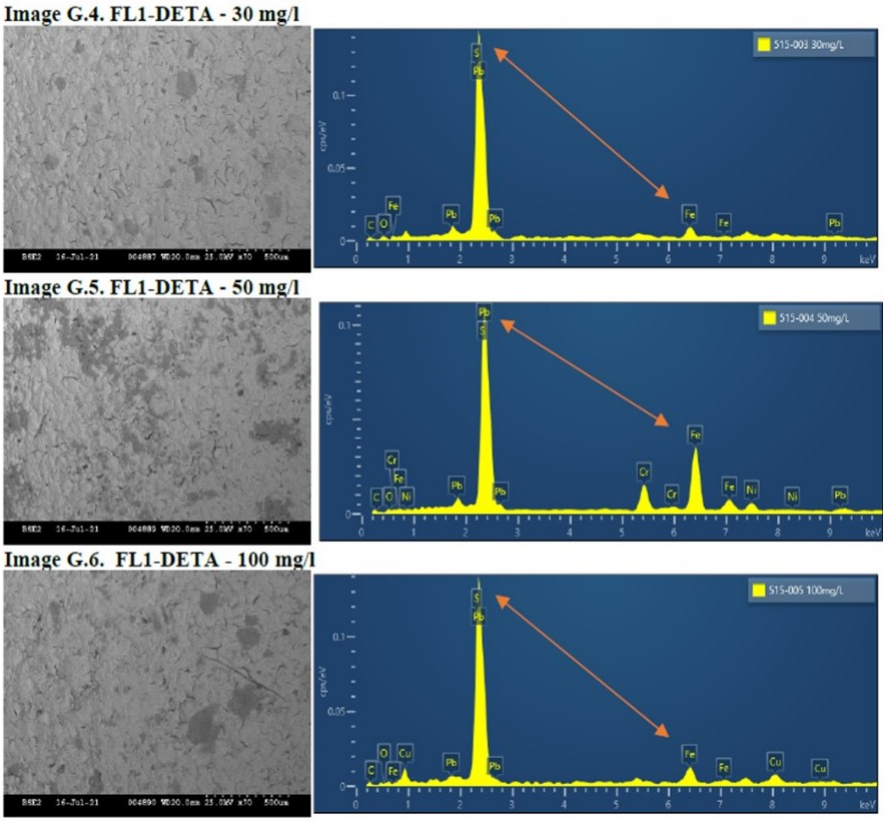

Figure 7.26: Tube blocking test for PbS scaling in the presence of different FL1-DETA concentration. SEM/EDx images results of the filter shows decreased signal for lead element in respect to chromium as a reference peak

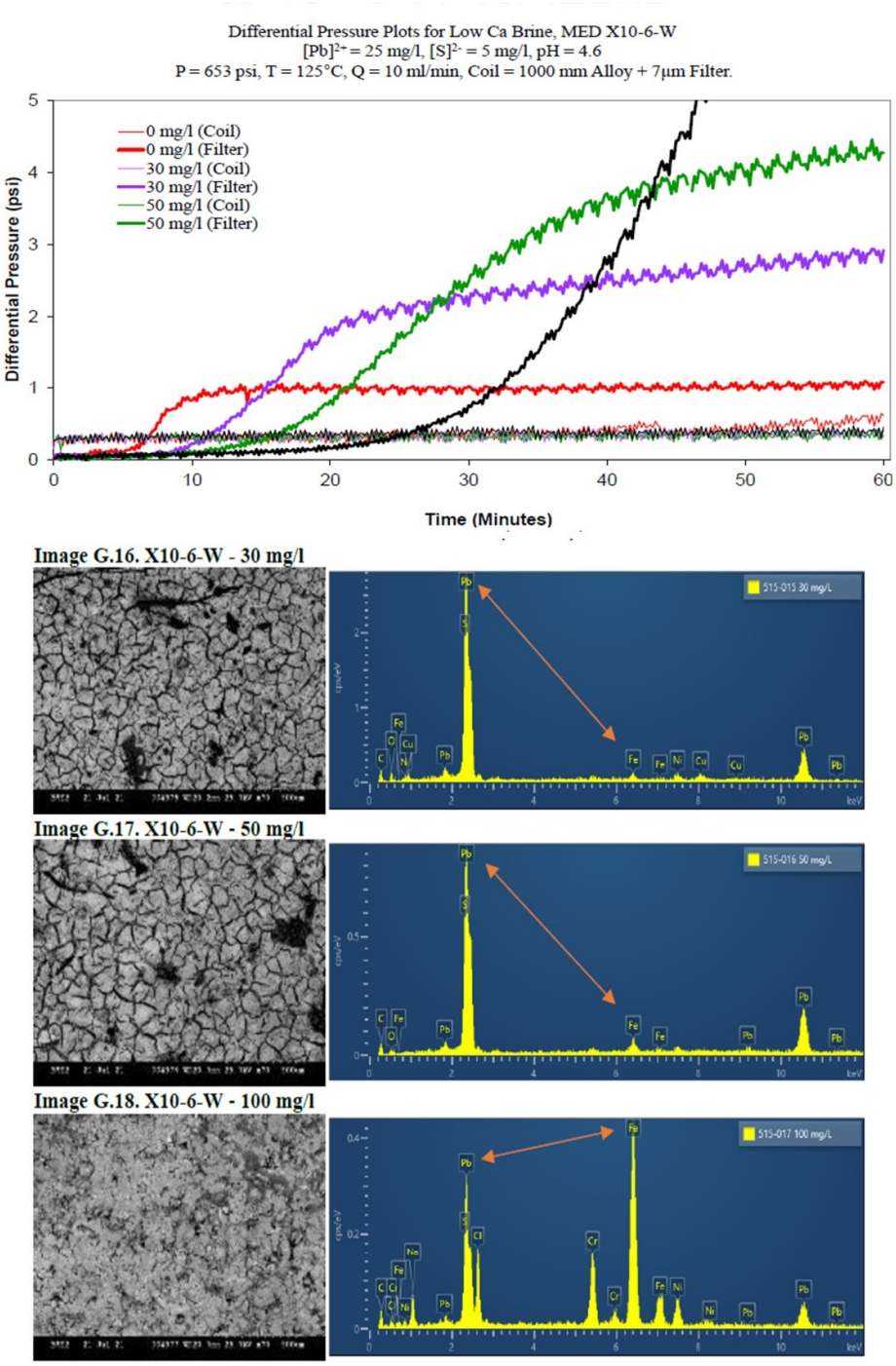

Figure 7.27: Tube blocking test for PbS scaling in the presence of different X10-6 concentration. SEM/EDx images results of the filter shows decreased signal for lead element in respect to chromium as a reference peak

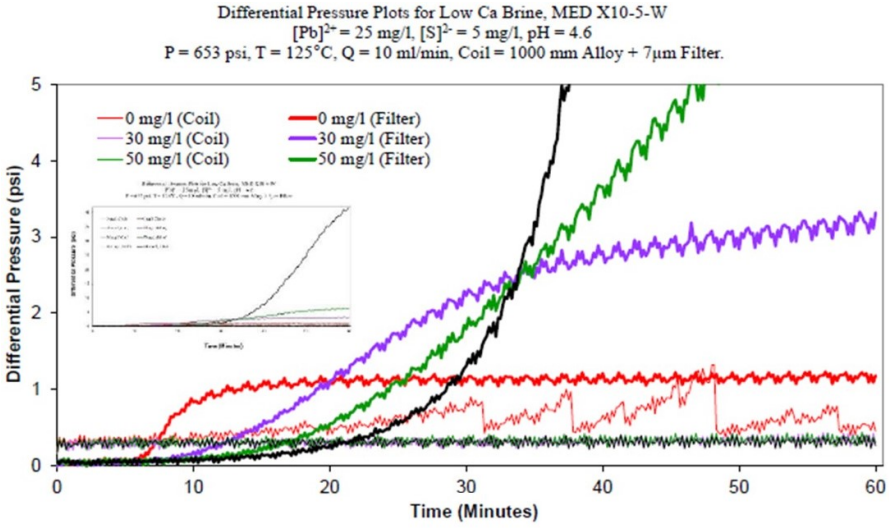

Image G.12. X10-5-W- 30 mg/l

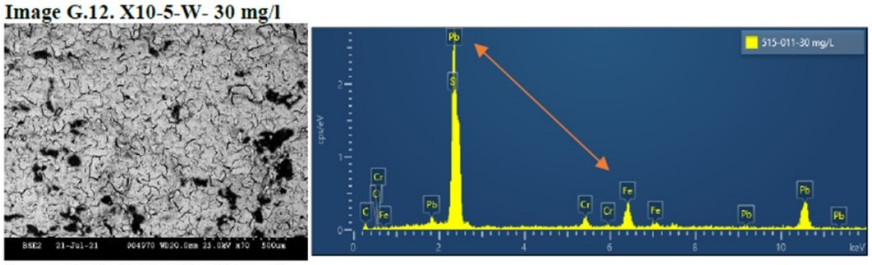

Image G.13. X10-5-W - 50 mg/l

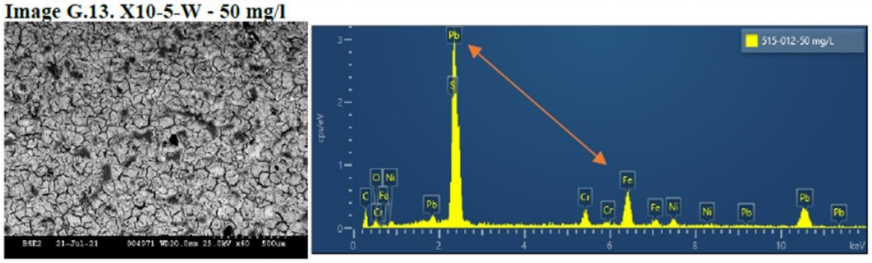

Image G.14. X10-5-W - 100 mg/l

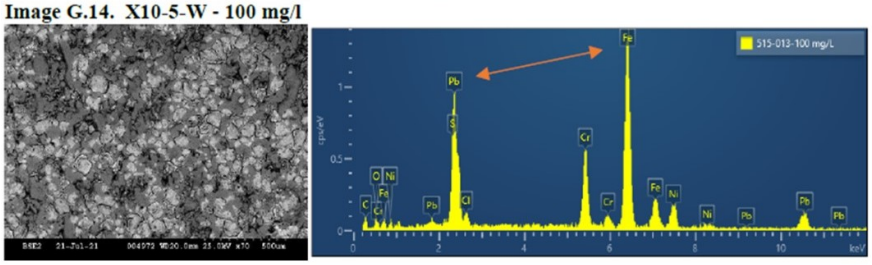

Figure 7.28: Tube blocking test for PbS scaling in the presence of different X10-5 concentration. SEM/EDx images results of the filter shows decreased signal for lead element in respect to chromium as a reference peak

7.3.3 Sandpack test

For the running the sandpack the experimental setup explained in Section 3.3.2 was followed. As it was explained, lithium is a non reacting element which will not adsorb on the sand particles. Hence, it can be used as a benchmark for evaluating the saturation period and adsorption of inhibitors before the shutdown and during the injection stage. The deviation between the SI and the lithium tracer profile is a measure of the amount of SI adsorption/precipitation [157]. As there are no complexing cations such as calcium in the SW brine composition, it is believed that the delay in saturation period of the column is solely caused by adsorption. Figure 7.29 depicts the profile of X10-5 (in green) and the lithium tracer (in purple) for MT and the initial PF with SW over 20 PV. Compared to the lithium tracer, X10-5 shows significant delay in saturation period which this is shown as the highlighted blue region in Figure 7.29, hence, the pure adsorption of X10-5 on the sand particles. Figure7.31, shows the MT and initial PF profile for the lithium tracer (in purple), X10-5 and FL1-DETA (in blue) over 20 PV. Comparing the MT profiles, both X10-5 and FL1-DETA show some level of adsorption to the sand particles, yet as expected based on the static adsorption test results presented at section 7.1.2, this was more significant for X10-5.

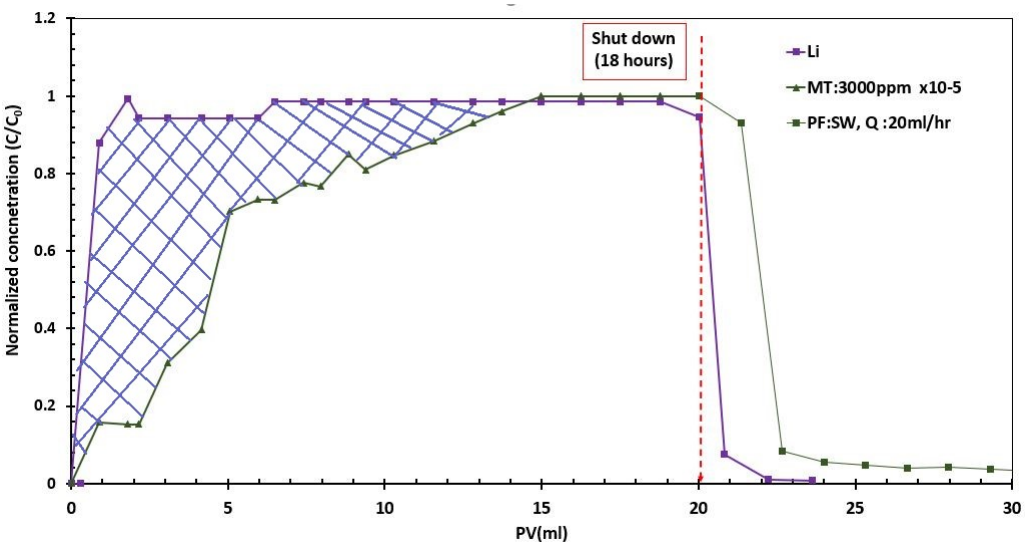

Figure 7.29: Pure adsorption of X10-5 through MT and the initial PF profile.

Figure 7.30 shows the change in sand's colour after the MT stage and X10-5 adsorption.

After 20 PV of MT and saturation of the column, the sand pack was shutdown for 18 hours at room temperature and the return profile was created using SW as the PF with Q = 20ml/hr. The first 10 PV of the PF (initial PF) is shown in Figure 7.31 and 7.29. As it can be seen clearly in Figure 7.31, FL1-DETA has shown an immediate

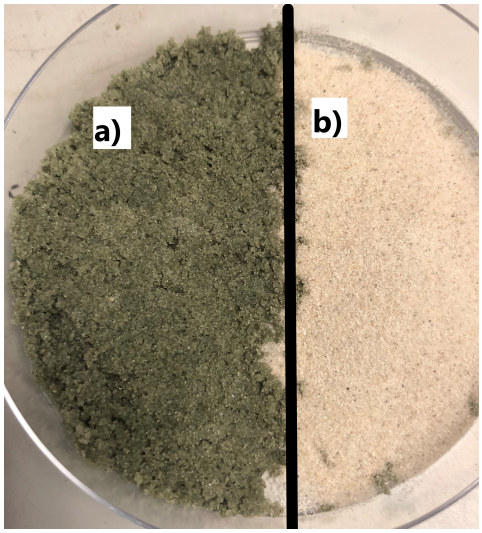

Figure 7.30: a)Adsorbed X10-5 from the MT on the sand, b)Plain sand

concentration drop in its return profile similar to the lithium steep return. However, in case of X10-5 this return was with a delay. Depending on the later stages of the PF the immediate drop of SI concentration can be a good sign of gradual return above MIC or in other words future long tail in the return graph [32]. However, Figure 7.32 shows the bigger picture of the PF over 200 PVs and the absence of the long tail return.

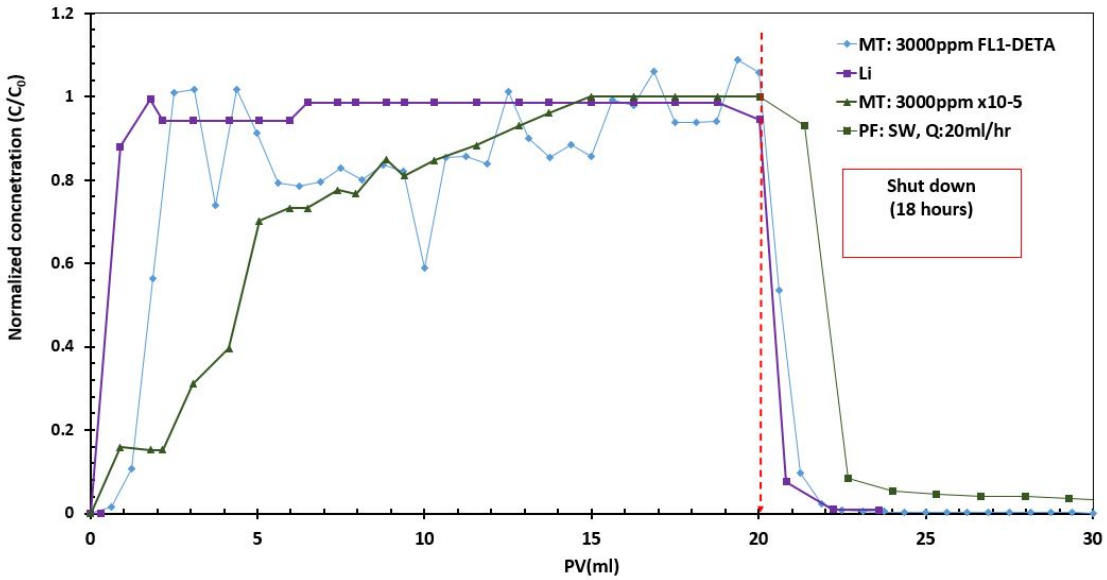

Figure 7.31: MT and the initial PF with SW of Lithium tracer, X10-5 and FL1-DETA for 20 PV

The PF was continued until the inhibitor concentration dropped below the MIC. For better visualisation, the x-axis in Figure 7.32 is highlighted with red at the MIC/MED = 3 mg/L for X10-5 and blue for FL1-DETA at MIC/MED = 1 mg/L. These values were earlier identified through dynamic tube blocking test against ZnS. Based on the return profile presented at Figure 7.32 FL1-DETA drops below 1 ppm before 76 PV or 50 PV after the shutdown stage. Nevertheless, X10-5 shows a higher concentration and more gradual release of the modified inhibitor at above the MIC i.e. 10ppm over 170 PV. This simply shows the better retention properties of X10-5 compared to FL1-DETA.

The sudden spike at 40 PV and the concentration increase at PV = 55 ml in the return profile of FL1-DETA, has been reported by different researchers [157] for other inhibitors such as OMTHP, DTPMP. One theory is that this could be due to the dissolution of the SI-metal complex that was formed during the shutdown period. However, since in this stage the PF brine was SW, this theory can not be applicable. It is worth mentioning that the sandpack test was carried at aerobic conditions, therefore, it could be presumed that the appearance of the spikes in the return profile for FL1-DETA might have been caused by this limitation in the experimental design and the re-dissolution of the inhibitor itself and not the metal complex formation by the brine. However, the increase in the return concentration for X10-5 above 80 PV could be due to metal complex dissolution caused by the Ca^{2+}, present in the CW brine.

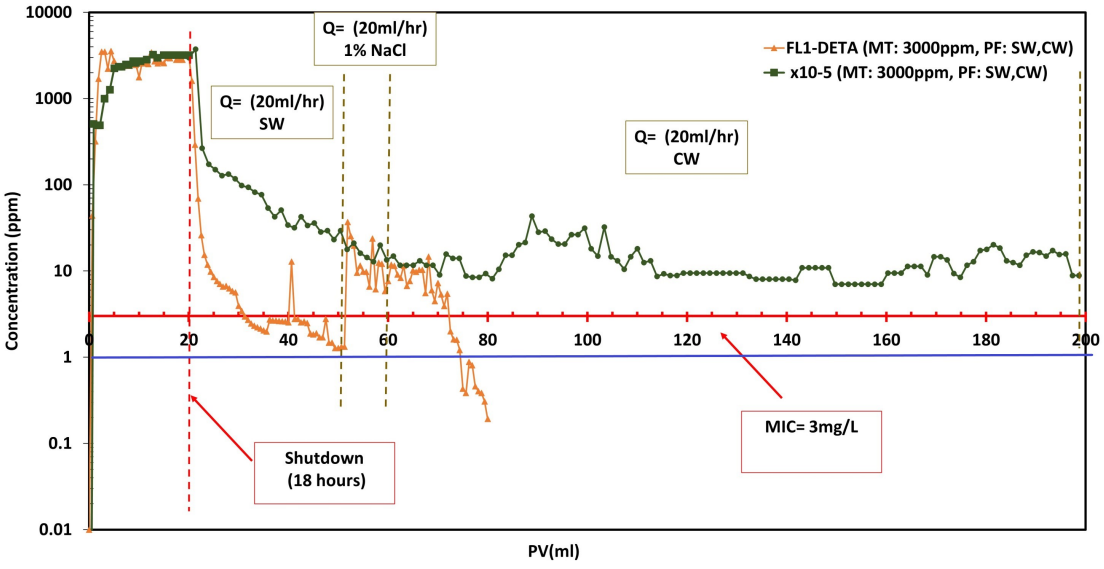

Figure 7.32: X10-5 vs FL1-DETA PF with SW over 200 PV

The mass balance of the column for the MT and PF of both inhibitors are listed in Table 7.7. Results show that after 200 PV of the post flush, there is still $\sim$ 18%

of X10-5 left in the packed column. Figure 7.33 shows the picture from the inside of this column. The changed colour of the sand which is caused by the X10-5 inhibitor adsorption, clearly shows that the column is still loaded with the inhibitor.

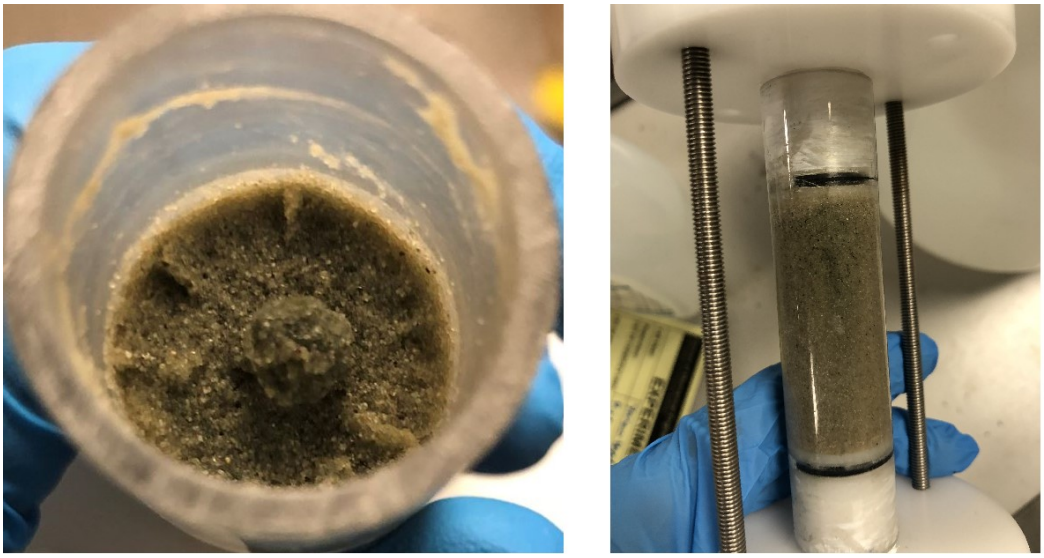

Figure 7.33: Remained X10-5 after 200 PV in the sandpack column

Interestingly, the remained mass after 80 PV in FL1-DETA test shows higher [inhibitor] in the column compared to X10-5. However, concentration measurement from the PF in Figure 7.32 shows the failure of FL1-DETA below the MIC with no following tail in the profile. This could be explained by the incompatibility of FL1-DETA with the CW and the formation of insoluble deposits of SI—Ba^{2+} which was explained in Chapter 5. This incompatibility was seen as a solid deposit at the bottom of collected vials from the PF with the CW. It is worth mentioning, that all collected vials were analysed with Uv-vis at once, in a 1 or 2 days intervals during the test period, meaning the incompatible cloudy returned post-flush collected from FL1-DETA column, had enough time to settle, thus showing no traces of inhibitor once filtered for the Uv-vis measurement.

Table 7.7: Mass balance of sandPack experiments on X10-5 and FL1-DETA Scale Inhibitor, applied in both adsorption and precipitation treatments

SI	MT (g)	PF(g) (g)	Remained(%) at PV = 80	Remained(%) at PV = 200
X10-5	85.123	69.792	38.72	18.01
Fl1-DETA	77.237	41.266	46.57	N/A

7.4 Summary

The modified SI, X10-5 and X10-6 performance were evaluated and compared to the original FL1-DETA. Collected Static tests and corresponding SEM/EDX and TEM show PSS-*co*-MA—PANI cannot suppress the formation of ZnS scale, however, it can disturb its crystal growth and morphology by wrapping around the ZnS crystals. As a result of this deformation, formed scale crystals will not accumulate in the porous media or tube blocking test coil to densify. Hence, PSS-*co*-MA—PANI operates through a crystal growth retardation mechanism. This can be seen through the changes in the d-spacing values as compared to the blank sample in the absence of any inhibitors.The static test results also showed that X10-6 and X10-5 prevent the deposition of ZnS and PbS scale as built-up layers on sand particles. Further analysis of the full brine through ICP-OES and the SEM images from static tests showed that PSS-*co*-MA—PANI can inhibit the formation of routine scales such as $BaSO_4$ and $CaCO_3$.

Dynamic tube blocking tests, shows that unlike FL1-DETA, X10-5 has an inhibition performance against PbS. The MED of X10-5 and X10-6 against ZnS scale was identified as 3 mg/L whereas this value was lower for FL1-DETA i.e. 1 mg/L. This shows that the modification might have effected the efficacy of the original inhibitor, in lieu of increasing the retention properties as well as performance against PbS. As a result, eventhough FL1-DETA does not have any MED identified against PbS, X10-6 and X10-5 show an MED of 100 mg/L. Regarding the improved retention properties of the modified SI, Sandpack results showed that X10-5 has higher adsorption in the injection stage compared to FL1-DETA and shows longer return tail on the PF profile.

CHAPTER 8

Conclusion and future works

8.1 Conclusion

The main aim of this PhD research project was to develop a modified version of FL1-DETA SI with enhanced retention properties on sandstone rock. To be deployed via a squeeze treatment for HTHPHS fields such as Elgin, the newly structured chemical should have been effective at threshold concentration. To this end, two key phases of experimental plan were defined:

1. Characterisation of FL1-DETA scale inhibitor and its mode of action
2. Retention enhancement of the SI, based on the data provided from the first phase

Therefore, in the first phase FL1-DETA was characterised and the influencing factors on its performance in the field, such as brine, temperature, condensed gas,etc. were considered.

SEM images from static tests results, showed that FL1-DETA cannot inhibit the formation of routine scales such as $BaSO_4$. In fact the inhibitor promotes $BaSO_4$ crystals to co-precipitate with ZnS and PbS scale, and leads to the formation of bigger scale crystals up to 20 microns in size, Figure 7.8.

Static test results with simplified brine number 1 composition listed in Table 3.4, showed FL1-DETA successfully disperse the forming ZnS scale. This was concluded due to the significant increase in the supernatant turbidity. However, the effect was only observed when sand particles were presented in the test tubes. Meaning in the bulk test, deposits of ZnS were forming and no turbidity was seen in any tubes, Figure 7.15. This implies that at simplified conditions, FL1-DETA have inhibition performance against ZnS scale through dispersion. One possible explanation can be based on the chemical structure of FL1-DETA and its negative zeta potential, owning to its –COOH and–SO_3H functional groups. As a result of the 20 kDa sized FL1-DETA, possibly the inhibitor is acting as a dispersing agent and is capable of dispersing the negatively charged ZnS scale through electrostatic repulsion. Tube blocking test results ran with simplified brine composition, also revealed that FL1-DETA shows inhibition/dispersion performance with MIC of 1 ppm against ZnS scale by reducing the accumulation of ZnS build up layers on the filter as well as delaying the increased dP caused by blocking the filter/coil, Figure 7.21. This confirms that FL1-DETA has a performance against ZnS scale in dynamic conditions, presumably though avoiding the aggregation of the formed scale particles.

The inhibitor was also tested against PbS with the simplified brine number 2 listed in Table 3.4. It was revealed that FL1-DETA has no performance against PbS scale through neither static test conditions nor the the dynamic tube blocking test. As explained in Section 7.2.1.2, the none paired electrons on DETA structure cannot form a ligand with Pb^{+2}. Hence, the only possible mode of action for FL1-DETA against PbS

scale, would be the dispersion caused by electrostatic repulsion as a result of negatively charged SI and the negative zeta potential of PbS scale. Therefore, the absence of any performance regarding PbS inhibition, could be explained by the heavy particles of PbS scale, owning to the atomic mass of 207 amu of Pb which is significantly higher than Zn with 72 amu. As such, deposits of PbS forms in static test tubes regardless of the presence of sand particles and blocks the filter/coil in dynamic TB test.

However, even as an SI against ZnS scale, the main short-coming of FL1-DETA was its poor retention when applied as squeeze treatment in Elgin field. This was also clearly seen through sandpack test results in Figure 7.32 for FL1-DETA with no return after almost 80 PV. Investigations showed that the poor retention routs to three main factors:

1. Negative zeta potential of FL1-DETA due the presence of –COOH and $–SO_3H$ functional groups on its structure, which would reduce its affinity to adsorb on sand based reservoir rock.
2. The incompatibility of FL1-DETA with Elgin brine composition and the formation of insoluble Ba^{2+}—SI composite.
3. Hydrogel structure of the inhibitor caused by DETA forming a 3D shape that traps water molecules.

All these three factors were identified through different stages of static adsorption/compatibility test explained in Chapter 5 with the Elgin full brine composition listed in Table 3.2. Unlike other common scale inhibitors owning negatively charged functional groups such as PVS, PPCA or DETPMP [86], FL1-DETA can not form a Ca^{+2}—SI complex to help with its retention on sandstone through precipitation adsorption. This is mainly due to the abundance of Ba^{+2} cations in Elgin brine composition. As explained in Chapter 5, sulfonic acid group has a relative selectivity factor which is governed by the hydrated radius of different ions [93]. Therefore, Ba^{+2} cations will be the first ones approaching the $–SO_3H$ side groups owning to their hydrated radius being the smallest amongst all other cations present in the brine composition, Table 5.4. As a result FL1-DETA adsorption is effectively low on sandstone particles as shown in Figure 5.11.

The effect of second factor can also be explained by the high mobility of Ba^{+2} cations compared to Ca^{+2}. As explained in Section 5.1.3, Ba^{+2}—SI complex formation through $–SO_3H$ side group on FL1-DETA structure, dissolublise the SI causing severe incompatibility with the brine. The insoluble formed deposits, will not only reduce the adsorption of the SI on the sand rock, but also will put both the facilities and the reservoir at high risk of damage and blockage.

The third factor was also detected through static tests ran by a very simple brine of 3.5% NaCl which reconfirmed the low affinity of FL1-DETA for the sand based substrate in the absence of assisting cations towards precipitation adsorption such as Ca^{+2}.

Concentration measurements of the supernatant during the static tests, showed that the concentration of the inhibitor was higher closer to the bottom of the beakers as compared to the top side and this was due to the hydrogel formation of FL1-DETA. This could easily lead to incorrect interpretation of the adsorption isotherms. The topic is thoroughly discussed in Section 5.2.2.

The low affinity of FL1-DETA on sandstone particles as a result of its chemical structure as well as hydrogel formation, also revealed itself in dynamic conditions of sandpack test. The MT stage of sandpack test in Figure7.31, indicates an unsteady saturation of the packed column with the SI over the period of 20 PV. This means that there is a continues cycle of loose adsorption and desorption of the FL1-DETA inhibitor on the sand particles. On the other hand, the PF stage in this test, showed the adverse effect of Ba^{+2}—SI complex with the CW on the return of the SI and its sensitivity to the brine composition, Section 7.3.3.

Considering FL1-DETA positive performance against ZnS scale and all above mentioned facts, FL1-DETA needed to be modified in order to retain in the field of interest, Elgin, as squeeze treatment. Therefore, the incompatibility of the SI with the brine composition caused by the Ba^{+2}—SI complex formation needed to be addressed. As Ba^{+2}—SI complex was caused by the bonding of Ba^{+2} with $–SO_3H$ groups and the formation of $BaSO_4$ structure, a blend of anti $BaSO_4$ scale inhibitor with FL1-DETA was suggested as a solution.

Followed by the failed attempts on brine dilution or SI blend mixtures, it was clear that for the SI to be functional in HTHPHS conditions of Elgin field, the chemical structure should be modified/altered. Since FL1-DETA and FL1 showed to have independent high thermal stability based on their TGA results, the FL1 part of the structure (PSS-*co*-MA) was retained and the DETA was replaced with polyaniline. Long fibre chains of polyaniline polymer are positively charged and contain none paired electrons located on its N atoms along the chain. The positively charged polymer increase the affinity of FL1 towards sandstone through opposite electrostatic attraction forces. Furthermore, the none paired electrons located on N atoms are capable of forming ligands with Zn^{+2} cations. Therefore, PSS-*co*-MA—PANI is a modified version of the PSS based SI (FL1) with aniline constructed functional groups that transforms this scale inhibitor to a suitable squeeze treatment candidate for HTHPHS conditions.

PSS-*co*-MA—PANI composites were synthesised through oxidation polymerisation based on eco-friendly and cost-effective polyaniline polymer as a carrier. Due to the long chains of PANI, $–SO_3H$ side groups on FL1 are protected from Ba^{+2} cations bonding with them, therefore, PSS-*co*-MA—PANI was completely compatible with the Elgin production brine composition listed in Table 3.2. Different formulas of PSS-*co*-MA—PANI composites were narrowed down based on their thermal stability, conductivity and the adsorption properties on the sand particles to X10-5, X10-6 and X5-5. The screening process was based on the optimisation of the ratio between FL1 and the

dopant (PANI) which was detailed in Chapter 6. All structures showed the thermal stability higher than 385°C as a result of having PANI in their structure. However, none of the formulas' performances were verified after the thermal ageing test.

As a result of the positive charges on its back bone and complete compatibility with the brine composition, PSS-*co*-MA—PANI, showed remarkable adsorption properties on sand particles Figure 7.2 as compared to FL1-DETA. Moreover, compared to DETA, PANI chains are longer and have more none paired electrons as an active site. These long chains, avoid the formation of hydrogels and therefore, have more opportunity to adsorb on the substrate.

PSS-*co*-MA—PANI performance tests in the presence of H_2S gas and simplified brine showed, that all formulas have a positive response on decreasing the amount of ZnS forming on TB test filters, Figure 7.23 and Figure 7.22. Nevertheless, X10-5 and X10-6 showed the best protection against ZnS scale with X10-5 also showing a decrease of PbS scale formation on the filters, Figure 7.28.

Static test SEM and TEM results, revealed that the PSS-*co*-MA—PANI structure acts through crystal growth retardation by wrapping around the sulphide scale crystals. Hence, the formed scale is disrupted and deformed. The polymer also decrease the adherence of the defected crystals on the substrate, leaving an amorphous flaky deposit on the sand particles that easily washes away in the dynamic conditions of the field. This could be explained by the possible adsorption of negatively charged ZnS and PbS particles on positively charged polymer. As a result of PANI wrapping around the defected scale, it will no longer possess positive charge on its structure as an attraction force toward sandstone, therefore, the SI detaches from the sand particles through the post flush stage of squeeze treatment and protects the reservoir rock and the upstream facilities by avoiding the agglomeration of sulphide scales..

The sandpack test compared both modified and the original inhibitor i.e. X10-5 and FL1-DETA, through injection and return profile. Results in Section 7.3.3, showed that the modified structure has higher retention properties on the sand particles as compared to FL1-DETA with a gradual release above its MED for a longer period of time.

8.2 Summary

In completion to of this research project following list of conclusions were achieved:

1. FL1-DETA does not show compatibility to high saline Elgin brine composition and forms an insoluble composite with barium, hence its poor retention performance in field trials. (Figure 5.1)

2. FL1-DETA has no inhibition performance against routine scales such as $BaSO_4$ and $CaCO_3$ as well as PbS. (Figure 7.8, Figure7.19, Figure 7.26)

3. FL1-DETA has low affinity to the sandstone reservoir due to its structural conformation. The adsorption isotherm in CW is governed by precipitation only (Figure 7.4)
.

4. PSS-*co*-MA—PANI has shown high affinity to sand particles through pure adsorption properties governed by the Freundlich model with n$<$ 1. (Figure 7.2, Figure 7.3 and Table 7.1)

5. PSS-*co*-MA—PANI shows inhibiting performance against $BaSO_4$ and $CaCO_3$ as well as PbS and ZnS. (Figure 7.9, Figure 7.10, Figure 7.22, Figure 7.23, Figure 7.27, Figure 7.28)

6. Characterisation results show complete compatibility of PSS-*co*-MA—PANI composites to high saline Elgin brine composition. (Figure 7.1)

7. PSS-*co*-MA—PANI has shown improved retention properties in comparison with FL1-DETA in sand pack test. (Figure 7.32, Figure 7.31)

8. PSS-*co*-MA—PANI has a threshold MED of $\sim$ 3 mg/L against ZnS. (Figure 7.23, Figure 7.18)

9. PSS-*co*-MA—PANI has MED of $\sim$ 100 mg/L against PbS. (Figure 7.28)

10. PSS-*co*-MA—PANI has high potential to be used as squeeze treatment against sulphide scale for HTHPHS fields. (Figure 6.19, Figure 7.1, Figure 7.32)

8.3 Suggestions on Future works

Due to the design and laboratory equipment limitations, the sandpack test was run in the absence of H_2S gas. Based on literature and the colour change of the inhibitor to slightly bluer shades compared to its original emraldin green, there might be a possibility that x10-5 reacts with H_2S own to it PANI on its structure. Therefore, there could be concerns that this could have an adverse effect on X10-5 retention properties on the sand particles.

It is highly recommended that the retention of X10-5 be evaluated in the presence of H_2S gas. Further proposed experimental plans as a future work would be as follow:

- **Molecular weight measurement.** Molecular weight (Mw) measurement of Pss-*co*-MA—PANI can be measured through High-performance liquid chromatography (HPLC) using a universal column or capillary viscometry by using the Ubbelohde U-tube viscometer. Mw can provide useful information on the composite adsorption and its behaviour through the pipe flow as well as the length of the polymeric chain.

- **Efficiency performance against ZnS verified with the thermally aged chemical.** Even though the inhibitor has shown to be thermally stable through the TGA results, its efficiency might decrease whilst exposed to constant heat flow or temperature fluctuation. Therefore, for a scale inhibitor to be identified as successful squeeze treatment it is worth to firstly age the chemical under standard procedure and then to repeat both dynamic and static tests and compare the performance with the fresh chemical.

- **Efficiency tests against PbS with and without ages SI.** As tube blocking tests, are showing that X10-5 has positive performance against PbS, running static tests with simplified brine including only Pb^{+2} and S^{-2} can give useful information on the inhibitor mode of action against PbS. TEM and SAED images can also be collected from this stage.

- **Evaluation of SI functionality against sulphide scale inhibition via Atomic force microscopy (AFM) technique and Quartz crystal microbalance with dissipation (QCM-D).** Both AFM and QCM can provide useful information on the SI interaction with the PbS/ZnS crytals and the Quartz substrate, respectively. AFM images can provide information in nano scale on possible crystal kink and defect formation in the presence of inhibitor. Whereby, QCM will evaluate the thickness and the formation of inhibitor film on the quartz substrate under dynamic condition and its affinity in micro scale.

- **Producing static and dynamic Γ_{app} and desorption profiles in an autoclave under HT/HP conditions while purging H_2S gas**. The results from this stage could be more in line with the real governing conditions in the well bore, hence, leading to a clearer image on the modification outcome and the amount of enhancement.

- **Introducing oil as the second phase to the experimental matrix** This will evaluate the inhibitor performance in the presence of oil phase. The result

for this experiment can replicate more actual conditions of the field, as there will always be a mixture of both oil and brine phase.

- **Core flood test.** This can be a pre-industrial test which would closely resemble to an actual squeeze treatment in the oil field. Changes in permeability, possible core damage and fine migration can be seen through this test which is not possible to be traced through sandpack test. A positive response on this stage would highly be expected to follow through the field conditions an onwards. Thus, the new product or method could be verified before being industrially advised. The core flood test could be expanded to :

  1. Single phase HTHPHS condition
  2. Two phase (oil and water) HTHPHS condition
  3. Core flood in the presence of H_2S

- **Field trial** This would be the last step before industrialisation of the chemical as an official squeeze treatment against exotic scale to be applied in Elgin field, North sea UK.

References

[1] Kevin Adjevi Bahun-Wilson. *Transport and Adsorption Properties of Carboxylated Carbon Nanotubes for Enhanced Scale Inhibitor Squeeze Lifetime Performance*. PhD thesis, 2018. xix, 3, 49, 50, 63, 72, 73

[2] Mike Crabtree. Fighting Scale-Removal and Prevention. Technical report, Aberdeen, 1999. 2, 12, 18, 19, 20, 26, 29

[3] Abass A. Olajire. A review of oilfield scale management technology for oil and gas production, 11 2015. 2, 13, 14, 16, 19, 26, 42, 47

[4] Ghorbani, Wilson, MCT, Kapur, Fleming, Tjomsland, and Neville. Adsorption of polyphosphinocarboxylic acid (PPCA) scale inhibitor on carbon nanotubes (CNTs): A prospective method for enhanced oilfield scale prevention. 2016. 2, 3, 42

[5] Cyril Okocha, Anton Kaiser, Jonathan Wylde, Lena Petrozziello, Matthias Haeussler, Christoph Kayser, Tao Chen, Wang Qiwei, Frank Chang, and Markus Klapper. Review of iron sulfide scale: The Facts & Developments and Relation to Oil and Gas production. In *Society of Petroleum Engineers - SPE Kingdom of Saudi Arabia Annual Technical Symposium and Exhibition 2018, SATS 2018*. OnePetro, 4 2018. 3, 21, 31

[6] Salima Baraka-Lokmane, Christian Hurtevent, Honggang Zhou, Pratik Saha, Nourdine Tots, Frédéric Rieu, Ronan Lastennet, and Tomi Sugiarto. Total's experience on the development and implementation of a scale management strategy in central graben fields. In *Society of Petroleum Engineers - SPE International Conference and Exhibition on Oilfield Scale 2014*, pages 120–136. Society of Petroleum Engineers, 5 2014. 3, 5, 18, 24, 31, 33, 35

[7] H.A. Nasr-El-Din and A.Y. Al-Humaidan. Iron Sulfide Scale: Formation, Removal and Prevention. In *International Symposium on Oilfield Scale*. Society of Petroleum Engineers, 4 2001. 3, 13, 16, 21

[8] M. M. Jordan, K. Sjursaether, M. C. Edgerton, and R. Bruce. Inhibition of Lead and Zinc Sulphide Scale Deposits Formed during Production from High Temperature Oil and Condensate Reservoirs. In *SPE - Asia Pacific Oil and Gas Conference*, pages 599–610. OnePetro, 10 2000. 3, 5, 21, 23, 25, 52

[9] Clare Johnston and Morag Elrick. Improvements in environmental profile and cost effectiveness of scale squeeze inhibitors - A case study from the North Sea. In *Proceedings - SPE International Symposium on Oilfield Chemistry*, volume 1, pages 301–323. OnePetro, 4 2013. 3, 33, 35

[10] A.J.. J Savin, B Adamson, J.J.. J Wylde, J.R.. R Kerr, C.W.. W. Kayser, T Tralenkamp, D Fischer, and C.. Okocha. Sulfide Scale Control: A High Efficacy Breakthrough Using an Innovative Class of Polymeric Inhibitors. OnePetro, 5 2014. 3, 33, 52

[11] Ully Zakyatul Husna, Khaled Abdalla Elraies, Juhairi Aris B.M. Shuhili, and Ahmed Abdulla Elryes. A review: the utilization potency of biopolymer as an eco-friendly scale inhibitors. *Journal of Petroleum Exploration and Production Technology*, 12(4):1075–1094, 11 2021. 3

[12] C.Hurtevent et al. Use of a copolymer made from styrene sulphoncacid to inhibit or slow the formation of sulphide deposts., 2016. 4, 12, 61, 119, 122, 164

[13] Bader Alharbi, Norah Aljeaban, Alexander Graham, and Ken Sorbie. Inhibition and interaction between iron sulphide, zinc sulphide and lead sulphide. In *Society of Petroleum Engineers - SPE Kuwait Oil and Gas Show and Conference 2019, KOGS 2019*. Society of Petroleum Engineers, 2019. 5

[14] Marina Maya Marchioretto, Harry Bruning, and Wim Rulkens. Heavy metals precipitation in sewage sludge. *Separation Science and Technology*, 40(16):3393–3405, 12 2005. 5, 20, 23, 24

[15] Kiana Peyvandi, Ali Haghtalab, and Mohammad Reza Omidkhah. Using an electrochemical technique to study the effective variables on morphology and deposition of CaCO 3 and BaSO 4 at the metal surface. *Journal of Crystal Growth*, 354(1):109–118, 9 2012. 5, 20

[16] Bader Al-Harbi, Norah Aljeaban, Alexander Graham, and Ken Sorbie. Critical review on sulphide scale formation, removal and inhibition. In *NACE - International Corrosion Conference Series*, volume 2020-June. OnePetro, 6 2020. 5, 12, 21

[17] H.A. Nasr-El-Din and A.Y. Al-Humaidan. Iron Sulfide Scale: Formation, Removal and Prevention. OnePetro, 1 2001. 5, 27

[18] S.L. Fisher and B.D. Mercer. Iron sulfide dispersing agents, 1994. 6

[19] Q Ke, M;Qu. Method for inhibiting or controlling inorganic scale formations, 2013. 6

[20] Marc Lehmann and Fafa Firouzkouhi. A new chemical treatment to inhibit iron sulfide deposition. In *Society of Petroleum Engineers - 9th International Conference on Oilfield Scale 2008 - "Managing Scale Through the Field Lifetime"*, pages 286–316. Society of Petroleum Engineers, 4 2008. 6

[21] Moir G. Todd M., Strachan C. and Goulding J. Process for inhibition of sulfide scales, 2013. 6

[22] Medhat Abdou, Andrew Carnegie, S George Mathews Kevin McCarthy, Wei Wei Chevron Houston, Greg Bowen, Abu Dhabi, Ahmed Berrim, Abu Dhabi Marine Operating Company, Hadrien Dumont, Will Haug, Cuong Jackson, Oliver Mullins, Chee Kin Khong, and Cholid Mas. Finding Value in Formation Water. *Oilfield Review Spring*, 23(1), 2011. 11, 12

[23] Erick Alvarez, Colin MacBeth, and Jonathan Brain. Quantifying remaining oil saturation using time-lapse seismic amplitude changes at fluid contacts. *Petroleum Geoscience*, 23(2):238–250, 5 2017. 11

[24] Ali Haghtalab, Mohamad Javad Kamali, and Abbas Shahrabadi. Prediction mineral scale formation in oil reservoirs during water injection. *Fluid Phase Equilibria*, 373:43–54, 7 2014. 11

[25] R. Hosny, S. E.M. Desouky, M. Ramzi, Th Abdel-Moghny, F. M.S. El-Dars, and A. B. Farag. Estimation of the scale deposits near wellbore via software in the presence of inhibitors. *Journal of Dispersion Science and Technology*, 30(2):204–212, 2009. 11

[26] Amer Badr Bin Merdhah and Abu Azam Mohd Yassin. Barium sulfate scale formation in oil reservoir during water injection at high-barium formation water. *Journal of Applied Sciences*, 7(17):2393–2403, 9 2007. 11, 13, 17, 25, 26

[27] Jianbo Li, Mingjin Tang, Zhengrong Ye, Longli Chen, and Yuqin Zhou. Scale formation and control in oil and gas fields: A review, 5 2017. 11, 13, 28, 30, 31, 32

[28] waterflooding — industrial process — Britannica. 12

[29] Mehdi Safari, Alireza Golsefatan, and Mohammad Jamialahmadi. Inhibition of Scale Formation Using Silica Nanoparticle. *Journal of Dispersion Science and Technology*, 35(10):1502–1510, 10 2014. 13

[30] J. Moghadasi, M. Jamialahmadi, H. Müller-Steinhagen, A. Sharif, M.R. Izadpanah, E. Motaei, and R. Barati. Formation Damage in Iranian Oil Fields. In *International Symposium and Exhibition on Formation Damage Control*. Society of Petroleum Engineers, 4 2002. 13, 19, 26

[31] Sangho Lee and Chung Hak Lee. Effect of operating conditions on CaSO4 scale formation mechanism in nanofiltration for water softening. *Water Research*, 34(15):3854–3866, 10 2000. 14

[32] S. Baraka-Lokmane, K. Sorbie, N. Poisson, and N. Kohler. Can green scale inhibitors replace phosphonate scale inhibitors?: Carbonate coreflooding experiments. *Petroleum Science and Technology*, 27(4):427–441, 3 2009. 14, 76, 182

[33] Peter Risthaus, Dirk Bosbach, Udo Becker, and Andrew Putnis. Barite scale formation and dissolution at high ionic strength studied with atomic force microscopy. *Colloids and Surfaces A: Physicochemical and Engineering Aspects*, 191(3):201–214, 11 2001. 14, 16

[34] Wen Yi Shih, Anditya Rahardianto, Ron Wai Lee, and Yoram Cohen. Morphometric characterization of calcium sulfate dihydrate (gypsum) scale on reverse osmosis membranes. *Journal of Membrane Science*, 252(1-2):253–263, 4 2005. 15

[35] Alice Antony, Jor How Low, Stephen Gray, Amy E. Childress, Pierre Le-Clech, and Greg Leslie. Scale formation and control in high pressure membrane water treatment systems: A review, 11 2011. 15, 27

[36] J R Luft and G T DeTitta. A method to produce microseed stock for use in the crystallization of biological macromolecules. *Acta crystallographica. Section D, Biological crystallography*, 55(Pt 5):988–93, 5 1999. 15

[37] Otakar. Sohnel and John Garside. *Precipitation : basic principles and industrial applications*. Butterworth-Heinemann, 1992. 15

[38] J.W. Mullin. Crystallization: Chpater 5- Nucleation. In *Crystallization*, pages 181–215. 2001. 16

[39] Violette Eroini. Kinetic study of calcium carbonate formation and inhibition by using an in-situ flow cell. 2011. 16

[40] Andrea C Levi and Miroslav Kotrla. Theory and simulation of crystal growth - IOPscience. *Journal of Physics: Condensed Matter*, 9(2), 1997. 16

[41] A. W. Vere. *Crystal Growth: Principles and Progress*. Plenum Press, New York, NY, USA, 1 edition, 1987. 16

[42] Barium Sulfate Scale - Chemical Contaminant Removal. 17

[43] K. S. Sorbie and N. Laing. How scale inhibitors work: Mechanisms of selected barium sulphate scale inhibitors across a wide temperature range, 2004. 17, 31

[44] Alison Hennessy, Gordon Graham, Jerry Hastings, D. Peter Siddons, and Zhong Zhong. New pressure flow cell to monitor BaSO4 precipitation using synchrotron in situ angle-dispersive X-ray diffraction. *Journal of Synchrotron Radiation*, 9(5):323–324, 9 2002. 17

[45] F. Jones, A. Oliviera, G. M. Parkinson, A. L. Rohl, A. Stanley, and T. Upson. The effect of calcium ions on the precipitation of barium sulphate 1: Calcium ions in the absence of organic additives. *Journal of Crystal Growth*, 262(1-4):572–580, 2 2004. 17

[46] Alison J.B. Hennessy and G. M. Graham. The effect of additives on the co-crystallisation of calcium with barium sulphate. *Journal of Crystal Growth*, 237-239(1-4 III):2153–2159, 4 2002. 17

[47] V. Tantayakom, H.S. Fogler, and S. Chavadej. Study of Scale Inhibitor Reactions in Precipitation Squeeze Treatments. In *SPE International Symposium on Oilfield Chemistry*. Society of Petroleum Engineers, 4 2005. 17, 20, 30

[48] A. Valiakhmetova, K. S. Sorbie, L. S. Boak, and S. S. Shaw. Solubility and inhibition efficiency of Phosphonate scale inhibitor-calcium-magnesium complexes for application in a precipitation-squeeze treatment. In *SPE Production and Operations*, volume 32, pages 343–350. Society of Petroleum Engineers, 8 2017. 18

[49] A. C. Todd and M. D. Yuan. Barium and strontium sulfate solid-solution scale formation at elevated temperatures. *SPE Production Engineering*, 7(1):85–92, 1992. 18

[50] Mitsutaka Kitamura. Controlling factor of polymorphism in crystallization process. *Journal of Crystal Growth*, 237-239(1-4 III):2205–2214, 4 2002. 18

[51] Carl W. Turner and David W. Smith. Calcium Carbonate Scaling Kinetics Determined from Radiotracer Experiments with Calcium-47. *Industrial and Engineering Chemistry Research*, 37(2):439–448, 1998. 18

[52] M. Ben Amor, D. Zgolli, M. M. Tlili, and A. S. Manzola. Influence of water hardness, substrate nature and temperature on heterogeneous calcium carbonate nucleation. *Desalination*, 166(1-3):79–84, 8 2004. 18

[53] Lester C. Howick. Book reviews - The formation and properties of precipitates. *Analytical Chemistry*, 39(14):80A–81A, 1967. 18

[54] Amer Badr BinMerdhah. Inhibition of barium sulfate scale at high-barium formation water. *Journal of Petroleum Science and Engineering*, 90-91:124–130, 7 2012. 19, 20

[55] S. J. Dyer and G. M. Graham. The effect of temperature and pressure on oilfield scale formation. *Journal of Petroleum Science and Engineering*, 35(1-2):95–107, 7 2002. 19

[56] Amer Badr Merdhah and Abu Azam Mohd Yassin. Solubility Of Common Oil Field Scales Of Injection Water And High–barium Concentration And High–salinity Formation Water. *Jurnal Teknologi*, 50(1):67–77, 6 2012. 19

[57] O. J.G. Vetter. HOW BARIUM SULFATE IS FORMED: AN INTERPRETATION. *JPT, Journal of Petroleum Technology*, 27(12):1515–1524, 12 1975. 20, 26

[58] B. G. Al-Harbi, A. J. Graham, and K. S. Sorbie. Iron Sulfide Inhibition and Interaction With Zinc and Lead Sulfides. *SPE Production & Operations*, 34(03):551–563, 8 2019. 20, 22, 23, 24, 26

[59] S Dyer, C Simpson, G Graham, K Orski, C Menezes, S Heath, C Macpherson, Scaled Solutions, Total UK Ltd, and Clariant. Prediction and optimisation of Pb/Zn/Fe sulphide scales in gas production fields. In *17th International Tekna Oil Field Chemistry Symposium (Geilo, Norway, 3/19-22/2006) Proceedings*, number 200639, 2006. 21, 26, 27

[60] I. R. Collins and M. M. Jordan. Occurance, prediction and prevention of zinc sulfide scale within gulf coast and north sea high temperature/high salinity production wells. In *Society of Petroleum Engineers - International Symposium on Oilfield Scale 2001*. OnePetro, 1 2001. 21, 22, 23, 27, 52

[61] Geir Thorolfsson. Scaling Problems in HS Orka's Geothermal Power Plants, an Overview., 3 2019. 21

[62] J. L. Przybylinski. Iron sulfide scale deposit formation and prevention under anaerobic conditions typically found in the oil field. In *SPE International Oilfield Chemistry Symposium Proceedings*, pages 1–8. Society of Petroleum Engineers (SPE), 2001. 22, 23, 51

[63] Joginder Singh Galsin. Crystal Structure of Solids. *Solid State Physics*, pages 1–36, 2019. 22

[64] The Materials Project. Materials Data on PbS , 7 2020. 22

[65] Zhang Chenglong, Zhao Youcai, Guo Cuixiang, Huang Xi, and Li Hongjiang. Leaching of zinc sulfide in alkaline solution via chemical conversion with lead carbonate. *Hydrometallurgy*, 90(1):19–25, 1 2008. 23

[66] Zhang Chenglong and Zhao Youcai. Mechanochemical leaching of sphalerite in an alkaline solution containing lead carbonate. *Hydrometallurgy*, 100(1-2):56–59, 12 2009. 23

[67] Bader G. Al-Harbi, Alexander J. Graham, and Ken S. Sorbie. Laboratory investigation of zinc and lead sulphide inhibition. In *Proceedings - SPE International Symposium on Formation Damage Control*, volume 2018-Febru. Society of Petroleum Engineers (SPE), 2018. 23

[68] C.. Okocha and K. S. Sorbie. Sulphide scale co-precipitation with calcium carbonate. In *SPE - European Formation Damage Conference, Proceedings, EFDC*, volume 2, pages 757–781. OnePetro, 2 2014. 23

[69] Christopher Tortolano, Tao Chen, Ping Chen, Harry Montgomerie, Thomas Hagen, Ronald Benvie, and Lucy Zou. Mechanisms, New Test Methodology and Environmentally Acceptable Inhibitors for Co-deposition of Zinc Sulfide and Calcium Carbonate Scales for High Temperature Application. OnePetro, 5 2014. 23

[70] Amy T. Kan, Gongmin Fu, Hamad Al-Saiari, Mason B. Tomson, and Dong Shen. Enhanced scale-inhibitor treatments with the addition of zinc. *SPE Journal*, 14(4):617–626, 12 2009. 23

[71] J Kvarekval, R Nyborg, and Hojin Choi. Formation of multilayer iron sulfide films during high temperature CO2/H2S corrosion of carbon steel. In *NACE - International Corrosion Conference Series*, volume 2003-April. OnePetro, 3 2003. 24

[72] T. J. Barrett and G. M. Anderson. The solubility of sphalerite and galena in 1–5 m NaCl solutions to 300°C. *Geochimica et Cosmochimica Acta*, 52(4):813–820, 4 1988. 25

[73] Ting Gu, Pengcheng Su, Xiaoyan Liu, Junchen Zou, Xinying Zhang, and Yan Hu. A composite inhibitor used in oilfield: MA-AMPS and imidazoline. *Journal of Petroleum Science and Engineering*, 102:41–46, 2013. 26

[74] Ting Gu, Xiaoyan Liu, Wenbo Chai, Beibei Li, and Haoyuan Sun. A preliminary research on polyvinyl alcohol hydrogel: A slowly-released anti-corrosion and scale inhibitor. *Journal of Petroleum Science and Engineering*, 122:453–457, 8 2014. 26

[75] A. L. Kavitha, T. Vasudevan, and H. Gurumallesh Prabu. Evaluation of synthesized antiscalants for cooling water system application. *Desalination*, 268(1-3):38–45, 3 2011. 26

[76] Pavlos G. Klepetsanis and Petros G. Koutsoukos. Precipitation of calcium sulfate dihydrate at constant calcium activity. *Journal of Crystal Growth*, 98(3):480–486, 11 1989. 26

[77] Laura Sanders, Xinming Hu, Eleftheria Mavredaki, Violette Eroini, Richard Barker, and Anne Neville. Assessment of combined scale/corrosion inhibitors - A combined jar test/bubble cell, 6 2014. 26, 28

[78] Georgiana A. Moldoveanu and Vladimiros G. Papangelakis. Effects of thermal pre-treatment and ore dryness on the recovery of lanthanides from ion-adsorption clays. *Hydrometallurgy*, 158:180–185, 12 2015. 26

[79] Alexander Saul, Anne Neville, Salima Baraka-Lokmane, Aurelie Le Beulze, Thibaut Charpentier, Suparit Tangparitkul, and John-Richard Ordonez-Varela. Iron Carbonate Based Slippery Liquid Infused Porous Surfaces (SLIPS) for Enhanced Mineral Fouling Resistance, 4 2021. 27

[80] Ahmed Hamza, Ibnelwaleed A. Hussein, Rem Jalab, Mohammed Saad, and Mohamed Mahmoud. Review of Iron Sulfide Scale Removal and Inhibition in Oil and Gas Wells: Current Status and Perspectives, 9 2021. 27, 31

[81] Johannes Karl Fink. Scale Inhibitors. In *Hydraulic Fracturing Chemicals and Fluids Technology*, pages 129–145. Elsevier, 1 2013. 28, 30, 34

[82] G. M. Graham, S. J. Dyer, K. S. Sorbie, W. R. Sablerolle, P. Shone, and D. Frigo. Scale inhibitor selection for continuous and downhole squeeze application in HP/HT conditions. In *Proceedings - SPE Annual Technical Conference and Exhibition*, volume 1999-Septe, pages 645–659. Society of Petroleum Engineers, 4 1998. 28

[83] Y. Duccini, A. Dufour, W. M. Hann, T. W. Sanders, and B. Weinstein. High performance oilfield scale inhibitors. In *NACE - International Corrosion Conference Series*, volume 1997-March. NACE International, 1 1997. 28

[84] Gordon M. Graham and Craig Paul McMahon. The effect on scale inhibitor performance against bulk (Homogeneous) and surface (heterogeneous) Scale Nucleation and growth by the addition of film forming corrosion inhibitors. In *NACE - International Corrosion Conference Series*, volume 2002-April. NACE International, 1 2002. 29, 30, 31

[85] M. D. Yuan, E. Jamieson, and Paul Hammonds. Investigation of scaling and inhibition mechanisms and the influencing factors in static and dynamic inhibition tests. In *NACE - International Corrosion Conference Series*, volume 1998-March. NACE International, 1 1998. 29

[86] N. Farooqui. *A Detailed Study of the Scale Inhibitor Phase Envelope of Ppca in the Context of Precipitation Squeeze Treatments*. PhD thesis, 2015. 29, 31, 32, 33, 34, 44, 45, 46, 71, 72, 73, 74, 188

[87] Musa Mpelwa and Shan Fa Tang. State of the art of synthetic threshold scale inhibitors for mineral scaling in the petroleum industry: a review, 8 2019. 29, 31, 32, 33, 34, 42, 43, 45, 47, 51, 110, 123

[88] Balasubramanian Senthilmurugan, Bisweswar Ghosh, and Siva Sanker. High performance maleic acid based oil well scale inhibitors-Development and comparative evaluation. *Journal of Industrial and Engineering Chemistry*, 17(3):415–420, 5 2011. 29

[89] Michael Schwamborn. Chemical synthesis of polyaspartates: A biodegradable alternative to currently used polycarboxylate homo- and copolymers. *Polymer Degradation and Stability*, 59(1-3):39–45, 1 1998. 30

[90] Chunfang Fan, Amy T. Kan, Ping Zhang, Haiping Lu, Sarah Work, Jie Yu, and Mason B. Tomson. Scale prediction and inhibition for unconventional oil and gas production. In *Society of Petroleum Engineers - 10th SPE International Conference on Oilfield Scale 2010*, pages 247–268. Society of Petroleum Engineers, 4 2010. 31

[91] Zahra Kiaei and Ali Haghtalab. Experimental study of using Ca-DTPMP nanoparticles in inhibition of CaCO3 scaling in a bulk water process. *Desalination*, 338(1):84–92, 4 2014. 32

[92] K.P. Davis, S.D. Fidoe, G.P. Otter, R.E. Talbot, and M.A. Veale. Novel Scale Inhibitor Polymers with Enhanced Adsorption Properties. In *International Symposium on Oilfield Scale*. Society of Petroleum Engineers, 4 2003. 32

[93] Konrad Dorfner. Ion exchangers. In *Ion Exchangers*, pages 1–6. Wiley-VCH Verlag GmbH & Co. KGaA, Weinheim, Germany, 4 2011. 33, 109, 110, 188

[94] Stuart Holt, Jannifer Sanders, Klin Rodrigues, and Matthew Vanderhoof. Biodegradable alternatives for scale control in oilfield applications. In *Proceedings*

- *SPE International Symposium on Oilfield Chemistry*, volume 2, pages 922–931. Society of Petroleum Engineers, 1 2009. 34

[95] Shaheen Taj, Sankara Papavinasam, and R. Winston Revie. Development of green inhibitors for oil and gas applications. In *NACE - International Corrosion Conference Series*. NACE International, 1 2006. 34

[96] Arash Shadravan and Mahmood Amani. HPHT 101-What Petroleum Engineers and Geoscientists Should Know About High Pressure High Temperature Wells Environment. *Energy Science and Technology*, 4(2):36–60, 2012. 35, 36

[97] Joerg Zotzmann, Alexandra Vetter, and Simona Regenspurg. Evaluating efficiency and stability of calcite scaling inhibitors at high pressure and high temperature in laboratory scale. *Geothermal Energy*, 6(1):1–13, 12 2018. 35

[98] Gunnar DeBrujin, Robert Greenaway, and Kevin Wutherich. High -pressure, High -temperature Technologies. *Oilfiled review*, 2008. 36

[99] Mesoporous Materials - Nanomaterials — Sigma-Aldrich. 37

[100] Dorota Bielska, Anna Karewicz, Tomasz Lachowicz, Katarzyna Berent, Krzysztof Szczubiałka, and Maria Nowakowska. Hybrid photosensitizer based on halloysite nanotubes for phenol-based pesticide photodegradation. *Chemical Engineering Journal*, 262:125–132, 2 2015. 38

[101] Qingqing Pan, Neng Li, Yu Hong, Heng Tang, Zongfu Zheng, Shaohuang Weng, Yanjie Zheng, and Liying Huang. Halloysite clay nanotubes as effective nanocarriers for the adsorption and loading of vancomycin for sustained release. *RSC Advances*, 7(34):21352–21359, 4 2017. 38

[102] A Vidyadhar, Neha Kumari, and R P Bhagat. Flotation of Quartz and Hematite: Adsorption Mechanism of Mixed Cationic/Anionic Collector Systems. In *XXVI INTERNATIONAL MINERAL PROCESSING CONGRESS(IMPC)*, page 548, New Delhi, India, 9 2012. 38, 44, 45, 56, 97

[103] Jairo Tronto, Ana Cludia, Zeki Naal, and Joo Barros Valim. Conducting Polymers / Layered Double Hydroxides Intercalated Nanocomposites. In *Materials Science - Advanced Topics*. InTech, 6 2013. 39

[104] AC Bordonal, Z Naal, and JB Valim. Hybrid organic-inorganic materials: conductive polymers interspersed in double lamellar hydroxides. *Anais*, 2010. 39

[105] Enrica Caló and Vitaliy V. Khutoryanskiy. Biomedical applications of hydrogels: A review of patents and commercial products. *European Polymer Journal*, 65:252–267, 4 2015. 40

[106] Md. Shirajur Rahman, Md. Minhajul Islam, Md. Sazedul Islam, Asaduz Zaman, Tanvir Ahmed, Shanta Biswas, Sadia Sharmeen, Taslim Ur Rashid, and Mohammed Mizanur Rahman. Morphological Characterization of Hydrogels. pages 819–863. Springer, Cham, 2019. 40

[107] Alideertu Dong, Jinfeng Huang, Shi Lan, Tao Wang, Linghan Xiao, Weiwei Wang, Tianyi Zhao, Xin Zheng, Fengqi Liu, Ge Gao, and Yuxin Chen. Synthesis of N-halamine-functionalized silica-polymer core-shell nanoparticles and their enhanced antibacterial activity. *Nanotechnology*, 22(29), 7 2011. 41

[108] Jun-Peng Wang, Jun-Kuo Wang, Qiong Zhou, Zhan Li, Yongsheng Han, Yan Song, Shuo Yang, Tao Qi, Helmuth Möhwald, Dmitry Shchukin, and Guo Liang Li. Adaptive Polymeric Coatings with Self-Reporting and Self-Healing Dual Functions from Porous Core-shell Nanostructures. 41

[109] Yongsoo Kim, Hyuk Jun Kwon, Jun Won Kook, Jae Jung Park, Chanmin Lee, Won Gun Koh, Ki Seob Hwang, and Jun Young Lee. Wetting properties and morphological behavior of core-shell polymer-based nanoparticle coatings. *Progress in Organic Coatings*, 163:106606, 2 2022. 41

[110] Tariq S Najim and Ali J Salim. Polyaniline nanofibers and nanocomposites: Preparation, characterization, and application for Cr(VI) and phosphate ions removal from aqueous solution. 2014. 41, 42

[111] Oscar Vazquez, E. Mackay, K. Al Shuaili, K. Sorbie, and M. Jordan. Modeling a surfactant preflush with non-aqueous and aqueous scale inhibitor squeeze treatments. In *70th European Association of Geoscientists and Engineers Conference and Exhibition 2008: Leveraging Technology. Incorporating SPE EUROPEC 2008*, volume 4, pages 2219–2231. Society of Petroleum Engineers, 4 2008. 44, 48

[112] Niall Fleming, Kari Ramstad, Anne Mette Mathisen, Olav Martin Selle, Tore Tjomsland, and Finn Hallstein Fadnes. Squeeze related well productivity impairment mechanisms & preventative/remedial measures utilised: Norwegian continental shelf. In *Society of Petroleum Engineers - 10th SPE International Conference on Oilfield Scale 2010*, pages 1–16. Society of Petroleum Engineers, 4 2010. 44

[113] Oscar Vazquez, Ilya Fursov, and Eric Mackay. Automatic optimization of oilfield scale inhibitor squeeze treatment designs. *Journal of Petroleum Science and Engineering*, 147:302–307, 11 2016. 45, 46

[114] M. Kahrwad, K. S. Sorbie, and L. S. Boak. Coupled adsorption/precipitation of scale inhibitors: Experimental results and modelling. In *Society of Petroleum Engineers - 9th International Conference on Oilfield Scale 2008 - "Managing Scale Through the Field Lifetime"*, pages 494–503. Society of Petroleum Engineers, 1 2008. 45, 46, 111, 116, 145

[115] G.M. Graham, K.S. Sorbie, L.S. Boak, K. Taylor, and L. Blilie. Development and Application of Accurate Detection and Assay Techniques for Oilfield Scale Inhibitors in Produced Water Samples. Society of Petroleum Engineers (SPE), 1 1995. 45

[116] Kenneth S. Sorbie and Rick David Gdanski. A Complete Theory of Scale Inhibitor Transport, Adsorption/Desorption and Precipitation in Squeeze Treatments. In *SPE International Symposium on Oilfield Scale*. Society of Petroleum Engineers, 4 2005. 46, 47, 110

[117] Anietie N. Okon and Dulu Appah. Water Coning Prediction Review and Control: Developing an Integrated Approach. *Journal of Scientific Research and Reports*, 14(4), 2017. 47

[118] M. M. Jordan, K. S. Sorbie, Ping Jiang, Ming Dong Yuan, A. C. Todd, and K. E. Hourston. Phosphonate scale inhibitor adsorption/desorption and the potential for formation damage in reconditioned field core. In *Proceedings - SPE International Symposium on Formation Damage Control*, pages 451–464. Society of Petroleum Engineers, 4 1994. 47

[119] J. Stewart James, Dario Marcello Frigo, Maria M. Townsend, Gordon M. Graham, F. Wahid, and Stephen Mark Heath. Application of a fully viscosified scale squeeze for improved placement in horizontal wells. In *SPE Seventh International Symposium on Oilfield Scale 2005: Pushing the Boundaries of Scale Control, Proceedings*, pages 61–72. Society of Petroleum Engineers, 4 2005. 47, 51

[120] Nasser Ghorbani. *Nanotechnology enhanced squeeze treatments for efficient oilfield scale management - University of Leeds*. PhD thesis, University of Leeds, Leeds,UK, 2012. 48, 126

[121] Linyi Bai, Soo Zeng Fiona Phua, Wei Qi Lim, Avijit Jana, Zhong Luo, Huijun Phoebe Tham, Lingzhi Zhao, Qiang Gao, and Yanli Zhao. Nanoscale covalent organic frameworks as smart carriers for drug delivery. *Chemical Communications*, 52(22):4128–4131, 3 2016. 48

[122] Kamonchanok Thananukul, Chariya Kaewsaneha, Pakorn Opaprakasit, Noureddine Lebaz, Abdelhamid Errachid, and Abdelhamid Elaissari. Smart gating porous particles as new carriers for drug delivery. *Advanced Drug Delivery Reviews*, 174:425–446, 7 2021. 48

[123] Wan Li, Xiaoping Zeng, Hong Wang, Qin Wang, and Yajiang Yang. Polyaniline-poly(styrene sulfonate) conducting hydrogels reinforced by supramolecular nanofibers and used as drug carriers with electric-driven release. *European Polymer Journal*, 66:513–519, 5 2015. 48

[124] Jean d.Amour K. Twibanire and T. Bruce Grindley. Polyester Dendrimers: Smart Carriers for Drug Delivery. *Polymers 2014, Vol. 6, Pages 179-213*, 6(1):179–213, 1 2014. 48

[125] C Gao. FACTORS AFFECTING PARTICLE RETENTION IN POROUS MEDIA. Technical Report 3, 2007. 49

[126] M. A. Kelland. *Production Chemicals for Oil and Gas Industry. s.l. : CRC Press, 2009. pp. 53-109, cap.3.* CRC Press, 2009. 50

[127] Ping Zhang, Gedeng Ruan, Amy T. Kan, and Mason B. Tomson. Functional scale inhibitor nanoparticle capsule delivery vehicles for oilfield mineral scale control. *RSC Advances*, 6(49):43016–43027, 4 2016. 50, 69

[128] M. M. Jordan, K. Mackin, C. J. Johnston, and N. D. Feasey. Control of Hydrogen Sulphide Scavenger Induced Scale and the Associated Challenge of Sulphide Scale Formation Within A North Sea High Temperature/High Salinity Fields Production Wells. Laboratory Evaluation to Field Application. *Proceedings - SPE Sixth International Symposium on Oilfield Scale; Exploring the Boundaries of Scale Control*, pages 65–79, 5 2004. 51

[129] Daniel Emmons and Gary R. Chesnut. US4762626A - Hydroxyethylacrylate/acrylate copolymers as zinc sulfide scale inhibitors - Google Patents, 1988. 51

[130] Thomas Henry Lopez, Mingdong Yuan, Danny Andy Williamson, and John L. Przybylinski. Comparing efficacy of scale inhibitors for inhibition of zinc sulfide and lead sulfide scales. In *SPE Seventh International Symposium on Oilfield Scale 2005: Pushing the Boundaries of Scale Control, Proceedings*, pages 221–226. OnePetro, 5 2005. 51

[131] R. I Kaplan. US5171459A-Scale deposition inhibitor, 3 1992. 52

[132] Haixin Chang, Ying Yuan, Nanlin Shi, and Yifu Guan. Electrochemical DNA biosensor based on conducting polyaniline nanotube array. *Analytical Chemistry*, 79(13):5111–5115, 7 2007. 53

[133] Xiao-Wei Hu, Chang-Jie Mao, Ji-Ming Song, He-Lin Niu, Sheng-Yi Zhang, and Hai-ping Huang. Fabrication of GO/PANi/CdSe nanocomposites for sensitive electrochemiluminescence biosensor. *Biosensors and Bioelectronics*, 41(1):372–378, 3 2013. 53

[134] Yung Chien Luo and Jing Shan Do. Urea biosensor based on PANi(urease)-Nafion®/Au composite electrode. In *Biosensors and Bioelectronics*, volume 20, pages 15–23, 7 2004. 53

[135] B. Ramezanzadeh, P. Kardar, G. Bahlakeh, Y. Hayatgheib, and M. Mahdavian. Fabrication of a Highly Tunable Graphene Oxide Composite through Layer-by-Layer Assembly of Highly Crystalline Polyaniline Nanofibers and Green Corrosion Inhibitors: Complementary Experimental and First-Principles Quantum-Mechanics Modeling Approaches. *Journal of Physical Chemistry C*, 121(37):20433–20450, 9 2017. 53

[136] Y. Hayatgheib, B. Ramezanzadeh, P. Kardar, and M. Mahdavian. A comparative study on fabrication of a highly effective corrosion protective system based on graphene oxide-polyaniline nanofibers/epoxy composite. *Corrosion Science*, 133:358–373, 4 2018. 53, 55, 56, 62, 129, 131, 140

[137] Mohammad Ramezanzadeh, Morteza Asghari, Bahram Ramezanzadeh, and Ghasem Bahlakeh. Fabrication of an efficient system for Zn ions removal from industrial wastewater based on graphene oxide nanosheets decorated with highly crystalline polyaniline nanofibers (GO-PANI): Experimental and ab initio quantum mechanics approaches. *Chemical Engineering Journal*, 337:385–397, 4 2018. 53

[138] Debajyoti Mahanta, Giridhar Madras, S. Radhakrishnan, and Satish Patil. Adsorption and desorption kinetics of anionic dyes on doped polyaniline. *Journal of Physical Chemistry B*, 113(8):2293–2299, 2 2009. 53

[139] Niloufar Notghi Taheri, Bahram Ramezanzadeh, Mohammad Mahdavian, and Ghasem Bahlakeh. In-situ synthesis of Zn doped polyaniline on graphene oxide for inhibition of mild steel corrosion in 3.5 wt.% chloride solution. *Journal of Industrial and Engineering Chemistry*, 63:322–339, 7 2018. 53

[140] Triveni Kumar Mahto, Soumen Chandra, Chanchal Haldar, and Sumanta Kumar Sahu. Kinetic and thermodynamic study of polyaniline functionalized magnetic mesoporous silica for magnetic field guided dye adsorption. *RSC Advances*, 5(59):47909–47919, 5 2015. 54

[141] Ermelinda Falletta. *"Re-discovering" an old material, Polyaniline, for modern applications*. PhD thesis, Milan University (Universita degli studi di Milano), 2013. 55, 137, 140

[142] Sunghun Cho, Jun Seop Lee, Jaemoon Jun, Sung Gun Kim, and Jyongsik Jang. Fabrication of water-dispersible and highly conductive PSS-doped PANI/graphene nanocomposites using a high-molecular weight PSS dopant and their application in H 2 S detection †. 6:15181, 2014. 55

[143] Anca-Dana Bendrea, Luminita Cianga, and Ioan Cianga. Review paper: Progress in the Field of Conducting Polymers for Tissue Engineering Applications. *JOURNAL OF BIOMATERIALS APPLICATIONS*, 17:20–24. 55

[144] Rebecca L. Li, Cheng Wei Lin, Yuanlong Shao, Che Wei Chang, Fu Kai Yao, Matthew D. Kowal, Haosen Wang, Michael T. Yeung, Shu Chuan Huang, and Richard B. Kaner. Characterization of Aniline Tetramer by MALDI TOF Mass Spectrometry upon Oxidative and Reductive Cycling. *Polymers 2016, Vol. 8, Page 401*, 8(11):401, 11 2016. 56

[145] SciMed. What is X-Ray Diffraction (XRD) — SciMed, 2022. 66

[146] Utz Kramar. X-Ray Fluorescence Spectrometers. *Encyclopedia of Spectroscopy and Spectrometry*, pages 2989–2999, 1 1999. 66

[147] Barbara L Dutrow. X-ray Powder Diffraction (XRD). pages 1–4, 1912. 66

[148] Elena V. Fomenko, Vladimir V. Yumashev, Sergey V. Kukhtetskiy, Anatoliy M. Zhizhaev, and Alexander G. Anshits. Scanning Electron Microscopy–Energy-Dispersive X-ray Spectrometry (SEM–EDS) Analysis of PM1–2 Microspheres Located in Coal Char Particles with Different Morphologies. *Energy & Fuels*, 34(7):8848–8856, 7 2020. 67

[149] L. Reimer and C. Tollkamp. Measuring the backscattering coefficient and secondary electron yield inside a scanning electron microscope. *Scanning*, 3(1):35–39, 1980. 67

[150] C. J.F.P. Jones. Multifunctional uses of geosynthetics in civil engineering. In *Geosynthetics in Civil Engineering*, pages 97–126. Woodhead Publishing, 1 2006. 68

[151] Andrei S. Dukhin and Philip J. Goetz. Applications for nanodispersions. In *Studies in Interface Science*, volume 24, pages 343–368. Elsevier, 1 2010. 68

[152] Krista S. Walton and Randall Q. Snurr. Applicability of the BET method for determining surface areas of microporous metal-organic frameworks. *Journal of the American Chemical Society*, 129(27):8552–8556, 7 2007. 68

[153] U. P. Fringeli. ATR and Reflectance IR Spectroscopy, Applications. *Encyclopedia of Spectroscopy and Spectrometry*, pages 94–109, 1 1999. 69

[154] Marieta L.C. Passos, Mafalda C. Sarraguça, and M. Lúcia M.F.S. Saraiva. Spectrophotometry — Organic Compounds. *Encyclopedia of Analytical Science*, pages 236–243, 1 2019. 70

[155] Fondriest Environmental Inc. Measuring Turbidity, TSS, and Water Clarity - Environmental Measurement Systems, 2015. 70

[156] Azizollah Khormali, • Dmitry, and G Petrakov. Laboratory investigation of a new scale inhibitor for preventing calcium carbonate precipitation in oil reservoirs and production equipment. 71

[157] Jamal Mohamad Bin and Mohamad Ibrahim. Establishing Scale Inhibitor Retention Mechanisms In Pure Adsorption And Coupled Adsorption/Precipitation Treatments. 2011. 72, 74, 181, 183

[158] Vinicius Kartnaller, Fabrício Venâncio, Francisca F. do Rosário, and João Cajaiba. Application of multiple regression and design of experiments for modelling the effect of monoethylene glycol in the calcium carbonate scaling process. *Molecules*, 23(4), 2018. 79

[159] Xiaomei Zhang, Qinlu Zhang, Ting Ma, Qian Liu, Songdi Wu, Kai Hua, Chao Zhang, Mingwei Chen, and Yali Cui. Enhanced Stability of Gold Magnetic Nanoparticles with Poly(4-styrenesulfonic acid-co-maleic acid): Tailored Optical Properties for Protein Detection. *Nanoscale Research Letters*, 12(1):1–9, 9 2017. 82

[160] Jean Louis Gustin. Runaway reaction hazards in processing organic nitro compounds. *Organic Process Research and Development*, 2(1):27–33, 1998. 82

[161] Yuanyuan Cao and Tiancheng Mu. Comprehensive investigation on the thermal stability of 66 ionic liquids by thermogravimetric analysis. *Industrial and Engineering Chemistry Research*, 53(20):8651–8664, 5 2014. 82

[162] Laura Espinal. Porosity and Its Measurement. In *Characterization of Materials*, pages 1–10. John Wiley & Sons, Inc., Hoboken, NJ, USA, 10 2012. 93, 97

[163] L.L. LYON, G.R. CROCKER, and J.S. DAHLER. PHYSICAL ADSORPTION AND THE SURFACE AREAS OF CARBON BLACKS. In *Carbon*, pages 71–77. Elsevier, 1 1960. 93

[164] Djebbar Tiab and Erle C. Donaldson. *Petrophysics*. Elsevier Inc., 2012. 94

[165] Zhelin Wang, Xuewei Jiang, Mao Pan, and Yongmin Shi. Nano-scale pore structure and its multi-fractal characteristics of tight sandstone by n2 adsorption/desorption analyses: A case study of shihezi formation from the sulige gas filed, ordos basin, china. *Minerals*, 10(4):377, 4 2020. 94, 137, 226, 227

[166] Matthias Thommes, Katsumi Kaneko, Alexander V Neimark, James P Olivier, Francisco Rodriguez-Reinoso, Jean Rouquerol, and Kenneth S W Sing. IUPAC Technical Report Physisorption of gases, with special reference to the evaluation of surface area and pore size distribution (IUPAC Technical Report). 2015. 94, 96, 111, 112, 226

[167] Matthew J. Meagher, Bridget Leone, Travis L. Turnbull, Ryan D. Ross, Zhenyuan Zhang, and Ryan K. Roeder. Dextran-encapsulated barium sulfate nanoparticles prepared for aqueous dispersion as an X-ray contrast agent. *Journal of Nanoparticle Research*, 15(12):1–10, 11 2013. 107, 119

[168] P Muhammed Shafi and A Chandra Bose. Impact of crystalline defects and size on X-ray line broadening: A phenomenological approach for tetragonal SnO2 nanocrystals. *AIP Advances*, 5(5):57137, 2015. 107

[169] T. Ungár. Microstructural parameters from X-ray diffraction peak broadening. *Scripta Materialia*, 51(8 SPEC. ISS.):777–781, 10 2004. 107

[170] Kuen Song Lin, Yao Jen Mai, Shin Rung Li, Chia Wei Shu, and Chieh Hung Wang. Characterization and hydrogen storage of surface-modified multiwalled carbon nanotubes for fuel cell application. *Journal of Nanomaterials*, 2012:12, 2012. 107

[171] Da-Wei Li, Shi-Hua Sang, Rui-Zhi Cui, and Cui Wei. Solid-Liquid Equilibria in the Ternary Systems NaCl-SrCl 2 -H 2 O and KCl-SrCl 2 -H 2 O at 348 K. 2015. 107

[172] Wei Cheng, Caihong Liu, Tiezheng Tong, Razi Epsztein, Meng Sun, Rafael Verduzco, Jun Ma, and Menachem Elimelech. Selective removal of divalent cations by polyelectrolyte multilayer nanofiltration membrane: Role of polyelectrolyte charge, ion size, and ionic strength. *Journal of Membrane Science*, 559:98–106, 8 2018. 109

[173] G.M. Graham, L.S. Boak, and K.S. Sorbie. The Influence of Formation Calcium and Magnesium on the Effectiveness of Generically Different Barium Sulphate Oilfield Scale Inhibitors. *SPE Production & Facilities*, 18(01):28–44, 2 2003. 110, 124

[174] Jeferson Steffanello Piccin, Tito Roberto Sant Anna Cadaval, Luiz Antonio Almeida De Pinto, and Guilherme Luiz Dotto. Adsorption isotherms in liquid phase: Experimental, modeling, and interpretations. In *Adsorption Processes for Water Treatment and Purification*, pages 19–51. Springer International Publishing, 7 2017. 111, 112, 116, 146, 220, 221

[175] Sérgio Roberto Montoro, Simone de Fátima Medeiros, and Gizelda Maria Alves. Nanostructured Hydrogels. In *Nanostructured Polymer Blends*, pages 325–355. Elsevier Inc., 12 2013. 117, 218

[176] S. S. Shaw and K. S. Sorbie. Synergistic Properties of Phosphonate and Polymeric Scale Inhibitor Blends for Barium Sulphate Scale Inhibition. *NACE - International Corrosion Conference Series*, 5 2014. 123

[177] P Savitha and DN Sathyanarayana. Copolymers of aniline witho- andm-toluidine: synthesis and characterization. *Polymer International*, 53(1):106–112, 1 2004. 126

[178] Jiang Yue, Zhao H. Wang, Keith R. Cromack, Arthur J. Epstein, and Alan G. MacDiarmid. Effect of sulfonic acid group on polyaniline backbone. *Journal of the American Chemical Society*, 113(7):2665–2671, 3 1991. 126, 137

[179] Shi Jian Su and Noriyuki Kuramoto. Synthesis of processable polyaniline complexed with anionic surfactant and its conducting blends in aqueous and organic system. *Synthetic Metals*, 108(2):121–126, 1 2000. 126, 137

[180] Yanyin Yang, Yong Min, Jen Chieh Wu, Derek J. Hansford, Stephen E. Feinberg, and Arthur J. Epstein. Synthesis and characterization of cytocompatible sulfonated polyanilines. *Macromolecular Rapid Communications*, 32(12):887–892, 6 2011. 126

[181] Venkanna Meriga, Sreeramulu Valligatla, Sivaprakash Sundaresan, Caroline Cahill, Vinod R. Dhanak, and Amit K. Chakraborty. Optical, electrical, and

electrochemical properties of graphene based water soluble polyaniline composites. *Journal of Applied Polymer Science*, 132(45):1–9, 2015. 126, 127

[182] Kohshin Takahashi, Kunihiro Nakamura, Takahiro Yamaguchi, Teruhisa Komura, Shoji Ito, Ryuji Aizawa, and Kazuhiko Murata. Characterization of water-soluble externally HCl-doped conducting polyaniline. *Synthetic Metals*, 128(1):27–33, 4 2002. 127

[183] Shoji Ito, Kazuhiko Murata, Seiichi Teshima, Ryuji Aizawa, Yoshinobu Asako, Kohshin Takahashi, and Brian M. Hoffman. Simple synthesis of water-soluble conducting polyaniline. *Synthetic Metals*, 96(2):161–163, 7 1998. 127

[184] Wei Liu, Jayant Kumar, Sukant Tripathy, Kris J. Senecal, and Lynne Samuelson. Enzymatically Synthesized Conducting Polyaniline. *Journal of the American Chemical Society*, 121(1):71–78, 1 1999. 127, 137

[185] Lynne A. Samuelson, Althea Anagnostopoulos, K. Shridhara Alva, Jayant Kumar, and Sukant K. Tripathy. Biologically derived conducting and water soluble polyaniline. *Macromolecules*, 31(13):4376–4378, 6 1998. 127

[186] Zanna Boeva, Lomonosov Moscow, and Olga Pyshkina. Matrix Polymerization of Aniline in the Presence of Polysulfonic Acids. *Scientific Journal of Riga Technical University Material Science and Applied Chemistry*, 21:104–108, 2010. 127, 137

[187] Yen Wen Lin and Tzong Ming Wu. Synthesis and characterization of externally doped sulfonated polyaniline/multi-walled carbon nanotube composites. *Composites Science and Technology*, 69(15-16):2559–2565, 2009. 127, 141

[188] Jaroslav Stejskal, Andrea Riede, Drahomíra Hlavatá, Jan Prokeš, Martin Helmstedt, and Petr Holler. The effect of polymerization temperature on molecular weight, crystallinity, and electrical conductivity of polyaniline. *Synthetic Metals*, 96(1):55–61, 7 1998. 127, 131

[189] Shiow Jing Tang, An Tsai Wang, Su Yin Lin, Kuan Yeh Huang, Chun Chuen Yang, Jui Ming Yeh, and Kuan Cheng Chiu. Polymerization of aniline under various concentrations of APS and HCl. *Polymer Journal*, 43(8):667–675, 2011. 127, 132, 133

[190] Mehdi Jaymand. Recent progress in chemical modification of polyaniline Dedicated to Professor Dr. Ali Akbar Entezami. *Progress in Polymer Science*, 38(9):1287–1306, 2013. 127

[191] Mohammad Shahadat, Mohammad Zain Khan, Parveen Fatemeh Rupani, Asha Embrandiri, Saima Sultana, Shaikh Ziauddin Ahammad, S. Wazed Ali, and T. R. Sreekrishnan. A critical review on the prospect of polyaniline-grafted biodegradable nanocomposite. *Advances in Colloid and Interface Science*, 249:2–16, 2017. 127

[192] Yangyong Wang and Xinli Jing. Formation of polyaniline nanofibers: A morphological study. *Journal of Physical Chemistry B*, 112(4):1157–1162, 1 2008. 127

[193] Michal Bláha, Martin Varga, Jan Prokeš, Alexander Zhigunov, and Jiří Vohlídal. Effects of the polymerization temperature on the structure, morphology and conductivity of polyaniline prepared with ammonium peroxodisulfate. *European Polymer Journal*, 49(12):3904–3911, 2013. 127

[194] Utpal Rana, Kuntal Chakrabarti, and Sudip Malik. Benzene tetracarboxylic acid doped polyaniline nanostructures: Morphological, spectroscopic and electrical characterization. *Journal of Materials Chemistry*, 22(31):15665–15671, 2012. 129, 130, 137

[195] H. S.O. Chan, S. C. Ng, W. S. Sim, S. H. Seow, K. L. Tan, and B. T.G. Tan. Synthesis and Characterization of Conducting Poly(o-aminobenzyl alcohol) and Its Copolymers with Aniline. *Macromolecules*, 26(1):144–150, 1993. 131, 132

[196] H. S.O. Chan, S. C. Ng, W. S. Sim, K. L. Tan, and B. T.G. Tan. Preparation and Characterization of Electrically Conducting Copolymers of Aniline and Anthranilic Acid: Evidence for Self-Doping by X-ray Photoelectron Spectroscopy. *Macromolecules*, 25(22):6029–6034, 10 1992. 131

[197] Romklaw Boonpoo-Nga, Manus Sriring, Pitak Nasomjai, and Surangkhana Martwiset. Electrospun fibres from polyvinyl alcohol, poly(styrene sulphonic acid-co-maleic acid), and imidazole for proton exchange membranes. *ScienceAsia*, 40(3):232–237, 2014. 131, 134

[198] Gao Ren Li, Zhan Ping Feng, Jin Hui Zhong, Zi Long Wang, and Ye Xiang Tong. Electrochemical synthesis of polyaniline nanobelts with predominant electrochemical performances. *Macromolecules*, 43(5):2178–2183, 3 2010. 132

[199] B. Behera and Puspendu K. Das. Blue- and Red-Shifting Hydrogen Bonding: A Gas Phase FTIR and Ab Initio Study of RRCO···DCCl3 and RRS···DCCl3 Complexes. *Journal of Physical Chemistry A*, 122(18):4481–4489, 5 2018. 132, 133

[200] Yaping Guo and Yu Zhou. Polyaniline nanofibers fabricated by electrochemical polymerization: A mechanistic study. *European Polymer Journal*, 43(6):2292–2297, 6 2007. 132

[201] Noriyuki Kuramoto and Eugène M. Geniès. Micellar chemical polymerization of aniline. *Synthetic Metals*, 68(2):191–194, 1 1995. 132

[202] Ivana Šeděnková, Miroslava Trchová, Natalia V. Blinova, and Jaroslav Stejskal. In-situ polymerized polyaniline films. Preparation in solutions of hydrochloric, sulfuric, or phosphoric acid. *Thin Solid Films*, 515(4):1640–1646, 12 2006. 132

[203] Dali Yang, Wen Lu, Russell Goering, and Benjamin R. Mattes. Investigation of polyaniline processibility using GPC/UV-vis analysis. *Synthetic Metals*, 159(7-8):666–674, 4 2009. 135

[204] Jadwiga Laska. Conformations of polyaniline in polymer blends. *Journal of Molecular Structure*, 701(1-3):13–18, 9 2004. 135

[205] C. Dhivya, S. Anbu Anjugam Vandarkuzhali, and N. Radha. Antimicrobial activities of nanostructured polyanilines doped with aromatic nitro compounds. *Arabian Journal of Chemistry*, 12(8):3785–3798, 2019. 136

[206] Jie Han, Jie Dai, Chuanqiang Zhou, and Rong Guo. Dilute cationic surfactant-assisted synthesis of polyaniline nanotubes and application as reactive support for various noble metal nanocatalysts. *Polymer Chemistry*, 4(2):313–321, 1 2013. 137

[207] Yangyong Wang and Xinli Jing. Formation of polyaniline nanofibers: A morphological study. *Journal of Physical Chemistry B*, 112(4):1157–1162, 2008. 137

[208] Raushan N. Nurdillayeva, Benjamin R. Horrocks, and Andrew R. Pike. Electronic and Electrochemical characterization of DNA - Templated CdS nanowires. In *Materials Today: Proceedings*, volume 5, pages 22825–22834. Elsevier Ltd, 1 2018. 137

[209] Charles J. Brumlik, Vinod P. Menon, and Charles R. Martin. Template synthesis of metal microtubule ensembles utilizing chemical, electrochemical, and vacuum deposition techniques. *Journal of Materials Research*, 9(5):1174–1183, 3 1994. 137

[210] Michael Woodson and Jie Liu. Guided growth of nanoscale conducting polymer structures on surface-functionalized nanopatterns. *Journal of the American Chemical Society*, 128(11):3760–3763, 3 2006. 137

[211] Rui Xiao, Il Cho Seung, Ran Liu, and Bok Lee Sang. Controlled electrochemical synthesis of conductive polymer nanotube structures. *Journal of the American Chemical Society*, 129(14):4483–4489, 4 2007. 137

[212] Wusheng Yin and Eli Ruckenstein. Soluble polyaniline co-doped with dodecyl benzene sulfonic acid and hydrochloric acid. *Synthetic Metals*, 108(1):39–46, 2000. 137

[213] Valerie Rumbau, Jose A. Pomposo, Juan A. Alduncin, Hans Grande, David Mecerreyes, and Estibalitz Ochoteco. A new bifunctional template for the enzymatic synthesis of conducting polyaniline. *Enzyme and Microbial Technology*, 40(5):1412–1421, 4 2007. 137

[214] Khosro Jarrahian, Morteza Aminnaji, Alexander Graham, and Kenneth Sorbie. Experimental Analysis of Scale Inhibitors Retention in Carbonate Formations for Application in Squeeze Treatments. *Energy and Fuels*, 36(4):1776–1791, 2022. 145

[215] Richard M. Hartshorn, Karl Heinz Hellwich, Andrey Yerin, Ture Damhus, and Alan T. Hutton. Brief guide to the nomenclature of inorganic chemistry. *Pure and Applied Chemistry*, 87(9-10):1039–1049, 10 2015. 164

[216] William Keogh, Gifty Oppong Boakye, Anne Neville, Thibaut Charpentier, John Helge Olsen, Violette Eroini, Frank MØller Nielsen, Jon Ellingsen, Oeystein Bache, Salima Baraka-Lokmane, and Etienne Bourdelet. Lead sulfide (PbS) scale behavior and deposition as a function of polymeric sulfide inhibitorconcentration in multiphase. In *NACE - International Corrosion Conference Series*, volume 2018-April. OnePetro, 4 2018. 164

[217] Andrey V. Dobrynin and Michael Jacobs. When Do Polyelectrolytes Entangle? *Macromolecules*, 54(4):1859–1869, 2 2021. 174

[218] Mohammad Atif, Faiz Afzal, Jarod M Younker, and George Rodriguez. The Effect of Tacticity and Side Chain Structure on the Coil Dimensions of Polyolefins. 6 2018. 174

[219] Shelley Sazer, Helmut Schiessel, Shelley Correspondence, Verna Sazer, and Marrs Mclean. The biology and polymer physics underlying large-scale chromosome organization. *Traffic*, 19(2):87–104, 2 2018. 174

[220] O. K. Simya, P. Radhakrishnan, Anuradha Ashok, K. Kavitha, and R. Althaf. Engineered nanomaterials for energy applications. In *Handbook of Nanomaterials for Industrial Applications*, pages 751–767. Elsevier, 1 2018. 217

[221] Hari Madhav, Neetika Singh, and Gautam Jaiswar. Thermoset, bioactive, metal-polymer composites for medical applications. In *Materials for Biomedical Engineering: Thermoset and Thermoplastic Polymers*, pages 105–143. Elsevier, 1 2019. 217

[222] Phuong Nguyen Tri, Sami Rtimi, and Claudiane M.Ouellet Plamondon. *Nanomaterials-based coatings: Fundamentals and applications*. Elsevier, 1 2019. 217

[223] C. H. Giles, T. H. MacEwan, S. N. Nakhwa, and D. Smith. 786. Studies in adsorption. Part XI. A system of classification of solution adsorption isotherms, and its use in diagnosis of adsorption mechanisms and in measurement of specific surface areas of solids. *Journal of the Chemical Society (Resumed)*, (0):3973–3993, 1 1960. 220

[224] Chung hai Yang. Statistical mechanical study on the Freundlich isotherm equation. *Journal of Colloid and Interface Science*, 208(2):379–387, 12 1998. 223

[225] Azlan Abdul Aziz, Mohd Raihan Taha, Zamri Chik, and Kamaruddin Ahmad. Geoenvironmental aspects of tropical residual soils. In *Tropical Residual Soils Engineering*, chapter 12, pages 213–229. A.A Balkema Publishers, London, 4 edition, 2004. 223

[226] Nimibofa Ayawei, Augustus Newton Ebelegi, and Donbebe Wankasi. Modelling and Interpretation of Adsorption Isotherms, 9 2017. 224

[227] Nimibofa Ayawei, Seimokumo Samuel Angaye, Donbebe Wankasi, and Ezekiel Dixon Dikio. Synthesis, Characterization and Application of Mg/Al Layered Double Hydroxide for the Degradation of Congo Red in Aqueous Solution. *Open Journal of Physical Chemistry*, 05(03):56–70, 2015. 224

[228] Nimibofa Ayawei, Augustus Newton Ebelegi, and Donbebe Wankasi. Modelling and Interpretation of Adsorption Isotherms, 2017. 224, 225

[229] B. R. Venkatraman, M. Hema, T. Rajachandrasekar, and S Arivoli. Adsorption of ferrous ion from aqueous solution by acid activated low cost carbon obtained from natural plant material. *Research Journal of Chemistry and Environment*, 11(1):70–78, 2007. 225

[230] Ahmet Günay, Ertan Arslankaya, and Ismail Tosun. Lead removal from aqueous solution by natural and pretreated clinoptilolite: Adsorption equilibrium and kinetics. *Journal of Hazardous Materials*, 146(1-2):362–371, 7 2007. 225

[231] Kent S Knaebel. *Adsorbent Selection*, volume 20. 2004. 225

[232] A. Dabrowski. Adsorption - From theory to practice, 10 2001. 226

[233] Amanollah Ebadi, Jafar S. Soltan Mohammadzadeh, and Anvar Khudiev. What is the correct form of BET isotherm for modeling liquid phase adsorption? *Adsorption*, 15(1):65–73, 2 2009. 226

APPENDIX A

Appendix A

A.1 Conductive polymers

Conductive polymers are a special group of organic materials that show the electrical and optical properties of both metals and semiconductors. They consistently store and discharge through redox processes. When oxidation occurs, ions are transferred to the polymer. When reduction occurs the ions are released back into the solution. Unlike polyelectrolytes that only become conductive while dissolved, conductive polymers are intrinsically conductive[220].
Conducting polymers have backbones of contiguous sp^2 hybridised carbon centres. One valence electron on each centre resides in a p_z orbital, which is orthogonal to the other three sigma-bonds. All the p_z orbitals combine with each other to a molecule wide delocalised set of orbitals. The electrons in these delocalised orbitals have high mobility when the material is "doped" by oxidation, which removes some of these delocalised electrons. Thus, the conjugated p-orbitals form a one-dimensional electronic band, and the electrons within this band become mobile when it is partially emptied.

A.2 Polyelectrolytes

Polyelectrolytes are polymers whose repeating units contain an electrolyte group. Polyelectrolytes are macromolecules that, by dissolving in a polar solvent like water, (large) number of charged groups covalently are linked to them. In general, polyelectrolytes may have various kinds of such groups. Homogeneous polyelectrolytes have only one kind of charged group, e. g. only carboxylate groups. If both negative (anionic) and positive (cationic) groups occur, we call such a molecule a polyampholyte and same for polycations and polyanions. These groups dissociate in aqueous solutions (water), making the polymers charged. Polyelectrolyte properties are thus similar to both electrolytes (salts) and polymers (high molecular weight compounds) and are sometimes called polysalts. Like salts, their solutions are electrically conductive and like polymers, their solutions are often viscous [221].

A.3 Water soluble polymers

The synthetic water-soluble polymer is an organic material which can be modified through dispersion or dissolution in water and become gelled, stabilised, concentrated, or emulsified [222]. PVA is a water-soluble polymer and a so-called hydrophilic polymer depending on the wide range of temperature. Its water solubility is a function of its molecular weight, degree of hydrolysis, and hydrogen bonding tendency toward an aqueous solution. Moreover, the relative equilibrium between the total hydrocarbon content of the functional group, the arrangement and the repeating units in the copolymer structure also influence water solubility.

A.4 Hydrogel

Water-soluble polymers may acquire three-dimensional structures in an aqueous solution in a reversible way by promoting or increasing physical interactions between polymer chains. While precipitating and collapsing, macromolecules may capture cells and other bio-molecules from an aqueous solution together with water molecules, thus creating hydrogel structures that contain active compounds [175].
Physically cross-linked nanostructured hydrogels can also be prepared by varying the pH of the medium or using additional molecules to significantly increase polymer-polymer interactions such as hydrogen bonding, complex coacervation, ionic interaction, and so on. An example of hydrogel formation by promoting hydrogen-bounds is the carboxymethyl cellulose dispersed in aqueous solution (0.1 M) of HCl [175]. Complex coacervate [1] gels can be formed by mixing a polyanion with a polycation. Finally, ionic polymers can be cross-linked by the addition of a multivalent ion of opposite charges to a polyelectrolyte solution[175].

[1] Coacervate is an aqueous phase rich in macromolecules such as synthetic polymers, proteins or nucleic acids. It forms through liquid-liquid phase separation, leading to a dense phase in thermodynamic equilibrium with a dilute phase.

APPENDIX B

Appendix B

B.1 Classification of the equilibrium isotherms

The classification of liquid–solid adsorption isotherms describes a system and suggests how their form can be used to identify the adsorption mechanism [174]. This gives an information regarding the physical nature of the adsorbate and the adsorbent surface and also to measure the specific surface area of the adsorbent. In this classification, the equilibrium curves are categorised according the initial slope into four main classes. Subgroups are described for each class, based on the shapes of the upper parts and slope changes. FigureB.1 shows the classification proposed by Giles *et.al* [223]. The main classes are (i) S curves or vertical orientation isotherm, (ii) L curves or normal or "Langmuir" isotherms, (iii) H curves or high affinity isotherms, and (iv) C curves or constant partition isotherm.

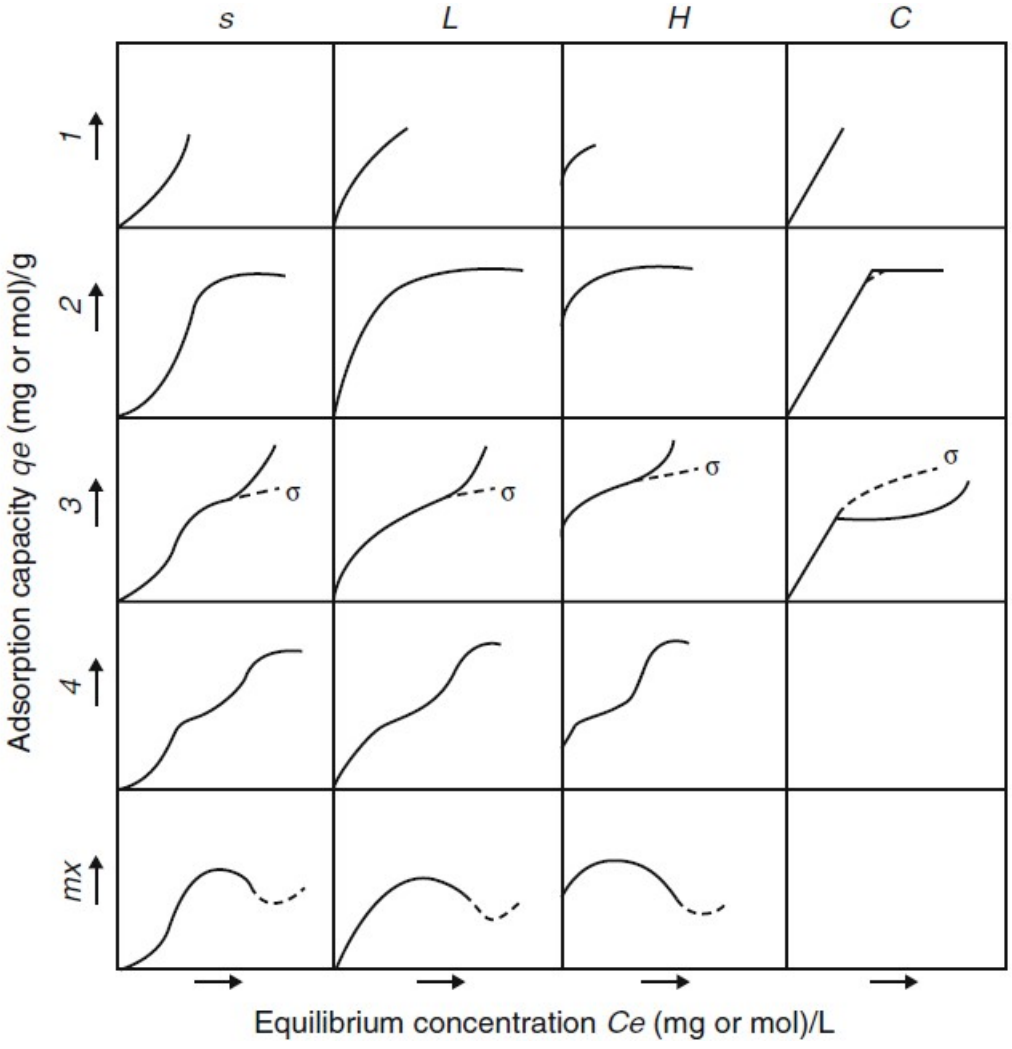

Figure B.1: Adsorption isotherm classification [223]

B.1.1 S curve

the S type isotherm shows an inclining slope of the curve that is followed by a vertical trend. Initially, when the adsorbate concentration increases, there is a chance of the adsorbate to find an available site so that it can occupy based on the competition between solute molecules. As, the adsorption capacity is "limited," it reaches a plateau. However, this behavior in type S isotherms is opposed, causing the increase of curve slope caused by a vertical orientation tendency of the solute molecules in a higher concentration that leaves more sites available for adsorption [174]. In practice, the S curve usually appears when three conditions are fulfilled: (a) the solute molecule is monofunctional; (b) there is a moderate intermolecular attraction, leading to pack vertically in regular array in the adsorbed layer; and (c) there is strong competition, for substrate sites, from molecules of the solvent or another adsorbed species. FigureB.1 shows a schematic representation of the orientation of the molecules in S type isotherms.

B.1.2 L curve

The normal or Langmuir isotherms are most commonly found in solute adsorption in aqueous solution. The initial shape of the equilibrium curve follows the basic rule of the higher the solute concentration, the greater the adsorption capacity. Since, the number of adsorption site clearance is limited, a competition occurs between solute molecules for the available sites. This type of isotherm typically, indicates that the molecules are adsorbed flat on the surface or, sometimes, of vertically oriented adsorbed ions with particularly strong intermolecular attraction [174]. Thus they either: (i) are the adsorbed molecules that more likely to be adsorbed flat or (ii) are systems with high polar solute and substrate. This isotherm type indicated that the adsorption occurs due to relatively weak forces, such as van der Waals forces.

B.1.3 H curve

The basic difference between the normal isotherms or L type with the high affinity isotherm relates to the beginning of the equilibrium curve. While L type isotherm has its beginning in the origin, H type isotherm shows an initial portion with a vertical orientation, and qe values are higher than zero, even when the concentration of solute tends to values close to zero. The adsorbed species are often large units, for example, ionic micelles or polymeric molecules However, sometimes, they can be simple ions, which exchange with others of much lower affinity with adsorbent surface, for example, sulfonated dye. This isotherm type indicates chemisorption and adsorption by electrostatic forces. Other classifications commonly used for H type isotherms are like an irreversible isotherm, because when an adsorption occurs at a high concentration, a concentration reduction does not change the adsorption capacity.

B.1.4 C curve

The isotherms with partition constant are characterised by a linear behaviour of the equilibrium data at low concentrations of solute. This behaviour follows Henry's law for ideal gas equilibrium phases, which translated to adsorption processes, and suggests that the adsorption capacity is proportional to the solute concentration, up until the maximum possible adsorption, where an abrupt change to a horizontal plateau occurs. This is the type of curve obtained for the partition of a solute between two practically immiscible solvents. In such cases, the affinity of the solute by the solid is greater than the affinity for the solvent, or when the adsorption sites are available in quantities sufficient for the adsorption of all solute, but the bonding forces between the solute and the solvent are weak and depend on the liquid phase concentration.

B.1.5 Sub classes

The subclass 1 of S type isotherm indicates a complete vertical behaviour of the adsorption capacity, possibly caused by surface precipitation of solute on the surface of the adsorbent. In the case of classes L, H, and C, they occur when the adsorption sites were not fully occupied, or there was not a complete vertical orientation of the molecules of the solvent. This isotherm type is usually described by the Freundlich model (for the case of L and H type) or Henry's law (for the C type).

The subclass 2 indicates that there is no intermolecular interaction between the solute, forming a long plateau, indicating a saturation of the adsorbent monolayer. In this case, a high energy barrier should be overcome before the additional adsorption can occur on new sites, after the surface has been saturated to the first degree. Therefore, the solute has high affinity for the solvent, but low affinity for the layer of solute molecules already adsorbed. In this case, equilibrium data can be represented by Langmuir model and the plateau is represented by the maximum adsorption capacity (qm) (for the case of L and H isotherm type).

In subclass 3, a short plateau must mean that the adsorbed solute molecules expose a surface, which has nearly the same affinity for more solute as the original surface possessed. This indicates that the solute in the solution has some intermolecular interaction with the solute in the adsorbent surface, leading to the formation of multilayers.

The subclasses 4 are attributed to the development of a fresh surface in which adsorption can occur. The second plateau represents the complete saturation of the new surface. This additional layer may occur when (i) a proportion of the original surface may be uncovered by reorientation of the molecules already adsorbed, due to intermolecular interactions, (ii) formation of new surfaces in crystalline solids, generating new adsorption sites, or (iii) already exposed parts that allow the formation of two layers, for example, due to formation of micelles.
Finally, the mx subclass occurs occasionally when a fall in slope occurs after the first

inflection. This is probably due to the association of the solutes in solution; with increase in concentration, the solute–solute attraction begins to increase more rapidly than the adsorbent–solute attraction.

B.2 Freundlich model

The Freundlich model is applicable to both monolayer (chemisorption) and multilayer adsorption (physisorption) and is based on the assumption that the adsorbate adsorbs onto the heterogeneous surface of an adsorbent[224] The Freundlich isotherm describes as follow:

$$q_e = K_F C_e^{\frac{1}{n}} \tag{B.1}$$

Where $q_e = (\frac{X}{m})$ is the amount of adsorption in $(\frac{mg}{g})$,X is the amount of adsorbate in mg and m is the amount of adsorbent in g, K_F is adsorption capacity with unit of $(\frac{L}{mg})$ and n is adsorption intensity; it also indicates the relative distribution of the energy and the heterogeneity of the adsorbate sites. C_e represent the equilibrium concentration of the SI. Isotherms with $n > 1$ are classified as L-type and H-type isotherms. This value shows that when the concentration of chemical under investigation increases, the relative adsorption decreases (L-type and H-type isotherm). This tends to be indicative of saturation of adsorption sites available to the chemical, resulting in relatively less adsorption[225].

B.3 Langmuir model

The Langmuir model assumes monolayer adsorption on a uniform surface with a finite number of adsorption sites. Once a site is filled, no further sorption can take place at that site. As such the surface will eventually reach a saturation point where the maximum adsorption of the surface will be achieved. the Langmuir isotherm model is described as:

$$q_e = \frac{K_L q_m C_e}{1 + K_L C_e} \tag{B.2}$$

with the linear form of:

$$\frac{C_e}{q_e} = \frac{1}{K_L q_m} + \frac{C_e}{q_m} \tag{B.3}$$

where $q_e = \frac{x}{m}$,K_L is the Langmuir constant related to the energy of adsorption that can be correlated with the variation of the suitable area and porosity of the adsorbent which implies that large surface area and pore volume will result in higher adsorption capacity.

$q_m$is the maximum adsorption capacity($\frac{mg}{g}$). Both K_L and q_m can be calculated from linear regression of the above equation where $\frac{c_e}{q_e}$ is plotted against C_e. The essential characteristics of the Langmuir isotherm can be expressed by a dimensionless constant called the separation factor R_L that is calculated based on C_0, the initial concentration of adsorbent in $\frac{mg}{g}$ and K_L[226].

$$R_L = \frac{1}{1 + K_L C_0} \tag{B.4}$$

For $R_L > 1$ the adsorption is unfavorable , whereas $R_L = 1$ implies a linearity. $0 < R_L < 1$ shows that the adsorption is favourable and that for $R = 0$ the adsorption is irreversible[227]. Hence, the Langmuir theory is based on the following assumptions:

- All surface sites have the same adsorption energy for the adsorbate, which is usually argon, krypton or nitrogen gas. The surface site is defined as the area on the sample where one molecule can adsorb onto.
- Adsorption of the solvent at one site occurs independently of adsorption at neighboring sites.
- Activity of adsorbate is directly proportional to its concentration.
- Adsorbates form a monolayer.
- Each active site can be occupied only by one particle.

B.4 Temkins model

The Temkins isotherm model assumes that the adsorption energy decreases linearly as a result of increase surface coverage due to increase in surface coverage. Temkin model considers the effects of indirect adsorbate/adsorbate interactions on the adsorption process [228] and is only valid for an intermediate range of ion concentrations [226, 227]. The linear form of Temkin isotherm model is given by the equation:

$$q_e = BlnA + BlnC_e \tag{B.5}$$

$$B = \frac{RT}{b_T} \tag{B.6}$$

Where B is in ($\frac{J}{mol}$) corresponding to heat of adsorption with R as the ideal gas constant, 8.314 ($kJ/kmol$) and T(K) as an absolute temperature. b_T is the Temkins isotherm constant and A(L/g) is the equilibrium binding energy constant corresponding to maximum binding energy.

B.5 D-R model

Dubinin-Kaganer-Radushkevich model also known as DKR or D–R model, is reported to be more general than the Langmuir and Freundlich isotherms as it helps to determine the apparent energy of adsorption. D–R model characterises the porosity of adsorbent toward the adsorbate pore filling mechanism and does not assume a homogeneous surface or constant sorption potential [229]. This empirical adsorption model is generally applied to express adsorption mechanism with Gaussian energy distribution onto heterogeneous surfaces and is only suitable for intermediate range. It presumes a multilayer character involving Van Der Waal's forces, applicable for physical adsorption processes, of adsorbate concentrations [228]. A distinguishing feature of the Dubinin-Radushkevich isothermis the fact that it is temperature dependent; hence when adsorption data at different temperatures are plotted as a function of logarithm of amount adsorbed versus the square of potential energy, all suitable data can be obtained [230]. The Dubinin-Kaganer-Radushkevich (DKR, D–R) model has the linear form of :

$$lnq_e = lnq_m - \beta\epsilon^2 \tag{B.7}$$

Polanyi potential, ϵ, can be calculated with following equation where R is gas constant (8.31 $Jmol^{-1}\ k^{-1}$) and T is absolute temperature:

$$\epsilon = RTln(1 + \frac{1}{C_e}) \tag{B.8}$$

$$E = \frac{1}{\sqrt{2\beta}} \tag{B.9}$$

Where $\beta(mol^2/J^2)$ is D–R constant and E (kJ/mol) is mean adsorption energy

B.6 Herkin-Jura model

Harkin-Jura isotherm model assumes the possibility of multilayer adsorption on the surface of absorbents having heterogeneous pore distribution. This model is expressed as :

$$\frac{1}{q_e^2} = \frac{B}{A} - (\frac{1}{A})logC_e \tag{B.10}$$

B and A are both Herkin-Jura constant and q_e is the maximum adsorption whilst C_e is the equilibrium concentration.

B.7 Jovanovic model

The Jovanovic model is a sub model of Langmuir theory, whilst it assumes the possibility of some mechanical contacts between the adsorbate and adsorbent [231]. The

linear form of the Jovanovic isotherm is expressed as follows, K_J is Jovanovic constant:

$$lnq_e = lnq_{max} - K_J C_e \tag{B.11}$$

B.8 BET model

The concept of the BET theory is an extension of the Langmuir theory [232], which is a theory for monolayer molecular adsorption to multilayer adsorption with the following hypotheses:

1. Gas molecules physically adsorb on to solid surfaces in layers of infinite thickness;
2. There is no interaction between each adsorption layer;
3. The Langmuir theory can be applied to each layer;

Gas adsorption measurement is widely used for determining the surface area and pore size distribution of variety of solid materials via gas. BET model can only be applied for liquid on solid media, if correction terms are considered [233]. Gas adsorption as a function of pressure does not follow a simple linear relationship. Therefore, an appropriate mathematical model must be used to calculate the surface area: The BET equation describes the relationship between the number of gas molecules adsorbed (X) at a given relative pressure (P/P_0), where C is a second parameter related to the heat of adsorption [166].

$$\frac{1}{X[(P_0/P)-1]} = \frac{1}{X_m C} + \frac{C-1}{X_m C}(\frac{P}{P_0}) \tag{B.12}$$

P is the vapour pressure or equilibrium vapour pressure that is the pressure of a vapour in thermodynamic equilibrium with its condensed phases in a closed system. All liquids and solids have a tendency to evaporate into a gaseous form, and all gases have a tendency to condense back to their liquid or solid form. P_O is saturation pressure that is the pressure for a corresponding saturation temperature at which a liquid boils into its vapour phase. Based on BET model, there are 6 types of possible adsorption isotherms as presented in Figure B.2 [165]. Type IV, V of N_2 adsorption/desorption hysteresis loops can be divided into four main types, which correspond to cylindrical pores, ink bottle-shaped pores, parallel plate shaped pores, and wedge slit-shaped pores as they are shown in Figure B.2.

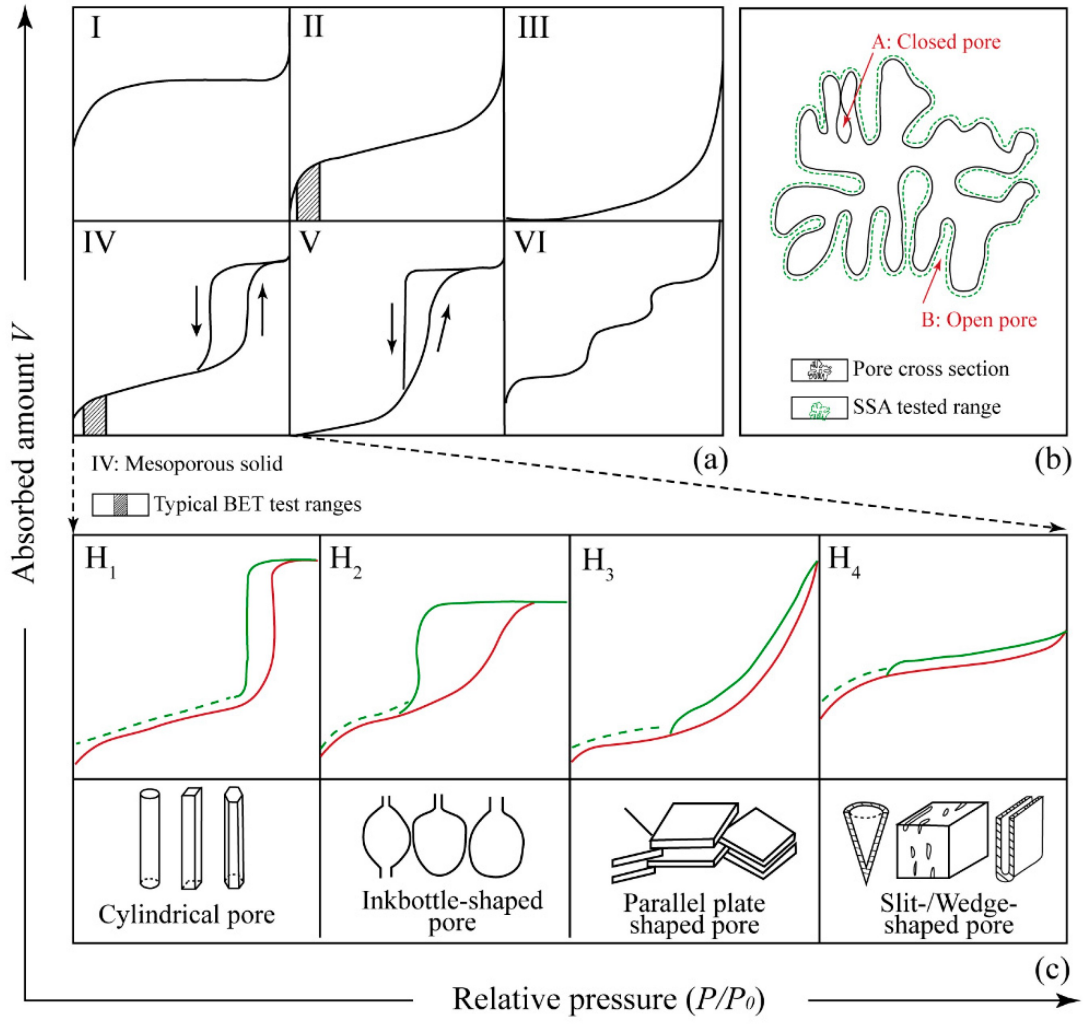

Figure B.2: IUPACK isotherm classification [165].